



University
of Glasgow

Burnside, Neil Murray (2010) *U-Th dating of travertines on the Colorado Plateau: implications for the leakage of geologically stored CO₂*. PhD thesis.

<http://theses.gla.ac.uk/1988/>

Copyright and moral rights for this thesis are retained by the Author

A copy can be downloaded for personal non-commercial research or study, without prior permission or charge

This thesis cannot be reproduced or quoted extensively from without first obtaining permission in writing from the Author

The content must not be changed in any way or sold commercially in any format or medium without the formal permission of the Author

When referring to this work, full bibliographic details including the author, title, awarding institution and date of the thesis must be given

**U-Th dating of travertine on the Colorado
Plateau: Implications for the leakage of
geologically stored CO₂**

Neil Murray Burnside

B.Sc. (Hons.), Glasgow

Thesis presented for the degree of Doctor of Philosophy (Ph.D)

University of Glasgow

Department of Geographical and Earth Sciences

March 2010

© Neil M. Burnside, 2010

Dedication

In loving memory of my papa

William Alexander Burnside

Abstract

In order to avoid the damaging climatic consequences of rising atmospheric CO₂, and reduce current atmospheric CO₂ concentrations to pre-industrial levels, anthropogenic CO₂ emissions must be mitigated by capturing CO₂ at power plants and storing it for thousands of years. Underground storage within deep geological formations, such as depleted gas and oil fields or deep saline aquifers, is the best understood solution for storage of CO₂. In order for this method to gain more public and political acceptance it is important to characterise the potential causes, quantities and rates of CO₂ release that could result if leakage were to occur from anthropogenic storage projects.

This study examines two sites in the Colorado Plateau where faulted and actively leaking CO₂ reservoirs provide natural analogues for failed anthropogenic storage sites. The two sites in question, the Little Grand Wash and northern Salt Wash graben faults are situated at the northern end of the Paradox Basin in Utah and represent classic three way traps due to juxtaposition of the shallow, north plunging Green River anticline against a set of east-west trending normal faults. In addition to active leakage sites in each area there are numerous fossilised travertine deposits. Along the Little Grand Wash fault the ancient mounds are restricted to the fault trace whereas ancient travertine mounds associated with the northern fault of the Salt Wash graben are far more numerous and occur up to ~530 m into the footwall of the fault. This more diffuse pattern of flow is due to the outcropping of unconfined aquifer units at the surface. A total of 45 U-Th dates from the majority of these travertine mounds provides a unique data set. The oldest deposits from the Little Grand Wash and northern Salt Wash graben faults produced ages of $113,912 \pm 604$ and $413,474 \pm 15,127$ years respectively. Repeat ages show reasonable reproducibility and analytical errors on results are of the order of 1% of the ages. The coupling of travertine elevation measurements with their radiometric ages gives an incision rate for each site. A rate of 0.342 m/ka for the Little Grand Wash fault relates directly to Green River incision and agrees with previous work on the Colorado Plateau, providing a further data point for characterisation of uplift of the province. For the northern fault of the Salt Wash graben a rate of 0.168 m/ka for the tributaries running through the area gives a robust method with which to estimate ages for un-dated mounds.

The results of radiometric dating and incision rate age estimation of travertine mounds shows that leakage can last for timescales of 100,000's of years, while high resolution U-Th dating of an individual mound demonstrated that leakage from a single point can last for a minimum of ~11,000 years. A range of travertine ages show that leakage to the surface has constantly switched location through time, while the presence of three mounds of distinct age at one location demonstrate that pathways can become repeatedly re-used over periods of ~45,000 years. There is no evidence of temporal periodicity in travertine deposition but there is a distinct spatial pattern of leakage as shown by localised similarities in the initial uranium chemistries of travertine mounds. Initial leakage is proximally located to the axial trace of the Green River anticline and subsequent leakage spreads from this central point along the fault plane in both east and west directions. The switching of fluid flow pathways to the surface can be explained by three main mechanisms: mineralisation, 3-phase interference of CO₂ related fluid flow and seismically triggered alteration in dynamic strain acting upon the hydrology of the faults. These mechanisms have differing influences in each area - demonstrating that the behaviour of fluid flow switching in a system confined to damage zone fractures (Little Grand Wash fault) is different to a system leaking through an unconfined aquifer (northern fault of the Salt Wash graben).

Coupling of travertine ages with estimates of their volumes provided a total worst case scenario for quantity of CO₂ leakage of $6.2 \times 10^6 \pm 1.7 \times 10^6$ tonnes for the Little Grand Wash fault and $7.4 \times 10^6 \pm 2 \times 10^6$ tonnes for the northern fault of the Salt Wash graben. From these totals time averaged leakage rates of 55 ± 15 and 47 ± 13 tonnes/year were estimated for each fault. The leakage rate for the actively precipitating Crystal Geyser travertine (which is the result of anthropogenic exploration drilling) is estimated to be $3,153 \pm 851$ tonnes/year. These total and modern rates provide analogues for leakage via caprock failure and catastrophic wellbore failure. Applying them to large scale storage sites such as Weyburn and Gorgon revealed that for caprock failure complete leakage of these reservoirs will take place over timescales of 10^5 - 10^6 years, while for catastrophic failure of a single well complete leakage of these reservoirs could occur over as little as $10^3 - 10^4$ years. This finding has important implications for the successful monitoring of anthropogenic storage sites.

Table of Contents

Dedication	i
Abstract	ii
Table of Contents	iv
List of Figures	ix
List of Tables	xi
Acknowledgements	xii
Author's declaration	xiv
1 Introduction	1
1.1 The control of fault zones on fluid flow	4
1.2 Properties of fluid flow that influence the subsurface migration of fluids	5
1.2.1 Introduction	5
1.2.2 Single fluid phase	5
1.2.3 Multiple fluid phases	6
1.2.4 Properties of CO ₂ at depth	7
1.3 The influence of fault zones on fluid migration	8
1.3.1 Introduction	8
1.3.2 Fault zone architecture	8
1.3.2.1 The effect of fault zone components on fluid flow	10
1.3.2.2 Juxtaposition and cap rock seals	13
1.3.2.3 Vertical fluid migration	13
1.4 Temporal variations in fault permeability	15
1.4.1 Introduction	15
1.4.2 Evidence of temporal flow	16
1.4.3 Processes which lead to episodic fluid flow along faults	17
1.5 Addressing the gaps in our understanding	18
1.6 The U-series dating technique	19
1.7 The phenomenon of radioactivity	21
1.7.1 Introduction	21
1.7.2 Radioactive decay	21
1.7.3 The U-series decay chain	22
1.7.4 Geochemistry of the actinides and their daughters	22
1.7.5 Secular equilibrium and Disequilibrium	23
1.7.6 Cause of Disequilibria	25
1.7.6.1 Introduction	25
1.7.6.2 Oxidation	26
1.7.6.3 Weathering	26
1.7.6.4 Alpha recoil into solution	27
1.7.6.5 Leaching from radiation damaged sites	27
1.7.6.6 Biological Activity	27
1.7.6.7 Further processes	28

1.8	Uranium Series Dating	28
1.8.1	Introduction.....	28
1.8.2	The U-Th dating method.....	29
1.8.3	Uranium series application.....	30
1.8.3.1	Requirements for dating.....	30
1.8.3.2	Checks on the validity of samples for dating	31
1.9	Analytical Procedure	32
1.9.1	Introduction.....	32
1.9.2	Preconcentration	33
1.9.3	Separation Scheme	33
1.9.4	Mass Spectrometry.....	34
1.9.4.1	Variety of techniques available	34
1.9.4.2	Comparison of the TIMS and ICP-MS spectrometric techniques.....	34
1.9.4.3	MC-ICP-MS analysis.....	35
1.9.4.4	Processing of results and error on measurements	37
2	U-series methodology: a case study from the Gulf of Corinth, Greece.	39
2.1	Introduction	39
2.2	Sea level highstand and correlation with coral age	40
2.3	U-series dating of coral.....	40
2.4	The South Alkyonides fault segment	42
2.4.1	Introduction.....	42
2.4.2	C.caespitosa sample sites and U-Th results	43
2.5	Discussion of U-series results	50
2.5.1	Initial Uranium of coral through time	50
2.5.2	Variation in global seawater $\delta^{234}\text{U}$ through time	51
2.5.3	Diagenetic effects on coral $\delta^{234}\text{U}$ and their implications for U-Th dating...52	
2.5.4	Evidence for diagenesis of coral samples	55
2.5.5	Further complications- geological setting of the Gulf of Corinth	60
2.6	Accuracy of Sea level curve and coral growth depth	62
2.6.1	Introduction.....	62
2.6.2	Uncertainty in growth depth of C. caespitosa.....	62
2.6.3	Uncertainty in the sea level curve	64
2.6.4	Conceptual model for correlation of ancient coral ages with sea-level highstand65	
2.6.5	Implications for correlation of previous Corinth studies	67
2.6.6	Implication for correlation in the present study.....	68
2.7	Summary: U-series methodology and slip rate	69
2.7.1	U-series methodology.....	69
2.7.2	Calculating slip rates of the South Alkyonides fault segment	70
3	The Little Grand Wash fault and northern fault of the Salt Wash graben	74
3.1	Introduction	74
3.2	Geological setting.....	74
3.2.1	Tectonic history of the Paradox Basin.....	80
3.3	Stratigraphy and lithology.....	82
3.3.1	Stratigraphy within the field areas	82
3.3.2	Important lithologies.....	82
3.4	Travertine.....	85

3.4.1	Source of CO ₂	86
3.4.2	Source of water supplying springs	87
3.4.3	Classification of travertine.....	88
3.4.4	Formation of travertine.....	89
3.4.5	Previous work on travertine of the Little Grand Wash and northern Salt Wash Graben faults	91
3.4.6	Travertine lithofacies.....	92
3.4.6.1	Introduction.....	92
3.4.6.2	Altered host rock.....	92
3.4.6.3	Cemented breccia.....	93
3.4.6.4	Layered mats.....	94
3.4.6.5	White banded veins	97
3.4.6.6	Brown banded veins	98
3.4.7	Conceptual model of travertine mound evolution	101
3.5	Observations from the field.....	104
3.5.1	Introduction.....	104
3.5.2	Travertine deposits	104
3.5.3	Actively precipitating travertine	108
3.5.4	Ancient travertine deposits.....	111
3.5.4.1	Ancient travertine occurrence and preservation	111
3.5.4.2	Association of layered mat and white banded vein facies	112
4	Results of U-series analysis of travertine deposits.....	117
4.1	Introduction	117
4.2	U-series analysis of travertine deposits	118
4.2.1	Uranium incorporation into travertine mounds.....	118
4.2.2	Travertine morphologies useful for dating.....	118
4.3	Discussion of U-series age results.....	124
4.3.1	Introduction.....	124
4.3.2	Reproducibility	124
4.3.3	Detailed study of travertine L4	126
4.3.4	Age analysis to support field observations	128
4.3.5	Layered mat analysis.....	129
4.3.5.1	Suitability of layered mat facies for age determination	130
4.3.5.2	Geochemical association of layered mats and white banded vein.....	132
4.4	Variation of uranium chemistry between mounds	132
4.4.1	Introduction.....	132
4.4.2	Variation in $\delta^{234}\text{U}$	133
4.4.3	Spatial trend of $\delta^{234}\text{U}$	135
4.4.4	Analysis of modern waters.....	137
4.5	Age estimation of un-dated travertine	138
4.5.1	Introduction.....	138
4.5.2	Incision on the Little Grand Wash	139
4.5.3	Incision on the Salt Wash graben	141
4.5.4	Travertine age estimate results.....	145
4.6	Travertine Volumetrics.....	147
4.6.1	Introduction.....	147
4.6.2	Volume and lifespan estimates of travertine mounds	147
4.6.3	Volume and number of travertine through time	152
4.7	Discussion.....	155

4.7.1	U-Th age analysis of travertine	155
4.7.2	Implications for determination of incision rate	156
4.7.3	Volumetric comparison of Little Grand Wash and Salt Wash graben travertine deposits.....	157
4.7.4	Actively precipitating travertine	159
4.7.5	Pattern of flow to the surface	159
4.7.6	Timing of fluid flow as recorded by U-series results	159
4.7.6.1	Statistical Analysis of timing of travertine deposition	160
4.7.6.2	Gaps in the record	163
4.7.7	Spatial relationships of travertine deposits.....	164
4.7.7.1	Relationships from U-Th age analysis.....	164
4.7.7.2	Relationships from $\delta^{234}\text{U}$	165
4.8	Summary: Lessons from U-Th dating	168
5	Implications for fluid flow.....	171
5.1	Introduction	171
5.2	External factors	171
5.2.1	Seismic activity	171
5.2.1.1	Earthquake activity on the Little Grand Wash and northern Salt Wash graben faults	174
5.2.1.2	Geomorphological constraint on fault movement	175
5.2.1.3	Constraining movement on the Little Grand Wash fault	175
5.2.1.3.1	Evidence from travertine deposits	175
5.2.1.3.2	Evidence from river terrace deposits.....	176
5.2.1.4	Constraining movement on the northern Salt Wash graben fault	178
5.2.1.4.1	Evidence from travertine deposits	178
5.2.1.4.2	Evidence from stream profiles.....	179
5.2.1.5	Qualitative and quantitative estimates of fault quiescence	179
5.2.1.6	Hydrological changes induced by seismicity on other faults.....	181
5.2.1.6.1	Introduction.....	181
5.2.1.6.2	Stress orientation of the Little Grand Wash and northern Salt Wash graben faults	183
5.2.1.6.3	Yellowstone case study	184
5.2.1.6.4	Potential sources for triggering of seismicity at the Little Grand Wash and Salt Wash graben faults.....	188
5.2.2	Climatic Effects.....	191
5.2.2.1	The past climate of the Colorado Plateau	192
5.2.2.2	Comparison with regional and global climatic records.....	195
5.3	Internal forcing factors.....	196
5.3.1	Fault structure and fluid flow effects.....	196
5.3.1.1	Variation in fault structure	196
5.3.1.2	Structural setting of springs.....	197
5.3.1.3	Variations in fault permeability	198
5.3.1.4	Maintenance of fracture permeability	199
5.3.1.5	Potential fluid flow regime	200
5.3.1.6	The effect of CO_2 on fluid flow.....	202
5.3.2	The potential effects of mineral precipitation.....	207
5.3.2.1	Mineralisation observed in the field.....	207
5.3.2.2	Previous work on precipitation	209
5.3.2.3	Precipitation rates.....	209
5.4	Summary: The likely causes of switching	210

6	Calculation and risk assessment of CO₂ leakage	219
6.1	Introduction	219
6.2	Quantity and leakage rates of CO ₂	219
6.2.1	Total volume of leaked CO ₂	219
6.2.2	Leakage rates and Flux	223
6.3	Discussion	226
6.3.1	Comparison with other leakage rate estimates on LGW	226
6.3.2	Comparison with other natural CO ₂ sources	227
6.3.3	Implications for anthropogenic storage sites	230
6.3.4	Monitoring and verification of leakage	233
6.4	Leakage risks for storage sites	236
6.4.1	Site characterisation	237
6.4.2	Escape scenarios	238
6.4.3	Risk assessment and lessons for anthropogenic storage	239
7	Concluding remarks and suggestions for future work	243
7.1	Conclusions	243
7.2	Future work	249
7.2.1	Future work at the Utah field sites	250
7.2.2	Future work on CO ₂ leakage in general	253
	Appendix A	256
	Standard data for uranium and thorium analyses	256
	A-1 Uranium standards	256
	A-2 Thorium standards	257
	Appendix B	258
	XRD results of <i>C.caespitosa</i> samples	258
	Appendix C	260
	Seismic record of major regional faults	260
	C-1 The Hurricane fault	260
	C-2 The Wasatch Front	261
	C-3 The Rio Grande Rift	261
	C-4 The Pajarito fault	262
	C-5 The Calabacillas fault	262
	C-6 The Hubbell Spring fault	262
	C-7 The La Jencia fault	263
	Appendix D	265
	GPS reference points for travertine mounds	265
	D-1 The Little Grand Wash fault	265
	D-2 The northern fault of the Salt Wash graben	266
	References	267

List of Figures

Figure 1.1: The fault zone conceptual model of Caine et al. (1996).	9
Figure 1.2: Schematic of the main structural elements of a fault damage zone.	10
Figure 1.3: 3D numerical modelling of the mechanical behaviour of fault intersections. ...	12
Figure 1.4: Time-slice through a seismic data cube of a large scale fault system.....	12
Figure 1.5: Schematic fluid flow model for temporal permeability.	16
Figure 1.6: The U-series decay chain.	24
Figure 1.7: Variation of [$^{234}\text{U}/^{238}\text{U}$] and [$^{230}\text{Th}/^{234}\text{U}$] with time in a closed system.	30
Figure 1.8: Work flow for processing of U-Th results.....	38
Figure 2.1: Gulf of Corinth and the Perachora Peninsula.	43
Figure 2.2: Log of the east wall of the hotel complex excavation.....	46
Figure 2.3: Plots of Uranium chemistry for coral studies.	53
Figure 2.4: Model evolution curves for diagenetic effects on coral $\delta^{234}\text{U}$	54
Figure 2.5: Photomicrograph images of <i>C. caespitosa</i> samples.....	56
Figure 2.6: XRD analysis results of U-Th dated coral samples.....	57
Figure 2.7: EBSD phase map images of <i>C. caespitosa</i> samples.....	58
Figure 2.8: Strontium analysis results for coral samples.	59
Figure 2.9: Hydrological evolution of the Gulf of Corinth through time.....	61
Figure 2.10: Relative sea level curve with marked ages of <i>C. caespitosa</i> samples.	63
Figure 2.11: Global sea level curve showing uncertainty around sea level highstand.	66
Figure 2.12: Slip rate calculation for the South Alkyonides fault segment.	72
Figure 3.1: Geological features of the Paradox Basin and surrounding region.	76
Figure 3.2: Regional geology of the Little Grand Wash and northern Salt Wash faults.....	78
Figure 3.3: Surface geology of the Little Grand Wash and Salt Wash graben field sites. .	79
Figure 3.4: Sketch cross section of the geomorphology of the Little Grand Wash.	83
Figure 3.5: Generalised stratigraphic section down to the upper Mississippian for the Green River area.	84
Figure 3.6: Generalised cross section of ground water sources for spring deposits.	87
Figure 3.7: Field photographs of travertine facies.	95
Figure 3.8: EBSD image of layered mat facies.....	97
Figure 3.9: Field photographs of banded vein facies.....	100
Figure 3.10: Photomicrographs of banded vein morphologies.....	101
Figure 3.11: Conceptual model of travertine mound evolution.....	103
Figure 3.12: The Little Grand Wash and Salt Wash graben field sites.....	106
Figure 3.13: The Crystal Geyser (mound L1).	107
Figure 3.14: Active springs of the Salt Wash graben.....	110
Figure 3.15: Ancient travertine mounds on the Little Grand Wash fault.....	112
Figure 3.16: Ancient travertine along the northern fault of the Salt Wash graben.	114
Figure 3.17: Evidence for association of layered mats and white banded veins.	116
Figure 4.1: EBSD images of layered mats from mound L1.....	119
Figure 4.2: Travertine maps of the Little Grand Wash and Salt Wash graben field sites.	121
Figure 4.3: Field image and schematic of the L4 travertine mound.	127
Figure 4.4: Field images of mounds L2 and L3.	129
Figure 4.5: Comparison of $\delta^{234}\text{U}$ for layered mat and white banded vein facies.	131
Figure 4.6: Variation of $\delta^{234}\text{U}$ vs. time and space.....	134
Figure 4.7: Conceptual models for observed variations in $\delta^{234}\text{U}$ chemistry	135
Figure 4.8: Satellite image of the Little Grand Wash tributary.....	140

Figure 4.9: Incision rate graph for the Little Grand Wash.140

Figure 4.10: Satellite image of the Salt Wash graben tributaries.142

Figure 4.11: River terraces associated with the travertine mounds.143

Figure 4.12: Incision rate graphs for the Salt Wash graben.....144

Figure 4.13: Timing of travertine activity.146

Figure 4.14: Volume estimates for the Little Grand Wash travertine.....148

Figure 4.15: Cumulative plots for number and volume of travertine deposits.154

Figure 4.16: Travertine volume maps.....158

Figure 4.17: Timing of travertine occurrence for both field areas.....161

Figure 4.18: Statistical analysis of mound timing.....162

Figure 4.19: Age maps and distance plots of U-series results.....168

Figure 4.20: Age distance plot for the Salt Wash graben including estimated ages.....168

Figure 5.1: Evidence for lack of recent movement on the Little Grand Wash fault.....177

Figure 5.2: Sketch cross section of the geomorphology of the Little Grand Wash.....178

Figure 5.3: Evidence for lack of recent movement on the northern Salt Wash graben fault.
.....180

Figure 5.4: Data from World Stress Map and Location of major regional faults.185

Figure 5.5: Timeline of travertine occurrence against regional seismic activity.....189

Figure 5.6: Timeline of travertine occurrence against climatic records.193

Figure 5.7: Structural settings of springs associated with faulting.197

Figure 5.8: Plot of protolith against fault permeability for fluid flow regimes.....201

Figure 5.9: Possible phase conditions of two component water- CO₂ systems.....203

Figure 5.10: CO₂ saturation line and fluid pressure- temperature profiles for a setting with
typical geothermal profile.204

Figure 5.11: Flow through time for CO₂ rich fluid.....205

Figure 5.12: Plot of potential switching mechanisms.....215

Figure 5.13: Methods for switching of fluid flow pathways.....217

Figure 6.1: Plots of total leakage and leakage rates.....225

Figure 7.1: Travertine deposit from the St.Johns area.251

List of Tables

Table 1.1: Operating conditions for the MC-ICP-MS (Ellam and Keefe, 2006).	36
Table 2.1: U-Th chemical and isotopic data for <i>C. caespitosa</i> coral samples	48
Table 2.2: Comparison of several U-Th coral studies from the Gulf of Corinth.	49
Table 3.1: Permeability and porosity of lithologies present in the field areas.	85
Table 3.2: Breakdown of ancient travertine mounds.	105
Table 4.1: Age results of radiometric dating of travertine samples from the Little Grand Wash fault.....	122
Table 4.2: Age results of radiometric dating of travertine samples from the northern fault of the Salt Wash graben.	123
Table 4.3: Table of repeat U-series analysis.	125
Table 4.4: U-Th ages for testing field observations.	128
Table 4.5: Comparison of layered mat and white banded vein results.....	130
Table 4.6: Age estimation of non-dated mounds.	146
Table 4.7: Volume estimates for the Little Grand Wash travertine.....	148
Table 4.8: Volume estimates for the Salt Wash graben travertine.....	149
Table 4.9: Lifespan estimates of Little Grand Wash travertine.	150
Table 4.10: Lifespan estimates of Salt Wash graben travertine.....	150
Table 4.11: Summary of travertine volumes and lifespan.	158
Table 5.1: Permeability and porosity of strata present in the field.	183
Table 6.1 CO ₂ leakage and flux estimates.	222
Table 6.2: Worst case scenario for leakage and flux of CO ₂	223
Table 6.3: CO ₂ flux measurement comparisons.	228
Table 6.4: FEP analysis for the faults in this study.	239

Acknowledgements

This thesis mainly comprises of the thoughts and work of one man, however, it could have never been completed without the guidance and support of many people. Off the top of my head there seems to be far too many to list- but here goes...

Firstly I would like to thank my supervisors, Rob Ellam and Zoe Shipton, for their guidance, support and detailed discussion throughout the development of this body of work. The initial concept of this thesis gave it room to grow in several directions which gave my talent for going off in a tangent the opportunity to run wild at times- so additional thanks goes to them for helping me to keep all the topics roped together and everything moving in as linear a fashion as possible. I would additionally like to thank Zoe for all her extra help and understanding when I was in the horrible depths of Lymes disease.

Special mention must go to the now majorly interdisciplinary faults and fluid flow research group (FAFF) set up by Zoe and Becky Lunn. All members deserve some credit for their little pieces of advice and useful criticisms of my work- it is always handy to have people to think outside of your box and state the otherwise obvious. So appreciation goes to Becky, Jamie, Stella, Heather, Susan, Yannick, Euan and Ally.

Most of the staff and students At the University of Glasgow have aided me even if it was in their own small way. I would like to thank all of the support staff especially Gary, John, Robert, Kenny, Mike and Peter for teaching me how to work the equipment and how to do all the grubby stuff. I would also like to thank my student colleges, past and present, from the 414 and some of those unlucky to be involved with the dark side that is human geography. So cheers to: Paul, Dan, Dunc, Fernando, Laura, Clare, Jo, Heikko, Dave and Cheryl for the totally random banter that proved a welcome distraction from the sometimes heavy going work. Also big thanks to Vern and Nick for insightful discussions about beasties and coral.

A huge slice of appreciation must also go to Kate Dobson, without her help in dealing with the devil that possessed my Microsoft word the computer that was

used to type up this thesis would have disappeared out of the window a very long time ago.

For my time at SUERC I have to say thank you to Kathy, Vinnie, Anne, Valerie and Maria for teaching me about all the techniques required to perform the analysis carried out for this body of work; Andrew for all my computer issues; and to Paul for in depth conversations about the state of Scottish Fitba and the perfect pub quiz.

Thanks to Stuart Gilfillan and Niko Kampman for stimulating discussion, both in the Utah field sites and especially over quite a few cheeseburgers and too many beers at Rays Bar. Steve Nelson also gave valuable insights both in relation to the field and the dress sense of the residents in southern Utah. Finally for Utah I would like to show appreciation to Joel Pederson for 'learning me' some geomorphology and showing me how all people should cut their grass. For the work in the Gulf of Corinth, I would like to thank Gerald Roberts for drawing our attention to this area and for letting me tag along on the Birkbeck University Easter field trip- I will never forget spending every morning watching the dolphin acrobatic display whilst enjoying my Greek buffet breakfast. Also than you to Charlie Underwood for teaching me about the wonders of crustaceans and Pinna shells.

Big thanks to my ever supportive flesh and blood for all their help and understanding especially during the tough times, and to the extended family of 'Team Spiderman' for not letting me take myself too seriously and dragging me off down the pub when I really didn't want to, but really desperately needed it.

Finally, I come to Maria. If it wasn't for her love and support it is fair to say that this thesis may never have been completed. She was the one who got me around the ineptitude of the NHS and into the hands of the SIS doctor who diagnosed my illness. During the darkest days of my Lyme disease when I couldn't physically get out of bed and felt like I was staring down a bottomless pit, it was her who pulled me back from the edge. At times over this last year, the most tormenting and difficult of my life, she has carried me on her shoulders, and for that, I am forever in her gratitude.

Author's declaration

The material presented in this thesis is the result of independent research undertaken by myself between October 2006 and March 2010. This work was supervised by Prof. Rob Ellam and Dr. Zoe Shipton. All work by other researchers that is quoted in this thesis is given full acknowledgement in the text.

Neil M. Burnside March

2010.

1 Introduction

World wide power generation from the combustion of fossil fuels such as oil, natural gas and coal currently discharges in excess of 11.4 billion tonnes of CO₂ per year into the Earth's atmosphere (CARMA, 2008). Because of the expanded use of fossil fuels, the atmospheric concentration of CO₂ has risen from preindustrial levels of 280 ppm to a present day value of approximately 365 ppm (Anderson and Bows 2008). It is no coincidence that as industry has developed over the last 100 years the Earth's surface has warmed by 0.6°C (Hulme and Jenkins, 1998). To stabilise the climate global emissions of CO₂ must be significantly reduced to pre-industrial levels. In order to achieve this whilst maintaining our current dependence on fossil fuels, bridging technologies such as CO₂ capture and storage must be utilised whilst alternative low emission energy production techniques, that use renewable sources such as wind and tidal power, are developed to the stage were they are economically competitive and able to meet current global energy demands.

Several possible methods exist for the storage of CO₂; burial in geological reservoirs and unmineable coal seams, and disposal in the deep sea, lakes beneath ice caps or in layered basalt provinces are just some of the suggested options (Baines and Worden, 2004; Broecker, 2008). Most of these strategies raise concerns regarding practicality, safety, and economics. Of the various options, storage underground in geological reservoirs, such as abandoned gas and oil fields or deep saline aquifers, is the best understood (Allis et al., 2001; Chadwick et al., 2004; Bachu, 2008). Large amounts of natural gas are already stored within these reservoirs and the existence of long-lived natural accumulations of CO₂ suggests that these storage systems are very stable (Holloway et al., 2007). In addition, injection of CO₂ into depleted oil reservoirs may allow for enhanced oil recovery which provides an economic incentive. However, there are signs that the general public are sceptical of the merits of geological storage due to the potential risk of leakage from anthropogenic CO₂ reservoirs (Van Noorden, 2010). It is therefore important to determine how leakage of CO₂ storage systems can occur and what the possible quantities and rates of CO₂ leakage will be so that the effects of CO₂ release at potential storage sites can be better understood.

Carbon dioxide reservoirs associated with the Little Grand Wash and northern Salt Wash graben faults, in Utah, USA, provide natural analogues for leaky anthropogenic storage sites. In these locations fault related flow of CO₂-charged waters to the surface demonstrates the effects of CO₂ leakage from a subsurface aquifer unit. The presence of numerous fault related travertine mounds in these areas makes them unique sites where the history of leakage over timescales of 100,000's of years can be studied. Within this thesis the fluid flow history of these faults has been quantitatively determined by U-Th dating of the travertine mounds. Coupling of radiometric ages with measurement of the dimensions of travertine mounds has also allowed for an estimation of the volume and rates of leakage of CO₂ to the surface. The results presented throughout this thesis therefore have potentially important implications for the acceptance of geological storage as a viable means of abating CO₂ emissions into the Earth's atmosphere. A brief summary of the thesis structure is provided in the following paragraphs.

The remainder of this chapter introduces the two main themes of this study-fault influenced fluid flow and radiometric dating. The aim of this thesis is to bring these themes together in order to quantify the history of fluid flow along the Little Grand Wash fault and the northern fault of the Salt Wash graben. The discussion of the control of fault zones on fluid flow mainly focuses on vertical flow as the migratory pathways of CO₂ charged waters to the surface along both the Little Grand Wash fault and the northern fault of the Salt Wash Graben are sub-parallel to the fault plane. The second part of the chapter is dedicated to the theory and application of the U-Th dating technique utilised in the study of the travertine deposits found within the field areas.

Chapter 2 presents an individual case study which involved dating of *Cladocora caespitosa* coral specimens in order to assess slip rates on the South Alkyonides fault segment on the Perachora Peninsula in the Gulf of Corinth, Greece. This was carried out in order to assess the U-series dating technique and to investigate active slip on a large normal fault. As coral is commonly used for application of U-Th age determination within palaeo-climate and palaeo-ocean studies this chapter also contains a critique of the suitability of coral for use in this type of analysis.

The Little Grand Wash and Salt Wash graben field sites are introduced in Chapter 3. In order to characterise the geological setting and tectonic history for the areas a discussion of previous work on these field sites and the Colorado Plateau is carried out. Building upon previous work, new observations from the field are then used to provide a detailed explanation of travertine formation for these particular areas. Within this explanation an insight into the components required for travertine construction and their possible sources is presented. Finally, an assessment of the timing of fault movement on both the Little Grand Wash fault and the northern fault of the Salt Wash graben is carried out using field evidence from geomorphological observations involving travertine and ancient river terrace deposits.

The results of U-Th dating of travertine are presented in Chapter 4. An examination of which travertine facies are suitable for dating is carried out in order to determine which gives the most reliable age results. The major aim of age analysis was to provide a data set with which to decipher the history of fluid flow to the surface along each fault, to this end a discussion of the evolution of leakage to the surface through time is presented. The size and quality of the data set also allowed for further use in several subsidiary studies. Age results of samples were used to help assess field observations, focussed dating of a single mound was implemented in order to learn more about life-spans of travertine mounds, whilst variation in chemistries of samples were used to determine the source of uranium within the deposits. By combining the U-Th age results with elevation measurements and thickness estimates an incision rate for each area was calculated and volume and lifespan estimates for each travertine mound were determined. This allowed for the age estimation of un-dated mounds and provided information for the comparison of travertine deposits across the Little Grand Wash and northern Salt Wash graben field sites.

The implications of U-Th results for fluid flow evolution along the Little Grand Wash and northern Salt Wash graben faults are discussed in Chapter 5. This chapter examines the cause of the switching of fluid pathways to the surface throughout the history of flow. The potential causes of switching are presented within two categories- external and internal forcing. External factors include seismic activity and climatic variation, whilst internal factors include local fault structure and mineral precipitation effects. These processes are investigated in

order to assess which is the most likely mechanism to cause the fluid flow switching observed from the results of Chapter 4.

The leakage of CO₂ along the Little Grand Wash and northern Salt Wash graben faults and the risk it poses is discussed in Chapter 6. In this chapter the total volume of CO₂ leaked to the surface in each field area is estimated. By combining these total leakage estimates with the radiometric dating of travertine leakage rates were calculated for the total length of fluid flow history on each fault and for current sites of active precipitation. These two separate rates represent proxies for caprock failure and wellbore failure and can therefore be used to discuss the implications of these two varieties of leakage for current anthropogenic storage examples. With emphasis placed on the findings of this thesis a review of site characterisation, and monitoring and verification of leakage for geological storage sites is carried out. To conclude, an assessment of the risk posed by leakage at the Little Grand Wash and northern Salt Wash graben faults is presented and recommended steps are suggested for the monitoring and remediation of the leakage displayed by these systems.

1.1 The control of fault zones on fluid flow

The following section presents a review of both the physical parameters and structural factors that can effect fluid migration, with particular emphasis on vertical fluid flow along faults. Direct observations of fault related fluid flow are infrequent; however, a wide range of information is available if both direct and indirect observations are integrated from a range of industries and research areas. The subsections comprising the first part of this chapter are therefore an overview of current research into, and observations of, fault controlled fluid flow. The physical properties of fluid flow are discussed within subsection 1.2. The influence of faults in fluid migration is then considered in subsection 1.3, with subsection 1.4 further developing this topic by discussing temporal variability in fault zone permeability. This section formed part of a position paper commissioned by Statoil Hydro. Though the following represents my own contribution to the report it was considerably aided by discussion with the co-authors of that paper; Zoe Shipton, Rebecca Lunn and Jerry Fairley.

1.2 Properties of fluid flow that influence the subsurface migration of fluids

1.2.1 Introduction

An important control on the migration of fluids is the fluid flow properties of rocks. The primary driver of subsurface fluid flow is gradients in hydraulic head between points, although other gradients, such as temperature and density, may also drive fluid flow. Relevant aspects to consider for predicting flow rate and direction depend on the number of fluid phases present. This is an especially important consideration for CO₂ systems where several phase combinations between liquid, aqueous, gaseous and supercritical CO₂, may be present. If two or more of these phases are present (e.g. water-gas/water-supercritical CO₂) multiphase flow properties such as relative permeability and capillary entry pressure of the rock system are more important.

1.2.2 Single fluid phase

The porosity of an earth material is the percentage of the rock or soil that is void of material and is dependant on grain size and distribution, arrangement of grains, and cementation (Fetter, 2001). Porosity of fault gouge, for example, may be lower than the host rock because brittle fracturing reduces the grain size and produces a wider grain size distribution. The shape of grains also has an affect with well rounded grains potentially creating low porosity due to their ability to pack closely together, whilst irregular grains can lead to higher porosities (Meinzer, 1923). An important aspect for flow through rocks is the size and interconnected nature of the pore spaces, so effective porosity is of potentially greater importance for fluid flow than the total porosity of a material. This property considers only the porosity that is available for fluid flow, excluding pores that are not large enough to contain water molecules and those that are not interconnected. Faulting and fracturing of rock during brittle deformation can lead to generation of further interconnected porosity, and lead to higher intrinsic permeabilities within affected rock. Intrinsic permeability is the ability of a material to permit fluid to flow through it. The size of pore throats, the degree of pore and fracture interconnection, and the amount of open space are all significant factors (Fetter, 1993). Intrinsic

permeability is often used in preference to other measures of the ease of fluid flow, such as hydraulic conductivity, because it is independent of the properties of the fluid and depends only on the properties of the rock.

1.2.3 Multiple fluid phases

The increased complexity introduced by two-phase flow places more importance on relative permeability and interfacial pressure in the determination of fluid flow. Relative permeability, the ratio of intrinsic permeability of fluid at given saturation ratio to total intrinsic permeability of the rock, provides a comprehensive description of the ease with which various phases can migrate because pore spaces tend to not be occupied by any one phase (Fetter, 1993). Most models of relative permeability include a provision for a residual saturation. This is the level of saturation below which a phase becomes disconnected and immobile. As a result of the presence of phases at or near the residual saturation the sum of the relative permeabilities for all phases is almost always less than one. Commonly used models of relative permeability for two-phase systems have been proposed by a number of authors (e.g., Mualem, 1976, Ringrose et al., 2003; Manzocchi et al., 2002; Pruess, 2004). There are fewer models for relative permeability in three-phase systems, in part due to the difficulty and expense of laboratory studies for such systems (Stone, 1970; 1973). This makes it more difficult to assess the effects on permeability of the presence of three CO₂ phases at any one time.

When two or more phases are present the influence of interfacial pressure (often referred to as capillary pressure) must be considered. When two immiscible substances are in contact, a curved surface will tend to develop at the interface. The curvature of this interface is a function of the difference between the pore pressures of the two fluids, and the contact angle of the fluids with the surrounding rock. The contact angle is the angle formed between the solid and a drop of liquid placed on the solid. It is a function of the surface free energy of the liquid and the change in area of the solid covered by the liquid (Adamson, 1990). If the contact angle between the solid and the liquid is greater than 90° the solid is deemed to be 'not wet'. Geological materials are commonly found to be "water wet" (the contact angle between water and most rocks is very nearly 0°). In order to invade a pore filled with a wetting phase, the interfacial pressure of the non-wetting phase must

equal or exceed that of the wetting phase, a pressure differential known as the 'capillary threshold' or 'pore entry pressure'.

1.2.4 Properties of CO₂ at depth

Carbon dioxide exhibits complex thermodynamic behaviour in the subsurface, where it may be present in a number of phases in several combinations (Pruess, 2003; 2005). For the range of temperature and pressure conditions found in normal crustal settings, CO₂ can be a gas, liquid or supercritical fluid. Below the CO₂ critical point (temperatures <31.04 °C and pressures <73.82 bars; Vargaftik, 1975) CO₂ can coexist as a free phase (gas or liquid) and in solution in the pore waters (Pruess and Garcia, 2002). With time, CO₂ will be chemically bound in solid minerals, though numerical modelling is needed to quantify this process adequately (Johnson et al., 2004). CO₂ will be governed by single-phase flow if it is completely dissolved in groundwater. Two-phase flow becomes prevalent if there is a drop in the pressure, caused by ascent of the fluid or fault movement, which releases CO₂ from solution. Alternatively, if the groundwater becomes supersaturated with CO₂ and a separate phase of gas or liquid CO₂ is present, the phases are immiscible (Pruess and Garcia, 2002) and will flow in two fluid phases.

To define the likely phase of CO₂ at a given location and time, the temperature and pressure must be known or estimated. Defining the proportion of CO₂ that is free or dissolved in the local groundwater is more difficult. Depending on CO₂ discharge-recharge rates, individual reservoirs could be free phase dominated, aqueous phase dominated or mixed. Free-phase CO₂ present within a reservoir will partition into the liquid phases over time. A drop in pressure, however, can release CO₂ from solution to return to a multiphase situation. Such a drop in pressure can be caused by fault movement and a subsequent change in effective stress; dilation caused by this change in effective stress can also change the rock properties and lead to a drop in pressure. The CO₂ phase(s) present can also cause changes in fault rock properties over time. For example, dissolved CO₂ decreases pH in the aqueous phase, leading to the dissolution of some types of fault rocks and subsequent changes in fracture porosity and permeability (Andreani et al., 2008; Detwiler, 2008). In other cases capture of CO₂ by

mineralization may locally decrease permeability by clogging pore space (Srivastava et al., 2000).

1.3 The influence of fault zones on fluid migration

1.3.1 Introduction

Faults normally represent complex zones composed of many fault segments, multiple fault strands, Riedel shears, splay faults, dilatational jogs, and relay ramps (Price and Cosgrove, 1990; van der Zee, 2002; Koledoye et al., 2003; Boutareaud et al., 2008). As such they can act as barriers to flow, conduits to flow, or combined conduit/barrier systems as their hydraulic properties vary in both space and time (Pratsch, 1991; Lopez et al., 1995; 1996; Braun et al., 2003; Malkovsky and Pek, 2004). A substantial body of research has focussed on predicting the across-fault flow properties of fault zones in oil and gas reservoirs (Fisher et al., 2001; Knipe et al., 1998). However, there is limited knowledge of fault influence on long-term vertical fluid migration through reservoirs. Observations of vertical fault flow are predominantly in crystalline basement rocks, where localised mineral deposition indicates that faults are commonly conduits for fluids migrating under thermal and chemical gradients. It is important to note that fault properties influence vertical fluid flow at two spatial scales; the individual fault zone and areas of fault interaction or network. The following subsections the influence of faults on fluid flow at both of these scales are examined.

1.3.2 Fault zone architecture

Upper crustal brittle fault zone fluid flow depends, in part, on fault zone architecture and permeability structure. Brittle fault zones are lithologically heterogeneous and anisotropic discontinuities (Martel et al., 1998; Antonellini and Aydin, 1994; Faulkner and Rutter, 2003; Shipton and Cowie, 2001; Rawling et al., 2001; Brogi, 2007). Individual fault planes can also show high variation in complexity along strike or down dip, even over relatively short distances (Childs et al., 1997; Schulz and Evans, 1998; van der Zee, 2002, Lunn et al., 2008). A three component fault zone model proposed by Caine et al. (1996) after Chester and Logan (1986a) splits the structure of a fault zone into fault core, damage zone and protolith (Figure 1.1), although not all of these components need be present in

every fault zone (Wibberley et al., 2008). Both the fault core and the damage zone are mechanically related to the growth of the fault zone (Sibson, 1977; Scholtz and Anders, 1994).

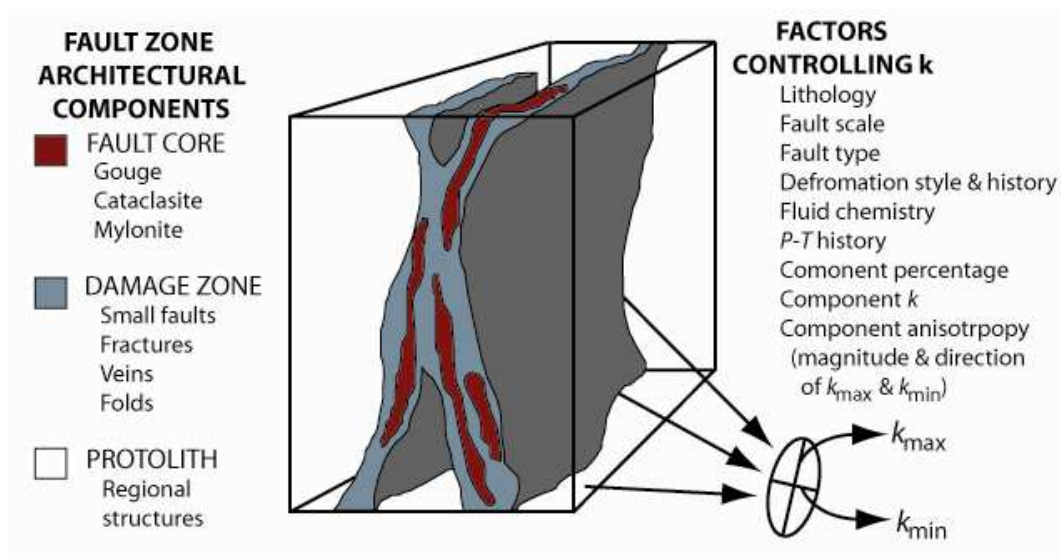


Figure 1.1: The fault zone conceptual model of Caine et al. (1996).

The figure depicts a fault zone with the protolith removed (after Chester and Logan, 1986; Smith et al., 1990) Ellipse represents relative magnitude and orientation of the bulk two-dimensional permeability tensor that might be associated with each distinct architectural component of fault zone.

The fault core is the central component of a fault zone where most of the fault slip has been accommodated. This portion of the fault zone may include single slip surfaces (Caine et al., 1991); unconsolidated clay-rich gouge zones (Anderson et al., 1983) brecciated and geochemically altered zones (Sibson, 1977) or highly indurated cataclasite zones (Chester and Logan, 1986b). Fluid flow properties of fault core are controlled by isotropic variation in thickness coupled with the composition of present lithologies (Caine et al., 1996). Reducing grain size during fault slip or mineral precipitation by fault induced fluid flow produces fault core with lower porosity and permeability than the surrounding protolith (Chester and Logan 1986a; Antonellini and Aydin, 1994), and leads fault core to act as a barrier to across fault flow.

The damage zone is an interconnected 3D network of subsidiary structures, including small faults, fractures, veins, deformation bands, cleavage and folds, that bound the fault core and may enhance fault zone permeability relative to the core and the undeformed protolith (Bruhn et al., 1994; Knipe et al., 1998; Shipton and Cowie, 2001; Shipton et al., 2002, 2006; Jourde et al., 2002; Brosch and Kurz,

2008). This component can be viewed as being composed of 'onion skins' (Knipe et al., 1998) each with different densities, architectures and connectivities between potential barriers. Damage zones can consist of two main domains, outer and inner, which often have different flow properties (Figure 1.2). The inner zone comprises of a higher volume of fault related subsidiary structures, the intensity of which gradually decreases toward the outer zone. An interconnected 3D array of fractures can be generated by the structural density and architecture of this inner zone. If the fault damage zone elements act as an effective barrier then fluid flow is controlled by tortuosity of interconnected host rock pathways within the damage zone (Hesthammer and Fossen, 2000).

On approaching the undeformed host rock, or protolith, there is commonly a diffuse boundary between the damage zone and the host rock, with a gradual decrease in fracture intensity and sometimes a change in fracture strike (Gudmundsson, 2001; Billi et al., 2003).

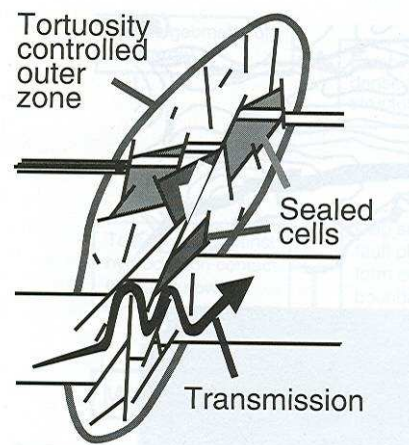


Figure 1.2: Schematic of the main structural elements of a fault damage zone.

Figure after Knipe et al. (1998). The zone is comprised of a cluster of deformation features around a large offset fault. Note that the juxtapositions seen differ from those that would occur if only a single fault was present and that the presence of an array of deformation features can induce the development of micro-compartments or sealed cells in the fault zone.

1.3.2.1 The effect of fault zone components on fluid flow

The amount and distribution of each fault zone component controls fluid flow within and near the fault zone. Permeability values of fault core and damage zone recorded from the same fault may contrast by as much as 10^{-6} m^2 (Forster and Evans, 1991). Fluid flow properties of a fault zone may change through time.

For example, a fault core may act as a conduit during deformation and as a barrier when open pore space is filled by mineral precipitation following deformation (Caine et al, 1996; Claesson et al., 2007). It is important therefore to consider the evolutionary stage of a fault when evaluating its fluid flow properties. The permeability of fault core is affected by the present lithology and its degree of alteration. In the example of core rock consisting of sedimentary units lithologies with the lowest phyllosilicate content will generally have the highest permeability. Laboratory determined permeabilities for natural fault core materials show a range of variation of approximately 10 orders of magnitude (10^{-12} to 10^{-22} m² from Smith et al., 1990).

Estimates of damage zone fracture permeability carried out by Caine et al. (1996) using the estimation methods of Oda et al. (1987) and Bruhn (1993) for both the Dixie Valley fault Zone and Triall Ø fault 6, East Greenland, are 2-3 orders of magnitude greater than the fractured protolith and 4-6 orders of magnitude greater than the fault core and imply that the damage zone acts as a conduit for fluid flow in these examples. Similar findings in other fault studies would be dependant on the composition of the damage zone components. For example zones comprised of a large volume of clay or salt may lead to a damage zone of lower permeability than the protolith (Figure 1.2).

Areas of fault interaction may provide the most important pathways for fluid flow in a basin (Gartrell et al., 2003, Ligtenberg, 2005). High permeability zones may be produced at locations where smaller subsidiary fault structures are in contact with the main fault or places where steps or bends occur (Gartrell et al., 2004). Depending on the geometry of the step these are the locations at which extensional, open structures may form that constitute zones of enhanced permeability (Price & Cosgrove, 1990; Curewitz and Karson, 1997; Gartrell et al., 2003; Ligtenberg et al., 2005, Lunn et al., 2008). High shear strain at fault planes normally results in the production of high volumes of fault gouge (Ligtenberg, 2005). Numerical modelling of the mechanical behaviour of faults demonstrates that at fault intersections the shear strain is low in relation to the fault planes involved (Gartrell et al., 2003; 2004). Due to the resultant reduced fault gouge production small open folds and faults can become highly concentrated and potentially form relatively open sub-vertical dilation zones which can enhance fluid migration pathways (Figure 1.3). The regional effect of fault intersections on

focusing vertical flow into distinct channels is demonstrated by data from Ligtenberg (2005) in Figure 1.4.

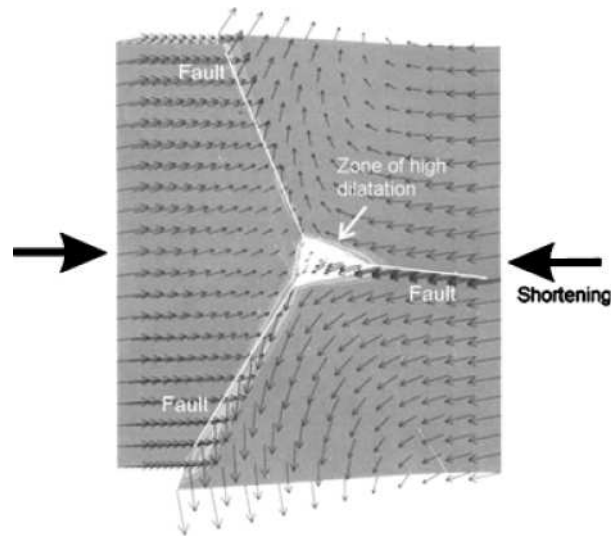


Figure 1.3: 3D numerical modelling of the mechanical behaviour of fault intersections.

Figure from Gartrell et al. (2003). A zone of high dilatation and low shear strain is created in the area of fault intersection, providing an ideal location for high fluid flux.

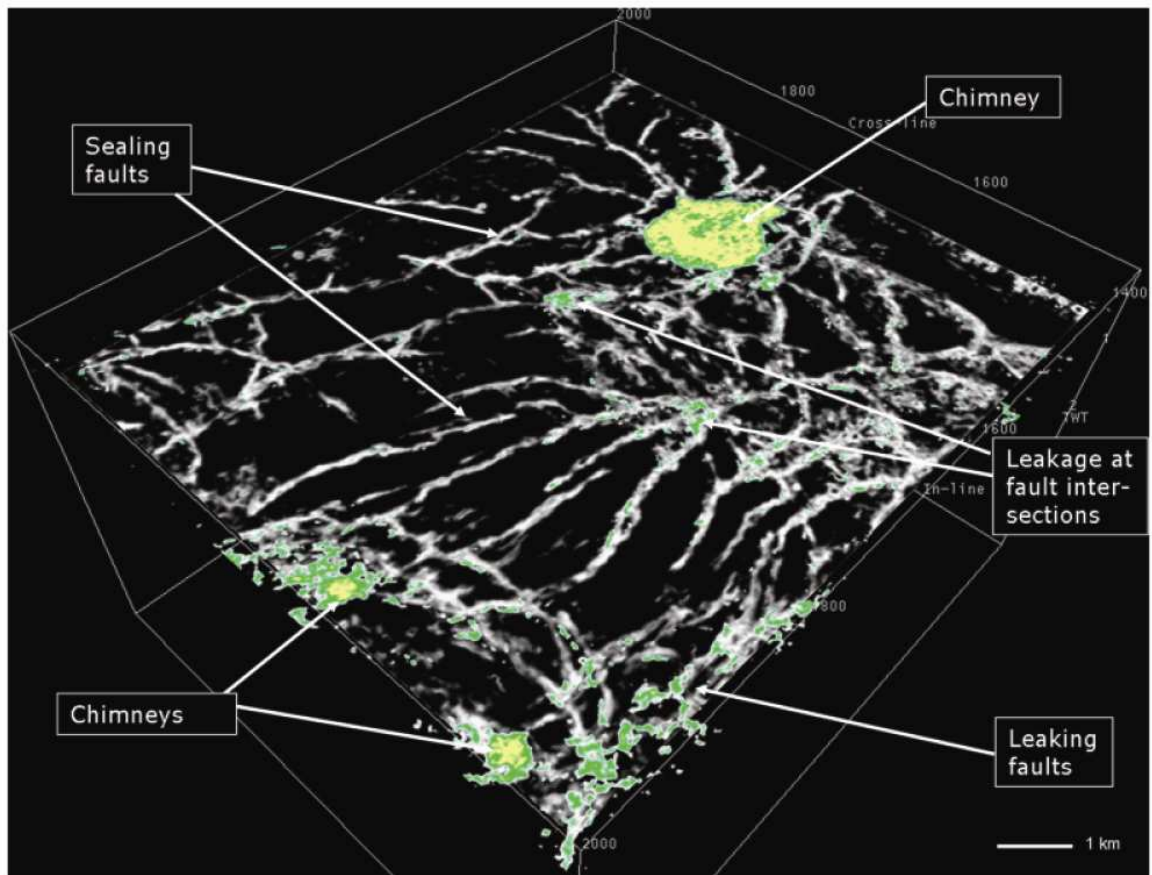


Figure 1.4: Time-slice through a seismic data cube of a large scale fault system.

Figure from Ligtenberg, 2005. Faults are highlighted in grey, whilst the yellow zones correspond to large gas chimneys with high fluid flux. Increased fluid activity is observed at fault intersections and along several faults, indicating leakage. Faults without enhanced fluid activity are interpreted to be sealing or having very low fluid flux.

1.3.2.2 Juxtaposition and cap rock seals

Juxtaposition of reservoir rock against low-permeability clay-rich non-reservoir rock can create juxtaposition seals (Watts, 1987; Allan, 1989; Knipe, 1997). The seal capacity of the trap is therefore related to the capillary properties of the juxtaposed unit (Hesthammer and Fossen, 2000; Fisher et al., 2001). If the pore pressure of the wetting phase is greater than that of the non-wetting phase and capillary entry pressure cannot be overcome then a lateral membrane seal will be formed (Underschultz, 2007). If the distribution of throw on a fault is known, Allan diagrams can be used to analyse the nature of fault juxtapositions across a fault plane (Allan, 1989). In order to aid the analysis of fault juxtaposition and sealing, Knipe (1997) developed triangle diagrams, based on the interaction of rock lithology and the fault throw magnitude. The advantage of triangle diagrams is that they can be constructed without detailed 3D mapping of stratigraphical horizons and fault planes, and allow rapid initial characterization of juxtaposition and fault seal types. Fault seal diagrams can be used as the basis for estimates of permeability, sealing capacity, critical fault displacements and transmissibility of fault zones.

For vertical migration, buoyant fluid must find a way of breaking through confining layers or cap-rock (that is if the damage zone has not provided an adequate conduit for flow). There are two main methods of cap-rock sealing, membrane and hydraulic seals. Membrane seals are controlled by the capillary properties of the caprock which acts as a kind of membrane with the weakest seal areas located around interconnected pore throats (Underschultz, 2007). Hydraulic sealing occurs when the capillary entry pressure is so high (e.g. for tight shales or some evaporites) that failure can only occur by fracturing of the caprock or wedging open of faults (Watts, 1987). The only way to fail this caprock is to increase pore pressure at the cap-rock reservoir interface so that the effective minimum stress reduced to zero, or even below zero, to overcome the tensile strength of the rock.

1.3.2.3 Vertical fluid migration

Current practice with respect to analysis of fluid flow in fault zones is almost entirely concerned with across fault flow, with emphasis based on modelling the effects of faults on fluid flow using quantities such as transmissibility multipliers

(Manzocchi et al., 1999; Manzocchi et al., 2002; Harris et al., 2002), or predictive algorithms such as the Shale Gouge Ratio (Yielding et al., 1997; Yielding, 2002; Manzocchi et al., 2008). Driven entirely by the hydrocarbon industry, much of this work is concerned with finding upscaled values for properties derived from host rock and fault properties for input into workflows at reservoir modelling grid block scales (~15 x 15 m). Information gained from studies in this area can have important implications for vertical fluid flow, as established low permeability fault zone components that retard across fault flow may encourage fluid flow along fault planes.

Direct observation of vertical fluid flow itself in faults is limited. Therefore, it is important to examine indirect evidence from a range of industries and research areas. Observations that link fault zones to vertical fluid flux are listed below. It should be noted that, to date, no studies have integrated evidence across these subject areas.

- 1) Springs (This study; Curewitz and Karson, 1997; Shipton et al., 2005; Rowland et al., 2008), mud mounds (Berryhill, 1986), hydrate mounds (Roberts et al., 2000) and pockmark craters (Heggland, 1997; Ligtenberg, 2005, Van Rensbergen et al., 2007) aligned along fault planes.
- 2) Temperature anomalies above faults (Kumar, 1977; Fairley and Hinds, 2004b; Becker et al., 2008) or within fault rocks (Roberts et al., 1996; Losh et al., 1999).
- 3) Fluid pressure distributions across faults (Berg and Habeck, 1982; Claesson et al., 2007; Jin and Johnson, 2008).
- 4) Pore water salinity (Lin and Nunn, 1997) or turbidity (Shipton et al., 2006) anomalies.
- 5) Hydrothermal deposits (Hedenquist and Henley, 1985), cementing phases (Eichhubl and Boles, 2000; Moore et al., 2005) or travertine mounds (This study; Doelling, 1994; Hancock et al., 1999; Shipton et al., 2004) associated with faults.
- 6) Clustering of gas-related amplitude anomalies stacked vertically in footwall or hanging wall traps along single wall faults (Heggland, 1997; Ligtenberg, 2005).

- 7) Reservoir induced seismicity due to fluid flow through faults beneath surface water reservoirs (Simpson et al., 1988; Gupta et al., 1997; Talwani, 2000; Chen and Talwani, 2001; Nascimento et al., 2005a, b).
- 8) Earthquake triggering (Muir Wood, 1994; Miller et al., 2004, Collettini, 2002, Collettini and Trippetta, 2007; Scholz, 2002; Rice and Coco, 2007).

1.4 Temporal variations in fault permeability

1.4.1 Introduction

Contradictory evidence for fault conductivity is found in various studies (Galloway, 1982; Morton and Land, 1987; Bodner and Sharp, 1988; Sibson, 1992; 1995; Kitagawa et al., 2007). Temporal permeability is a potential theory which explains the observed permeability discrepancies (Hooper, 1991). This theory suggests that a fault can act as both a conduit and a barrier to fluid flow through time due to temporal fluctuations in permeability and fluid potential. As a fault becomes active, and fluid movement is concentrated, a fluid potential gradient forms between the fault plane and the surrounding rocks (Hooper, 1991; Haney et al., 2005). This has been documented by the work of Losh et al. (1999) on the 'A' fault, a large growth fault on the South Eugene Island block 330 field, offshore Louisiana. They found that localised palaeothermal (from vitrinite reflectance data) and fluid pressure anomalies existed within the fault zone and deduced that this was the result of pulses of fluid sourced from a highly overpressured source below the reservoir. Such pulses of fluid may be expected to be at elevated pressure relative to the fluids either side of the fault, creating an envelope of low effective stress which could increase the permeability of the fault. If the fluid ascends a portion of the fault which is in contact with an aquifer its high pressure might increase permeability in nearby splay faults, which typically exist adjacent to any significant fault (Weber et al., 1978; Micklethwaite and Cox, 2004; 2006), driving flow into the lower pressure reservoir. The greater the pressure differential between the fault and the surrounding reservoir the greater the tendency of fluid to escape laterally from the fault during fluid flow; however, as fluid escapes into the reservoir pressure in the fault decreases and the fault is effectively shut off for further flow (Figure 1.5).

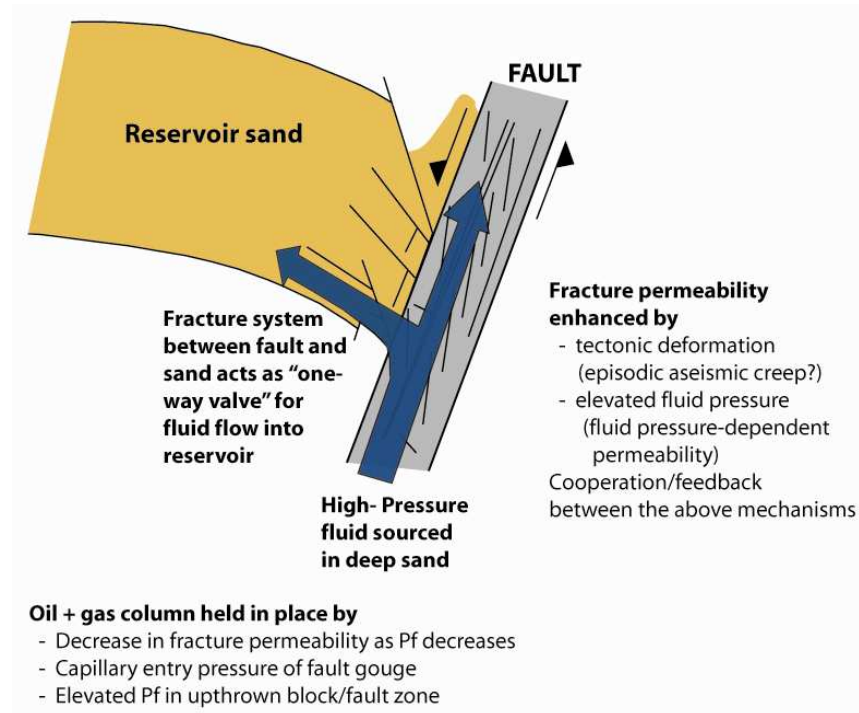


Figure 1.5: Schematic fluid flow model for temporal permeability.

Figure after Losh et al. (1999). P_f = fluid pressure.

1.4.2 Evidence of temporal flow

Several lines of evidence exist for periodic fluid flow along faults:

- 1) Geomechanical behaviour of faults demonstrated by episodic fluid flow effects, such as oxidation and reduction fronts, on faulted sedimentary rocks (Galloway, 1982); and fault reactivation caused by production of reservoirs (Wiprut and Zoback, 2000; Teanby et al., 2004; De Meersman et al., 2007).
- 2) Thermal signature of upwelling fluids. This is particularly evident in meteoric dominated regimes where ground water recharge has a relatively low temperature whilst upwelling fluids from depth have a higher heat flux (Bodner and Sharp, 1988; Fairley et al., 2003; Anderson and Fairley, 2008).
- 3) Salinity anomalies recorded within migrating fluids. Upwelling brine has been shown to be variable in its salinity content, with low saline waters associated with periods of lesser fault activity, allowing upward flow to be retarded and encouraging dilution by connate fresh water (Morton and Land, 1987; Keucher et al., 2001).

- 4) Mineral precipitation during episodes of fluid flow (this can also lead to mechanical changes in fault rock properties). Deposition of travertine or calcite veins in response to intermittent fluid flow (This study; Eichhubl et al., 2009; Uysal et al., 2009); precipitation of quartz altering deformation elements in the fault zone (Johansen et al., 2005); and faulted alluvial sediment acting as lithified material after fluid flow associated precipitation (Heffner and Fairley, 2006).

1.4.3 Processes which lead to episodic fluid flow along faults

There are three main mechanisms which can lead to the permeability (and therefore conductivity) of fault planes increasing as faults become more active (Hooper, 1991; Losh and Haney, 2006):

1. Dilation-increased permeability.
2. Re-fracturing or dissolution of mineral zones.
3. Seismic pumping.

At stresses close to failure micro cracks can form parallel to the fault plane causing dilation and increasing fault conductivity. If the fluid potential gradient is simultaneously parallel to the fault plane fluid will preferentially flow along the increased zone of permeability created by dilation. If the zone of increased permeability is wide (>200 m) relatively small increases in hydrostatic stress can lead to the fault forming a significant conduit for fluid flow (Hooper, 1990).

Re-fracturing or dissolution of mineralised zones can increase fault conductivity if previously cemented fractures are re-opened. This could potentially be caused by seismic activity or introduction of a fluid of different chemistry to the depositional fluid. The fractured host rock must be moderately to well consolidated in order for the cracks to remain open and increased permeability to be maintained. Evidence of this mechanism comes from the presence of cemented breccias within fault associated veins which implies several episodes of movement (Sibson et al., 1975).

Increase of fluid potentials within fault zones, as a result of seismic pumping, can promote the conductivity of associated faults (Scholtz and Krantz,

1974). This mechanism is initiated by rising tectonic shear stress of faults prior to seismic activity. This causes dilation around the focal points of earthquakes by opening extension cracks and fractures normal to the least principal compressive stress (Sibson et al., 1975). Dilation causes a drop in fluid pressure and a rise in frictional resistance to shear along the fault as migrating fluid fills the cracks fluid pressure rises and frictional resistance decreases. When the rising shear stress equals the frictional resistance, seismic failure occurs which leads to a relief of shear stress and a closure of dilational fractures (Sibson et al., 1975). This relaxation of fractures forces fluid to flow rapidly in the direction of least ambient pressurisation. The observation of spring flow around fault zones after earthquakes suggests that this is largely in the upwards direction (Muir Wood and Geoffrey, 1993, Esposito et al., 2001).

1.5 Addressing the gaps in our understanding

Although plenty of work has been carried out on across fault flow it is clear that there is still a lot to be learnt about fault parallel fluid flow. The properties of fluid flow and the effects of multiple fluid phases on permeability are well understood. This is important as within CO₂ systems several phases of CO₂ may present in various combinations depend on the pressure and temperature conditions. It is also generally accepted that faults are usually complex structures comprised of different components, core, damage zone and protolith, whose properties can vary both along strike and down dip. The varying properties of these components allow faults to act as barriers, conduits of combined barrier and conduit systems with relation to fluid flow. Due to gouge production and geochemical alteration during fault slip, fault core usually forms a low permeability barrier to across fault flow. The damage zone, an area of highly concentrated small faults, fold and fractures, may provide permeable pathways for fluid flow parallel to faults depending on the degree of interconnection between the subsidiary structures. Depending on the orientation of the ambient stress field during fault slip irregularities in a fault plane, such as bends and relay ramps, may be subjected to lesser shear strains in relation to the fault plane allowing for formation of relatively open zones of dilation that encourage the channelling of fluid flow through relatively impermeable media.

Direct observations of fluid flow are limited and therefore the understanding of the processes that instigate fluid flow has thus far been mainly based on indirect observations. Episodic fluid flow is also poorly understood as the causes and timescales involved are hard to determine for fluid flow in active fault zones. The work presented in this thesis presents a unique data set with the goal of answering some of these issues on fault parallel fluid flow. By studying the position of travertine mounds, which are the result of sub-vertical flow of CO₂-charged waters to the surface, in relation to two normal fault structures, the Little Grand Wash and northern Salt Wash graben faults, information can be gained on the subsurface pathways that allow for fluid flow to the surface. Radiometric dating of these travertine deposits provides information on the timescales of leakage along faults and for individual fluid flow pathways. By combining age data of travertine mounds with geological observation from the field the timescales and reasons for the closure and creation of fluid flow pathways can be determined. This information can be used to provide an increased understanding of the structure of faults and their fluid flow properties.

1.6 The U-series dating technique

In order to determine the ages of travertine deposits related to the Little Grand Wash and northern Salt Wash graben faults, and therefore quantitatively constrain the timing of fluid flow to the surface along these faults, uranium series dating was utilised. This also allowed the time spans between successive mounds to be determined which was key for developing an understanding of the processes that may be instigating changes in fluid flow pathways in the subsurface and gave an insight into evolution of fault structure through time.

U-series dating has been routinely applied to coral, speleothem and calcite veins for palaeoclimatic studies (Garnett et al., 2004; Placzek et al., 2006a; 2006b; Uysal et al., 2007; Alcaraz-Pelegrina et al., 2007), and has also found uses in topics as varied as magma chamber evolution; human evolution (through dating of bone) and ground water evolution (Van Calsteren and Thomas, 2006). It is increasingly common for this dating technique to be applied to palaeoseismic studies (e.g. Morewood and Roberts, 1999; Leeder et al., 2003; Cooper et al., 2007; Uysal et al., 2007). Dating carbonates that are deposited along the surface of faults or in fractures created by seismic activity can allow the history of

movement of these features to be deduced (Szabo and Rosholt, 1982). The use of this information can lead to the establishment of recurrence intervals of late Quaternary and prehistoric earthquake events (Uysal et al, 2007) and the slip rates on faults between these events (Roberts et al., 2009). There is a paucity of references in the literature to utilising U-series for the study of fluid flow, which is the main premise of this thesis.

The uranium decay series contain radioactive isotopes of many elements, the varied geochemical properties of which cause the nuclides in the chain to be fractionated in different geological environments. U-series disequilibrium dating methods are based on the measurement of the degree of restoration of radioactive equilibrium in a radioactive decay series following this fractionation. U-series measurements allow investigation of processes occurring on time scales from days to 10^5 years and offer some of the only quantitative constraints on time scales applicable to the physical processes that take place on the Earth. Several criteria, common to most types of radiometric clocks (Ivanovich, 1982b), must be satisfied for U-series dating before a particular method can be considered a geologically useful chronometer:

- Decay constants (or half lives) of the radionuclides must be accurately known.
- The analysed sample must be representative of the geological system for which the age is desired.
- The sample must be free of intermediary decay products and final daughter product during its initial formation.
- The system must remain closed with respect to migration of the parent and daughter nuclides since its time of formation.

The following sections provide a more in-depth introduction to the aspects involved with U-series dating, focusing on the $^{234}\text{U}/^{230}\text{Th}$ technique. A description of the basic principles of radioactivity is presented in subsection 1.7 which provides the basis of the theory behind U-series techniques. A discussion of the practical application of the U-Th dating method is then presented in section 1.8. Finally, a short section on analytical procedure is presented in section 1.9 to discuss the techniques used during the dating process.

1.7 The phenomenon of radioactivity

1.7.1 Introduction

Of the approximately three-hundred-and-fifty naturally occurring nuclides, most that occur are stable and do not change with time, but there are many like U, which are radioactive (Dalrymple, 1991). A radioactive nucleus is one which at any instant may change spontaneously into a different nuclear type. This is a statistical process called radioactive decay, whereby the decay is proportional to the number of radioactive nuclei of a particular kind at any time t . The constant of proportionality, λ termed the decay constant, is the probability of decay per unit time interval (Ivanovich, 1982a). It is related to the half-life of a radionuclide (which is the time required for the decay of exactly one half of the original number of its nuclei) by Equation 1.1;

$$\lambda = 0.693 / t_{1/2}$$

Equation 1.1

1.7.2 Radioactive decay

Radioactive decay is the process of transformation from a parent to a daughter nuclide. It is brought about by two alternative types of particle emission: either the moderately heavy alpha particle or the light beta particle. Due to the great energy released along with these particles, gamma rays are often produced, which like X-rays, are a form of penetrating electromagnetic radiation.

Alpha particles are nuclei of He atoms, two protons and two neutrons (supplying a positive charge of two units and an atomic mass of four), which when emitted causes a nucleus of atomic number Z and mass A to lose two protons and thus transform into an element of atomic number $Z-2$ and mass $A-4$. An example of this is the alpha decay of $^{234}\text{U}_{92}$ into $^{230}\text{Th}_{90}$ (Figure 1.6). The rate of alpha decay is highly dependant on the available energy. Increasing atomic number tends to provide more energy, though it is only for elements above Pb ($Z = 82$) that alpha decay is the dominant source of radiation.

Beta particles are electrons of negligible mass in comparison to a nucleon and carry a charge of -1 . A nucleus of atomic number Z which emits a beta particle

loses a unit of negative charge which is equivalent to gaining one positive charge with no gain in mass. For example $^{234}\text{Th}_{90}$ emits a beta particle to become $^{234}\text{Pa}_{91}$ which in turn decays to $^{234}\text{U}_{92}$ with the loss of a further beta particle.

1.7.3 The U-series decay chain

Most of the long-lived, heavy radioactive elements decay into daughter products that are radioactive themselves. These decay in turn and thus form series (or chains) which eventually end in a stable daughter nuclide. The process by which radioactive isotopes decay is known as ‘activity’, which is equal to the relevant decay constant multiplied by the number of atoms of a nuclide ($N\lambda$), where the decay constant represents the fraction of radioactive atoms that decays per unit time (Equation 1.2).

The atomic ratio of two isotopes is the ratio of the number of atoms in comparison to one another. To help differentiate between atomic and activity ratios, from this point forward all activity ratios will be highlighted by square parenthesis. All alpha-emitting nuclides can be divided into four independent decay series (all of which occur naturally bar the neptunium series: Ivanovich, 1982a). An essential characteristic of these decay-chains is that the process begins with a radiogenic actinide nuclide of much longer half life ($>0.7\text{Ga}$) than all the intermediate daughters and ends with a stable daughter isotope of lead (Bourdon et al., 2003). The U series chain is the longest decay series beginning with ^{238}U and ending with ^{206}Pb . It is of the sequence type $4n+2$ as every atom in the chain has a mass number that is two greater than a multiple of four (Ivanovich, 1982a) (Figure 1.6). The members of this decay chain utilised for U-Th dating are ^{234}U ($t_{1/2}= 245\text{ka}$) and ^{230}Th ($t_{1/2}= 75\text{ka}$). The relatively long half lives make these nuclides particularly suited to investigating many geological processes that occur over time scales similar to their decay period (Bourdon et al., 2003).

1.7.4 Geochemistry of the actinides and their daughters

Knowledge of the chemical properties of the U-series nuclides is essential to any understanding of the fractionation within the U-series chains. Most of the U-series nuclides are metals, with five of them belonging to the actinide family (Bourdon et al., 2003). The actinides are the heaviest naturally occurring elements in nature. Isotopes of the lowest members (Ac, Pa, Th, and U) are derived from

three parent nuclides ^{238}U , ^{235}U and ^{232}Th , which are sufficiently long lived to survive in abundance at the present time (Gascoyne, 1982). This group takes its name from actinium, the first in a series of elements which are characterised by infilling of the 5f electron shell (Gascoyne, 1982). The filling order of the electron orbitals of U-series atoms affects the possible oxidation states of their associated nuclide. The preferred oxidation state of each nuclide is reached when its electronic configuration matches that of the closest rare gas, radon (Bourdon et al., 2003).

An important chemical property of relevance to geochemistry is the ionic radius in different coordination. In general, Th has a larger ionic radius than U despite U having a larger atomic mass; this phenomenon is known as actinide contraction (Bourdon et al., 2003). In general the heavier actinides should be more easily accommodated in minerals than the lighter ones at a given oxidation state (Gascoyne, 1982).

1.7.5 Secular equilibrium and Disequilibrium

If the activity of the parent nuclide is equal to the activity of its subsequent daughter, a state of radioactive or secular equilibrium is reached:

$$N_2 \approx \left(\frac{\lambda_1}{\lambda_2} \right) N_1$$

Equation 1.2

Where N_1 , N_2 , λ_1 and λ_2 represent the number and the decay constants of the respective parent and daughter isotopes. Secular equilibrium between a parent and daughter implies an activity ratio of 1. The number of atoms of each intermediate daughter produced is in direct proportion to the daughter atom's half life or inverse proportion to its respective decay constant. The amount of stable daughter product at the end of the series will continue to increase with time but at a decreasing rate (Ivanovich, 1982b). In a system in which there is an initial disequilibrium in the chain a return to secular equilibrium will occur after roughly six half lives of the daughter nuclide (Bordon et al., 2003).

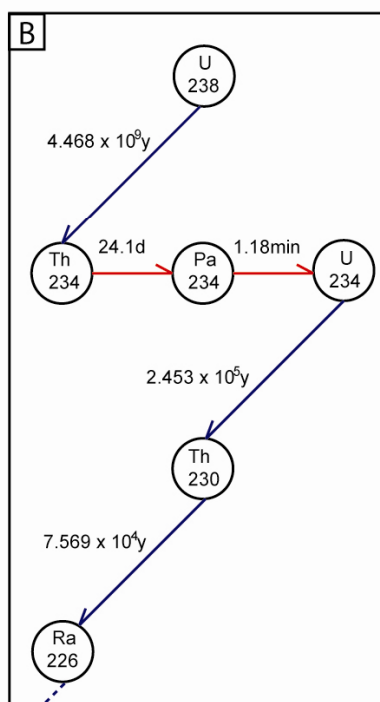
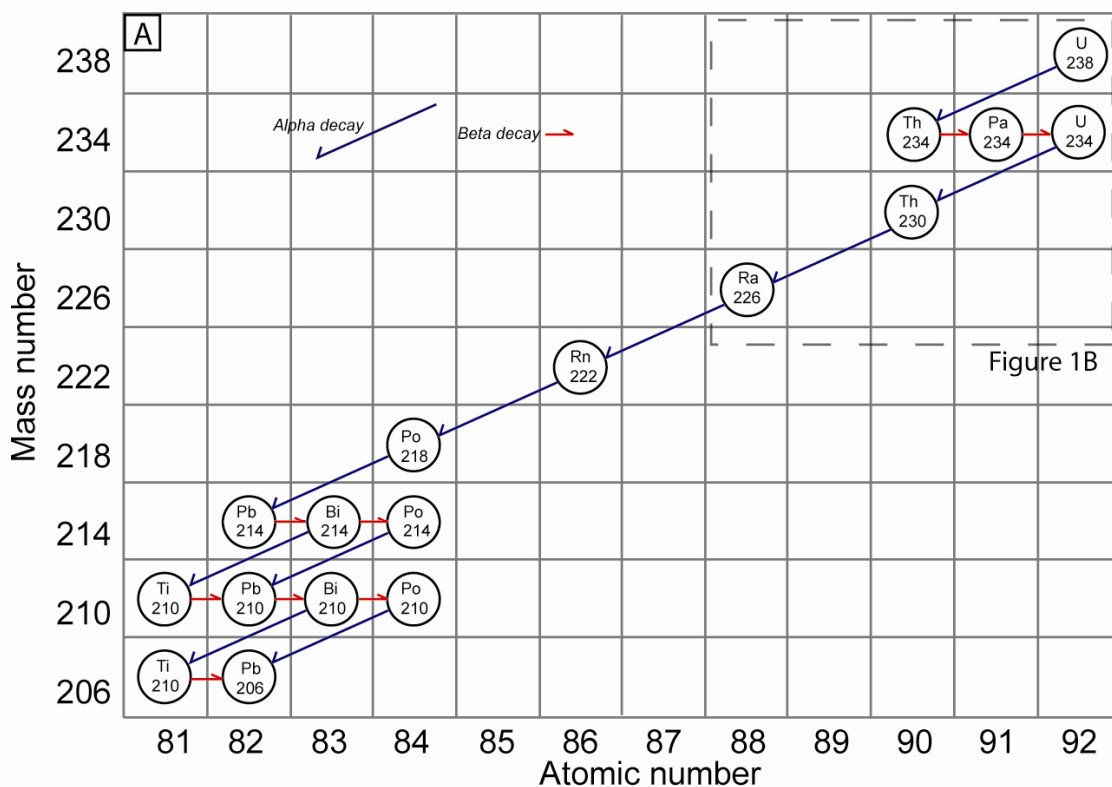


Figure 1.6: The U-series decay chain.

(A) The chain in its entirety. It begins with the nuclide ^{238}U and passes a second time through $Z=92$ as a consequence of an alpha-beta-beta sequence repeated twice so that the U-series terminates on the lightest of the radiogenic Pb isotopes, ^{206}Pb . ^{238}U is the chief constituent of natural U (99.27% abundance) and the progenitor of the $4n+2$ series. (B) A more detailed look at the start of the U-series chain complete with isotopic half lives. Note that for ^{234}Pa the half life shown is the most common form (99.86% of transitions); an isomeric form with a half life of 6.66 hours constitutes the remaining transitions. Half lives are taken from Jaffey et al. (1971), Knight and Machlin (1948), and Cheng et al. (2000).

In most geological environments the natural radioactive series are often in a state of near equilibrium, but instances where they are not are common. Due to the chemical difference between parent and daughter nuclei, it is possible for them to become naturally separated by ordinary geochemical processes. The nature and degree of this fractionation between different members within a decay chain, referred to as 'disequilibrium', frequently offers a clue to the geological history of a sample (Ivanovich, 1982b).

1.7.6 Cause of Disequilibria

1.7.6.1 Introduction

Radioactive disequilibrium results from geochemical sorting or differentiation processes, whereby one decay series daughter is more mobile than another. The U-series decay chain contains many elements that are subjected to fractionation by environmental and geological processes. Half lives of radioactive isotopes of such elements range from seconds to many millennia, so the degree of disequilibrium will depend on the natural timeframe of the fractionation process or the elapsed time (Van Calsteren and Thomas, 2006). Since large fractionation between ^{234}U and ^{238}U in rocks and their leach solutions has been observed (Cherdyntsev, 1955) and a small excess of ^{234}U in ocean water has been discovered (Thurber, 1962), disequilibrium between ^{234}U and ^{238}U has been found to be the rule rather than the exception (Gascoyne, 1982). Most examples of U-series disequilibrium observed in nature have their origin in the hydrosphere (Osmond and Cowart, 1982). Especially important are the ground water and aquifer environments where water and minerals are intimately mixed (i.e. where porosity, surface area, and residence times have large values) and where both chemical and physical differentiation have an opportunity to operate. Several culprits for this disequilibrium have been discussed (Harmon and Rosholt, 1982; Gascoyne, 1982; Osmond and Cowart, 1982; Bourdon et al., 2003; Van Calsteren and Thomas, 2006; Kaufman, 1993) with the following subsections highlighting some of the most important.

1.7.6.2 Oxidation

In the near surface environment, and at low temperature, both uranium and thorium are quadrivalent and chemically immobile. Uranium however, can become mobilized by oxidation to the hexavalent (+6) uranyl ion (Langmuir, 1978).



Equation 1.3

This increase in oxidation state of ^{234}U may occur either by removal of orbital electrons in the emission of alpha and beta particles, or by changes in energy levels between original and dislocated sites (Bourdon et al., 2003). Hexavalent uranium is fairly soluble as $\text{UO}_2(\text{CO}_3)_3^-$ and similar ionic complexes, whilst thorium remains quadrivalent and insoluble (Van Calsteren and Thomas, 2006), and therefore uranium is preferentially leached. Further complexing of the uranyl ion may also occur depending on pH and presence of other ions (Gascoyne, 1982).

1.7.6.3 Weathering

During weathering, fractionation of uranium and thorium is a very efficient process because thorium is extremely insoluble while in oxidising conditions hexavalent uranium is relatively soluble (Rosholt, 1982). Thorium tends to remain in the mineral grains during weathering because its partition coefficient (the ratio of the concentrations of an element, parent or daughter, before and after a fractionation process) is large in comparison to uranium (Van Calsteren and Thomas, 2006). However, thorium may still be mobilised by becoming bound in insoluble detrital minerals or adsorbed on to the surface of clay minerals as it is highly particle reactive (i.e. it has a high affinity for solid substances; Gascoyne, 1982; Moran et al., 2002). The movement of U and Th as particulate matter is controlled only by the physical properties and flow velocity of the transporting medium, except where chemical interaction occurs across the phase boundary between solid particles and associated fluid (Gascoyne, 1982). The most important factor in U transport and partitioning of U/Th is the solubility of the uranyl complex ions (UO_2^{2+}). Uranium can be removed from water during the precipitation of carbonates and phosphates, but also when it returns to the uranous state under reducing conditions that occur with the accumulation of

organic matter (Van Calsteren and Thomas, 2006). Thus weathering of rocks and mineral results in efficient leaching of uranium into the water where it can be transported in the form of carbonic or humic complexes (Gascoyne, 1982).

1.7.6.4 Alpha recoil into solution

Radioactive decay of ^{238}U to ^{234}U involves the emission of one alpha and two beta particles. Ejection of the former has the effect of damaging the crystal lattice around the parent ^{238}U atom. ^{234}Th , the daughter of ^{238}U , can be dislocated from its original site and ejected into the medium surrounding the grain by this 'recoil'. This displacement is not trivial (10-110 nm for ^{238}U to ^{234}Th) and it leaves a tube in the crystal of that length (Van Calsteren and Thomas, 2006). As a result, ^{234}Th is more exposed to removal by corrosive fluids (rainwater, groundwater, hydrothermal solutions, and others). Subsequent decay of ^{234}Th to ^{234}U leads to an increase of the $^{234}\text{U}/^{238}\text{U}$ ratio of the surrounding medium. Enrichment of ^{234}U via the alpha recoil effect is counteracted by the relatively short lifespan of ^{234}Th (35 days) and its insoluble nature which makes it likely to hydrolyse or adsorb onto a solid surface before decaying to ^{234}U .

1.7.6.5 Leaching from radiation damaged sites

This mechanism was first proposed by Cherdynstev (1955) to account for the small excess of ^{234}U in river water. It is also known as the Szilard-Chalmers, or 'hot-atom', effect and is especially hard to isolate and identify (Gascoyne, 1982; Osmond and Cowart, 1982). This occurs when a daughter is resident in an inhospitable lattice damaged by recoil. As the result of nuclear transformation this nuclide may also exhibit an unstable electronic configuration, thus making it more vulnerable to leaching than its neighbouring atoms.

1.7.6.6 Biological Activity

Microbiological activity in soils and waters has an important role in the mobility of U (Chabaux et al., 2003). Iron and sulphate reducing bacteria can reduce uranium from its uranyl to its less soluble uranous form (Spear et al., 1999; Fredrikson et al., 2000). Numerous mechanisms of U accumulation by microbes exist; these are divided into metabolism-dependant and metabolism-independent systems (Suzuki and Banfield, 1999). Metabolism-dependant mechanisms can

involve the activity of enzymes to encourage reduction or precipitation of U, or complexation by chelating molecules such as siderophores (Chabaux et al., 2003). The second grouping involves both live and dead cells and the physio-chemical interaction between their negatively charged microbial sites and species of U in the cationic form.

1.7.6.7 Further processes

Also worth mentioning in relation to disequilibrium are the processes of; solution plus precipitation, diffusion, and fixation. Solution and precipitation, a common differentiation process, occurs when ground water percolates past solid mineral grains and selectively leaches ions in an aquifer or soil (Osmond and Cowart, 1982). Diffusion involves the escape of short lived gaseous daughters of Radon and Radium in the U-series decay chain (Gascoyne, 1982). The fixation of radionuclides by colloids (which range in size from 1 to 1000 nm), encompassing a large variety of organic and inorganic components, is another important mechanism influencing the fractionation of the U-series nuclides (Chabaux et al., 2003).

1.8 Uranium Series Dating

1.8.1 Introduction

The U-series dating methods are based on the measurement of the activity of U and its various daughter nuclides. In any naturally occurring material which contains U and which has remained undisturbed for millennia, a state of secular equilibrium between the parent and the daughter will be formed. When a sedimentary deposit is formed various geochemical processes can cause isotopic and elemental fractionation initiating a state of disequilibrium between parent and daughter molecules (see section 1.7.6). If no diagenetic changes or other migratory mechanisms occur after the initial formation of the deposit in this state of disequilibrium it is possible, in principle, to determine the time of the original event by measuring the extent to which the radionuclide system has returned to the state of secular equilibrium (Ivanovich, 1982b).

1.8.2 The U-Th dating method

The U-Th method is based the accumulation of ^{230}Th , the direct daughter decay product via emission of an alpha particle, from ^{234}U . Because of the relatively short half lives of ^{230}Th in comparison to ^{234}U , its concentration is several orders of magnitude less. For this technique to work the parent nuclide must be deposited free of its daughters, and migration of nuclides must not have occurred (Gascoyne, 1982; Chabaux et al., 2003). This is what is known as a closed system, and with no radiogenic ^{230}Th in the deposit, the radiometric clock effectively starts at zero (Van Calsteren and Thomas, 2006). The age of the deposit can be determined from the extent of growth of daughters into secular equilibrium with their parent (Ivanovich, 1982b), If a sample contains no ^{230}Th at the time of formation, then at any later time, the $^{230}\text{Th}/^{234}\text{U}$ ratio is given by the relationship;

$$^{230}\text{Th}/^{234}\text{U} = \frac{1 - e^{-\lambda_{230}t}}{^{234}\text{U}/^{238}\text{U}} + \left(1 - \frac{1}{^{234}\text{U}/^{238}\text{U}}\right) \frac{\lambda_{230}}{\lambda_{230} - \lambda_{234}} \left(1 - e^{-(\lambda_{230} - \lambda_{234})t}\right)$$

Equation 1.4

Where t= time and λ = decay constant (the fraction of radioactive atoms that decays per unit time).

Figure 1.7 is an isochron plot showing a graphical solution of Equation 1.4. It illustrates the relationship between $[^{230}\text{Th}/^{234}\text{U}]$ and $[^{234}\text{U}/^{238}\text{U}]$ for closed systems of varying initial $[^{234}\text{U}/^{238}\text{U}]$ (Ivanovich, 1982b). In the age range of less than 3×10^4 y, the relation between the $^{230}\text{Th}/^{234}\text{U}$ activity ratio and age is virtually independent of the $[^{234}\text{U}/^{238}\text{U}]$ in the sample. $[^{234}\text{U}/^{238}\text{U}]$ has a much smaller effect on age, usually by more than an order of magnitude, than the $[^{230}\text{Th}/^{234}\text{U}]$ ratio (Kaufman, 1993). In this range the equation is reduced to the form (Ivanovich, 1982b):

$$^{230}\text{Th}/^{234}\text{U} = (1 - e^{-\lambda_{230}t})$$

Equation 1.5

If, after fractionation of nuclides, the decay chain remains undisturbed for a period of approximately five times the longest half-lived intermediate nuclide, then it will return to a state of secular equilibrium (Bourdon et al., 2003). This factor provides radiometric clocks, such as the U-series, with dating limits. In practice,

the effective dating range for this method is considered to be around 350 ka (the length of 6 half lives of the daughter product ^{230}Th), if however an excess of ^{234}U is present, and the $[\text{}^{234}\text{U}/\text{}^{238}\text{U}]$ is adequately high, as is the case with travertine samples from Utah (Chapter 3), then dating of material older than 350 ka is possible.

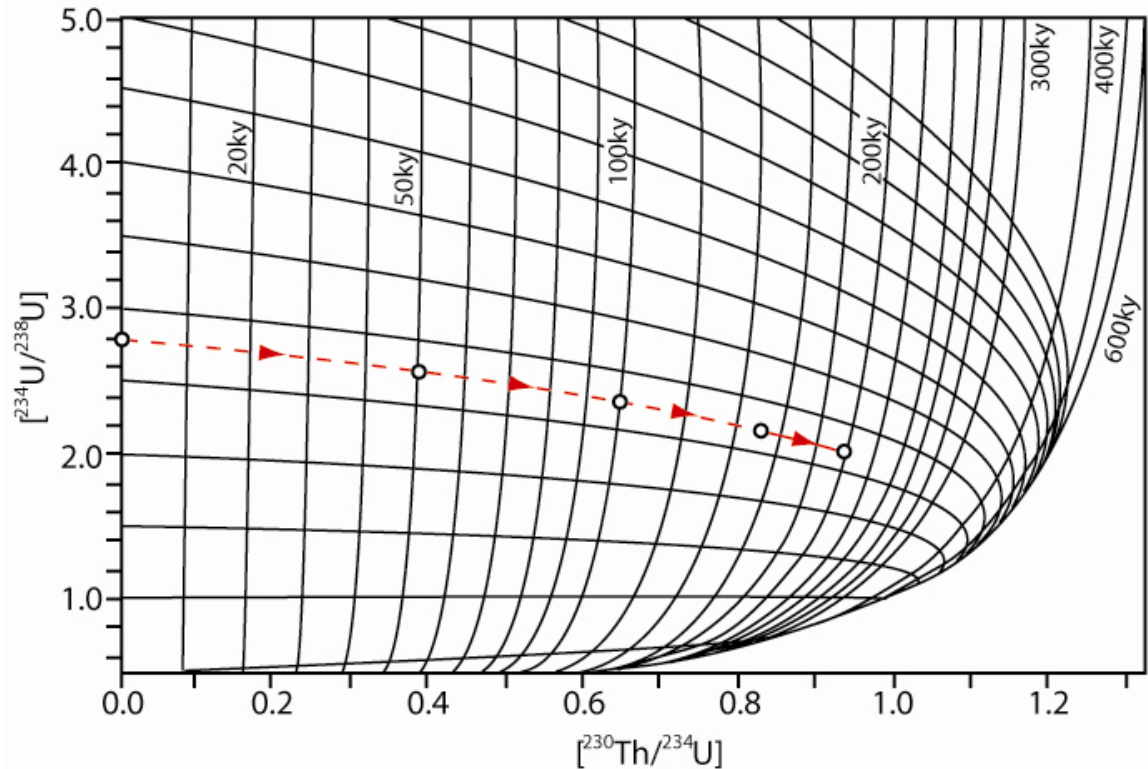


Figure 1.7: Variation of $[\text{}^{234}\text{U}/\text{}^{238}\text{U}]$ and $[\text{}^{230}\text{Th}/\text{}^{234}\text{U}]$ with time in a closed system.

Isochron plot after Ivanovich, (1982a). The near vertical lines are isochrons (lines of constant age) obtained from Equation 1.4. The near horizontal lines show change in the nuclide activity ratios as age increases for different initial $^{234}\text{U}/\text{}^{238}\text{U}$ activity ratios. The circles show the isotopic evolution of a carbonate with an initial $[\text{}^{234}\text{U}/\text{}^{238}\text{U}]$ of 2.8 and $[\text{}^{230}\text{Th}/\text{}^{234}\text{U}]$ of zero (as there is no initial ^{230}Th). As the carbonate ages uranium series nuclides decay into their daughter products changing the isotopic and therefore activity ratios (as indicated by the red arrows), this has the effect of decreasing the $[\text{}^{234}\text{U}/\text{}^{238}\text{U}]$ and increasing the $[\text{}^{230}\text{Th}/\text{}^{234}\text{U}]$ with time. For the carbonate example shown this leads to a $[\text{}^{234}\text{U}/\text{}^{238}\text{U}]$ of 2.4 and $[\text{}^{230}\text{Th}/\text{}^{234}\text{U}]$ of 0.65 at 100ky and leads to a $[\text{}^{234}\text{U}/\text{}^{238}\text{U}]$ of 2.0 and $[\text{}^{230}\text{Th}/\text{}^{234}\text{U}]$ of 0.93 at 200ky.

1.8.3 Uranium series application

1.8.3.1 Requirements for dating

Any process that is fast relative to the time that has elapsed may be an 'event' that can be 'dated' by U-series (Van Calsteren and Thomas, 2006), as long as the deposited material contains ^{234}U and lacks its daughter ^{230}Th . This

principally occurs in authigenic phases where U is incorporated in the mineral structure or simply co-precipitated. The predominant minerals are calcite and aragonite, both forms of CaCO_3 .

For accurate determination of U-series ages for carbonate deposits, samples should demonstrate that they have remained ideal, closed systems throughout their geological history. The extent to which this closed system requirement applies is subject to varying criteria for different types of samples, and these are discussed in detail for speleothems, travertine and coral by many different authors (e.g. Kaufman et al., 1998; Szabo et al., 1996; Stirling and Anderson., 2009). These criteria are listed below:

- The sample should be free of ^{232}Th as this would indicate the presence of detrital contamination of samples and the addition of non-radiogenic ^{230}Th .
- The samples should be impermeable to sea or groundwater because the flow of water through the system may cause alteration to the U or Th content.
- There should be no evidence of weathering in the sample.
- There should be no evidence of recrystallisation and/or deposition of void-filling cement.
- The $^{234}\text{U}/^{238}\text{U}$ ratio should be consistent with the $^{230}\text{Th}/^{234}\text{U}$ ratio in samples of different age from the same system (i.e. should show a systematic decrease with sample age).
- The $^{230}\text{Th}/^{234}\text{U}$ ages should be consistent with the stratigraphic position of the samples.

1.8.3.2 Checks on the validity of samples for dating

Any contamination of a sample can be checked by calculating its [$^{230}\text{Th}/^{232}\text{Th}$]. Ratios less than 15 to 20 (Bischoff and Fitzpatrick, 1991; Geyh, 2008) are thought to significantly effect the age analysis of a sample by making it appear older (Bischoff and Fitzpatrick, 1991). There are no simple chemical or physical means to separate the carbonate from non-carbonate detrital contaminants completely (Gascoyne and Schwarcz, 1982), primarily due to contamination of samples by detrital ^{230}Th (Kaufman, 1993). Relatively few

published works have indicated success in dating 'dirty' samples- though two main approaches have emerged- chemical separation techniques and isochron dating.

Different chemical separation and analyses methods of single and multiple leachates, residues and combination of all of these have been compiled by Schwarcz and Latham (1989), and Kaufman (1993). These methods involve a series of assumptions about the ratio of the concentrations of the relevant nuclides between different dissolved fractions and in the detrital material. In a study of palaeolake carbonates from the Bolivian Altiplano Placzek et al. (2006) found that initial Th may have two sources: (1) a siliciclastic fraction, and (2) 'unsupported' or 'hydrogenous' Th. They employed various Th isotope ratios to correct for single sample carbonates, with the simplest of these to assume that [$^{230}\text{Th}/^{232}\text{Th}$] is equal to the upper continental crustal value of ~0.8 (Polyak and Asmerom, 2001). However, this assumption can be problematic as [$^{230}\text{Th}/^{232}\text{Th}$] values for siliciclastic materials originating from soils, dust and alluvium can range from 0.25 to 1.7 (Szabo and Rosholt, 1982; Kaufman, 1993). High resolution dating of Holocene tufa has been reported by Garnett et al. (2004) to be problematic due to detrital contamination combined with short time for growth of radiogenic Th. They also found that a single value of [$^{230}\text{Th}/^{232}\text{Th}$] to correct for the presence of detrital ^{230}Th is not appropriate (as there is considerable variability in the isotopic composition of the detritus) in their study and suggest that this may apply to most Holocene tufa.

Isochron dating is a mathematical method of predicting a 'clean' age (Bischoff and Fitzpatrick, 1991; Przybylowicz et al., 1991; Placzek et al, 2006). It requires multiple subsamples of the same age, but with variable degrees of contamination, to be obtained and analysed. This coupled with the need to make an independent test of the range of isotopic variability of detritus at the sample site has the potential to turn this into a long and relatively time consuming process.

1.9 Analytical Procedure

1.9.1 Introduction

After appropriate samples had been selected for dating they had to be rendered into a form appropriate for analysis. Preliminary extraction of U-series elements from a sample is a straight forward procedure. Subsequent separation of

the desired nuclides, ^{234}U and ^{230}Th , from other chemically similar nuclides in the group and obtaining them at desired concentrations for age analysis (^{234}U and ^{230}Th at ppm and ppb levels respectively) required a lengthy chemical procedure. Once in a form suitable the samples were analysed by mass spectrometer and the resultant counts of nuclides were then used to calculate an age for the sample. The analysis process therefore involved four key stages; preconcentration of U and Th, separation of U and Th, analysis of samples using mass spectroscopy and processing of results for age calculation.

1.9.2 Preconcentration

Initially the sample was ground as finely as possible and well mixed in order to homogenize the sample before an aliquot is taken for analysis. Complete dissolution of the sample was achieved by nitric acid digestion. A mixed ^{229}Th - ^{236}U spike solution, an internal tracer containing known quantities of ^{229}Th , ^{232}Th , and ^{236}U , was added at the start of the procedure, before the sample had been subjected to any further chemical treatment. This was done in order to help assess the mass bias of the sample during analysis, and to achieve ion beams of desirable voltage for counting of nuclides during mass spectroscopy. No $^{235}\text{U}/^{238}\text{U}$ was incorporated into the spike as a natural atomic ratio is assumed for these isotopes and corrected accordingly. In order to remove any organic components from dissolved samples they were treated with hydrogen peroxide, in cases where the sample was rich in organics (and produced an orange or purple leachate) perchloric acid was used.

1.9.3 Separation Scheme

The column separation method outlined in the first stage of the separation procedure described by Yokoyama et al. (1999) was used to separate ^{234}U and ^{230}Th . This involved the use of an ion exchange resin (Eichrom Industries Inc. U/TEVA.spec resin), which utilises a synthetic high molecular weight polymer that contains a large amount of diamyl, amylphosphonate (DAAP) functional groups. In the ionic form these act as labile/unstable ions, capable of exchanging with ions in the surrounding medium without any major physical change taking place in the structure (Lally, 1982). Matrix elements of the sample were eluted with 4 M HNO_3 , ^{230}Th eluted with 5 M HCl and ^{234}U with 0.1 M HNO_3 . Five molar HCl was used to

prevent the carry-over of ^{230}Th into the ^{234}U fraction and optimise U-Th separation (Ellam and Keefe, 2006). This step is critical with concerns to the integrity of the $^{229}\text{Th}/^{232}\text{Th}$ mass bias correction- it is essential that no ^{230}Th is left over to contaminate the separated ^{234}U fraction. After separation the U fraction was diluted with 5% HNO_3 in order to achieve an appropriate concentration of ^{234}U (~50 ppb) for analysis. Similarly 50 ppb of certified reference material (CRM) NBL112-A (obtained from the US Department of Energy, New Brunswick Laboratory) is added to the ^{230}Th fraction.

1.9.4 Mass Spectrometry

1.9.4.1 Variety of techniques available

Once separated, aliquots of uranium and thorium were subjected to analysis by mass spectrometer. Four different mass spectrometry (MS) techniques are in use: thermal ionisation (TIMS), plasma ionisation using a quadrupole mass filter (ICP-QMS), plasma ionisation using a sector magnet with a single detector system (SD-ICP-MS) or a multi-collector system (MC-ICP-MS). In all instruments, the nuclides of interest are ionised, separated according to mass, passed through ion multipliers, and detected using Faraday detectors (Van Calsteren and Thomas, 2006). For analysis of the samples involved in this study the MC-ICP-MS technique was utilised, whilst many previous studies referred to in this thesis have used TIMS. It is therefore useful to compare these two techniques.

1.9.4.2 Comparison of the TIMS and ICP-MS spectrometric techniques

Among the different mass spectrometric techniques for precise isotope ratio measurements TIMS used to be the dominant one, however since the start of their commercial availability in 1983 ICP-MS have increasingly become more favourable for analysis (Gabler, 2002; Becker, 2003). ICP based systems have orders of magnitude better sensitivity than TIMS systems for both U and Th (Van Calsteren and Thomas, 2006), which leads to smaller required sample size and higher sample throughput (Shen et al., 2002). This is due to the superior ionization efficiency (the ratio of charged ions generated to neutral atoms evaporated) of ICP-MS (Luo et al., 1997; Potter et al., 2005). In TIMS this is inversely proportional to the first ionization potential of the analyte which for both ^{234}U (6.14 eV) and

^{230}Th (6.08 eV) is quite high. Typical ionisation efficiencies for ^{234}U are low (ca. 0.01%) and show a tendency to decrease with larger sample size (Chen et al., 1992; Ellam and Keefe, 2006). Due to this inefficiency TIMS analysis requires high purity samples in relation to ICP-MS. Another disadvantage of TIMS is instrumental mass fractionation which preferentially ionizes light isotopes as a sample is progressively evaporated and ionized from the mass spectrometer filament ion source. This is detrimental to the precision of the measurement; however accuracy can be improved depending on the ability to correct for the effect (Ellam and Keefe, 2006). The ICP-MS method also requires fewer preparation steps and shorter measurement times (Shen et al., 2002). Measurement of fairly intense isotope count signals over short acquisition times are less vulnerable to background than relatively low intensity TIMS measurements with longer time periods.

1.9.4.3 MC-ICP-MS analysis

Multiple-collector instruments are different in concept from single collector ICP instruments. Whereas the latter measures signals sequentially or at high speed over a broad mass range, the former simultaneously measures ion beams over a restricted mass range to obtain accurate and precise isotope ratios (Halliday et al., 1998). In the present study a MC-ICP-MS was used at the SUERC laboratories. Analysis of samples was carried out on an upgraded Micromass (now GV instruments) Isoprobe equipped with 9 Faraday collectors and an ion counting Daly-photo-multiplier detector located behind a wide-access retarding potential (WARP) filter. An Elemental Scientific Inc. Apex-Q device equipped with an ACM desolvating membrane was used to introduce the sample to the plasma source. An elemental Scientific Inc. PFA-ST nebuliser operated at a flow rate of $50 \mu\text{l min}^{-1}$ connects directly to the sample probe of a Ceta Technologies ASX-500 auto sampler controlled by the instrument software. Additional operating conditions are shown in Table 1.1.

Accelerating voltage	ca. 6000v
Rf generator	Serren IPS 12000
Rf power	1350 W
Ar gas flow rates;	
Cool gas	13.5 l min ⁻¹
Intermediate	1 l min ⁻¹
Collision gas	1.8 ml min ⁻¹
Sample introduction system	Elemental Scientific Inc. Apex-Q with ACM membrane desolvation unit
Nebuliser	PFA 50 µl min ⁻¹
Heating stage	100°C
Peltier cooling stage	2°C
Nebuliser 1 Ar	0.85 l min ⁻¹
Nebuliser 2 Ar	0.05 l min ⁻¹
Sweep gas	Argon
Carrier gas	Nitrogen

Table 1.1: Operating conditions for the MC-ICP-MS (Ellam and Keefe, 2006).

ICP-MS plasma uses many more times the energy required to overcome the first ionisation energy of both U and Th. This creates nuclides of various ionisation states with a ± 30 eV variance in energy. The plasma is collided with argon gas in a Hexapole collision cell to lessen the effect of this variance, dropping it to ± 1 eV on entering the magnetic sector. The plasma beam is then separated into multiple beams of various atomic masses by the energy of the magnet, before reaching the WARP filter with concentrations of ~ 25 ppm for the nuclides to be measured. This filter rejects any ions that have lost energy relative to their departure from the hexapole cell and greatly improves the abundance of sensitivity of the instrument (i.e. the ability to separate the tail of a minor peak from an adjacent major peak) from > 20 ppm at -1 atomic mass unit (amu) for the Faraday detectors to < 200 ppb at the Daly photomultiplier detector (Ellam and Keefe, 2006). Since the background noise of the Faraday cups is on the order of 10^{-14} amps, smaller signals need to be counted on the Daly detector. This is essentially a polished knob, sitting behind the Faraday cups, producing a charge of -25 kV. The Daly detector attracts ions which on collision produce electrons and a pulse of light for each arrival. A photomultiplier is used to amplify this signal for counting. The background on the Daly is essentially zero (6 counts per minute).

Spiking of the sample helps to achieve ion beams of approximately 0.2 V for ^{229}Th and ^{232}Th and 1-2 V for ^{238}U during analysis. For U runs ^{235}U , ^{236}U

(spike), and ^{238}U are counted simultaneously using Faraday detectors in dynamic collection mode. This involves two counts in which each nuclide is counted on a different Faraday cup. The Daly detector is used during the first count to measure ^{234}U and during the second count to measure ^{235}U . For Th analysis the Faraday detector measures ^{229}Th (spike), ^{232}Th , ^{235}U and ^{238}U . During the first count ^{229}Th is measured on the Daly, whilst this detector is utilised to measure ^{230}Th during the second count. For these two separate analysis runs ^{234}U and ^{230}Th are measured on the Daly photomultiplier detector with a beam intensity of about 4,000 cps.

All measurements are corrected for mass bias and Daly-Faraday gain. During the first counting stage of both U and Th runs ^{235}U and ^{238}U are measured on separate Faraday cups. Instrumental mass bias on these measurements is corrected by assuming natural $^{235}\text{U}/^{238}\text{U} = 0.007257$ and using an exponential fractionation law (Ellam and Keefe, 2006). The determined mass bias correction is then applied to the rest of the atomic measurements. Daly-Faraday gain is the measurement of the efficiency of the Daly Photomultiplier in relation to that of the Faraday, which is around 97% with a temporal drift on the order of <0.1% per hour. This bias is corrected for by measurement of either ^{235}U or ^{229}Th on both the Daly and Faraday detectors across the two counting stages. In addition all ion beams were corrected for background using on-peak zeroes measured in blank 5% HNO_3 for 60s prior to each analysis. Data for both samples and bracketing standards were collected as five blocks of 20 x 5 second cycles, with each analysis taking approximately 10 minutes and 20 minutes (allowing for sample to aspirate from the auto sampler tube to the plasma) for U and Th respectively.

1.9.4.4 Processing of results and error on measurements

Ages of the samples are calculated using the decay constants of Cheng et al. (2000) and Isoplot/Ex rev. 2.49 (Ludwig, 2001) (Figure 1.8). Measured atomic ratios of $^{236}\text{U}/^{238}\text{U}$, $^{234}\text{U}/^{238}\text{U}$, $^{230}\text{Th}/^{229}\text{Th}$ and $^{232}\text{Th}/^{229}\text{Th}$ are entered in to a U-Th dating spreadsheet. Within this spreadsheet the $^{230}\text{Th}/^{238}\text{U}$ atomic ratio is calculated from regression of the $^{230}\text{Th}/^{229}\text{Th}$ and $^{236}\text{U}/^{238}\text{U}$ atomic ratios coupled with the known concentrations of nuclides in the spike. The decay constants of the relevant isotopes are then used to determine the $[\text{}^{230}\text{Th}/^{238}\text{U}]$ and $[\text{}^{234}\text{U}/^{238}\text{U}]$ activity ratios to two standard errors. This information is then entered into the Isoplot/Ex rev. 2.49 program which uses a single-analysis array function called

'Th230AgeAndInitial' to plot the data on a [$^{230}\text{Th}/^{234}\text{U}$] evolution diagram (which is the result of a 2-D isochron of [$^{230}\text{Th}/^{238}\text{U}$] against [$^{234}\text{U}/^{238}\text{U}$]), which produces the age and initial chemistries of samples. The decay constant errors of ^{230}Th and ^{234}U are propagated into the age-error calculation along with errors on the activity ratio to provide final errors on the ages of sample.

As well as age results the Isoplot processing stage produces a value for the initial uranium, which is back calculated from the [$^{234}\text{U}/^{238}\text{U}$] of the sample. Initial uranium is the activity ratio of uranium, [$^{234}\text{U}/^{238}\text{U}$] or $\delta^{234}\text{U}$, at the time of formation of the sample. The symbol for this term, which is used extensively in subsequent chapters, is $\delta^{234}\text{U}$. The results of the samples in this study are accompanied by 2σ analytical error envelopes on the isotope ratios and decay constants. Uncertainty on measured isotope ratios reflects counting errors and variability within a single MC-ICP-MS analysis, whilst decay constant error envelopes are after Cheng et al (2000). The analytical error provided for each sample, which is symmetrical in both the older and younger direction, is of the order of 0.5 – 1% of the age measurement. In chapters 2 and 3 further sources of error are discussed which may have an affect on the age result of samples.

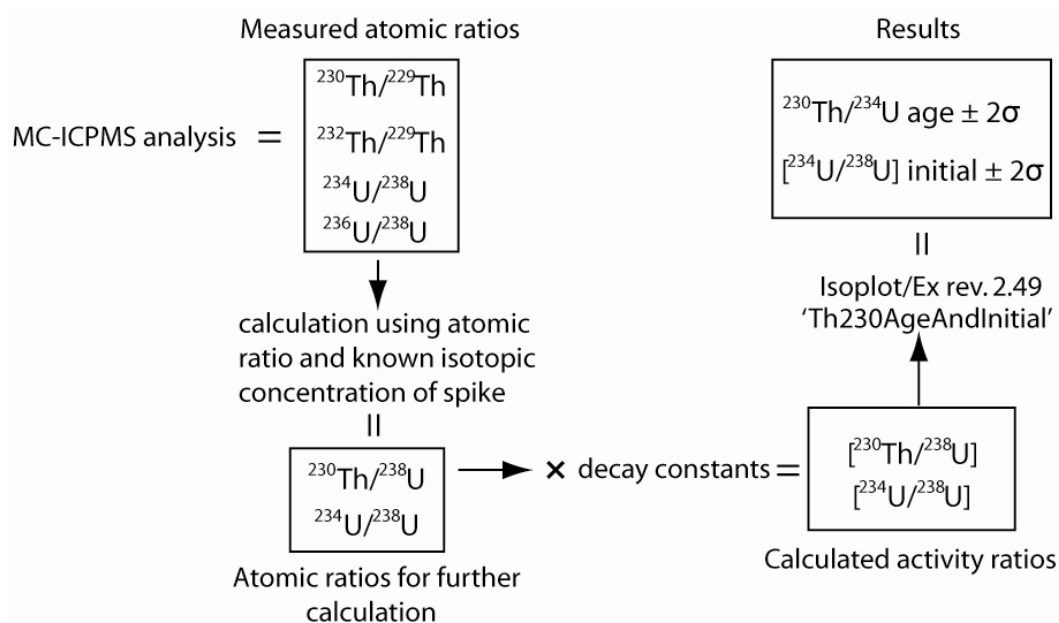


Figure 1.8: Work flow for processing of U-Th results.

2 U-series methodology: a case study from the Gulf of Corinth, Greece.

2.1 Introduction

In order to test the methods for U-Th dating outlined in Chapter 1, a study was carried out on coral which is a material that is commonly used for palaeoclimate and palaeo-ocean studies (Dumas et al., 2006; Stirling and Anderson, 2009). Samples of *Cladocora caespitosa* from the Gulf of Corinth, Greece, are investigated. This area is of particular interest as deposits that contain the ancient remains of *C.caespitosa* have been used to determine the slip rates of large normal faults (Collier et al., 1992; Dia et al., 1997; Morewood and Roberts, 1999; Haughton et al., 2003; Leeder et al., 2003; 2005; Roberts et al., 2009).

Section 2.2 presents the issue of correlation of U-Th coral ages with sea level highstand, an important factor for calculation of fault slip rate. U-series dating of coral specimens is discussed in Section 2.3, with emphasis on how uranium is incorporated into coral skeleton and checks on the validity of samples for analysis. Section 2.4 provides a background to previous work carried out in the Gulf of Corinth and outlines the parameters required to determine a slip rate for the main fault in question, the South Alkyonides fault segment. An in-depth review of the field locations from which the coral samples came from is also provided within this section. The results of U-Th dating of *C.caespitosa* samples are presented in section 2.5. Interpretation of these results is carried out by investigating the factors that can affect initial uranium (${}_0\delta^{234}\text{U}$) of coral specimens. As age results of coral are commonly interpreted to be representative of the nearest historical sea level highstand an overview of the uncertainties involved with both sea level curves and coral growth depths is presented in section 2.6. Section 2.7 discusses whether this study has formed a successful test for the dating method detailed in Chapter 1; reviews the suitability of coral in general as a tool for tectonic study, and assesses whether age information gained from coral in this particular region can be used with confidence for fault slip-rate calculations. Finally the results of this study are used to re-assess previous published slip rate values for the South Alkyonides fault segment.

2.2 Sea level highstand and correlation with coral age

The timings of ancient sea level highstand are determined from $\delta^{18}\text{O}$ isotopic records which have been compiled in order to produce global relative sea level curves (Siddall et al., 2003; Waelbrook et al., 2002). The presence of corals, on present day contemporary reef flats together with the frequent occurrence of their fossil equivalents throughout recent history suggests that the accretion of reefs closely tracks rising sea level and therefore represent periods of sea level highstand (Bryan and Stephens, 1993; Kench et al., 2009). As such ancient coral deposits should reflect the age of recognised highstand when dated. Eleven separate global sea level highstand are currently recognised within the time limits of U-Th dating (present day, 76, 100, 125, 175, 200, 216, 240, 290, 310 and 340 ka). U-series studies on coral often correlate their results to the closest timing of highstand even if the radiometric age of the sample does not closely match the highstand age within error (e.g. Stein et al., 1991; Wehmler et al., 2004; Omura et al., 2004). This practice highlights a real issue with the U-series dating of corals- if age results do not match with highstand ages then either there is a problem with the U-series technique or a problem with coral as a tool for U-Th dating.

2.3 U-series dating of coral

Coral is a colonial organism that takes up uranium from the water surrounding it during construction of its aragonite skeleton. Coral skeleton can contain U in concentrations of between 2-3.5 ppm (Shen and Dunbar, 1995), but is essentially free of ^{230}Th at the time of formation (Barnes et al., 1956; Swart and Hubbard, 1982) allowing it to be utilised for age determination by U-Th analysis. Uranium concentrations recorded by coral samples are thought to accurately reflect the uranium concentration of the environment of growth. Analysis of modern coral collected in open seawater environments from various locations including, Barbados, Galapagos, Tobago and Vanuatu, demonstrate the initial uranium activity ratio (${}_0\delta^{234}\text{U}$) of seawater accurately (Bard et al., 1991). The location of uranium within the coral skeleton has yet to be determined though it is possible that it substitutes for calcium in the mineral phase (Amiel et al., 1973a; 1973b; Swart et al., 1982; Pingitore Jr et al., 2002). Large variations in U concentration in sections of individual living corals have been observed from fission track analysis,

with high concentrations corresponding to low coral growth rates and vice versa (Schroeder et al., 1970, Robinson et al., 2006).

As coral grows in marine environments the known excess of [^{234}U] in seawater (14-15% over [^{238}U], Veeh and Burnett, 1982) can be used as a convenient check on the closed system assumption, and therefore reliability, when dating coral samples. This excess ^{234}U in ocean water has been ascribed to input by river water (average [$^{234}\text{U}/^{238}\text{U}$] approx 1.20, Cherdyntsev et al, 1955; Thurber, 1962) and diffusion of ^{234}U from deep sea sediments (Ku, 1965): This results in a greater than unity [$^{234}\text{U}/^{238}\text{U}$] of $1.145 \pm 2\%$ (Hamelin et al., 1991; Bard et al., 1991), a value that has remained constant for at least the past 800 ky in the open ocean (Henderson, 2002).

Of the criteria on U-series dating highlighted in section 1.8.3.1 of Chapter 1, coral and marine carbonates frequently violate the following stipulations:

- The samples should be impermeable to sea or groundwater because the flow of water through the system may cause alteration to the U or Th content.
- There should be no evidence of weathering in the sample.
- There should be no evidence of recrystallisation and/or deposition of void-filling cement.

The delicate structure of coral skeleton, short diffusion distance across the septa and porosity increasing degradation of inter-crystalline organic material are all factors which can contribute to open system behaviour of U-Th decay (Van Calsteren and Thomas, 2006). Despite these issues reliable ages can be obtained from carefully selected samples. Visual and microscopic inspection must be carried out to assess the absence of detritus, and XRD can be utilised to determine absence of re-crystallisation. After initial selection and sample analysis, it is usually assumed that if the initial [$^{234}\text{U}/^{238}\text{U}$] in the carbonate is the same as the surrounding seawater, the system has remained 'closed' (Henderson, 2002). Samples outwith the 2% error are considered as suspect and should be treated with caution. This can be potentially caused by initial ^{231}Pa in the corals (Imai and Sakanoue, 1973) or post depositional adsorption of ^{231}Pa and ^{230}Th into the corals from the surrounding sedimentary matrix (Veeh and Burnett, 1982). Restricted

basins with reduced salinity or hydrothermal input may have a different [$^{234}\text{U}/^{238}\text{U}$] to that of the open ocean (Van Calsteren and Thomas, 2006), so sample source and environment should also be taken into account when back-checking the initial uranium activity, ${}_0\delta^{234}\text{U}$.

2.4 The South Alkyonides fault segment

2.4.1 Introduction

Palaeoshorelines uplifted in the footwall of the South Alkyonides fault segment, central Greece (Figure 2.1) can potentially be used to assess its slip rate history relative to other faults in the area by dating of coral situated within them (e.g. Collier et al., 1992; Morewood and Roberts, 1998; McNeill et al., 2004). Central Greece is one of the most rapidly extending parts of the Earth's continental crust, with 10-15 mm/yr N-S extension localised within a <30km wide E-W zone associated with the Gulf of Corinth (Roberts et al., 2009). The South Alkyonides fault segment is an active E-W trending normal fault with downthrow to the north. These faults have been ruptured by seven >Ms 6.0 normal faulting earthquakes since 1909 (Ambraseys and Jackson, 1990), and last ruptured in 1981 (Ms 6.9-6.7) leaving a chasm 10-20cm wide and a vertical offset of up to 1.5 m. Uplifted Quaternary and Holocene palaeoshorelines decrease in elevation towards the western tip of the fault, exhibiting larger tilt angles with apparent age, showing that palaeoshoreline uplift is due to progressive fault slip (Roberts et al. 2009).

In order to estimate the slip rate of the South Alkyonides fault segment three parameters need to be understood: (i) the present day elevation of the palaeoshoreline inner edge, (ii) its absolute age and (iii) relative sea level during formation of the marine terrace. The first two parameters can be obtained from field work and laboratory analyses, but the third relies on the use of the relative sea level curve. This chapter details the suitability of coral for slip rate study in this region, focusing on the U-Th and Sr chemistry of the samples and discussing the accuracy of published relative sea level curves, addressing parameters (ii) and (iii) above. Parameter (i) above is addressed for each sample during a review of the sample areas below in section 2.4.2 and a discussion of correlation between U-Th dating results of corals and sea level highstand in section 2.6.6.

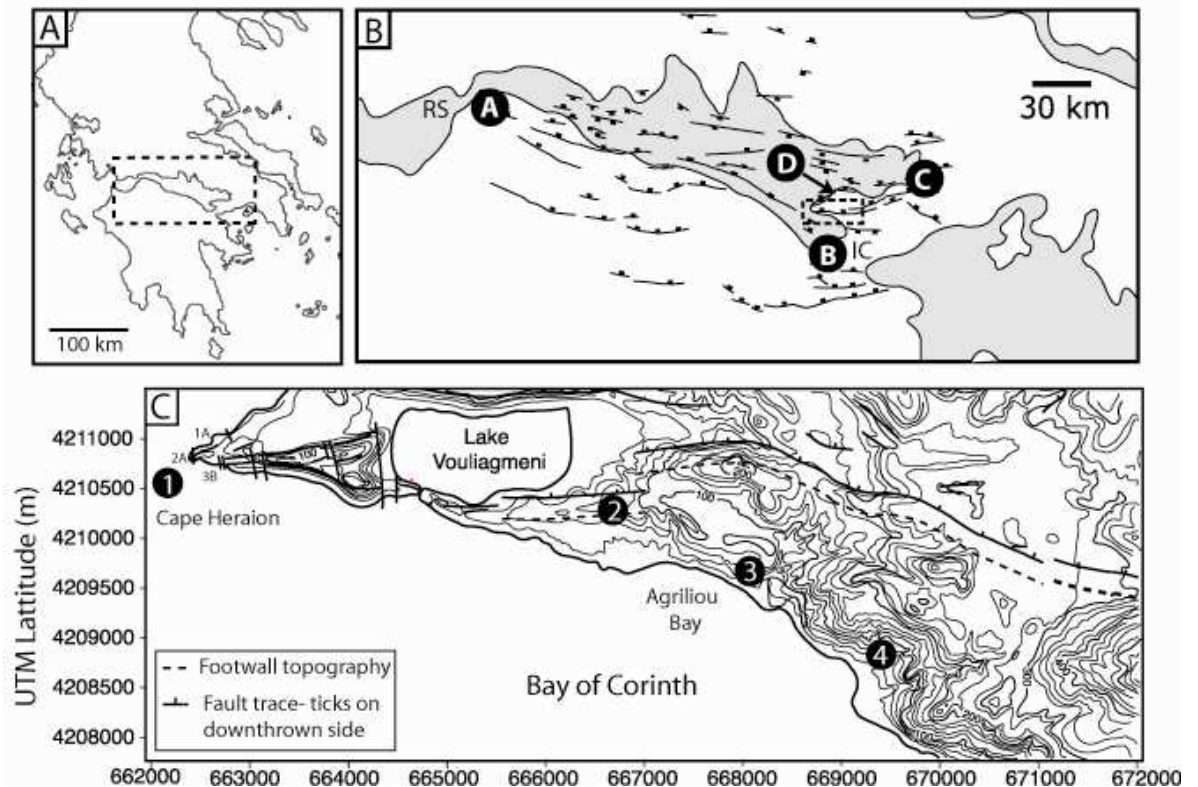


Figure 2.1: Gulf of Corinth and the Perachora Peninsula.

(A) Map of central Greece with the Gulf of Corinth highlighted by the dashed box. (B) Large scale view of the Gulf of Corinth after Haughton et al. (2003) showing major onshore and offshore faults. RS and IC stand for Rio Straits and Isthmus of Corinth respectively, whilst the letters represent the different study sites referred to in Table 2.2: A- Pspathopyrgos fault, B- South Corinth basin, C- Megara basin, D (and dashed box)- Perachora Peninsula. (C) Detailed map of Perachora Peninsula from Roberts et al. (2009) showing the trace of the South Alkyonides fault segment and the locations of the sites in this study referred to in the text and in Table 2.1: 1- Cape Heraion, 2- SE of Lake Vouligameni, 3- Agriliou Bay, 4- Hotel complex. The separate locations of samples 1A, 2A and 3B are also shown at Cape Heraion by the small black labels.

2.4.2 *C. caespitosa* sample sites and U-Th results

A total of twelve age analyses of *C. caespitosa* from four separate locations associated with the South Alkyonides fault segment on the Perachora Peninsula were carried out (Table 2.1, Figure 2.1C). This section will discuss each of these samples in terms of their location, relation to one another and also relation to reported ages and associated highstand from the same sites in previous studies.

Cape Heraion

Three samples, 1A, 2A and 3B, were dated from this location (Location 1 in Figure 2.1). The tip of Cape Heraion is defined by two E-W trending faults. If these

faults hosted a normal sense of slip during seismic events then the tip of the Cape could represent an uplifted horst structure. In order to determine if the central part of the Cape was indeed a horst block coral from atop the central section and from palaeoshorelines each side were sampled for age determination- if all the sections provided a matching age it would confirm the presence of this structure. Samples 1A and 3B were taken from two *in-situ* coral colonies from the north and south segments of the tip at similar elevations (7-8 m). Sample 2A was taken from the central section of the tip at 46 m. No *in-situ* coral was found at this location, and indeed sample 2A was the only coral found, consisting of a badly weathered looking single corallite within a layer of marine sediment. Optical microscope inspection of this sample showed it to be badly worn (Figure 2.5A) with the outer wall of the corallite completely smooth rather than ribbed.

The samples returned ages of 142.6 ± 1.2 , 138 ± 1.2 and 277.3 ± 7.7 ka for 1A, 3B and 2A respectively. The ages of 1A and 3B match well, suggesting they represent the same period of coral formation, whilst the age for 2A is markedly older. Optical inspection of 2A coupled with geochemical results (section 2.5.4) make its U-Th age suspect. This sample demonstrated a high Th concentration and high $[^{230}\text{Th}/^{232}\text{Th}]$. Its U concentration is also elevated in comparison to samples 1A and 3B (Table 2.1). As sample 2A did not provide a reliable age the present study cannot confirm Cape Heraion as a horst structure.

Both Roberts et al. (2009) and Leeder et al. (2005) report ages from the immediate area of this location. Roberts et al. (2009) provide two dates of 116 ± 1.4 and 141 ± 1.7 ka. They report low confidence in both dates as they found a trace of gypsum associated with the younger sample and the older age was provided by analysis of coral septa as opposed to the more robust wall. The younger 116ka sample provides a large ${}_0\delta^{234}\text{U}$ of 1.324 in comparison to coral of similar age (Figure 2.3C), whilst the older 141 ka date, although from coral septa provides similar chemistries to that of the samples in the present study (${}_0\delta^{234}\text{U}$ of 1.221, and a high $[^{230}\text{Th}/^{232}\text{Th}]$). Leeder et al. (2005) report two dates from the tip of the Cape of $136.5^{+13.6}_{-12.1}$ and $181.7^{+16.6}_{-14.3}$ ka. The former agrees well with the results of this study, while the latter seems marginally high. They record the elevation of the samples as +8 m MSL, similar to the findings of this study, and correlate these deposits to identical deposits higher in the cliff to the NE at an elevation of +23 m MSL suggesting that post depositional faulting has occurred at

this location. Due to its elevation this upper palaeoshoreline is interpreted by Leeder et al. (2005) to be a product of the 125 ka highstand.

South east of Lake Vouligameni

Sample 11A comes from a location that represents one of the upper terraces near the trace of the South Alkyonides fault segment (Location 2 in Figure 2.1C). The U-Th dating of this sample returned an age of 269.8 ± 13.3 ka. No previous geochronology has been carried out on coral from this location, but the sampling elevation of this sample at +73 m MSL and its location in relation to the mapping of Roberts et al. (2009) would suggest that this palaeoshoreline belongs to the 340ka highstand. However, its elevation lies closer to the Roberts et al. (2009) modelled shoreline estimate of +80 m MSL associated with the 290 ka highstand.

Agriliou Bay

Two samples were collected from Agriliou Bay (Location 3 in Figure 2.1). The first, sample 8A was from a colony that seemed undisturbed and in life position at the edge of an excavated area. The second, 10A, could not be correlated directly below 8A but occurred ~2 m lower in elevation on the path required to reach 8A. It is hard to determine if 10A was in life position but it was from a lower stratigraphic layer than 8A. Sample 8A produced an age of 158 ± 2.9 ka and its repeat analysis an age of 153 ± 1.6 ka. As the errors on these ages overlap good reproducibility of dating is demonstrated. Sample 10A produced an age of 169.2 ± 2.3 ka. Sample 8A was taken from an elevation of +34 m MSL, and could be traced to terrace deposits up to +51 m MSL. This location is mapped as the 125 ka highstand by Roberts et al. (2009).

Hotel Complex

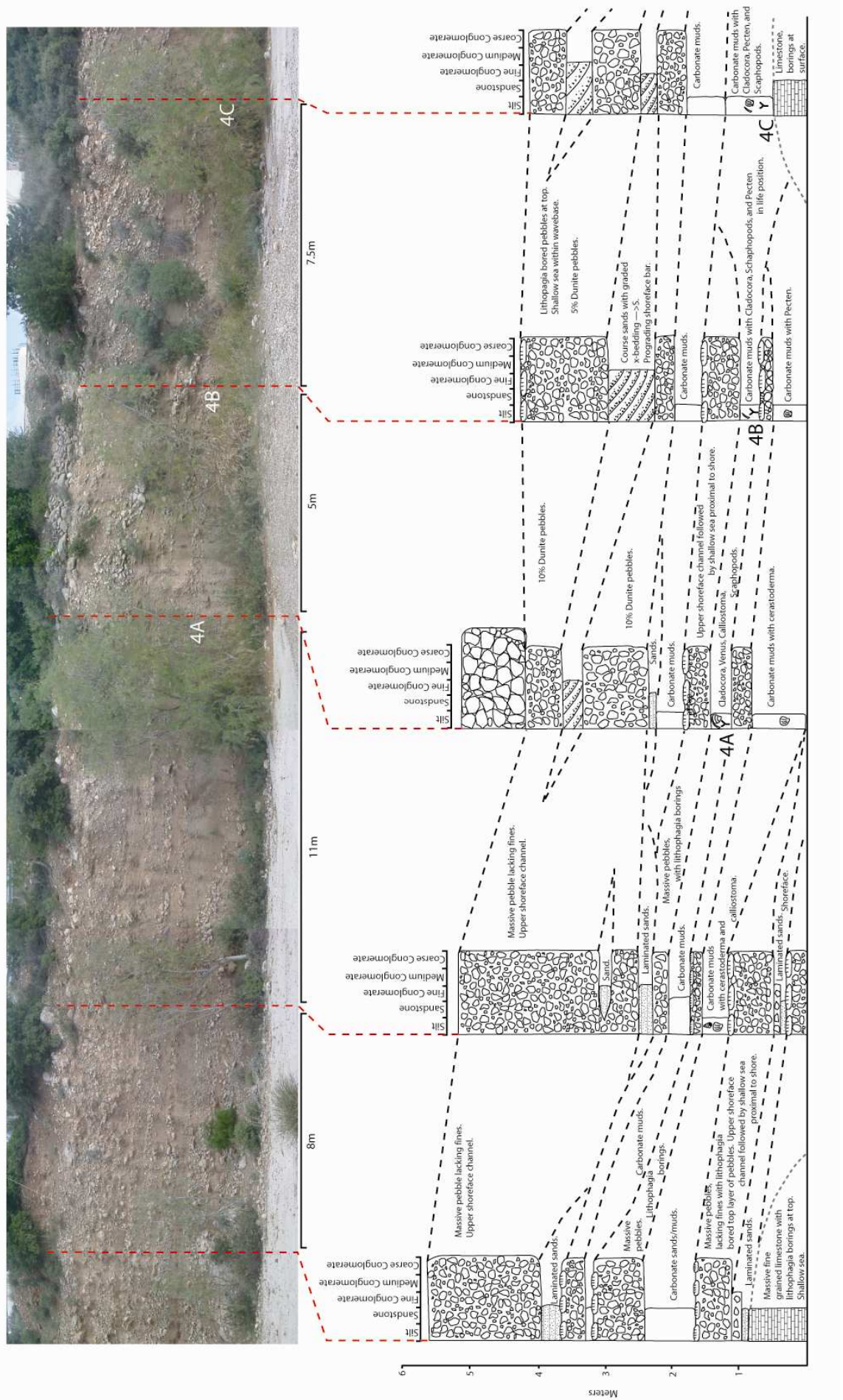
A total of five samples were dated from an excavated car park (Location 4 in Figure 2.1), two from a logged section reported in Roberts et al. (2009) on the west face of the excavation and three from the previously undated east face of the excavation. Samples 5A and 6A were taken from two additional *C.caespitosa* colonies, one from above and one from below the three layers reported, in the logged section of Roberts et al. (2009) from this location. Roberts et al. (2009)

report ages of 178 ± 6.4 , $201^{+3.4}_{-3.3}$ and $211^{+4.3}_{-4.4}$ ka which they correlate to the 175, 200 and 216 ka highstand respectively. The layers above and below, if in life position, should therefore provide a younger and an older age than these reported dates. Roberts et al. (2009) predict these layers to represent the 125 ka and 340 ka highstands. Sample 5A from above these layers, and 6A from below these layers return U-Th ages of 232.9 ± 6.1 and 247.0 ± 4.6 ka respectively. The age for 6A matches well with the previous dated layers whereas 5A gives a date that is out of stratigraphical order. Due to the small vertical distance between them sample 5A is interpreted as a reworked deposit of lower layer that 6A was sampled from. Since there are three layers in between the upper reworked layer and the bottom layer to which it correlates, it is reasonable to assume that the upper layer is likely a combination of reworked deposits of the four layers below it. The ages of these samples fall close to the 240 ka highstand.

Samples 4A, 4B, and 4C, were sampled from a single layer from the east face of the excavation (Figure 2.2). This layer did not consist of a continuous coral deposit along the face like the west side; instead these samples were small isolated colonies up to 7.5 m apart. These three specimens provide ages of 165.9 ± 1.6 , 152.1 ± 1.4 , and 147 ± 10.6 ka for 4A, 4B and 4C respectively. Whilst 4B and 4C overlap within error, the dates are quite distinct considering the samples originate from the same layer. This can perhaps be explained by varying degrees of alteration of the small coral colonies on this side of the excavation, with sample 4C coming from a heavily cemented section of carbonate mud.

Figure 2.2: Log of the east wall of the hotel complex excavation.

The log shows the relationship of samples 4A, 4B and 4C, and a correlation plus interpretation of the sedimentary units that are exposed in this wall of the excavation.



Sample	Location	U-Th age (ka) (2 σ with λ)	$^{234}\text{U}/^{238}\text{U}$ (2 σ with λ)	$^{230}\text{Th}/^{238}\text{U}$ (2 σ with λ)	Total U (ppm)	Total Th (ppb)	$^{87}\text{Sr}/^{86}\text{Sr}$ (1 SE %)	$^{230}\text{Th}/^{232}\text{Th}$	Sampling elevation (m)	A.H
1A	1	142.7 \pm 1.2	1.202 \pm 0.004	0.847 \pm 0.0017	2.833	3.55	0.709104 \pm 0.0013	2059	7	125 ka
2A	1	277.3 \pm 7.7	1.260 \pm 0.006	1.064 \pm 0.0050	4.642	97.44	-	91	46	-
3B	1	138.1 \pm 1.3	1.188 \pm 0.004	0.827 \pm 0.0023	2.730	11.41	0.709124 \pm 0.0012	1956	8	125 ka
4A	4	165.9 \pm 1.6	1.217 \pm 0.004	0.910 \pm 0.0012	3.380	7.52	0.709128 \pm 0.0013	1246	7	175 ka
4B	4	152.1 \pm 1.4	1.208 \pm 0.004	0.874 \pm 0.0021	5.452	11.23	0.709151 \pm 0.0014	884	6	175 ka
4C	4	147.1 \pm 10.6	1.221 \pm 0.046	0.869 \pm 0.0021	1.142	3.59	0.709123 \pm 0.0014	1063	6	175 ka
5A	4	232.9 \pm 6.1	1.274 \pm 0.006	1.041 \pm 0.0070	2.225	3.37	0.709099 \pm 0.0015	1533	10	240 ka
6A	4	247.0 \pm 4.6	1.300 \pm 0.005	1.068 \pm 0.0030	2.778	8.51	0.709083 \pm 0.0013	1061	8	240 ka
8A	3	158.1 \pm 2.9	1.211 \pm 0.005	0.890 \pm 0.0068	2.068	3.68	0.709146 \pm 0.0014	1520	34	175 ka
8Ar	3	153.7 \pm 1.6	1.213 \pm 0.005	0.881 \pm 0.0027	2.878	4.54	-	1234	34	175 ka
10A	3	169.2 \pm 2.3	1.220 \pm 0.005	0.919 \pm 0.0041	2.434	5.51	0.709089 \pm 0.0016	1704	32	175 ka
11A	2	269.8 \pm 13.3	1.301 \pm 0.012	1.083 \pm 0.0123	2.728	5.18	-	1732	73	290 ka

Table 2.1: U-Th chemical and isotopic data for *C. caespitosa* coral samples

Location numbers refer to the locations in section 2.4.2 and are shown in Figure 2.1C. Numbers represent the following sites: 1- Cape Heraion, 2--southeast of Lake Vouligameni 3- Agriliou Bay, 4 – Hotel Complex. A.H stands for assigned highstand- see section 2.6.6 for discussion.

Study	n	Sample location	Age (ka)	Age + error	Age - error	U (ppm)	${}_0\delta^{234}\text{U}$	% from 1.145
Collier et al., 1992	7	B- South Corinth Basin	232	23.6	19.7	2.31	1.31	12.6
		C- Megara Basin	126.6	6.1	5.8	2.66	1.17	2.1
Houghton et al., 2003	5	A- Psathopyrgos Fault	174.7	6.2	5.9	2.466	1.197	4.3
		A- Psathopyrgos Fault	147.4	2.9	4.3	2.211	1.097	-4.4
Roberts et al., 2009	28	D- Perachora Peninsula	356	50	32	2.503	1.429	19.9
		D- Perachora Peninsula	76.2	1	1	2.72	1.184	3.3
Leeder et al., 2005	19	D- Perachora Peninsula	133.4	0.9	0.9	3.52	1.257	8.9
		D- Perachora Peninsula	136.5	13.6	12.1	3.529	1.157	1.0
Dia et al., 1997	17	D- Perachora Peninsula	169.4	1.8	1.8	3.475	1.309	12.5
		D- Perachora Peninsula	68.6	0.5	0.5	3.064	1.163	1.5
Present study	12	D- Perachora Peninsula	269.8	13.3	13.3	2.728	1.301	12.0
		D- Perachora Peninsula	138.1	1.3	1.3	2.730	1.188	3.6
Modern Coral	2	Perachora Peninsula ^a	0.5	0.06	0.06	2.342	1.151	0.5
		Shallow Gulf ^b	-	-	-	2.336	1.139	-0.5

Table 2.2: Comparison of several U-Th coral studies from the Gulf of Corinth.

The data shown are both the largest and smallest ${}_0\delta^{234}\text{U}$ for the samples from each study and the deviation from the ${}_0\delta^{234}\text{U}$ of present day seawater (Henderson, 2002) in percent. 'n' refers to the number of samples presented in each study. Sample locations correspond to site locations in Figure 2.1B. The analysis from other studies provides results from both Alpha Spectrometry (Collier et al., 2005; Leeder et al., 2005) and TIMS (Houghton et al., 2003; Roberts et al., 2009; Dia et al., 1997; Leeder et al., 2005). All analysis was carried out on *Cladocora caespitosa*, bar the Collier et al. (2002) study which used another scleractinia order coral, *Acropora* sp. Modern coral analyses include: (a) specimen from Roberts et al. (2009) which was picked up from the discards of broken coral from local fisherman's nets, and (b) specimen from Leeder et al. (2005) which is attributed as a late Holocene coral trawled from the shallow Gulf.

2.5 Discussion of U-series results

The results of U-Th dating, along with $\text{Sr}^{87}/\text{Sr}^{86}$ data, for *C.caespitosa* samples analysed in the present study are shown in Table 2.1, whilst results from previous studies within the Gulf of Corinth are shown in Table 2.2. The coral samples utilised in this study, despite their overall pristine appearance, deviate from seawater $\delta^{234}\text{U}$ quite considerably, ranging from 3.5 – 12% above $\delta^{234}\text{U} = 1.145$. This is a common trend in previous U-Th analysis carried out on coral in the Gulf of Corinth; indeed other studies illustrate similar deviations from this value (Figure 2.3).

As stated in section 2.3, samples with ${}_0\delta^{234}\text{U}$ outwith 2‰ of modern seawater should be treated with caution. Previous studies using Corinth coral do take note of the large deviations of their analyses from this value, however they dismiss the significance of this check because samples with similar age produce widely different ${}_0\delta^{234}\text{U}$ (Haughton et al., 2003) or due to independent geological constraints such as stratigraphic position of the coral (Roberts et al., 2009; Collier et al., 2002; Leeder et al., 2005). Another control on the suitability of samples for dating, and dismissing the ${}_0\delta^{234}\text{U}$, is the correlation of sample ages to sea level high stands. Sediments containing the coral are transgressive marine units which, in the absence of evidence for syndepositional tectonic subsidence, can only have formed during high stand sea level phases (Collier et al., 1992; Roberts et al., 2009). This sedimentological setting coupled with assumptions about the accuracy of the sea level curve and coral depth, which are discussed later in sections 2.6.2 and 2.6.3, have led previous workers to conclude that the variation in ${}_0\delta^{234}\text{U}$ is not important. The following sections in this chapter will discuss the possible geochemical reasons for this deviation, negating the need for such assumptions and providing a sound reasoning for the departure from seawater chemistry of *C.caespitosa* specimens in this study.

2.5.1 Initial Uranium of coral through time

The $\delta^{234}\text{U}$ of modern day seawater is well defined, and recent coral samples reflect this ratio accurately. This tendency dissipates with time as older corals tend to produce higher ${}_0\delta^{234}\text{U}$ (Dia et al., 1997; Bard et al., 1991), a trend reflected by the data in the present study, and others from the Gulf of Corinth

(Figure 2.3A and C). Indeed elevated ${}_0\delta^{234}\text{U}$ of ancient coral analysis from locations from around the globe is the norm rather than the exception (Stein et al., 1991; El Moursi et al., 1994; Stirling et al., 1995; Omura et al., 2004- Figure 2.3D). This deviation from modern seawater $\delta^{234}\text{U}$ starts to become apparent in samples older than 70 ka (Chen et al., 1991; Bard et al., 1991). In a study of samples from the Galapagos, Barbados, Haiti and Curaçao Hamelin et al. (1991) showed that ${}_0\delta^{234}\text{U}$ for pristine samples 70-140 ka in age have a larger spread and higher mean value (1.160 with a standard deviation of 0.011) than present-day seawater and corals younger than 30 ka in age. Plots for these age ranges produced two distinct histograms with little overlap between the two distributions. Two possibilities exist to explain this global discrepancy; a change of global seawater $\delta^{234}\text{U}$ through time, or diagenetic alteration. With respect to samples from the Gulf of Corinth, the regional geology must also be taken into account when considering reasons for anomalous ${}_0\delta^{234}\text{U}$.

2.5.2 Variation in global seawater ${}_0\delta^{234}\text{U}$ through time

It has been suggested that variation in weathering rates and mean river fluxes may have caused a small decrease in the $\delta^{234}\text{U}$ of seawater during the last 100ka (Hamelin et al., 1991). This would give the simplest explanation of the observation that ancient corals have elevated ${}_0\delta^{234}\text{U}$. However, the response of uranium isotope composition of the oceans is likely to be slow because of the high solubility of uranium in seawater (Bard et al., 1991; Richter and Turekian, 1993), and resultant residence time of $\sim 300,000$ ka (Ku et al., 1977). As the mean modern $\delta^{234}\text{U}$ of river waters ranges from 1.2 to 1.3 (Collier et al., 1992) it is hard to see how uranium delivered to the oceans in this manner could generate the observed deviation. Further, the mixing time of oceans is fairly rapid (~ 1.5 ka) global change in $\delta^{234}\text{U}$ of seawater should produce uniform $\delta^{234}\text{U}$ values for samples of the same age, which is not seen when comparing studies from different localities (Dia et al., 1997). In addition, Henderson (2002) provides evidence from U-rich slope sediments from the Bahamas which show a scatter of $\delta^{234}\text{U}$ around the modern seawater value which does not increase with age of sample. This suggests that the $\delta^{234}\text{U}$ of the open ocean has remained within 15‰ of the modern value for the last 360ky. Over the time period from 360-800ky Henderson (2002) found a rather large diagenetic scatter of ${}_0\delta^{234}\text{U}$, but found no

indication of a trend in seawater $\delta^{234}\text{U}$ with age, or any evidence for higher values of $\delta^{234}\text{U}$. This lack of evidence for seawater $\delta^{234}\text{U}$ above modern values suggests that the physical weathering has not been higher than at present for any extended period during the last 800ka.

2.5.3 Diagenetic effects on coral $\delta^{234}\text{U}$ and their implications for U-Th dating

Living coral skeletons are homogeneous in uranium distribution (Amiel et al., 1973a; 1973b), whereas dead skeletons have been shown to contain a heterogeneous uranium distribution (Hamelin et al., 1991). Swart and Hubbard (1982) found that scleractinian skeletons in which the organic material had been removed readily exchange uranium with their environment. Experimentation shows that this occurs preferentially along septa and skeletal margins. Alteration of uranium concentration away from the margins and axes indicates the passage of fluids between adjacent crystals. These experiments therefore identify possible pathways for potential diagenetic fluid through the coral. Repeat analyses of two pieces of the same coral carried out by Hamelin et al. (1991) produced different $\delta^{234}\text{U}$, uranium concentrations and a significantly different age. The authors concluded that the sample was heterogeneous due to diagenetic effects. This evidence suggests that variability in $\delta^{234}\text{U}$ of ancient coral samples may be explained by diagenetic effects that lead to open system behaviour. The processes of $\delta^{234}\text{U}$ addition, $\delta^{234}\text{U}$ loss, and ^{230}Th addition have been suggested by Hamelin et al. (1991) to account for such variations.

Chemical or isotopic exchange with percolating groundwaters containing continental uranium enriched in ^{234}U during weathering may add $\delta^{234}\text{U}$ to the coral skeleton. Since ancient corals have been exposed to such weathering for hundreds of thousands of years it is likely that this diagenetic alteration has been a continuous process. The effects of this process can be bracketed between extreme cases of instantaneous addition, either early after the formation of the coral, or very recently. Early contamination would not change the calculated age dramatically as the U/Th ratio of the coral would evolve along a different evolution curve to that of seawater. In the case of recent U contamination, the $[\text{}^{230}\text{Th}/\text{}^{234}\text{U}]$ would decrease resulting in a younger U-Th age (Figure 2.4).

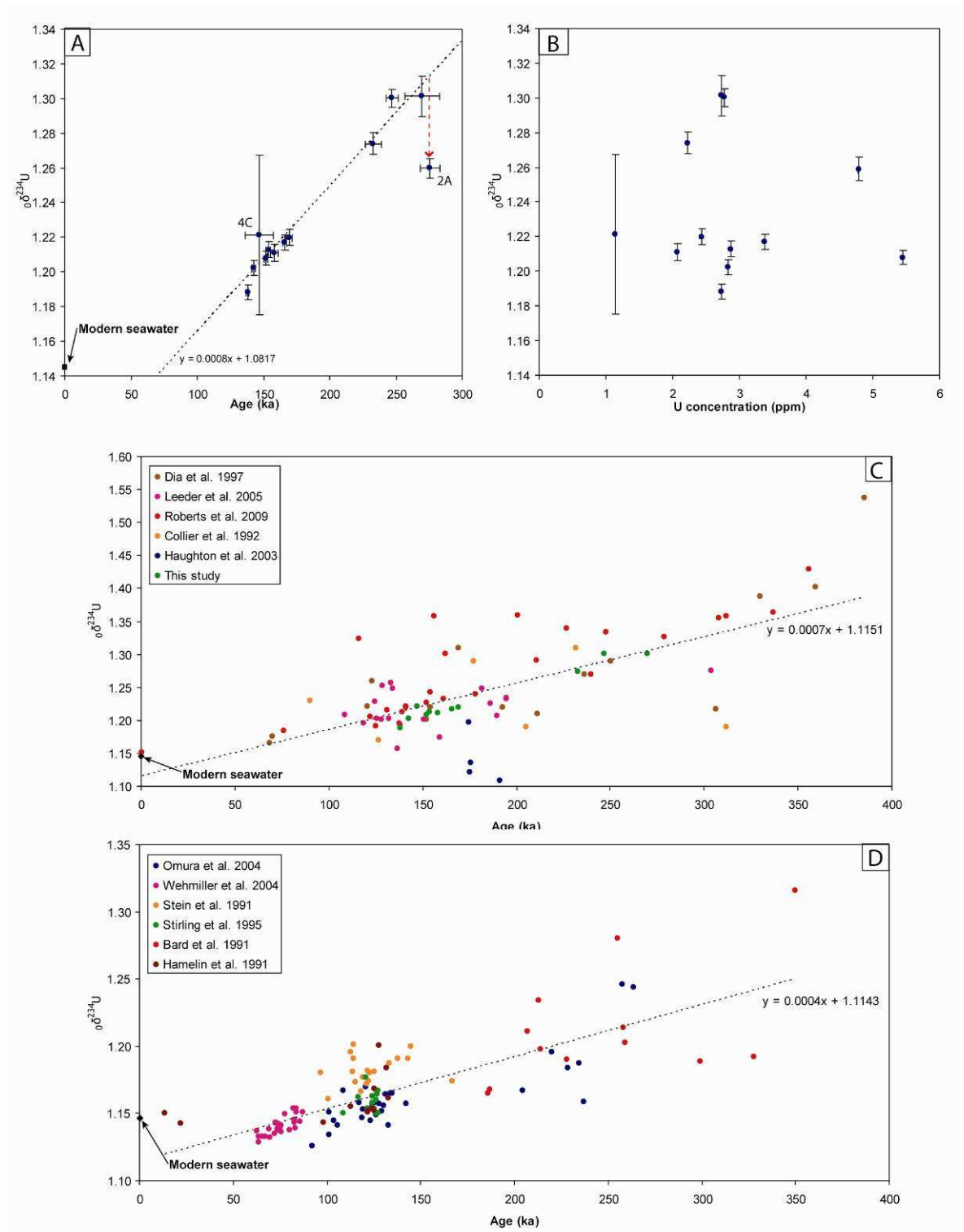


Figure 2.3: Plots of Uranium chemistry for coral studies.

(A) Plot of $\delta^{234}\text{U}$ against age for samples from this study alone including 2σ error on both measurements. The red arrow indicates how far sample 2A, which contains significant diagenetic contamination, falls from the line of best fit for the other samples. (B) Plot of $\delta^{234}\text{U}$ against uranium concentration for samples in this study. The lack of trend between the two suggests that there is no simple contamination model to explain the deviation of U chemistry from modern day value. (C) Plot of $\delta^{234}\text{U}$ against age for all Gulf of Corinth studies. (D) Plot of $\delta^{234}\text{U}$ against age for several studies from around the world (see text for discussion) - errors (which range from 0.5-22% of the age) have been omitted for clarity. Modern seawater value of 1.145 for $\delta^{234}\text{U}$ from Henderson (2002) is also shown for comparison. Note the similarities between the gradients of lines of best fit in B, C and D. The larger gradient shown by Gulf of Corinth examples may be a result of its geological setting as a restricted basin (see section 2.5.5).

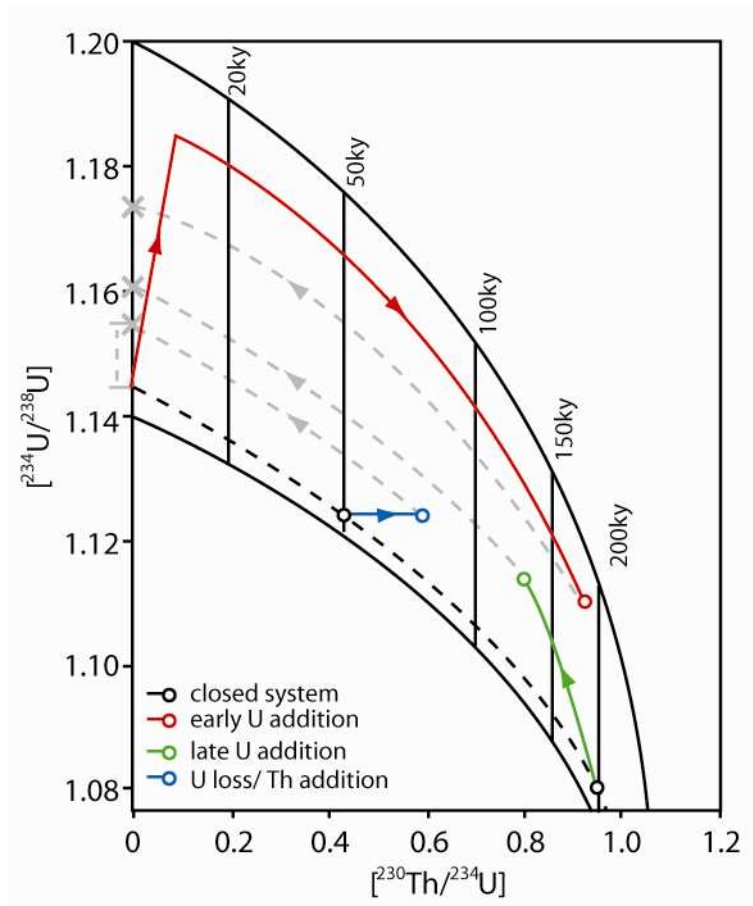


Figure 2.4: Model evolution curves for diagenetic effects on coral $0\delta^{234}\text{U}$.

$[^{234}\text{U}/^{238}\text{U}]$ against $[^{230}\text{Th}/^{234}\text{U}]$ isochron plot showing different examples of open system behaviour (base isochron from Hamelin et al., 1991). The black dashed line shows the isotopic progression of a 200 ky old coral that has remained a closed system. Red line demonstrates the evolution path of a coral contaminated by immediate U addition, as the curve has followed a path similar to that of the closed system example the age is not too dissimilar, ~190 ky. The green line shows late U addition which lowers $[^{230}\text{Th}/^{234}\text{U}]$ and makes the age significantly younger, ~130 ky. The blue line demonstrates the effect of U loss or Th addition which both cause $[^{230}\text{Th}/^{234}\text{U}]$ to increase quickly causing an older age (~75 ky as compared to 50 ky for the closed system example). The grey lines and X's demonstrate that when $0\delta^{234}\text{U}$ is back calculated from each of these contamination possibilities a higher value than the original is found.

Continuous loss of uranium from coral, due to interaction with leaching fluids, causes $[^{230}\text{Th}/^{234}\text{U}]$ to increase faster than expected under closed system conditions. This causes calculated $\delta^{234}\text{U}$ to be higher than the original ratio and results in an older calculated U-Th age than the true formation age of the coral (Figure 2.4). Collier et al. (1992) find clear evidence for uranium loss in Gulf of Corinth coral samples. They find specimens with a $[^{230}\text{Th}/^{234}\text{U}]$ of 1.15, a value which is much higher than could be obtained by radioactive decay in a closed system.

Addition of ^{230}Th can also lead to an increase of the calculated $\delta^{234}\text{U}$ by raising the $[\text{}^{230}\text{Th}/\text{}^{234}\text{U}]$ of specimens (Figure 2.4). This process can be caused by scavenging of ^{230}Th from the water column by the coral skeleton whilst still below sea level. Thorium concentrations of the samples in this study are generally similar to the abundances of 0.1 – 4 ppb found in open ocean corals (Stein et al., 1991; Hamelin et al., 1991). Some samples have concentrations of up to 11 ppb (sample 2A 97 ppb) which is relatively high in comparison. However the low ^{232}Th content of the samples, as alluded to by the high $[\text{}^{230}\text{Th}/\text{}^{232}\text{Th}]$, rules out direct precipitation of Th from seawater. Due to the extremely high $[\text{}^{232}\text{Th}/\text{}^{230}\text{Th}]$ of seawater (Chen et al., 1991), even a very low level of contamination would dramatically increase their ^{232}Th content, and subsequently decrease $[\text{}^{230}\text{Th}/\text{}^{232}\text{Th}]$.

2.5.4 Evidence for diagenesis of coral samples

The samples in this study have been directly exposed to precipitation and/or ground waters since their formation, giving plenty of time for potential diagenetic alteration. These effects are, in principle, detectable by independent mineralogical or chemical criteria. Common checks for alteration include determination of the presence of secondary calcite or recrystallised aragonite, variations in Sr and Mg content, and measurement of ^{232}Th of the samples (Hamelin et al., 1991; Collier et al., 1992; Henderson et al., 1993).

In this study, each sample of *C. caespitosa* was split into corallite wall and septa samples. This was done because septa are very thin (<0.2 mm) whilst corallite walls are between 0.3-0.5 mm thick and are likely to be less prone to alteration. This is demonstrated by photomicrograph images (Figure 2.5) and comparative analysis of wall and septa for the specimen in Roberts et al. (2009). Coral walls from the samples were extensively mechanically and chemically cleaned following standard methods (Houghton et al., 2003; Edwards et al., 1987) to ensure they consisted of pure aragonite. Prepared samples were then assessed for physical alteration using XRD and EBSD. All XRD analysis for samples showed pure aragonite mineralogy apart from sample 2A (Figure 2.6). This sample showed a calcite peak above background, providing doubts for its integrity with respect to age analysis (for further discussion of this specimen see section 2.4.2). Further EBSD analysis of two unprepared samples showed low total calcite compositions of 0.1% and 0.3% (Figure 2.7).

Values for $[\text{}^{230}\text{Th}/\text{}^{232}\text{Th}]$ are greater than 884 for all samples except sample 2A, which has a $[\text{}^{230}\text{Th}/\text{}^{232}\text{Th}]$ of 91. Typically, a value of <20 for $[\text{}^{230}\text{Th}/\text{}^{232}\text{Th}]$ indicates the presence of detrital Th (section 1.8.3.2) this is not the case for samples in this study and shows that both cleaning and sample integrity were excellent. All of the coral samples in this study, bar sample 2A, thus have the appearance of being well preserved.

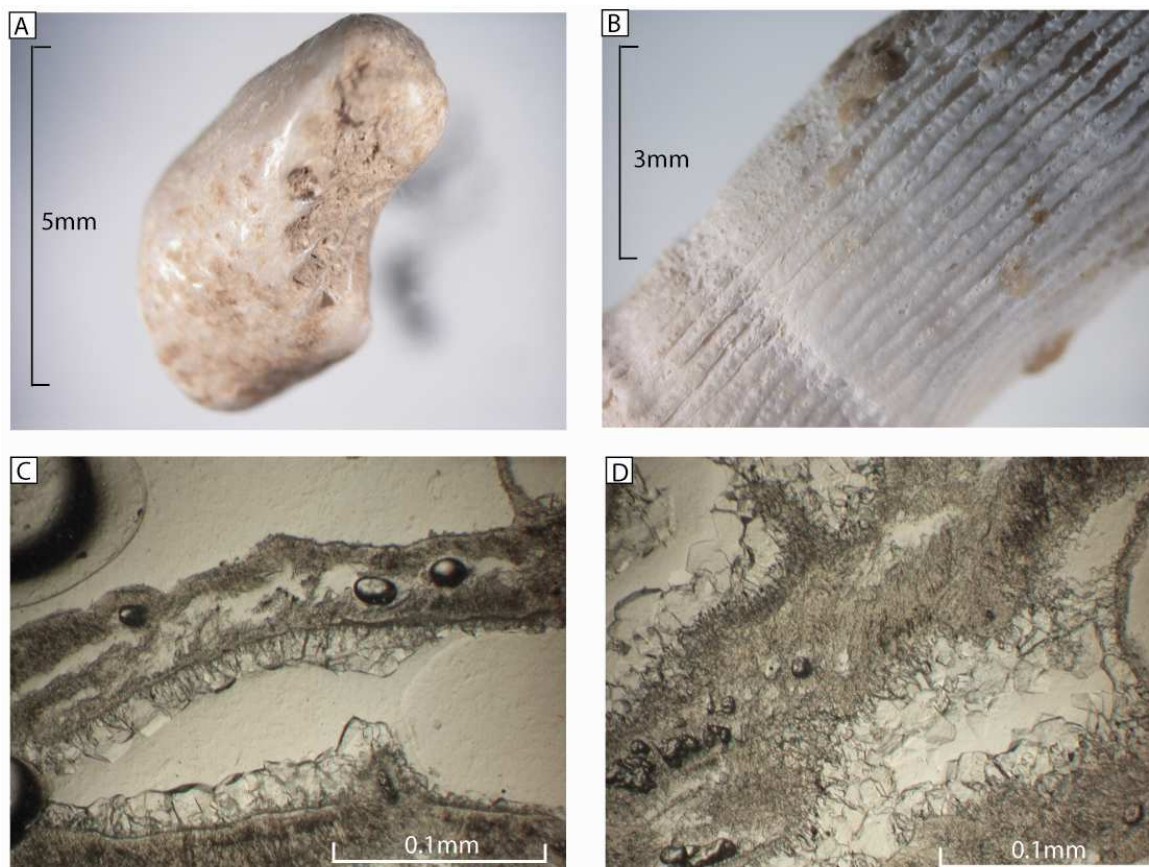


Figure 2.5: Photomicrograph images of *C. caespitosa* samples.

(A) An image of specimen 2A. Note its smooth weathered appearance in comparison to the well defined ribbed texture demonstrated by sample 10A, shown in **(B)**. **(C)** & **(D)** Thin section images of sample 6A. Large euhedral overgrowths are clearly visible on the septa of the coral. The grains of these overgrowths are much larger than those of the coral skeleton suggesting formation after skeleton construction. Septa were removed during preparation of samples for analysis and according to XRD scanning no calcite was present (bar sample 2A) after cleaning of coral. Due to the lack of calcite found in EBSD analysis, which was carried out on powdered samples of whole corallites (i.e. both walls and septa), it is possible that these overgrowths are aragonite.

It should be noted that the presence of pure aragonite does not necessarily discount diagenetic alteration of samples, as aragonite itself may be found as a product of diagenesis (Dia et al., 1997; Saller and Moore, 1989). The former observe aragonite overgrowths on coral, whilst the latter found microporous

aragonite in limestone and concluded that the formation of microporous aragonite preceded that of calcite during diagenesis. Gvirtzman et al. (1973) also report the precipitation of inorganic aragonite in coral voids.

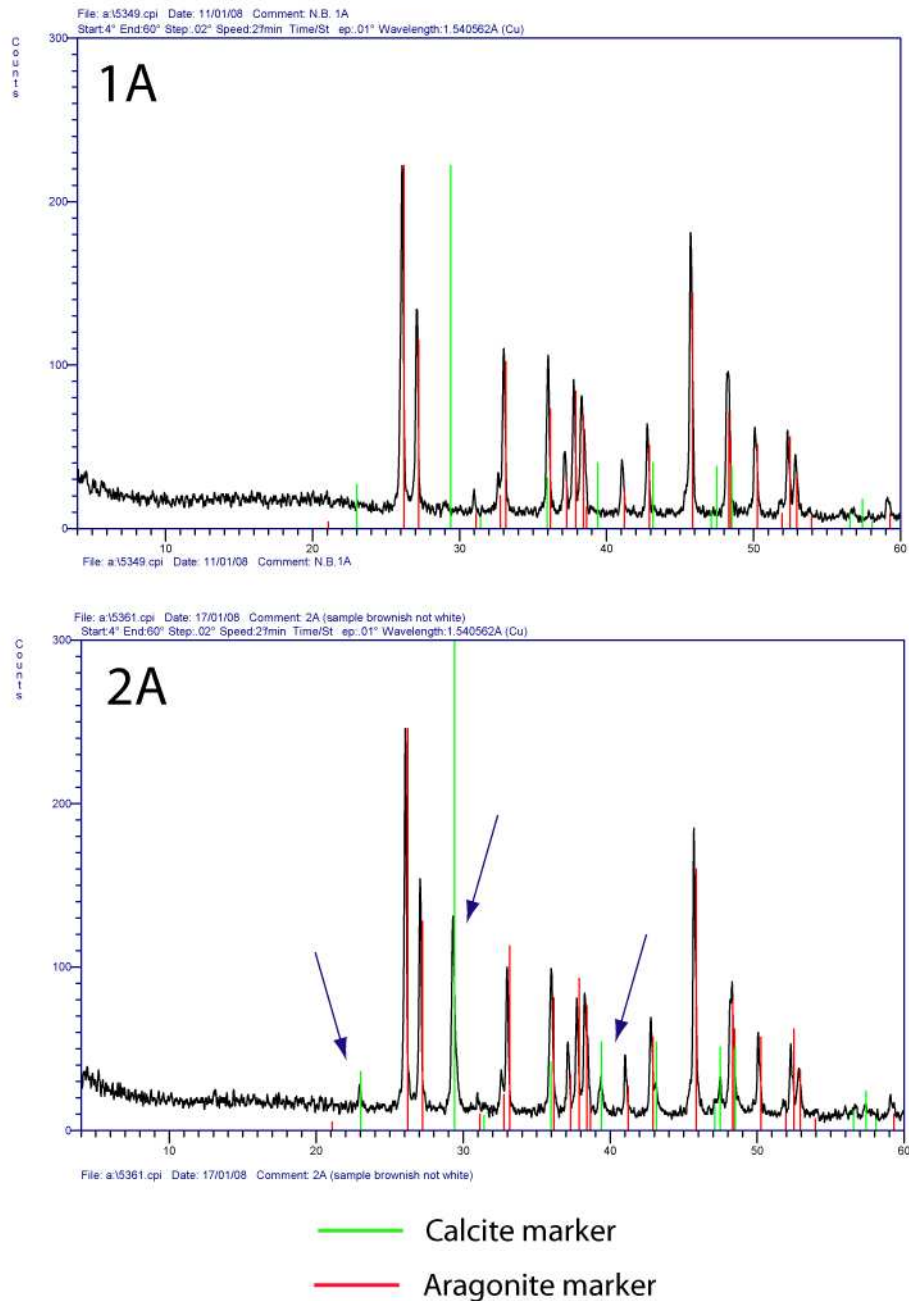


Figure 2.6: XRD analysis results of U-Th dated coral samples.

Sample numbers are indicated in the top left hand side of each XRD analysis. Sample 1A, which produced a result typical of the rest of the samples, is shown in comparison to sample 2A. For complete results of all analysis see Appendix B. Green lines and red lines represent calcite and aragonite markers respectively. The blue arrows show the presence of calcite peaks above background for sample 2A. This sample was also noted by the XRD technician to be brown after powdering further suggesting detrital contamination.

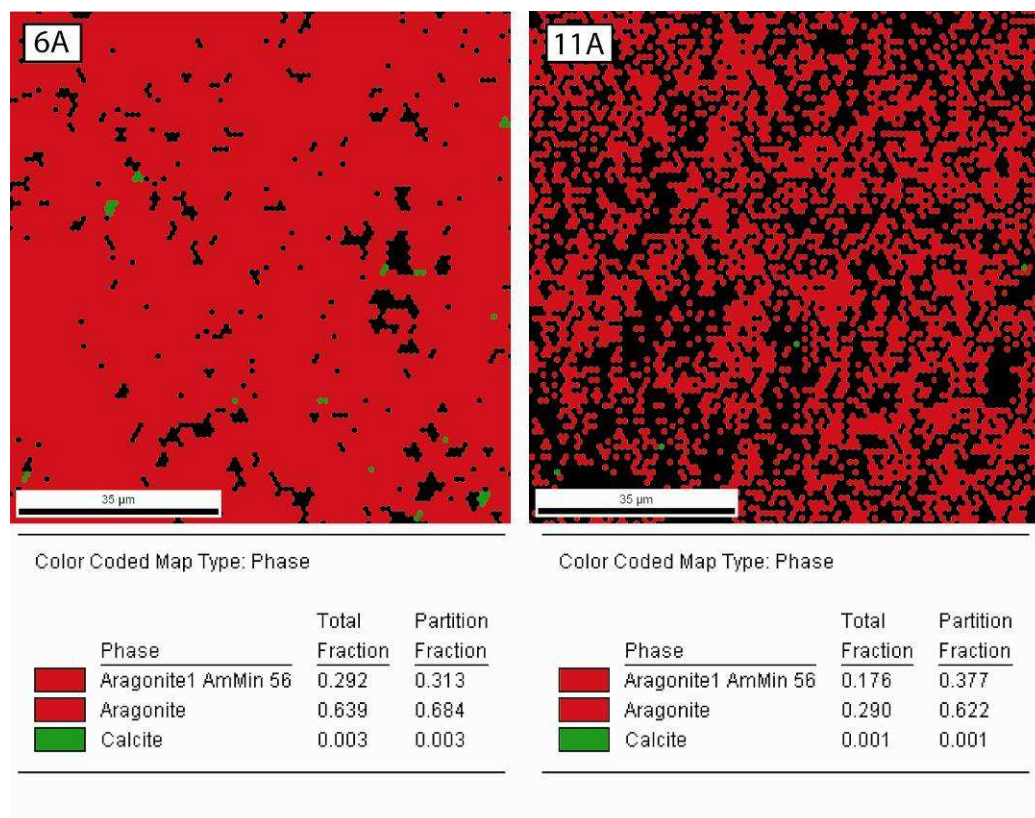


Figure 2.7: EBSD phase map images of *C. caespitosa* samples.

Electron backscatter diffraction (EBSD) scans of samples 6A and 11A adjusted to exclude Confidence Index values of <0.1 . Black sections of the images are due to the software being unable to index these areas. This can potentially occur due to the introduction of dust from polishing procedure, voids in the sample, or represent interphases between grain boundaries. Note the low fraction of calcite phases, highlighted in green, of 0.1 to 0.3%. This suggests that these samples are pristine with respect to potential re-crystallisation of aragonite.

Sr isotope composition provides a further check on of sample validity. In the Gulf of Corinth modern day seawater has an $^{87}\text{Sr}/^{86}\text{Sr}$ of 0.709185 ± 6 , which is indistinguishable from that of the North Atlantic (Dia et al., 1997). Sr isotope ratios for the coral in the present study range from 0.709120 to 0.709151, which is in agreement to the range found by Dia et al. (1997) of 0.709037 to 0.709134 in the Gulf of Corinth. Both of these ranges are significantly below the modern value (Figure 2.8). A similar trend exists in $^{87}\text{Sr}/^{86}\text{Sr}$ of coral of comparable age from Barbados and New Guinea, which range from 0.709155 to 0.709176 (Dia et al., 1992). The difference in these two ranges also shows that Gulf of Corinth coral has significantly lower $^{87}\text{Sr}/^{86}\text{Sr}$ value than coral of comparable age from the open ocean. A similar trend is found by Roberts et al. (2009), Sr concentration in their coral analyses ranged from 5600-7700 ppm. The upper limits of this range only slightly overlap the range reported by Stein et al. (1993) of 7300-9800 ppm for several studies on Indo-Pacific and Atlantic coral. Indeed the range of Roberts et al. (2009) falls below the mean value of Stein et al. (1993) of 7870 ± 300 ppm. The

discrepancy displayed by this study, and previous work on Corinth coral could potentially result from one of two processes. It is possible that circulation between the Gulf of Corinth, a marginal basin, and the open ocean may have been restricted at certain high stands (section 2.5.5). Alternatively the lower $^{87}\text{Sr}/^{86}\text{Sr}$ could be the result of diagenetic effects.

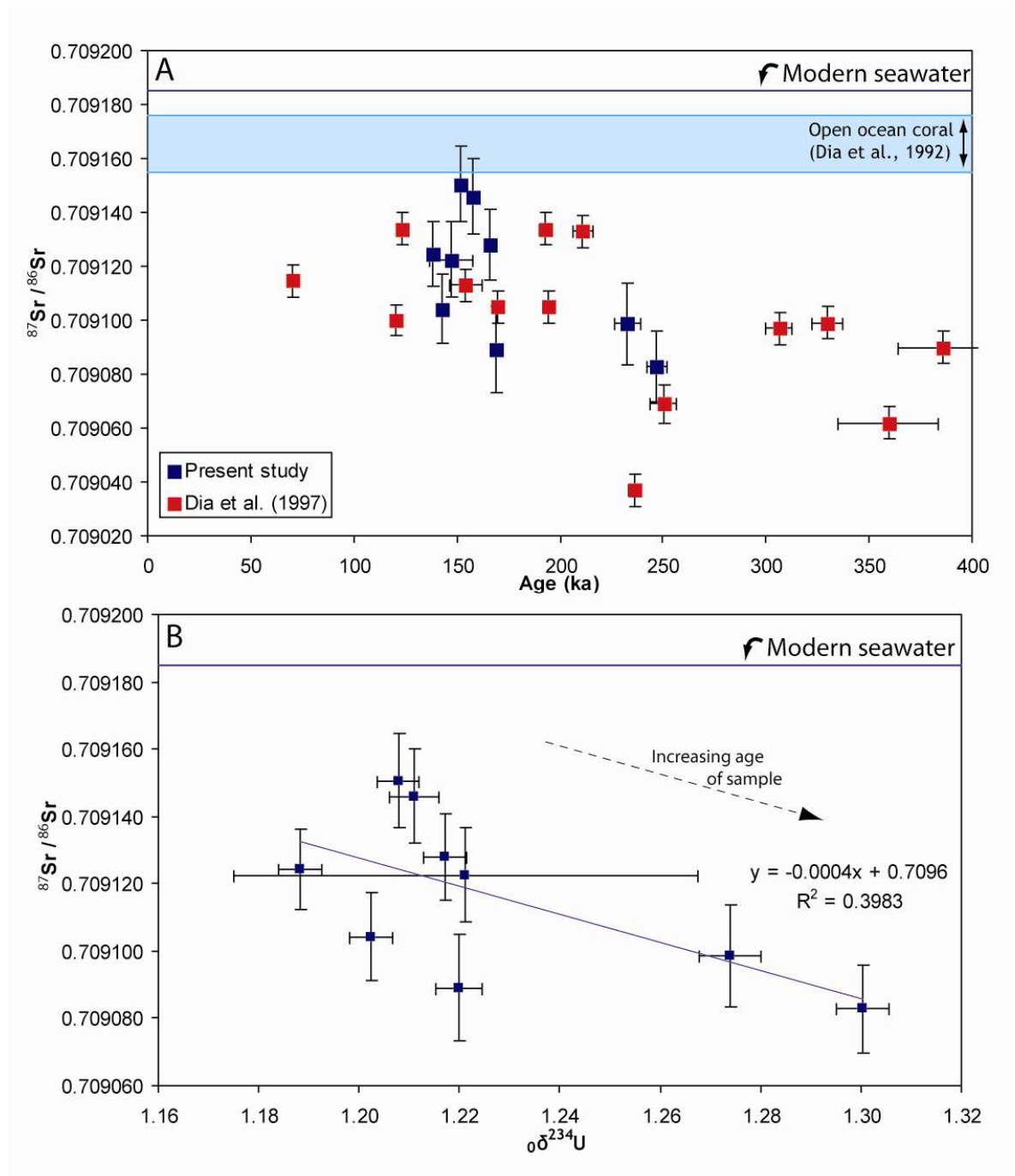


Figure 2.8: Strontium analysis results for coral samples.

(A) Comparison of $^{87}\text{Sr}/^{86}\text{Sr}$ ratio data from the present study including the results of Dia et al. (1997). The modern seawater value is from the analysis of a modern coral in Dia et al. (1997), and the range of $^{87}\text{Sr}/^{86}\text{Sr}$ of coral from Barbados and New Guinea (Dia et al., 1992) is shown by the blue box. Errors from both studies are presented as 2σ . The general trend is for older samples to have $^{87}\text{Sr}/^{86}\text{Sr}$ ratios that progressively decrease from the modern value. (B) Plot of $^{87}\text{Sr}/^{86}\text{Sr}$ against ${}^0\delta^{234}\text{U}$ for samples in the present study. Lower $^{87}\text{Sr}/^{86}\text{Sr}$ seems to correspond with higher ${}^0\delta^{234}\text{U}$ suggesting progressive alteration with age.

2.5.5 Further complications- geological setting of the Gulf of Corinth

The geological evolution of the Gulf of Corinth during the history of coral growth is another factor to take into account when considering potential causes of anomalous $\delta^{234}\text{U}$. The low Sr isotope ratio of the coral samples in relationship to ancient coral of comparative age in the open ocean suggests that the Gulf of Corinth may have behaved like a marginal marine basin and therefore had restricted circulation with the open ocean. If simple two end member river-ocean water mixing is assumed, the low $^{87}\text{Sr}/^{86}\text{Sr}$ values result from extensive dilution of basin water by terrestrial waters (Flecker et al., 2002). This suggests that the isotopic composition of the seawater may have been altered by mixing with fluvial water or submarine spring waters derived from the carbonate basement rocks. The high $\delta^{234}\text{U}$ of river water between 1.2 and 1.3 (section 2.5.2) and groundwaters, often >2 and exceptionally >10 (Osmond and Cowart, 1982) may have been able to raise the $\delta^{234}\text{U}$ of the basin during times of restriction. This heightened initial U ratio may have been maintained into periods of high stand as open circulation took time to mix and lower the $\delta^{234}\text{U}$. The dilution of re-entering seawater by freshwater from the large number of rivers draining the Peloponese Peninsula and entering the south side of the Gulf of Corinth could have contributed to a slow re-equilibration of open ocean seawater chemistry. As the corals were all growing near the shore of this essentially landlocked basin they will reflect the deviated isotopic signature of its waters (with respect to the open ocean). Modelling of the entry of the sea into the Gulf of Corinth via the Rio Straits and Isthmus of Corinth through time by Roberts et al. (2009) also demonstrate this restricted circulation idea (Figure 2.9).

Potential further complication of the chemistry of basin seawater is the presence of hot springs and fumaroles at Sousaki and the Methana volcano to the east (Figure 2.9). Sea-water re-entering the basin from the Isthmus of Corinth after a period of restriction would have to move past these active volcanic sites, which could provide a hydrothermal chemical aspect to the mix. It is possible that the basin was completely restricted during periods of sea level low stand, though modelling by Flecker et al. (2002) demonstrates that complete isolation is not necessary to explain Sr isotopic offset from coeval ocean samples.

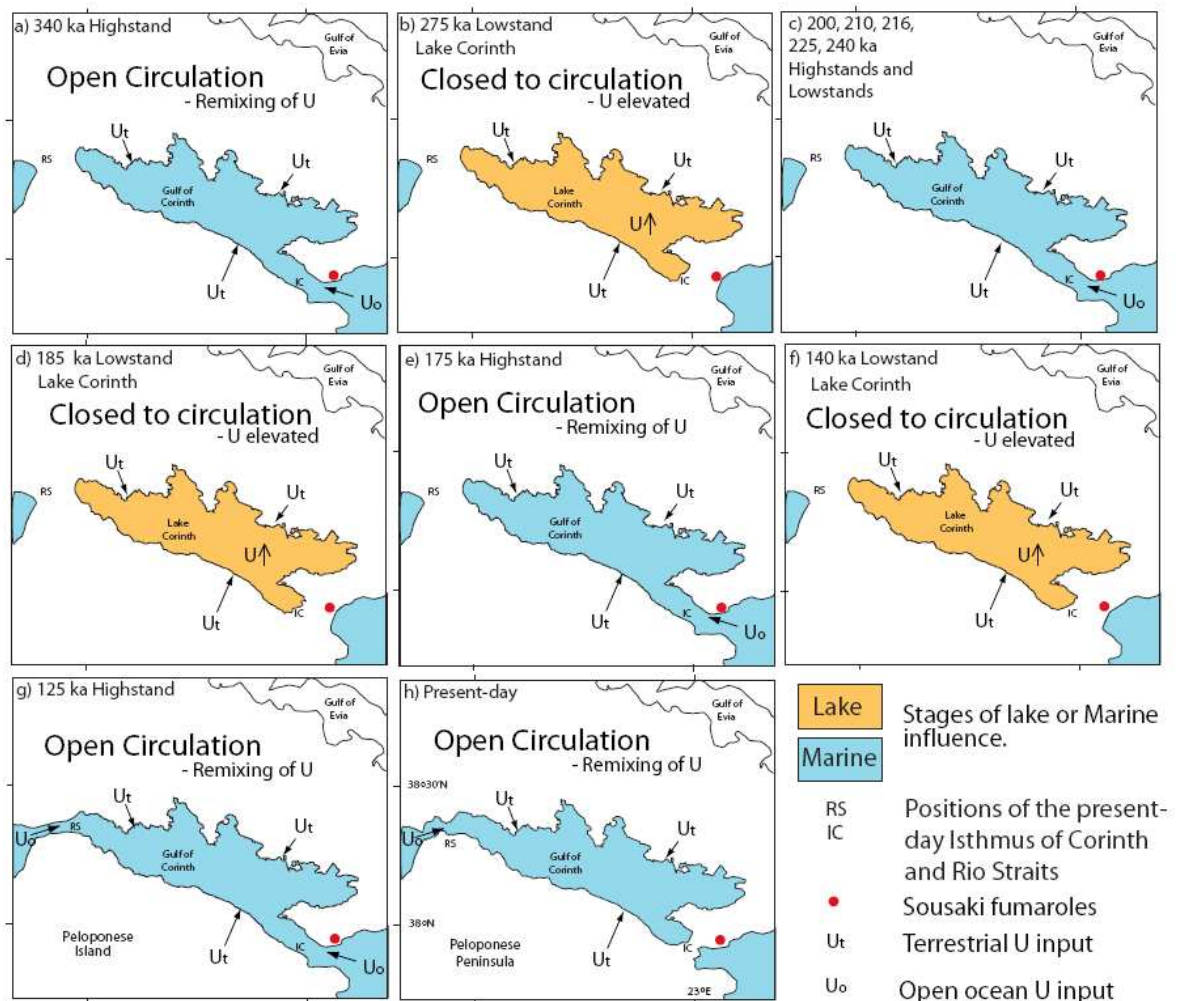


Figure 2.9: Hydrological evolution of the Gulf of Corinth through time.

This speculative figure, after Roberts et al. (2009), is based on modelling of the entry of the sea into the Gulf of Corinth via the Rio Straits and the Isthmus of Corinth through time by the same authors. During periods of closed or non-circulation $\delta^{234}\text{U}$ increases in the basin due to continual input from terrestrial run-off. Sea level rises and the basin becomes connected to the open ocean once more open circulation occurs. This will lower the $\delta^{234}\text{U}$ as mixing of the once closed Lake Corinth and open ocean progresses. The timescale of this mixing towards an open ocean $\delta^{234}\text{U}$ is unknown.

Also of importance is the situation of the coral themselves. Corinth corals did not grow as extensive reefs, but rather small isolated colonies, on Miocene carbonate (Dia et al., 1997). Optical examination of the underlying older massive carbonate revealed it has suffered extensively from diagenetic alteration (J.A. Dickson, reported in Dia et al., 1997). This hints at the possibility that exchange of Sr took place between the older carbonate and the coral, and could be responsible for the low Sr isotope ratio. However, it is unclear at what stage in its history the Miocene carbonate suffered alteration and it could have pre-dated coral formation. Seasonal variation in growth rates and thickening of corallite, combined with other

physiological effects, may also lead to a distortion of the environmental signal recorded by the coral (Silenzi et al., 2005).

2.6 Accuracy of Sea level curve and coral growth depth

2.6.1 Introduction

Previous workers have dismissed the anomalous chemistries of *C. caespitosa* in the Gulf of Corinth as the U-Th ages have been deemed significantly robust to link with eustatic sea level highstand. Similarly, the U-Th ages in the present study do not correlate closely with sea level highstand (Figure 2.10). As discussed in previous sections diagenetic alteration of *C. caespitosa* samples since their formation is likely to be playing a role in this observed disagreement. In addition to chemical alteration, discrepancies in the palaeobathymetry of *C. caespitosa* and accuracy of the sea level curves must be taken into account. The following section discusses both of these factors before suggesting a method with which to correlate coral ages with sea level highstand. The resulting conceptual model was produced in order to provide a useful tool for studies involving ancient coral.

2.6.2 Uncertainty in growth depth of *C. caespitosa*

Cladocora caespitosa is the main zooxanthellate colonial coral endemic in the Mediterranean Sea, abundant in both past and recent times (Rudolfo-Metalpa et al., 2008). In order to correlate deposits of this coral with sea level highstand the actual growth position of *C. caespitosa* in relation to sea level must be constrained. Whilst the exact depth of growth is strongly influenced by local factors including wave energy, sedimentation rate, predation and substrate, several independent studies report similar ranges for the growth depth of *C. caespitosa*. Montagna et al. (2007) found that *C. caespitosa* is restricted to the eutrophic, or light penetrating, zone ranging in depth from a few metres to around 40 m. More accuracy on growth in this range is suggested by Peirano et al. (2004) and Rudolfo-Metalpa et al. (2008) who commonly observed this species of coral growing in depths of 4-10 m and 7-15 m respectively. Both studies state that *C. caespitosa* can be found at depths of 40 m though this is a rarer occurrence due to the lower levels of radiance at these greater depths. Occurrence of the coral is

confirmed in this range by Silenzi et al. (2005) who describe *C. caespitosa* growing at a depth of 28 m.

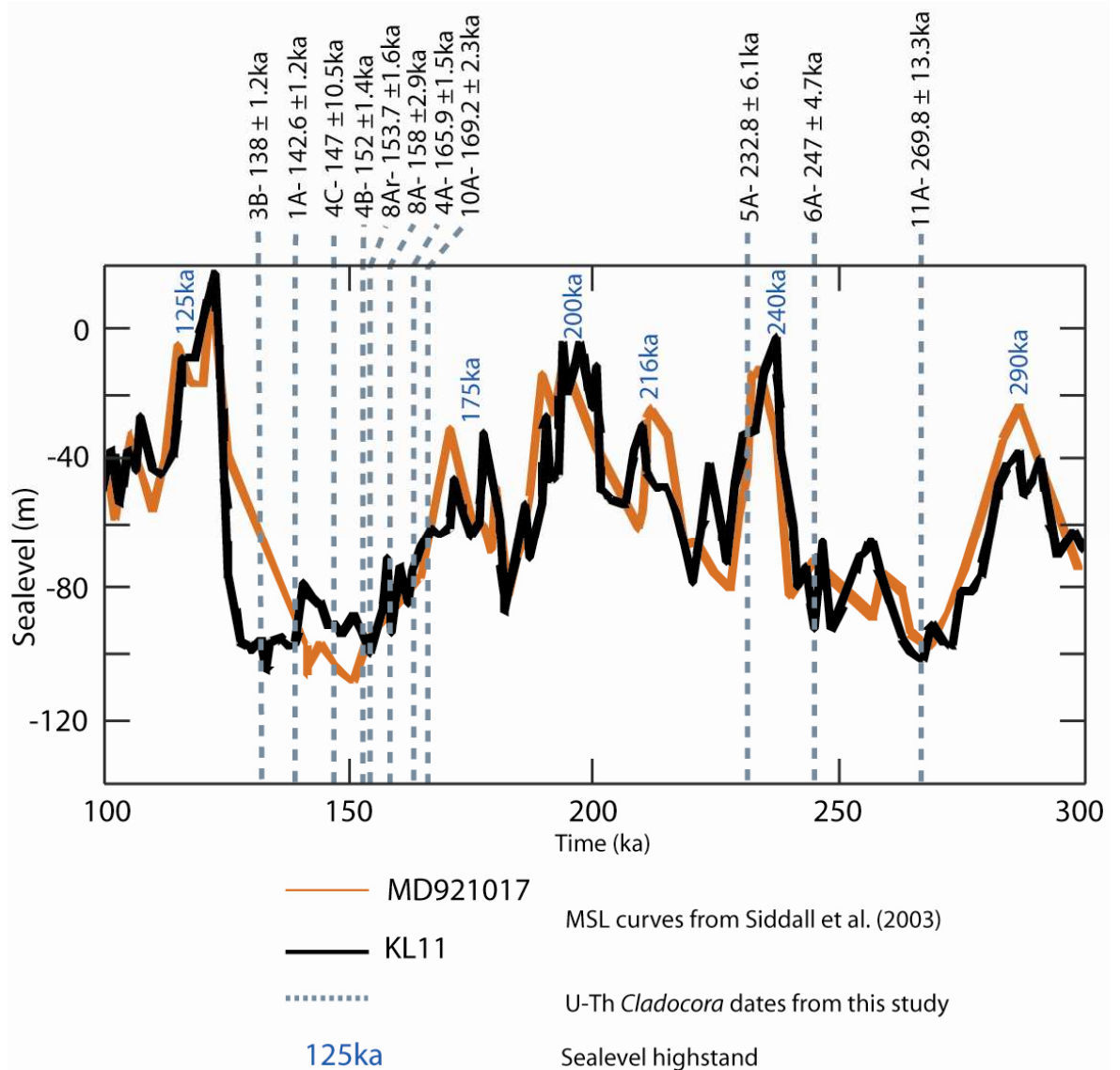


Figure 2.10: Relative sea level curve with marked ages of *C. caespitosa* samples.

Relative sea level shortened between 100 and 300 ky in order to clearly show position of *C. caespitosa* sample ages in relation to periods of sea level highstand.

Studies that report U-Th ages in order to discuss tectonic history of faults in the Gulf of Corinth vary widely in their estimation of coral growth depth. Dia et al. (1997) estimate the palaeobathymetry of the corals as 10 ± 10 m, whilst Leeder et al. (2005) provide a preferred growth depth of 5-25 m below sea level. Roberts et al. (2009) do not supply a depth range for *C. caespitosa* growth but have estimated that colonies were growing in depths of 50-79 meters according to calculations carried out to constrain contemporary shorelines (Pers comm., Birkbeck College Field trip to Gulf of Corinth guide). This would imply that the

corallites were once inhabited by non-photosynthetic polyps, azooxanthellate, as light cannot penetrate to this depth range. Unfortunately there is no test that can be carried out on the ancient samples to determine the type of polyp that constructed the corallite as zooxanthellate and azooxanthellate form similar structures. However, this final estimate of growth depth does not agree with any of the previous work in the area, and is well below observations in *C. caespitosa* studies in general. The first two studies suggest growth depths that agree well with independent study of *C. caespitosa*, which suggests that their estimates are more accurate. In the Corinth studies above, growth depth uncertainties of up to 29 m provide a significant error when trying to correlate coral growth to sea level maximum.

2.6.3 Uncertainty in the sea level curve

The accuracy of the relative sea level curves that these highstands are based on must also be considered. Records based on oxygen isotopes from sediment cores can contain major uncertainties. It is commonly accepted that a variation of 0.1‰ of the $\delta^{18}\text{O}$ corresponds to a variation of about 10 m in sea level (Caputo, 2007), with studies reporting uncertainties of up to ± 30 m (Siddall et al. 2003; Waelbrook et al., 2002). Roberts et al. (2009) use the sea level curves of Siddall et al. (2003) in their study to correlate their data to sea level highstand. The sea-level reconstruction in that paper is derived from inter-calibrated $\delta^{18}\text{O}$ measurements of benthic foraminifera from Red Sea sediment cores. $\delta^{18}\text{O}$ can vary as a function of many factors among which the more important are the variation of water temperature, the difference in isotopic composition between the cored and *insitu* sediment, and local hydrological effects within the oceans. Indeed, the $\delta^{18}\text{O}$ recorded in foraminifera shell also depends on the calcification temperature and the influence of local currents, which may affect the water temperature, the salinity and hence isotopic composition (Caputo, 2007). Taking potential variation in $\delta^{18}\text{O}$ and combining it with the sensitivity of their sea-level method to climatic effects, Siddall et al. (2003), calculate a confidence limit to an accuracy of ± 12 m on their sea-level reconstruction. Real analysis of the uncertainties associated with the proposed relative sea level curve is rarely presented in full (Caputo, 2007) so due to the above list of potential sources of error the uncertainties relative to sea level height presented by Siddall et al. (2003), as with many others, probably underestimate the real ones.

Uncertainties in relative sea level curves can also occur along the time axis. Imbrie et al. (1984) find that the accuracy of the astronomically tuned SPECMAP-stack timescale is ± 5 ka, whilst Petit et al. (1999) conclude that this value is only applicable to the last 110 ka and that time accuracy is up to ± 15 ka for the last 420ka. In a review of multiple (12 in total) RSL curves, including those of Siddall et al. (2003), Caputo (2007) found that several disparities occurred:

- Differences of up to 18 ka and 35 m can be observed in correspondence with major interglacial peaks (at 125, 240, 340 and 420 ka).
- The position (height and age) and the number of interstadial peaks differ markedly from curve to curve.
- In correspondence with the interstadial and/or interglacial periods, some curves represent a major couplet with peaks sometimes differing more than 15 ka.

2.6.4 Conceptual model for correlation of ancient coral ages with sea-level highstand

Figure 2.11 combines the sources and scales of potential error detailed above for coral growth and relative sea-level curves. Areas of uncertainty on sea level highstand overlap for the 175, 200, 216 and 240 ka highstands, and also the 290, 310 and 340 ka highstands. The majority of the overlaps between these uncertainties are ~ 5 ka, with the overlap between the 200 ka and 216 ka highstands quite significant (~ 14 ka) due to the ± 15 ka confidence limits in sea level highstand dates. If a coral age falls within one of these overlaps then it would be hard to say to which highstand the coral correlated to, even if it was closer in age to one high stand than the other. For example coral ages falling around the 190ka mark, although seemingly closer to the 200 ka highstand, could equally represent the 175 ka highstand as they would fall within the area of uncertainty for this earlier highstand. Unequivocal stratigraphic evidence would be required to separate the two.

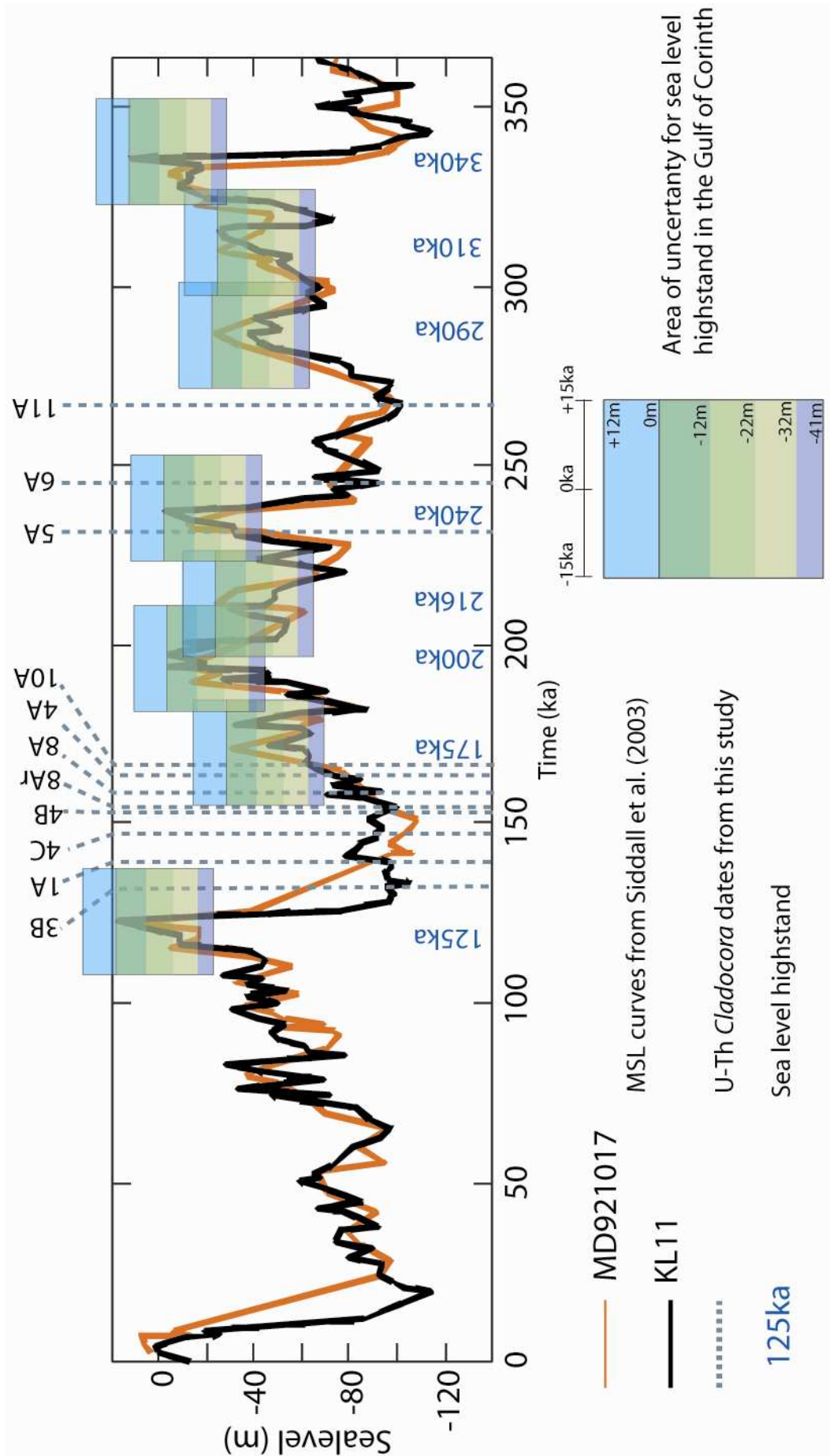


Figure 2.11: Global sea level curve showing uncertainty around sea level highstand.

Figure 2.11: Global sea level curve up to 350 ky complete with areas of uncertainty around sea level highstand. The area of uncertainty is derived from ambiguity of coral growth depth and sea level elevation for the vertical uncertainty and age variation for the horizontal uncertainty. The key shows the breakdown of these different aspects. For the vertical uncertainty, a ± 12 m accuracy for sea level elevation from Siddall et al. (2003) is included along with the various depth ranges of *C. caespitosa* growth quoted by various studies which includes values of 10 m (Dia et al., 1997), 20 m (Leeder et al., 2005) and 29 m (Roberts et al., 2009). When combined these give a total uncertainty on depth of growth of 22 m, 32 m and 41 m. Age uncertainty of sea level highstand is ± 15 ka from Petit et al. (1999). The sample ages have been omitted for clarity of the figure, these can be seen marked on Figure 2.10 and in Table 2.1.

2.6.5 Implications for correlation of previous Corinth studies

Previous published results correlated to highstands can either be confirmed or altered by the method outlined above. Roberts et al. (2009) correlate sample ages of 201 and 211 ka, from the Hotel Complex, with the 200 and 216 ka highstands respectively- these ages fall within the large area of uncertainty between these two highstands so they could belong to either. However, the stratigraphic relationships of the layers that contain the coral confirm that their interpretation is correct. In the same study samples dated at 161 and 162 ka are interpreted as belonging to the 175 ka horizon- this is confirmed as they would plot within the uncertainty envelope of only the 175 ka highstand. They also correlated an age of 356 to the 340 ka highstand, this age falls right on the edge of the 340 ka highstand even without taking into account the large errors (+50, -32 ka) on the date.

From a single location just south of Lake Vouligameni Roberts et al. (2009) report ages of $122^{+1.2}_{-1.2}$, $139^{+2.4}_{-2.4}$, $154^{+1.9}_{-1.8}$ and $156^{+2.0}_{-1.9}$ ka. This location therefore provides a problem as the first two of the ages fall within the uncertainty of the 125 ka highstand and the latter two within the 175 ka highstand. They correlate this location with the 125 ka highstand as the sediments can be mapped to a nearby location dated by Leeder et al. (2003; 2005) between 108.5 ± 0.7 to 134 ± 3 ka. Therefore it is likely that this correlation is correct and that the older samples are the result of reworked deposits from the 175 ka highstand.

In the same location at Cape Heraion as samples 1A and 3B from the present study, Leeder et al. (2005) report an age of $136.5^{+13.6}_{-12.1}$ ka, which agrees with the ages reported in this study. Similar to the samples in the present study, this date would plot within the error envelope of the 125 ka highstand. Leeder et al. (2005) also report two dates of 194.5 ± 0.8 and 189.5 ± 4.8 ka from the west side

of Lake Vouligameni. The authors interpret these coral as representing either the 200 or 216 ka highstand- I would suggest that the former is most likely as these ages do not fall within the uncertainty of the 216 ka highstand.

2.6.6 Implication for correlation in the present study

The field observations of section 2.4.2 can be used in conjunction with the conceptual model shown in Figure 2.11 to assign a sea level highstand to each location. These locations can therefore be used with greater confidence for slip rate calculations of the South Alkyonides fault segment. Despite not immediately seeming to correlate with highstand most of the samples fall within the error envelopes projected on to the relative sea level curve.

Of the samples from Cape Heraion, the ages of 1A (142.7 ± 1.2 ka) and 3B match well (138.1 ± 1.3 ka), suggesting they represent the same period of coral formation, whilst the age for 2A is markedly different (277.3 ± 7.7 ka). Sample 3B falls within the 125 ka highstand whilst sample 1A is right on the edge of this box- if the error on this sample age is taken into account then it overlaps this highstand uncertainty. Sample 2A was not plotted as the $[^{230}\text{Th}/^{232}\text{Th}]$ chemistry of this sample indicates that it has been detritally contaminated (Table 2.1, Figure 2.6). Including the results of Leeder et al. (2005) a total of six dates are reported for this location, of which five fall within the error envelope surrounding the 125 ka highstand.

At the sample location south east of Lake Vouligameni the U-Th dating of 11A returned an age of 269.8 ± 13.3 ka. This palaeoshoreline is mapped by Roberts et al. (2009) as the 340 ka highstand. As the error associated with the age overlaps the area of uncertainty of the 290 ka highstand the coral sample is more likely to be related to this highstand.

Three age results, including one from a repeat analysis, were obtained from two Agriliou Bay samples. Sample 8A produced ages of 158 ± 2.9 ka and 153 ± 1.6 ka, whilst sample 10A produced an age of 169.2 ± 2.3 ka. Both of these age results, when age error is taken into account, fall with the area of uncertainty surrounding the 175 ka highstand suggesting that they can only come from that highstand. This means that it is likely that sample 10A was not in life position, as originally thought (section 2.4.2). It is possible that this sample has been removed

by excavation and embedded in co-excavated sediment downhill of its original location. This uncovering of the sample and subsequent exposure to the open environment may have led to increased weathering hence the deviation in age of 10A from 8A.

The Hotel Complex locality provided five separate samples for dating. From the west side of the site samples 5A and 6A, at 232.9 ± 6.1 and 247.0 ± 4.6 ka in age, both fall within the 240 ka highstand uncertainty, which agrees with their stratigraphic position. Samples 4A, 4B and 4C from the east wall of the site produced ages of 165.9 ± 1.6 , 152.1 ± 1.4 , and 147 ± 10.6 ka respectively. Samples 4A and 4B plot within the error envelope surrounding the 175 ka highstand so they are interpreted as being representative of this highstand. The only sample in this study that does not fall within any of the uncertainties surround sea level highstand is 4C. From Table 2.1 it can be seen that this sample has an order of magnitude larger error on U-Th age (due to similar scale of larger error on $\delta^{234}\text{U}$) with respect to samples of a similar age. As discussed in section 2.5.1, despite their pristine nature, $\delta^{234}\text{U}$ and Sr isotope ratios suggest diagenetic alteration of samples; it is possible that sample 4C has been altered more than most. This is backed up by the field observation that this sample was extracted from a heavily carbonate cemented block which indicates post depositional alteration of the surrounding substrate (section 2.4.2). This suggests definite contact of this sample to diagenetic fluids. Due to its clear stratigraphic relationship with samples 4A and 4B (Figure 2.2), sample 4C must represent the same 175 ka highstand.

2.7 Summary: U-series methodology and slip rate

2.7.1 U-series methodology

The initial focus of this chapter was to test the application of the U-Th dating technique outlined in section 1.9. An appreciation of the stages involved with sample preparation and age analysis, and the timing required to take a sample through the entire process was gained during dating of coral samples from the Gulf of Corinth. As such several procedures for sample selection and preparation where noted.

- At each desirable site for dating, sample selection should focus on the most pristine examples of the material to be dated and aim to avoid areas of obvious contact with post depositional ground waters.
- Samples should be prepared in a clean lab area which must be cleaned thoroughly between each sample preparation to guard against cross-contamination.
- Any fragile sections of samples, such as coral septa, should be removed as their fine structure is easily altered by diagenetic fluids, which may have encouraged open system migration of ^{234}U and/or ^{230}Th .
- Samples should be inspected and cleaned thoroughly, any soft sections, areas of Fe staining, or internal detritus should be removed. Samples should then be re-inspected and cleaned again if there is still any hint of alteration. This process may have to be repeated several times.

The above stages can be very time consuming but are necessary to ensure that only pure samples are carried through to the next stage of preparation for U-Th age analysis, which was outlined in section 1.9.2.

Unfortunately, despite rigorous selection and preparation of samples, the radiometric results, as mainly demonstrated by $\delta^{234}\text{U}$, showed that the samples had been contaminated by non parent and daughter isotopes. This indicated that the coral has acted as an open system with respect to the uranium series decay chain. The original plan was to date these specimens and to check their accuracy with published sea level highstands. Due to the contamination the ages produced from analysis are deemed inaccurate and so direct correlation with high stands as a check on the ages, and of the dating technique, could not be carried out. One positive of dating these samples for testing the dating technique of Chapter 1 was the repeat analysis of coral sample 8A. Analysis results of this sample produced ages of 158.1 ± 2.9 and 153.7 ± 1.6 ka, which overlap within error and demonstrate good reproducibility of results.

2.7.2 Calculating slip rates of the South Alkyonides fault segment

In order to calculate a slip-rate for the South Alkyonides fault segment, or indeed any fault in the Gulf of Corinth region, three key components must be

addressed; (i) the elevation of palaeoshoreline inner edge, (ii) its absolute age and (iii) level of formative sea level highstand relative to present sea level. The first factor can be addressed by extensive and accurate mapping of marine terrace deposits. Roberts et al. (2009) and to a lesser extent Leeder et al. (2005) have mapped the Perachora Peninsula in great detail. Of the four sampling sites in this study, two (southeast of Lake Vouligameni and Agriliou Bay) can be traced upslope to the inner edge termination of the marine terrace whilst the Cape Heraion site has been correlated by Leeder et al. (2005) to identical deposits which display inner edge termination. Although there is a discrepancy in elevation between these identical deposits and the sample site in the present study (likely due to post-depositional faulting- section 2.4.2) the elevation of the correlated Leeder et al. (2005) deposits provides a further data point for calculation of slip rate for the South Alkyonides fault segment.

A further goal of this chapter was to address factor (ii) above and determine the suitability of coral in this region for dating terrace ages and hence, fault movement. The results of this study show that *C. caespitosa* specimens from the Gulf of Corinth are not robust enough for precise U-Th age analysis. Their U-Th and Sr chemistries suggest diagenetic alteration of samples, whilst geological factors at the time of formation may also have played a part in the anomalous ratios. Indeed this is a trend seen in previous studies involving ancient corals from the Gulf of Corinth, whose $\delta^{234}\text{U}$ deviate from modern day values with age at a similar rate (Figure 2.3D), and show distinctly lower $^{87}\text{Sr}/^{86}\text{Sr}$ than coral of similar age from the open ocean (Figure 2.8). This makes the accuracy of the ages of coral in this region highly suspect, which leads me to conclude that taken in isolation U-Th ages determination of these samples is not enough to correlate them to sea level highstand, a key factor in using these marine organisms for slip rate calculation of the South Alkyonides fault segment. In previous works in the region it has thus far been a common practice to ignore these facts and assign *C. caespitosa* age results with highstand well outside the error of the age based on solely on stratigraphic relationships, which can leave interpretations of correlation with highstand open to criticism.

However, the work within this chapter has reviewed all of the likely errors involved with the ages of coral samples and highstand dates and has found that large areas of uncertainty exist around each sea level highstand (Figure 2.11).

This uncertainty is formed from a combination of the large growth depth range of *C. caespitosa* and the inherently large inaccuracies on both sea level elevation and timing of sea level highstand associated with relative sea level curves. Despite their initial mismatch with highstand ages, *C. caespitosa* age results of eleven separate samples in the present study fall within the large error envelopes associated with sea level highstand. This finding therefore makes it possible to determine a slip rate for the South Alkyonides fault segment from the three sampling sites that can be traced or correlated to the inner edge terminations of marine terraces.

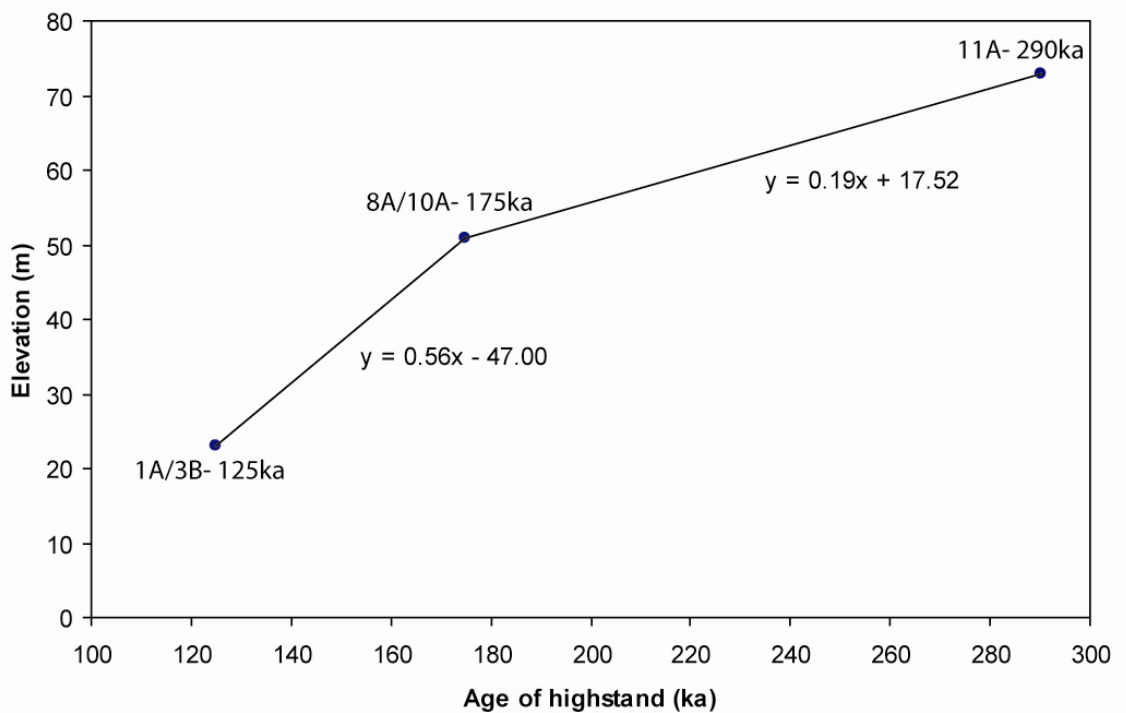


Figure 2.12: Slip rate calculation for the South Alkyonides fault segment.

Slip rate is calculated by using a plot of the elevation of the inner edge of the marine terrace correlated to the sample site against the age of the sea level highstand associated with each of the sample sites. Each point is marked with the sample numbers and associated highstand. As can be seen from the trend lines slip rate between 175 and 125ka (0.56 mm/yr) is greater than that between 290 and 175 ka (0.19 mm/yr).

Figure 2.12 shows the results of slip rate calculation between these sites. The trend lines between each of the points suggest that the slip rate on the fault has increased from between 290 and 175 ka to between 175 and 125 ka. Though it should be remembered that only three data points are being used in this estimation, the pattern displayed matches well with that found in the work of Roberts et al. (2009). Through construction of topographic profiles and use of

iterative calculation Roberts et al. (2009) found slip rates to be 0.1 to 0.16 mm/yr from west to east for the time period before 175 ka and from 0.3 to 0.52 mm/yr from west to east for the time period since 175 ka. The rates found in the present study are estimated from three locations that are not immediately stratigraphically related to each other and that stretch over a ~5.5 km section of the coast line. As such they span across several of the Roberts et al. (2009) slip profiles which demonstrate variable slip along strike. However, if the results of the present study of 0.19 mm/yr between 290 and 175 ka and 0.56 mm/yr between 175 and 125 ka are considered as a general slip rate for the South Alkyonides fault segment then they agree well with the findings of Roberts et al. (2009).

The method demonstrated in this chapter acts as an important tool as it validates the approach of previous Gulf of Corinth studies and allows for further justification of assigning these otherwise uncertain samples to periods of sea level highstand; a key pre-requisite for calculation of slip rate of faulting in the region. As clearly elevated $\delta^{234}\text{U}$ of ancient coral samples is common around the globe, indicating open system behaviour with respect to U-Th decay, it is suggested that coral based studies in other locations should follow the example shown by the work in this chapter.

- Take into account the chemistry of sample analysis results and attempt to find the causes of any observed deviation of atomic or activity ratios.
- Research any potential source of error in recognised sea levels in the local sea level record or relative sea level curve.
- Find the range of depths that the coral particular to study grows between.

By combining the above steps a real understanding of the uncertainty involved with the correlation of sample elevations with previous highstand can be achieved and a conceptual model, such as Figure 2.11, can be combined with observations, such as stratigraphic relationship, in order to provide a more accurate correlation between samples and associated highstands.

3 The Little Grand Wash fault and northern fault of the Salt Wash graben

3.1 Introduction

The Little Grand Wash and the Salt Wash graben field areas are of particular interest as they contain multiple modern and ancient fault related travertine mounds, which are the direct result of past and present leakage of CO₂ rich fluid to the surface along both fault zones. Parts of the travertine mounds provide pristine samples for uranium series dating. Results of analyses carried out on the mounds, presented in the next chapter, provide a unique data set with which to quantitatively characterise the fluid flow history of a pair of faults which provide vertical pathways for leakage from a natural accumulation of CO₂.

This introduction to the Little Grand Wash fault and Salt Wash graben field sites is divided into four sections. In section 3.2 an overview of the geology and tectonic events that shaped the region around the Little Grand Wash fault and Salt Wash graben is presented. Lithologies of particular importance to the thesis will be discussed in section 3.3, with reference to the source of CO₂ and groundwaters that precipitate the travertine. The process behind travertine formation, published literature on travertine in this area, and an introduction to the five separate units that form travertine mounds in this study is presented in section 3.4. In the final section, 3.5, new field observations and interpretations of travertine morphology in both sites are presented in order to evaluate the field relationships of the separate facies and to determine if the faults have been active during the history of travertine deposition. This is an important question to answer as it gives insights to the potential mechanisms that cause switching of fluid flow pathways to the surface. The interpretation of travertine mounds, combined with an understanding of river gravel deposits, suggests that there has been no surface offset on the faults during the deposition of travertine mounds.

3.2 Geological setting

The Little Grand Wash and Salt Wash graben faults are situated at the northern end of the Paradox basin in east central Utah (Figure 3.1). This late

Palaeozoic to Mesozoic intracratonic basin forms part of the Colorado Plateau and is defined by the extent of organic rich Pennsylvanian and Permian limestones, shales and evaporites which cover a large area of southern Utah and western Colorado (Baars and Stevenson, 1981). Rocks exposed within the basin range in age from Late Pennsylvanian to Early Cretaceous. The basin is bordered by a series of monoclines and structural highs (Figure 3.1) and can be generally be divided into three areas: the Paradox fold and fault belt in the north, the Blanding sub-basin in the south-southwest, and the Aneth platform in south easternmost Utah (Chidsey and Morgan, 2005). The field areas are bracketed by the San Rafael Swell to the west and the Uncompahgre uplift to the east. The San Rafael Swell is an arcuate anticline with a broad west limb and a steep east limb (Hintze, 1993), whilst the Uncompahgre uplift is a near rectangular, northwest-trending anticline (Barbeau, 2003). Both of the studied faults cut the open, north plunging Green River anticline (Figure 3.2).

Within the basin the middle Pennsylvanian Paradox Formation contains nearly 2km of evaporites deformed into a series of salt anticlines and faults by Pennsylvanian to Permian uplift of the Uncompahgre Plateau (Doelling et al., 1988; Dockrill and Shipton, 2010). Salt related anticlines in the carbonate and clastic sedimentary rocks overlying the evaporites have proved to be ideal traps for the accumulation of natural CO₂-rich gas. Numerous accumulations have been discovered (Figure 3.1) and commonly have CO₂ concentrations in excess of 90% with the remainder a mixture of nitrogen, helium and/or hydrocarbon gases (Cappa and Rice, 1995; Allis et al., 2001; Gilfillan et al., 2008; Wilkinson et al., 2008). Dominant reservoir lithologies include sandstone, dolomite and fractured basement, while overlying sealing lithologies range from low permeability mudstones to anhydrites (Allis et al., 2001). There are at least nine producing or abandoned CO₂ fields containing up to 8.5 trillion cubic meters of CO₂ gas (Allis et al., 2001). Five of these (Bravo Dome, McElmo Dome, Sheep Mountain, Big Piney-LaBarge and McCallum) are currently being exploited for enhanced oil recovery, dry ice and industrial uses (Allis et al., 2001). Also present in the Paradox basin are a number of actively producing oil and methane fields, including the Lisbon and McElmo Dome fields (Chidsey and Morgan, 2005; Morgan et al., 2007). Immediately to the south of the study area is the abandoned Salt Wash oil field (Peterson, 1973). Many of the active methane fields, present in the San

Rafael Swell to the north, also produce large volumes of CO₂ (Cappa and Rice, 1995), much of which is vented into the atmosphere (Allis et al., 2001).

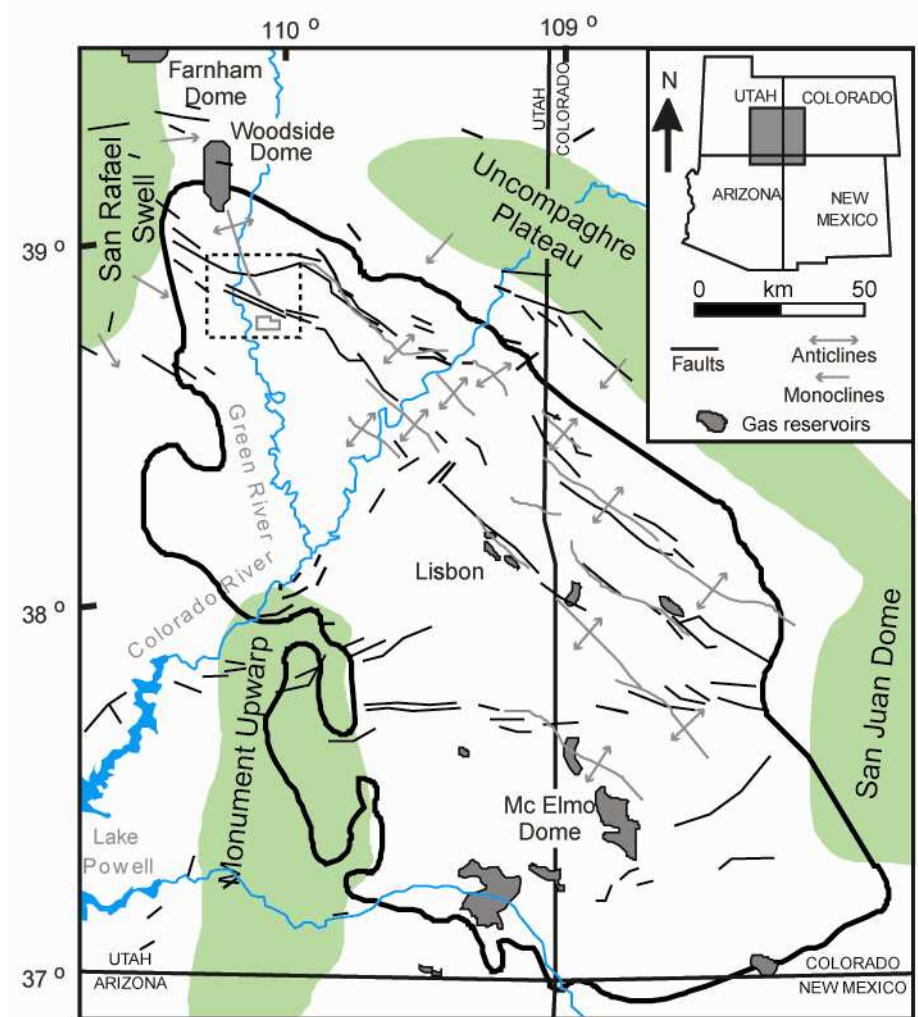


Figure 3.1: Geological features of the Paradox Basin and surrounding region.

Figure after Shipton et al., (2005), Nuccio and Condon (1996) and Cappa and Rice (1995). The extent of the basin is shown by the black line. Dashed box to the north of the basin displays the location of Figure 3.2. The area outlined in grey within this box represents the extent of the Salt Wash oil field (after Peterson, 1973). Inset shows location of basin within the mid-western USA.

The dominance of northwest to north-northwest striking normal faults within the Colorado Plateau suggests that maximum principal stress across the area is close to vertical and that the Plateau is currently undergoing northeast to southwest trending extension (Wong and Humphrey, 1989). The strike of both the Little Grand Wash fault (west-east) and northern fault of the Salt Wash graben (northwest – southeast) suggests that they are close to optimally oriented within the current regional stress field, and it is therefore possible that they are accommodating active slip. However, evidence based on field observations and interpretation of U-Th dating of travertine (discussed in section 5.2.1.2) suggests

there has been no recent movement, at least throughout the history of travertine deposition.

The Little Grand Wash fault is a 70-80° south dipping arcuate normal fault with a surface trace of 61km (Shipton et al., 2005). In the region of the axial trace of the Green River anticline the fault consists of main two strands which stretch from 3.2km east to 0.1km west of the Green River (Figure 3.3A), the rest of the fault trace only has one strand (Shipton et al., 2004). In the field area this is further complicated as the fault zone consists of several anastomosing normal faults defining structural terraces with varying dips (Vrolijk et al., 2005; Dockrill and Shipton, 2010). Travertine mounds situated along this fault all occur in the immediate footwall which suggests that fluid flow has been restricted to the damage zone. This is likely to be the result of upwelling CO₂ rich waters having to migrate through fractures in several low permeability sealing lithologies from their immediate source in the Navajo Aquifer (section 3.4.2). Fracture analysis along the fault demonstrates a higher fracture density around relay zones than in structurally simpler sections of the fault (Dockrill and Shipton, 2010). Further to this travertine mounds are also confined to fault bends and relay zones. These observations suggest that permeability pathways may be preferentially associated with more structurally complex sections of the fault.

The total vertical separation on the fault is ~260 m, most of which is accommodated by the southern fault strand (Dockrill and Shipton, 2010). Both strands of the fault were encountered at depth in an abandoned well (Amerada Hess, Green River number 2 drilled in 1949 to a depth of 1798 m, Figure 3.2B). Drilling records state that the deeper of the two faults has Permian Cutler Group sediments in the hanging wall and Pennsylvanian Hermosa Group sediments in the footwall (Shipton et al., 2004). It is unclear what the offset of the fault is at this depth, or whether it cuts the Paradox formation.

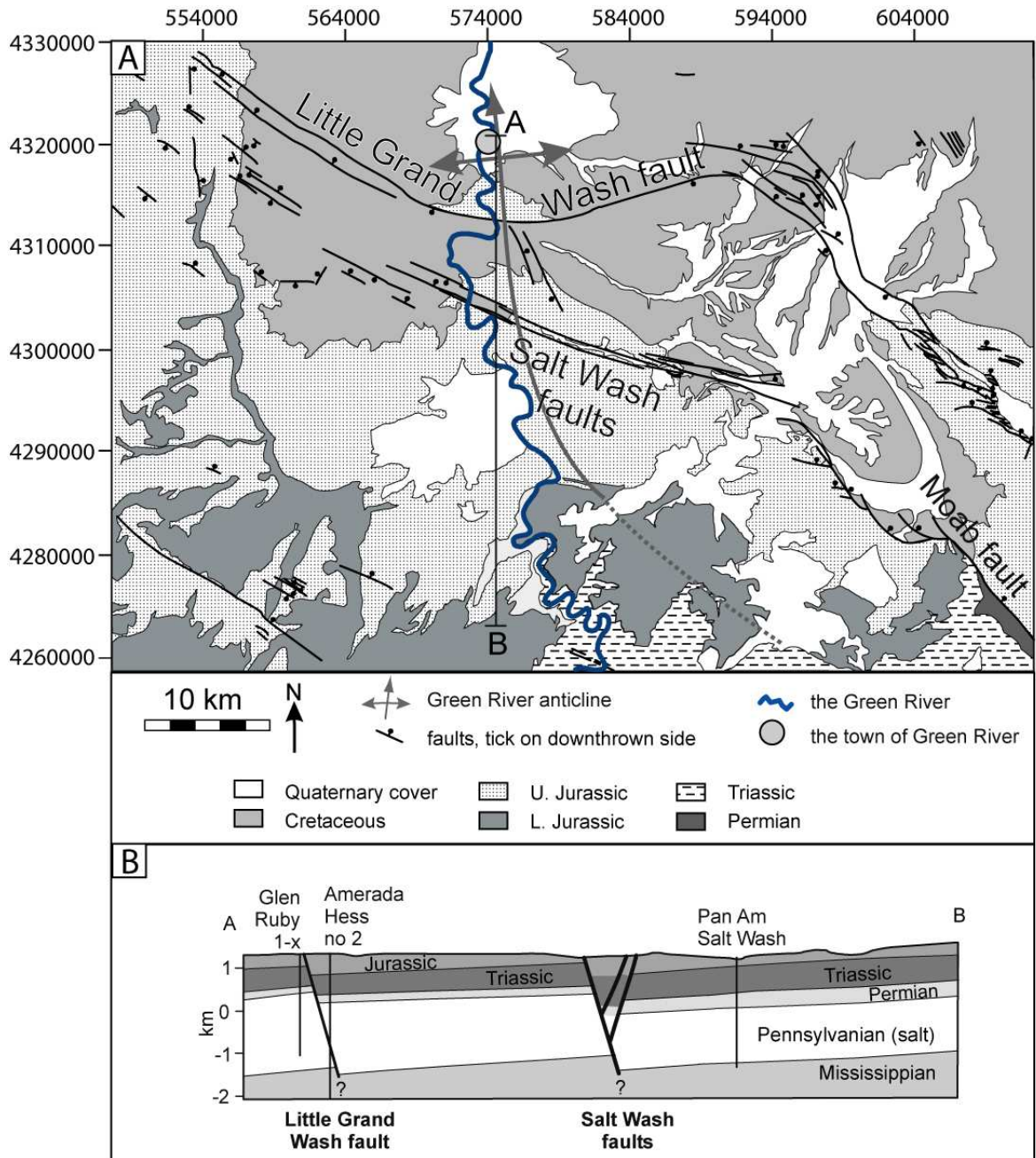


Figure 3.2: Regional geology of the Little Grand Wash and northern Salt Wash faults.

Figure after Shipton et al. (2004). (A) Geological map compiled from Doelling (2001), Williams (1964) and Williams and Hackman (1971). Grid co-ordinates are given in UTM using the NAD83 datum. (B) Cross section of line A-B from Figure (A). Also shown is the location of exploration wells that have been used to decipher stratigraphy at depth.

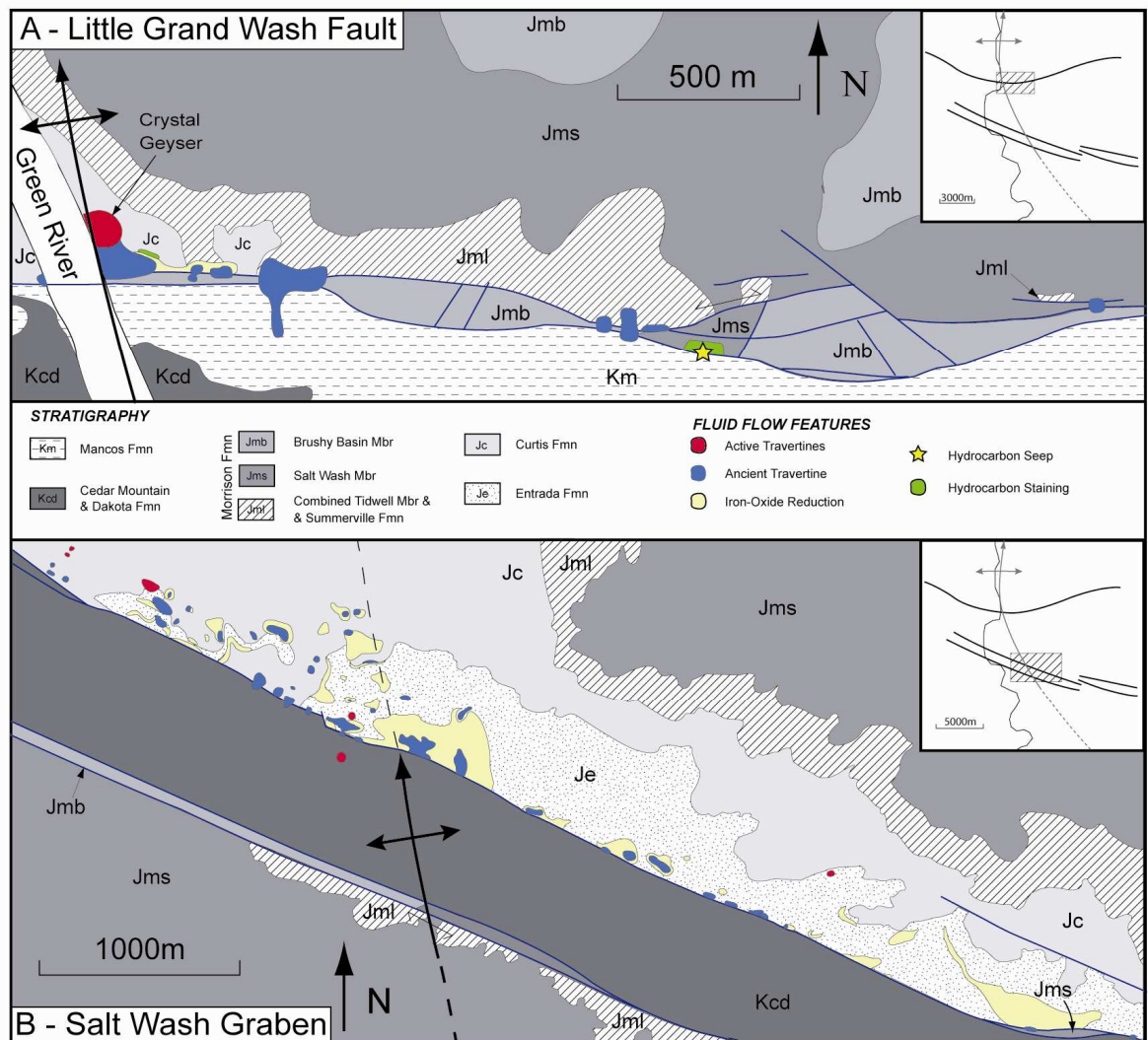


Figure 3.3: Surface geology of the Little Grand Wash and Salt Wash graben field sites.

Figure after Dockrill (2006). Maps show distribution of both active and ancient travertine along the (A) Little Grand Wash fault and (B) Salt Wash Graben. Insets show the relative location of the maps along each fault. For GPS coordinates of each travertine mound see Appendix D. A sketch cross section of the Little Grand Wash fault, taken within the plane of the fault and focusing on the relationship of quaternary deposits, is shown in Figure 3.4.

The Salt Wash graben is a shallow, 15km long, 290° striking dip-slip graben with a left stepping relay zone to the east (Shipton et al., 2005; Dockrill and Shipton, 2010). It may be structurally linked to the Moab fault system to the southeast (Shipton et al., 2004). Maximum vertical separation on the northern fault of the Salt Wash Graben is ~366 m (Dockrill and Shipton, 2010). This fault offsets the Jurassic Entrada Sandstone in the footwall against Cretaceous and Jurassic Cedar Mountain Formation in the centre of the graben (Figure 3.3B). The depth to which the faults extend is uncertain but they may sole into the Paradox Salt sequence (Shipton et al., 2004) (Figure 3.2B). Unlike the Little Grand Wash fault, travertine associated with this fault are not restricted to the immediate footwall and can be found up to ~530 m north of the fault trace (Figure 3.3B). This is likely due

to the simpler stratigraphy present above the immediate spring source in this area. Upward migrating fluid has only to penetrate a single sealing lithology (the Carmel Formation) before it can travel uninterrupted to the surface through the Entrada Sandstone, which is an unconfined aquifer unit (Figure 3.5). The observations that constrain the different fluid flow patterns in the Little Grand Wash fault (representing leakage confined to damage zone fractures) and the northern Salt Wash graben (representing leakage through an unconfined aquifer) is discussed in greater detail in sections 5.3 and 5.4 of Chapter 5.

In both field sites faulting of the Green River anticline has created a series of stacked three-way anticlinal closures in the footwalls of the faults, which creates a series of multiple stacked traps. This is also true of most of the other CO₂ reservoirs in the basin (Allis et al., 2001). Many of these reservoirs are good natural analogues for anthropogenic storage of CO₂ as they have successfully accumulated the gas since its formation. The Little Grand Wash and northern Salt Wash graben faults however have provided pathways for the vertical migration of CO₂ rich fluid from depth. This has allowed large volumes of CO₂ to leak from an accumulation at depth to the surface and escape into the atmosphere. Both of these faults therefore provide analogues for failed CO₂ storage attempts.

3.2.1 Tectonic history of the Paradox Basin

The development of the Paradox Basin began in the mid-Proterozoic, at 1700 to 1600 Ma, when movement on high-angle basement faults and fractures initiated the formation of large scale north-westerly trending anticlines within the Paradox fold and fault belt (Stevenson and Baars, 1986). During the Cambrian and Mississippian, this region, along with most of eastern Utah, was the site of thin marine deposition within the mid-continental U.S. craton while thick deposits accumulated on the continental margin to the west (Hintze, 1993).

Major changes occurred at the start of the Pennsylvanian. A series of basins and fault-bounded uplifts developed from Utah to Oklahoma as a result of the collision of the South America, Africa, and south-eastern North American continents (Kluth and Coney, 1981; Kluth, 1986; Dickerson, 2003); or from a smaller scale collision of a microcontinent with south-central North America (Harry and Mickus, 1998; Dickinson and Lawton, 2003). This tectonic event initiated the uplift of the ancestral Rocky Mountain orogeny and the crystalline Uncompahgre

Plateau in the central part of the western United States (Stevenson and Baars, 1986). This latter event, caused by northwest orientated reverse faulting, created an asymmetric basin to the immediate west complete with a peripheral uplift-parallel bulge ~200km southwest of the plateau (Barbeau, 2003). Flow of marine waters into the basin was restricted by this bulge, leading to accumulation of thick evaporite-shale-carbonate successions which would later become the Paradox Formation. Near shore carbonates and terrestrial siliclastic sediments shed from the highland area to the northeast infilled the basin during the later stages of subsidence (300-260 Ma) (Hintze, 1993; Barbeau, 2003).

Sedimentary loading of the Paradox Formation coupled with reactivation of basement faults below the Paradox Basin initiated displacement and flow of evaporites, creating a series of northwest-trending, salt-cored anticlines and pillows sometime during the late Pennsylvanian (Doelling, 1988). Seismic surveys and exploration drilling have identified northwest-striking, high angle basement faults beneath several of the salt-cored anticlines (Chidsey and Morgan, 2005; Morgan et al., 2007). Movement of the evaporites continued until the late Triassic (Doelling, 1988), with the rising salt anticlines being buried by sediments sourced from the Uncompahgre uplift. As a result, thickness of the overlying sediments varies significantly with upper Pennsylvanian to mid Jurassic units being thin to absent over some salt anticlines and much thicker in the intervening synclines (Doelling, 1988; Condon, 1997), an observation which is supported by isopach modelling of Permian to late Jurassic strata (Dockrill, 2006).

Reactivation and uplift of the Uncompahgre Plateau and the formation of a series of basement fault-cored monoclines bordering the Paradox Basin occurred throughout the Laramide orogeny between 70-40 Ma (Davis, 1978; Heyman et al., 1986). Regional north to northwest trending open folds formed during this period superimposed on the salt-induced anticlines (Cater, 1970; Doelling, 1988). Prominent faults within the sedimentary cover, such as the Moab and Lisbon Faults, were also preferentially formed along the margins of thick salt bodies or reactivated during this period (Doelling, 1988; Foxford et al., 1996).

Since the late Cenozoic, the salt-cored anticlines have been brought close to the surface or exhumed by regional erosion related to epeirogenic uplift of the Colorado Plateau (Pederson et al., 2002; Moucha et al., 2009). Infiltration of ground waters through fractures and joints has dissolved the salt bodies, causing

collapse of some anticlines and formation of valley and graben structures, bordered by escarpments, and since infilled with Quaternary deposits (Doelling, 1988).

3.3 Stratigraphy and lithology

3.3.1 Stratigraphy within the field areas

Lithologies present in the Little Grand Wash and Salt Wash Graben field areas range in age from middle Pennsylvanian to Cretaceous whilst the surface lithology consists of middle Jurassic to Cretaceous strata. Figure 3.5 shows a stratigraphic section of the formations present in the area, with units of particular interest to this study highlighted. A large unconformity spanning ~ 70 Ma in age exists between the most recent deposits and ancient lithologies. The presence of Upper Cretaceous and Tertiary stratum in the Book cliffs to the north suggests that they were once present in the study area. Based on this assumption Nuccio and Condon (1996) have estimated that ~2,500 m of Cretaceous and Tertiary rocks have been removed by erosion. The following section explores the key lithologies of interest to this thesis. For a more detailed review of the stratigraphy the reader is directed to Trimble and Doelling (1978) and Nuccio and Condon (1996). The lithologies discussed below are of importance as they provide the pathways and storage sites for groundwater that supply the springs and the CO₂ that leaks to the surface. Strata present at the surface in each area are noteworthy for the discussion of concentrated and diffuse flow to the surface later in the thesis (Chapter 5).

3.3.2 Important lithologies

Of the thick sedimentary sequence that composes the stratigraphy of the field sites several key units are of particular interest to this thesis. These are namely the rocks that produce the CO₂ within the areas, and good aquifer/reservoir units plus their top seals. Regionally important aquifers are formed by the Glen Canyon Group sandstones, which are defined as the 'Navajo aquifer' by Naftz et al. (1997), and the Permian White Rim Sandstone. Highly permeable lithologies are also found outcropping in the field sites and include the Entrada Sandstone and Curtis Formation (Table 3.1 and Figure 3.5). The White

Rim Sandstone aquifer is capped by the Kaibab Limestone which is composed of inter-bedded dolomites and limestones (Condon, 1997). The Navajo aquifer is situated below the mixed fossiliferous marine sequence that composes the Carmel Formation aquitard (Trimble and Doelling, 1978). Throughout the region in places where the Entrada and Curtis Formation sandstones are not exposed at the surface they are capped by the gypsiferous siltstones and mudstones of the Summerville Formation. The strata above the Summerville Formation mainly consists of shales, siltstones and low permeability sandstones (Hood and Patterson, 1984) up to the youngest formation exposed in the field area, the Lower Cretaceous Mancos Shale, a dark organic rich marine deposit (Johnson, 2003).

Recent deposits in the field areas range in age from Late Pleistocene through to the present day, and sit unconformably on top of Jurassic and Cretaceous strata exposed at the surface. These deposits include travertine formed by emergence of CO₂ charged water at the lands surface, gravels deposited by the Green River and its tributaries, and alluvial fans and scree slopes formed by erosion and deposition of debris from buttes and cliff faces (Figure 3.4). The two former are especially significant to this thesis as interpretation of the morphology of both gravel and travertine deposits and determination of travertine ages provide the tools with which to determine field relationships and quantify the history of fluid flow along the faults. These deposits are discussed in more detail later in the thesis in sections 3.4 (travertine) and 5.2.1.2 (river gravels).

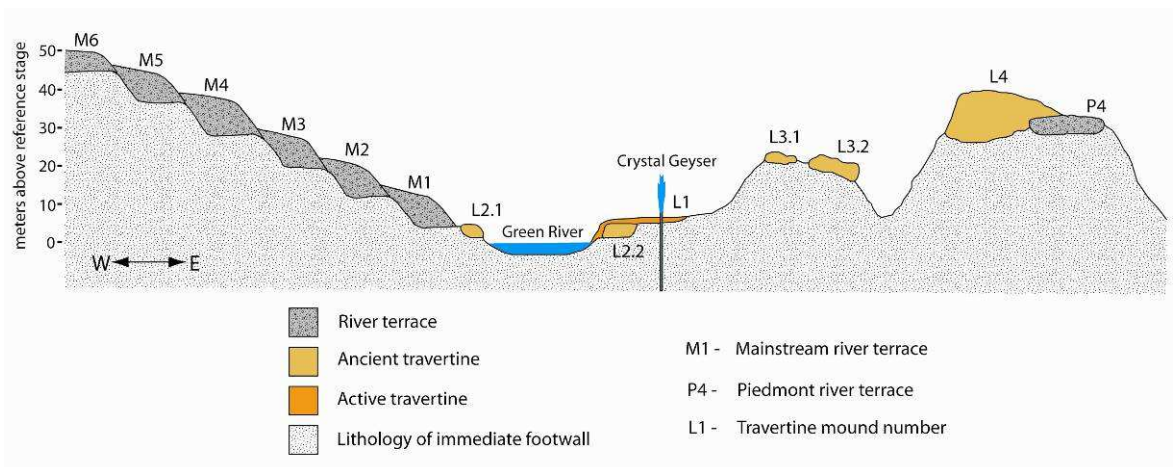


Figure 3.4: Sketch cross section of the geomorphology of the Little Grand Wash.

Section is shown in the plane of the Little Grand Wash Fault. A detailed understanding of the geomorphology of river gravel deposits and travertine becomes important later on within chapters 4 and 5.

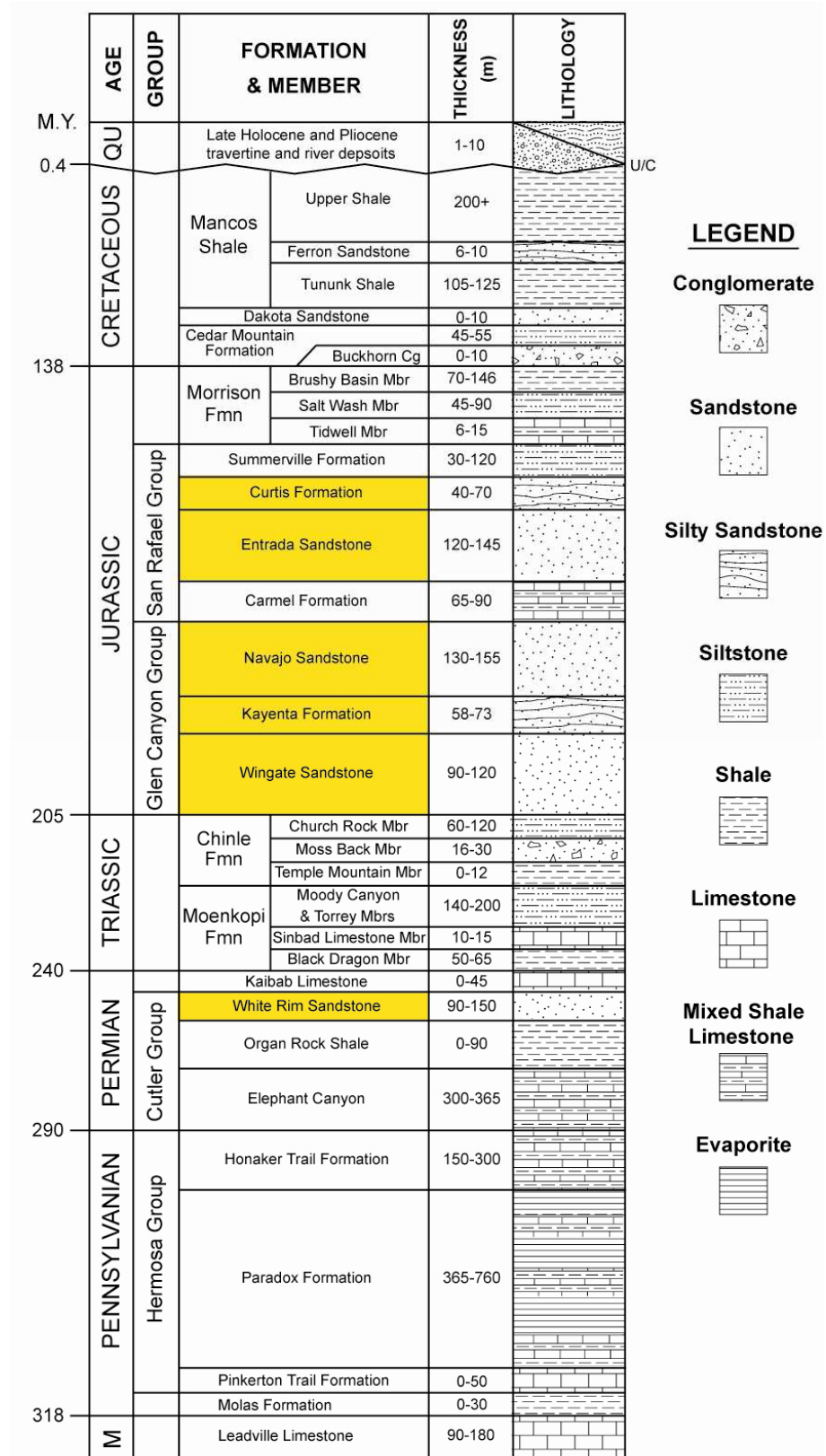


Figure 3.5: Generalised stratigraphic section down to the upper Mississippian for the Green River area.

Figure modified from Dockrill (2006). Thickness data is compiled from Trimble and Doelling (1978) and Hintze (1993). Good reservoir units within the succession are highlighted by yellow. Within the age period column 'QU' stands for Quaternary whilst 'M' stands for Mississippian.

Unit	Boyle's Law Porosity (%)	Calculated Porosity (%)	Permeability (Millidarcies)	Permeability (m ²)	Average thickness (m)	Area (km ²)
Entrada Sandstone	-	26.4	-	-	-	-
Navajo Sandstone	17.7	19.5	534.5	5.28 x 10 ⁻¹³	125	3,700
Kayenta Formation	19.6	21.4	500	4.93 x 10 ⁻¹³	-	-
Wingate Sandstone	20	21	340	3.56 x 10 ⁻¹³	122	3,780
Moss Black Member	-	14.3	-	-	-	-
Sinbad Limestone	8.2	-	-	-	-	-
Kaibab Limestone	8.6	-	-	-	-	-

Table 3.1: Permeability and porosity of lithologies present in the field areas.

The Navajo sandstone, Kayenta Fm, and Wingate sandstone make up the main aquifer supplying the springs in the field areas- the Navajo aquifer. Also included is data from the Entrada Sandstone, one of the surface lithologies of the Salt Wash graben, and Permian and Triassic strata. The Moss Back member is a conglomerate of the Chinle Fm, whilst the Sinbad limestone is a 10-15 m thick section of limestone from the Moenkopi Fm. The Kaibab limestone is late Permian. Data collated from Hood and Patterson (1984).

3.4 Travertine

At distinct locations along both the Little Grand Wash fault and northern fault of the Salt Wash graben evidence of leakage of CO₂ enriched waters is present in the shape of ancient and actively precipitating travertine mounds. The following section investigates the origin of the CO₂ and water that the travertine in the present study is precipitated from; provides a definition of travertine and discusses its formation. A review of previous work on the travertine of the Little Grand Wash and Salt Wash graben is carried out and a conceptual model of travertine evolution is presented. Finally, the separate units present within the travertine of this area will be examined and the interaction between them considered.

3.4.1 Source of CO₂

Unusual volumes of CO₂ are generated within the Paradox Basin (Evans et al., 2004); however uncertainty surrounds the source of this CO₂. Geochemical work on the composition of CO₂ within the basin from several studies allows for likely scenarios for the mechanism that triggered formation of the CO₂, and provides candidates for the rocks from which the gas is sourced.

Potential sources of CO₂ within basins include bacterial degradation of organic matter, metamorphism or decarbonation of carbonate sediments, hydrocarbon maturation, and mantle degassing (Wycherley et al., 1999). Bacterial degradation of organic matter typically produces a gas that is < 20% CO₂, measurements from the study area show that the gas percentage of CO₂ are >95% (Heath et al., 2002), thus bacteria is not the major contributor to CO₂ formation. This conclusion is supported by the lack of hydrogen sulphide and methane within gases analysed from the field sites (Heath et al., 2009). Maturation of hydrocarbons can also be excluded based on measurement of $\delta^{13}\text{C}$ of the CO₂ gas in comparison to that of an oil seep within the footwall of the Little Grand Wash fault located roughly 1km east of the Green River (Heath et al., 2009). Low helium isotope and CO₂/³He ratios measured from springs in both areas suggests only a minor component of mantle derived helium (Heath et al., 2002; Heath et al., 2009; Wilkinson et al., 2008), which rules out a mantle source for the CO₂.

The most likely source for the CO₂ is clay carbonate diagenetic reactions, which can involve silicate hydrolysis and carbonate dissolution (Heath et al. 2004). These reactions could have been instigated at temperatures of about 100 to 200°C (Evans et al., 2004) during deep burial of impure carbonate sedimentary rocks during the burial of the Colorado Plateau from the middle Cretaceous to the end of the Miocene (Nuccio and Condon, 1996). The work of Heath et al. (2009) shows that if isotopic equilibrium is assumed between the source carbonates and the gases then clay-carbonate reactions involving rocks with $\delta^{13}\text{C}$ CaCO₃ values of +1 to -3‰ (i.e. marine carbonates) could have produced the CO₂. The $\delta^{13}\text{C}$ values of the gas are close to the range of values for carbonate samples from the Pennsylvanian Honaker trail formation and the Permian White Rim Sandstone. Other evidence from petrography and observation of free phase CO₂ accumulation

in other regions of the Paradox Basin suggests that the source of CO₂ could be the deeper Mississippian Leadville Limestone (Figure 3.6) (Kampman et al., 2009).

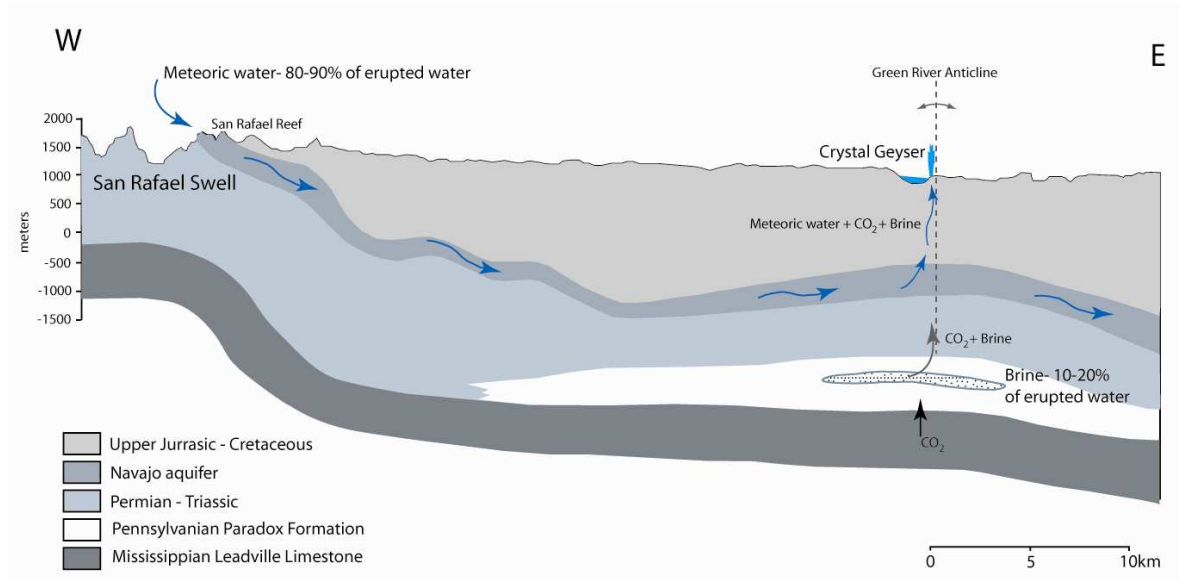


Figure 3.6: Generalised cross section of ground water sources for spring deposits.

Figure adapted from Kampman et al. (2009). Section is shown along the plane of the Little Grand Wash fault.

3.4.2 Source of water supplying springs

Assuming the waters supplying the springs did not cool during ascent, their low emergence temperature (15.7- 18.0°C) suggests a shallow source. Stable isotopes of δD and $\delta^{18}O$ from modern day springs occurring in the field areas indicate that the waters are mainly meteoric in origin with a small brine contribution (up to 20%) coming from a deep saline aquifer, possibly situated within the Paradox Formation (Wilkinson et al., 2008; Heath et al., 2009; Kampman et al., 2009). The large meteoric component suggests that the waters haven't exceeded temperatures of 100°C (Shipton et al., 2005), which given local geothermal gradients (Reitler et al., 1979; Nuccio and Condon, 1996), means that the groundwaters are likely to have originated from the Navajo aquifer (Evans et al., 2004). The source of this large meteoric component, as evidenced by southeast directed regional ground water flow (Hood and Patterson, 1984), is precipitation on the San Rafael Swell where the Navajo aquifer crops out some 35km west of the Green River (Figure 3.6). Groundwater pools within the four-way structural closure formed by the juxtaposition of the Green River anticline against the faults (Shipton et al., 2004) where it becomes charged with CO₂ migrating vertically from below or within the Paradox salts.

Stable isotope data indicates that travertine deposits along both faults have resulted from a common CO₂ rich fluid (Shipton et al., 2005). Geologic and isotopic evidence shows that leakage is confined to the footwalls of both faults. Ancient and modern travertine deposits are only ever found in the footwall of the faults, whilst there are geochemical differences in spring waters either side of the faults (Heath et al., 2004). To the north, spring water is highly saline, acidic, and supersaturated with respect to bicarbonate whilst to the south; waters are alkaline with low salinities and bicarbonate contents. The location and chemistries of springs and travertine therefore suggests that although both faults form effective barriers to lateral fluid flow, fracturing of the cap rock in the damage zone above reservoir units allows for vertical migration of CO₂ charged fluid to the surface.

3.4.3 Classification of travertine

The definition of travertine in the literature varies widely depending on hydrological setting, temperature and formation process. Definitions are often insufficiently precise as they tend to be site specific and fail to completely describe all of the aspects involved with travertine formation. Recent work from Pentecost (2005b) provides an all-encompassing description of travertine which is as follows:

“A chemically-precipitated continental limestone formed around seepages and springs, consisting of calcite or aragonite, of low to moderate intercrystalline porosity and often high moldic or framework porosity within a vadose or occasionally phreatic environment. Precipitation results primarily through the transfer of carbon dioxide from or to a groundwater source leading to calcium carbonate supersaturation, with nucleation/crystal growth occurring upon a submerged surface.”

This definition emphasises inorganic processes, with reactions involving gaseous carbon dioxide and calcium bicarbonate rich solutions being the main source of precipitation of calcium carbonate in a terrestrial setting. Biological processes and evaporation are not discounted but they are considered as subsidiary effects. Depending on temperature of the source waters travertine can be subdivided into three main categories; hot spring (waters warmer than 36.7°C, the core human body temperature), ambient spring (waters ~equal to mean annual air temperature [MAAT]), and cold spring (waters below MAAT) (Pentecost, 1995a; Pentecost, 2005a). As the spring waters actively forming travertine deposits in the

field range from 16.4 - 18.0°C, and the MAAT for central Utah is ~17°C (Pope and Brough, 1996) the travertine in these field areas are ambient in nature. Spring-deposited travertine can be further subdivided based on morphology into mound, fissure ridge or plaudal deposits (Li and Riding, 1999; Chafetz and Guidry, 2003; Pentecost, 2005b). The travertine in this study form sub-circular domes around spring vents, reaching up to 6 m in thickness and 600 m in perimeter, and so fall into the mound category.

3.4.4 Formation of travertine

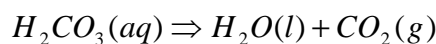
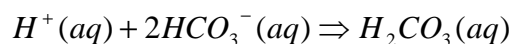
Waters giving rise to travertine deposits undergo rapid chemical change upon contact with the near-surface atmosphere. This is due to a decrease in hydrostatic pressure as saturated fluids rise to the surface which leads to the reduction of the partial pressure of CO₂ and results in degassing of CO₂ according to Equation 3.1.



Equation 3.1

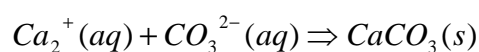
This is the carbonate equilibrium equation (Clark and Fritz, 1997). Degassing, or loss of CO₂ from solution, causes displacement of this equation to the right. Other factors that can have a similar effect are evaporation of water, and an increase of Ca²⁺ activity via breakdown of complexing ligands or dissociation of Ca complexes (Gascoyne and Swartz, 1982). This is a very simplified description of the chemical equilibria in the low temperature system Ca-H-C-O. The degree of calcite saturation can also be influenced by factors such as temperature, pH, kinetic factors and concentration of other ions in solution (Herman and Lorah, 1987; Dreybrodt et al., 1992; Zaihua et al., 1995; Janssen et al., 1999; Fouke et al., 2000; Zhang et al., 2001; Xu et al., 2003; Jamtveit et al., 2006). Carbonate precipitation can also be mediated organically by the microbes and algae that flourish in the CO₂ rich water (Chafetz and Folk, 1984; Pentecost, 1995b; Ford and Pedley, 1996; Chafetz and Guidry, 1999; Merz-Preiß and Riding, 1999; Van Calsteren and Thomas, 2006). Biotic effects such as these greatly influence travertine deposition in ambient conditions (Pentecost, 2003; 2005b) as are found in within the present study areas.

Some authors suggest that calcium carbonate does not precipitate out of solution straight away (Zhang et al., 2001; Hammer et al., 2005) but is lost according to the reaction:



Equation 3.2

The escape of CO_2 leads to the consumption of H^+ and HCO_3^- and an increase in CO_3^{2-} . Over a period of time the solution will become supersaturated with $CaCO_3$ until nucleation occurs:



Equation 3.3

Once nucleation begins reaction 3.2 simplifies to reaction 3.1 (Viles and Goudie, 1990).

Travertine deposits have a lifespan of geologically short duration (Alcaraz-Pelegrina and Martinez-Aguirre, 2007; Zentmyer et al., 2008; Zhao et al., 2009) and in contrast with most of the land surface, are constructive in nature during active precipitation. Once inactive, mounds can become rapidly affected by erosion. Travertine can therefore be uniquely utilised to investigate the events of deposition and erosion simultaneously side by side, which makes this carbonate an important tool for geomorphological studies (Pederson et al., 2002; Marks et al., 2006). Travertine is commonly found along or in close proximity to fault traces with precipitation generally being concentrated in high-flow, structurally complex zones such as fault tips or intersections (Hancock et al., 1999; Uysal et al., 2007; Faccenna et al., 2008; Uysal et al., 2009). This structural affinity allows travertine to be exploited in the field of neotectonics (Hancock et al., 1999; Minissale et al., 2002; Piper et al., 2007; Haluk Selim and Yanik, 2009). Travertine precipitated from meteoric and surface waters have also been utilised for palaeohydrology (Gasse and Fontes, 1989; Minissale et al., 2002; Anzalone et al., 2007) and palaeoclimatology (Szabo, 1990; Winograd et al., 1992; O'Brien et al., 2006; Sun and Liu, 2010).

3.4.5 Previous work on travertine of the Little Grand Wash and northern Salt Wash Graben faults

Recognition of travertine deposition within the field areas may stretch back as far as 1867 when John Wesley Powell documented the presence of “satin spar” during an expedition down the Green River (Powell, 1895). This could have been a description of fossil mound terraces or bright white calcite veins visible in some of the ancient mounds from the river within the Little Grand Wash (Shipton et al., 2004). The first published description of travertine deposits for the Little Grand Wash area is provided by Baer and Rigby (1978). It is likely that the deposits were recognised as travertine before this time as hydrocarbon exploration in the area dates from 1935. Indeed the Glen Ruby #1-X petroleum test well was drilled during this time. As this well is spudded into an ancient travertine mound it suggests that the drillers had picked this site due to evidence of prior leakage. Since its inception the Glen Ruby #1-X test well has provided a conduit to the surface which has led to the formation of the spectacular Crystal Geyser (section 3.5.3). Baer and Rigby (1978) recognised difference in ages of the travertine deposits and separated them into three separate groups, or levels, based on their elevation. Actively precipitating mounds were consigned to ‘Level 3’. Ancient mounds that occurred just above this base elevation were termed ‘Level 2’. Finally older fossil deposits found at significantly higher elevations, up to 37 m above level 3, were grouped together as ‘Level 1’. Recognition of travertine in the Salt Wash Graben was first published by Doelling (1994), whilst extensive mapping of both the Little Grand Wash and Salt Wash Graben areas was first completed by Doelling (2002).

Little Grand Wash and Salt Wash Graben travertine were first viewed as a tool for studying CO₂ leakage from a natural reservoir by Shipton et al. (2004). Subsequent work by Shipton et al. (2005) and Dockrill and Shipton (2010) further characterises the area and discusses structural controls on the leakage of CO₂ charged waters and the deposition of travertine. Dockrill et al. (in review) provide great detail on the formation of mounds from these particular sites and provide a conceptual model for travertine evolution. An updated version of this model, taking into account new investigation, is detailed in the following section.

3.4.6 Travertine lithofacies

3.4.6.1 Introduction

The model of Dockrill et al. (in review) is based on field interpretation coupled with petrological and geochemical analyses. By combining observations from these areas the travertine deposits were found to be composed of four distinct lithofacies; (1) cemented conglomerate, (2) layered carbonate mats, (3) white-banded veins, and (4) brown-banded veins. The cemented conglomerate facies was described as having 'sub-angular to sub-rounded pebbles' and to 'extend up to 200 m away from the main travertine deposit'. Further detailed field investigation carried out during the present study has since found relict river terraces associated with numerous travertine mounds in both field sites (3.5.4.2). The main travertine deposit referred to is the most prominent mound in the Little Grand Wash and largest ancient travertine across both areas. The L-shaped conglomerate deposit that extends south of this mound is actually the well carbonate cemented remains of a palaeo-stream channel (section 5.2.1.2). As it is likely that the sub-rounded conglomerate described by Dockrill (2006) is a river derived deposit, and in order to avoid confusion during discussion of river gravels later 'cemented conglomerate' facies will be described as 'cemented breccia' for the remainder of the thesis.

Surrounding the base of numerous travertine deposits in the field is host sandstone well cemented by carbonate. As this altered host rock appears to be closely associated with the travertine mounds I will include it as a fifth variety of lithofacies in addition to the original four proposed by Dockrill et al (in review). The following subsections provide a description of each facies and discuss their interaction. This is followed by conceptual model of travertine mound evolution, based on that of Dockrill et al. (in review), but updated to take into consideration further work in field interpretation carried out during the present study.

3.4.6.2 Altered host rock

The host rock at the base of the ancient travertine mounds is generally altered in close proximity to fractures and bedding planes. The formation of carbonate cement within the host sandstone makes it more robust and resistant to

weathering. In severely eroded travertine mounds, where layered mats have been completely removed, this facies is often the only remnant. Altered host rocks tend to display a distinct orange colouration which makes them stand out from the surrounding outcropping sandstone. The texture of the cement ranges from massive to poikilotopic. This latter texture involves the entrapment of mineral grains of the host sandstone within larger crystals of carbonate and gives a distinct appearance (Figure 3.7A-C). Within sandstone-dominated lithologies bedding planes are exploited by white-banded veins up to 15 cm thick. In mud-dominated lithologies, networks of fine scale box-work veins (5 to 10 mm thick) locally overprint and even destroy the host rock fabrics Figure 3.9.

3.4.6.3 Cemented breccia

Cemented breccia is found on top of the altered host rock and is overlain by layered mats. This facies comprises of locally derived colluvium cemented by carbonate. Clasts within this unit are angular to sub-angular and consist of poorly sorted rock fragments and quartz grains (Figure 3.7D). Some horizons within this facies contain sedimentary structures such as planar cross bedding and imbricated lenticular clasts.

The relative positions of cemented breccia and layered mats suggests that vertical and lateral cementation of the breccia by emanating CO₂ charged waters supplied a relatively impermeable substrate for the growth of the layered mats. A transitional zone exists between these two facies. At the centre of the deposits this zone consists of well-defined layers of each unit that repeatedly alternate. The transition zone gradually thickens away from the central part of the deposits and the boundaries of layering between the facies become harder to define. Layered mats become thinner and more discontinuous, whilst the breccia layers become thicker, from the centre to the outer edge of the mounds. This transition between the two facies may be due to extended periods of spring and non-spring activity or episodic flooding of the travertine by non-spring waters. The proximity of streams and rivers to the ancient deposits and the presence of sedimentary structures within the breccia suggest that episodic flooding is the most likely reason.

3.4.6.4 Layered mats

Layered mats consist of sub-horizontal, layered carbonate deposits with moderate to highly visible porosity. It is this facies that truly defines a travertine mound as it is universally present in all reported travertine deposits from across the globe, where it is commonly referred to as tufa or travertine (e.g. Chafetz and Folk, 1984; Ford and Pedley, 1996; Faccenna et al., 2008). As travertine is used as the all encompassing term for the five separate units that comprise the mounds in the present study the term layered mats is used to describe this surficial expression of the deposit.

Layered mats are generally composed of alternating layers of porous and dense horizons that have a gently dipping surface which demonstrate the direction of flow from the conduit which supplied the CO₂ rich waters. The porous horizons consist of vertically stacked layers that range from 5 to 50 mm thick (Figure 3.8). Each sub-horizontal layer has an irregular, sinuous shape formed by dendritic precipitate which is composed of elongate blocky calcite crystals that branch and terminate in rounded knobby shrub-like structures (Figure 3.8). The irregular sinuous shapes create mm-deep pools and raised rims, forming hemispherical ponds which en-mass produce microterraces. The rims of the hemispherical pools always form sub-horizontally regardless of whether they are formed on relatively flat platforms or on steeply slanted slopes (Figure 3.13). The dense horizons are composed of fine-grained micrite that partially to completely envelope the shrub texture of the porous horizon. Thicker micrite horizons commonly contain angular to sub-rounded clasts of fine to medium-grained detrital quartz and feldspar grains, plus the occasional detached piece of substrate from the porous horizons.

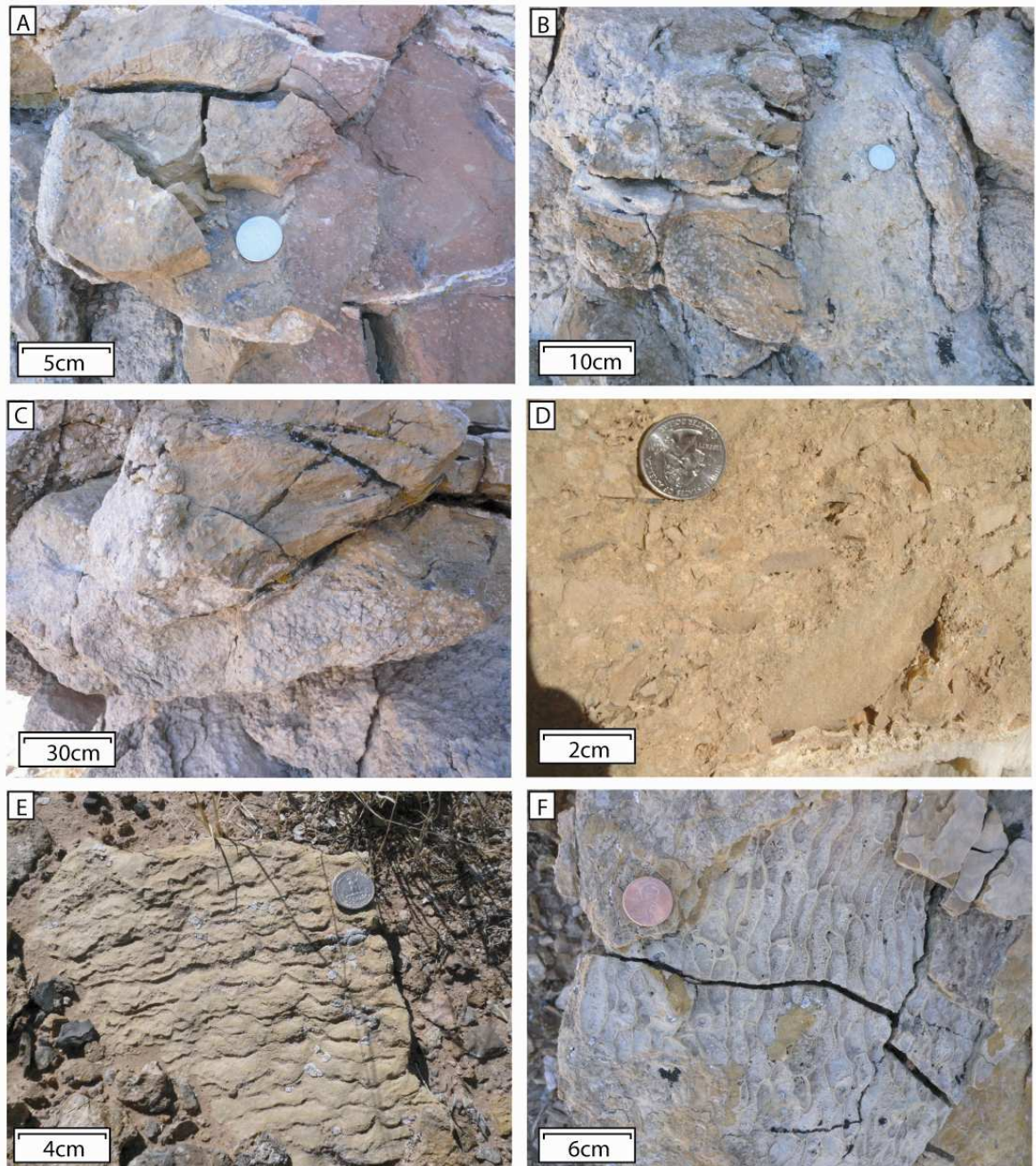


Figure 3.7: Field photographs of travertine facies.

(A) Image of an altered section of Entrada Sandstone host rock (orange) compared to its unaltered appearance (red). (B) Further alteration leads to a poikilotopic texture, as the amount of carbonate cement increases a further colour alteration from orange to dull white occurs. (C) As carbonate crystals increase in size they start to give a joined up appearance that encloses entire faces of outcrops. (D) Initial surface stage of travertine formation, cemented breccia, which consists of angular pieces of surface colluvium entrained within carbonate cement. (E) Example of fossilised layered mat facies. The rim pool structures that can be seen in modern examples are often well worn in ancient deposits. (F) Rare example of pristine preservation of ancient layered mat facies. Images (A-C) taken from mound S39, (D-E) from mound L4 and (F) from mound S16. For location of these mounds see Figure 3.12.

Shrub fabrics were first described by Kitano (1963) and have been subsequently documented in many other studies (Chafetz and Folk, 1984; Guo and Riding, 1994; Ford and Pedley, 1996; Fouke et al., 2000). Chafetz and Guidry (1999) distinguish three varieties of shrub: bacterial, crystal and ray crystal. The former is solely due to biotic process while the later were thought to be formed by a combination of bacterial and abiotic processes. Dockrill (2006) found that shrub fabric of the travertine from these field sites was petrologically similar to the spar-rhomb and micritic components of Guo and Riding (1994), who attributed biotic and abiotic precipitation for the formation of this texture. These interpretations suggest that the layered mats in the present study precipitate from a combination of abiotic and biotic processes.

Shrubs form preferentially in quiescent shallow pools on travertine slopes and are also known to coat grains (Pentecost, 2005b). A continual supply of supersaturated waters is required to replenish the pools and provide the environment needed for shrub growth (Chafetz and Folk, 1984), with precipitation ceasing once supersaturated waters are evaporated from the pools. Extended periods of little or no flow of supersaturated waters allow for deposition of dense horizons of micrite on top of the more porous shrub horizons. Clastics within the micrite may have been transported by aeolian processes or flooding of the deposit from periods of high rainfall or increased discharge of adjacent streams and rivers. The switching between deposition of porous shrub and dense micrite horizons could potentially be a result of periods of spring and non-spring activity, occasional flooding of the deposit by non-spring waters, or a combination of both.

In the majority of ancient deposits across both field sites the layered mats unit is poorly preserved, whilst in several mounds found along the northern fault of the Salt Wash graben it is completely absent. These potentially incomplete mounds consist of bodies of altered host rock and veining, but as they don't contain all or most of the travertine facies, especially the layered mats, outlined in this section they could potentially be the result of some other fluid flow process that is unrelated to leakage along the fault. This poses a problem for confirmation of these mounds as travertine for use in the study of the fluid flow history of this fault, and is discussed in further detail in section 3.5.4.

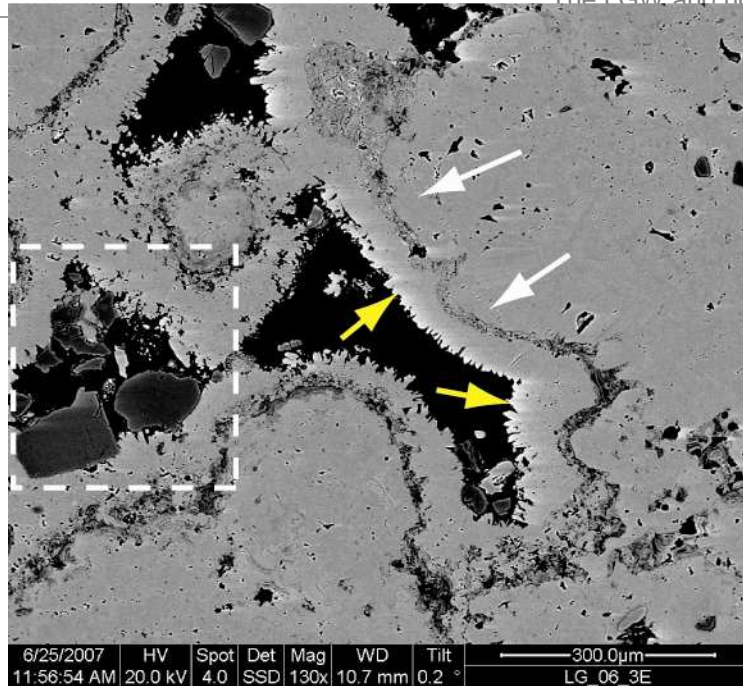


Figure 3.8: EBSD image of layered mat facies.

Radiating shub like growth is shown by the white arrows. Knobby and rounded shub textures are regularly coated by a layer of elongated micritic crystals (yellow arrows). Denser micrite horizons often contain angular to sub-rounded clasts which have been transported in from the surrounding country rock and have become engulfed in the layered mat structure (white box).

Ancient layered mats that are present generally consist of a thin, weathered crust in which demonstrates poorly defined features. Some examples, however, have beautifully preserved features that look very similar to the pool-and-rim geometries of microterraces on active travertine deposits (Figure 3.7E-F). As the rims of the ponds within microterraces form horizontally, regardless of the slope of the surface they form on, they can be used to deduce if ancient layered mats are have remained insitu since the mound ceased activity.

3.4.6.5 White banded veins

A series of dense aragonite veins that are composed of bands of white crystals cut through the layered mats, cemented breccia and altered host rock facies. These white banded veins mainly range in thickness from 5cm to 50 cm, though main veins within mounds may reach up to 2.5 m. Banding within each vein is up to ~30 mm thick and is composed of acicular to columnar crystals that are orientated perpendicular to the depositional surface and increase in size with direction of growth (Figure 3.10A). Within each band the crystals radiate out in a fan pattern (Figure 3.10B) to form a mammilated surface (Figure 3.10C). Thin

laminations, ranging in colour from orange to dark brown, can be found parallel to the growth surface in most veins.

Sub-horizontal veins are thicker, more common and tend to exploit bedding surfaces within other facies, though some crosscut horizons (Figure 3.9A). Vertical veins are usually thinner and line fractures walls or minor faults, and mostly terminate at the base of thicker horizontal veins. Thick vertical veins do exist at the base of some mounds, though they become sub-horizontal at shallower levels. Veins often have a paired symmetrical appearance (Figure 3.9E) that is occasionally separated by a central cavity which can be tens of centimetres wide and contain sub-vertical speleothems up to 10cm in length. In some instances, an outer layer of white-banded vein material has precipitated over the speleothems. This suggests alternating intervals of growth within flooded and drained fractures, perhaps due to periods of waning flow. Cavities within mounds would have been ideal for fluid flow and so are likely to represent the main conduits through which CO₂ charged water migrated to the surface.

Sub-surface vein deposits have not been described in previous travertine studies; however, deposits demonstrating a similar morphology have been documented as surficial features formed by rapid loss of CO₂ in areas of extremely agitated waters (Folk et al., 1985; Guo and Riding, 1994). Similar findings are reported by Uysal et al. (2007) who describe substantial $\delta^{13}\text{C}$ enrichment within samples of detritus free fracture-filling vein travertine which most likely represents isotope fractionation during rapid CO₂ degassing. It is therefore probable that rapid degassing of CO₂ from highly agitated subsurface waters is the mechanism for the precipitation of the banded veins within the travertine mounds of the Little Grand Wash and northern Salt Wash graben faults.

3.4.6.6 Brown banded veins

All of the units previously described are crosscut by sub-vertical brown banded veins that often display dendritic terminations (Figure 3.9F). These veins are similar to white banded veins in that each band consists of radial fans formed from acicular crystals; however, they differ in colour as they are constructed from alternating brown, orange, and white bands up to 3cm in thickness.

Microscopic comparisons of white and brown banded veins, carried out by Dockrill (2006), revealed fine-scale differences between the two lithofacies. Brown banded veins were found to possess significantly thinner bands and a much higher proportion of iron-rich laminations, which were found to terminate underlying crystal growth and promote precipitation of finer-grained crystals on top of the lamination (Figure 3.10D). Iron can inhibit carbonate growth when it is adsorbed onto crystal surfaces as it blocks nucleation and growth sites (Meyer, 1984; Gutjhar et al., 1996).

The higher proportion of iron-rich laminations in the brown-banded veins could indicate a change in precipitation conditions to that of the white banded veins. It is probable that continual recharge of CO₂-charged groundwater leads to the precipitation of aragonite. If this recharge wanes or stops altogether incompatible elements precipitate out of the waters to form the iron oxide in the laminations. Such fluctuations in recharge would imply episodic fluid-flow conditions and therefore a period of alternating spring and non-spring activity. Sporadic channelling of supersaturated waters through the travertine mound may be a precursor to the changing of the fluid migration pathway at depth. If this is the case, then the brown banded veins likely represent the terminal stages of travertine precipitation.

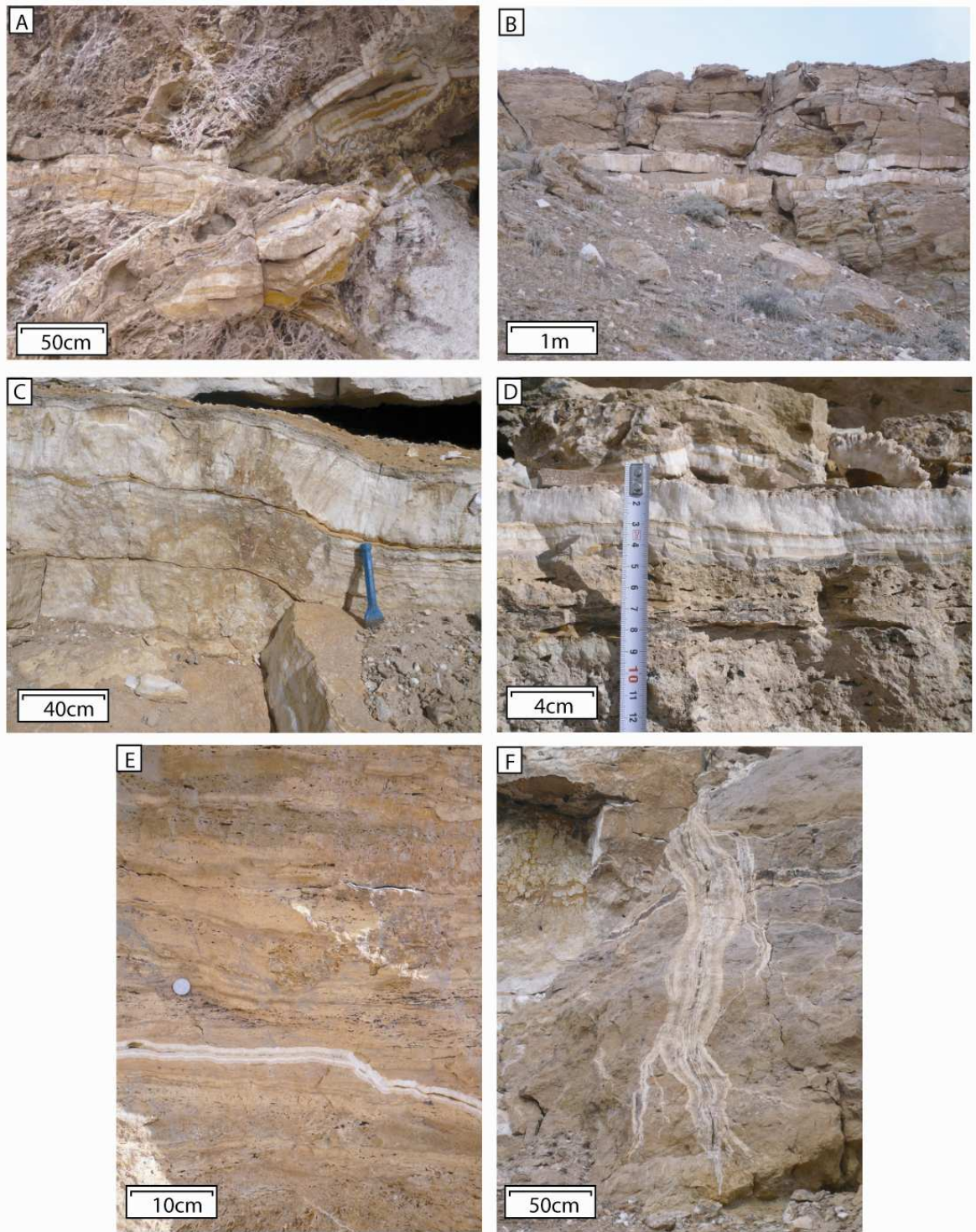


Figure 3.9: Field photographs of banded vein facies.

The images are all taken from the Little Grand Wash field site, for location of deposits see Figure 3.12. (A) View of veins destroying the soft fabric of the clay rich Brushy Basin Member in the hanging wall of the Little Grand Wash fault beneath mound L8. (B) Image of horizontally orientated main vein and subsidiary vein within layered mat facies of mound L6. (C) The main white banded vein of travertine mound L4. (D) Finer scaled white banded vein within mound L4 exploiting a weak horizon within the layered mat facies. (E) Transitional stage between cemented breccia and layered mats which consists interlayered examples of each facies. Also present in this section within the cemented breccia is a white banded vein. (F) Vertically orientated brown banded vein displaying dendritic termination from mound L4.

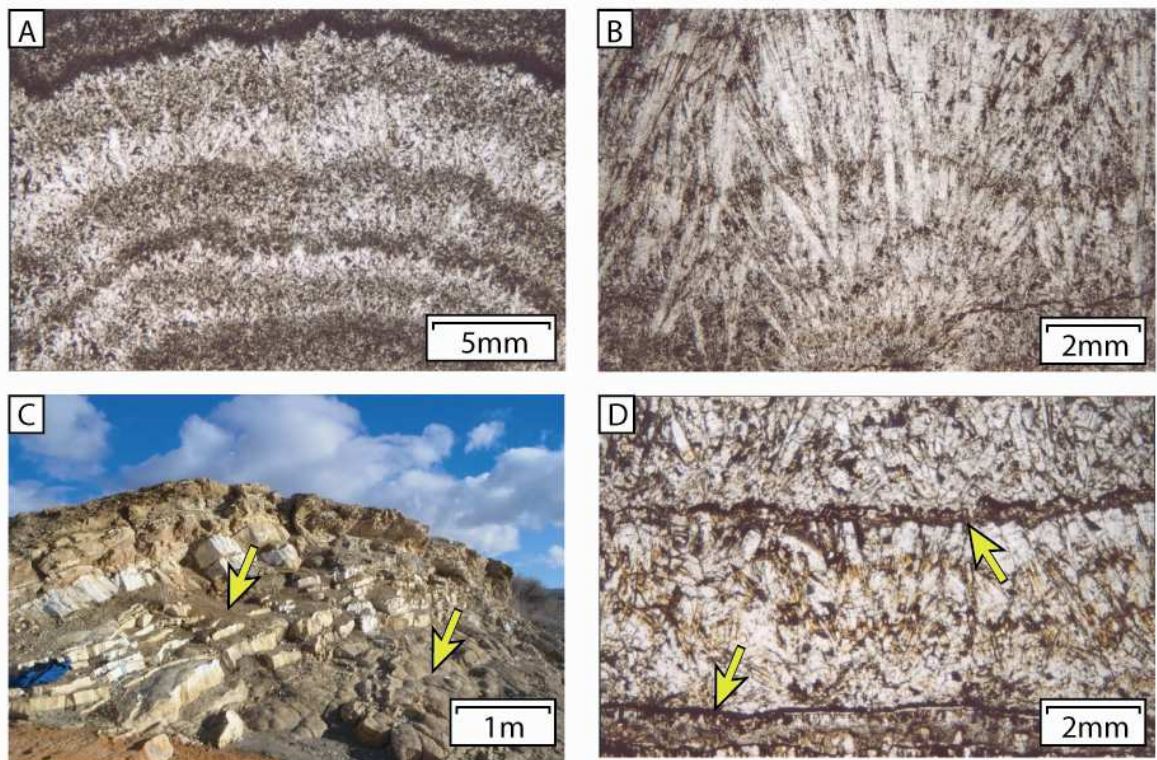


Figure 3.10: Photomicrographs of banded vein morphologies.

Images A, B and D from Dockrill (2006), image C courtesy of Zoe Shipton. (A) Image of white banded vein showing multiple bands of radiating columnar to acicular aragonite crystals. (B) Increased magnification of a single aragonitic band that demonstrates the radial fan pattern formed by aragonite crystals. (C) Layers of white banded veins in the field demonstrating a mammillated surface texture. (D) Brown banded vein with yellow arrows highlighting the dark coloured iron rich laminations that terminate the growth of aragonitic crystals.

3.4.7 Conceptual model of travertine mound evolution

Illustrated in Figure 3.11 and documented below is a reappraisal of the facies model of Dockrill (2006) based on new field interpretations. The model provides a mode of formation for the travertine deposits by describing their physical and geochemical evolution as well as the interaction between the five distinct lithofacies that have been detailed in the previous subsections.

1. Supersaturated carbonate-rich waters migrate to the surface via a fault-related fracture network and initiate a cold-water spring. The carbonate-rich waters emerge from the spring vent and flow into the surrounding colluvium, progressively infilling pore spaces within surface sediments and capturing any present angular clasts within carbonate cement to form a breccia. Just beneath the surface some of the upward migrating fluid diffusely flows into the outcropping sandstones, infilling open pore spaces with carbonate

cement. This process alters the colouration of host rocks from buffs and browns to orange (Figure 3.11A).

2. As the carbonate cemented breccia develops around the spring vent, it forms a relatively impermeable horizon enabling the waters to flow across the surface and precipitate layered carbonate mats by abiotic and biotic processes (Figure 3.11B). The layered mats gradually extend from the spring vent, limited by the development of the underlying breccia, to form a surficial terraced deposit with hemispherical ponds. Contemporaneously, highly agitated waters migrate through conduits to the spring vent and penetrate weak horizontal bedding horizons within the host sandstone. Bands of white aragonite veins are precipitated within the altered host rock. Each set of bands grows parallel to the surface of deposition, increasing in crystal grain size to produce a white banded vein morphology.
3. Continued precipitation of carbonates in the distal colluvium and proximal mound expand and thicken the travertine mound (Figure 3.11C). Rapidly flowing waters start to penetrate sub-horizontal bedding contacts and sub-vertical fractures within the layered mats and breccia, producing bands of radiating aragonite crystals within these facies.
4. In the later stages of activity for the spring system, the supply of carbonate-rich waters to the spring becomes episodic, leading to unstable and alternating environmental conditions reflecting periods of spring and non-spring activity. The drop in kinetic energy of vertical fluid flow allows the precipitation of white banded veins on conduit walls, perpendicular to the substrate. These variable conditions also result in the development of a late set of brown-banded veins characterised by numerous iron-rich laminations interspersed between thinner bands of radial aragonite crystals (Figure 3.11D).
5. Eventually, the spring system dries up and the travertine deposit becomes inactive. Subsequent erosion can remove the deposit, though in the study area they have tended to provide a resistant cap to form a series of buttes that display cross-sectional exposures of the internal and external components of ancient deposits.

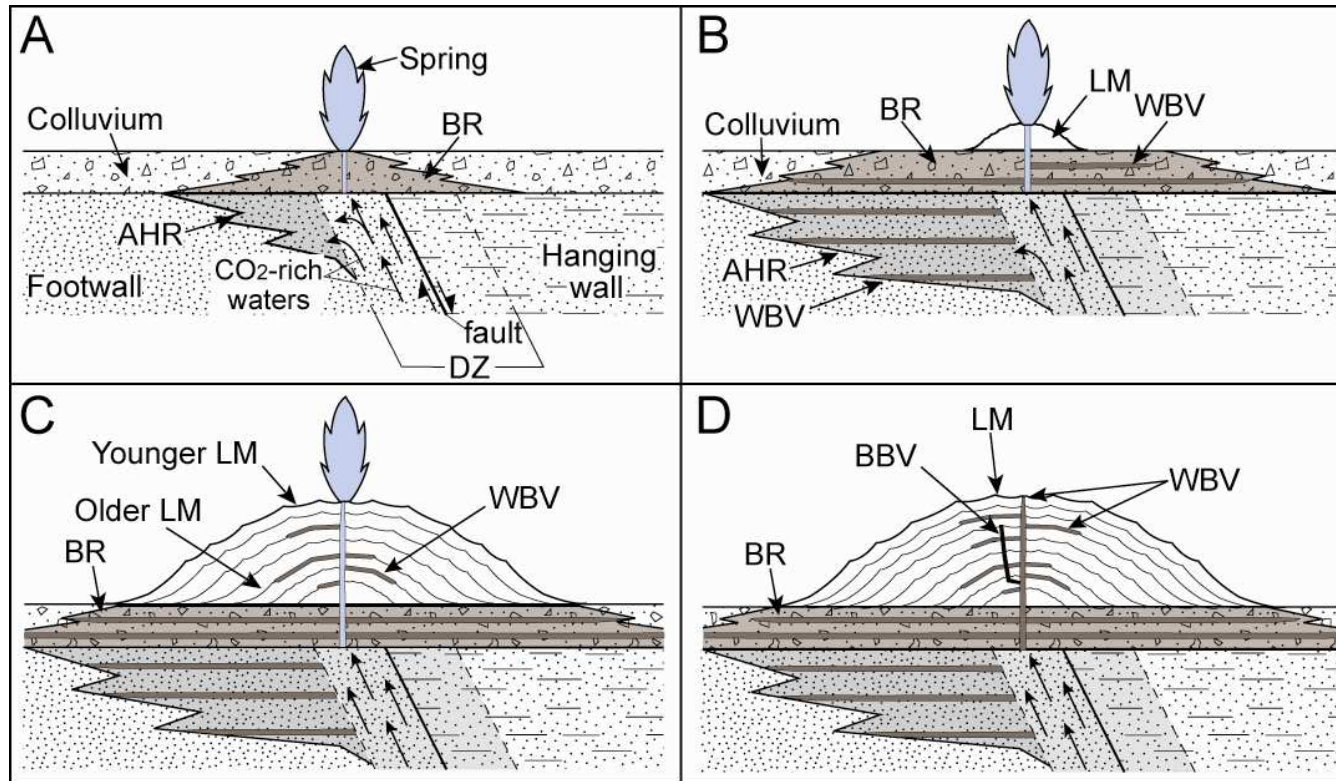


Figure 3.11: Conceptual model of travertine mound evolution.

Figure modified from Dockrill (2006). (A) CO₂ charged waters migrate up through damage zone (DZ) within the footwall of the fault, reach the surface and initiate a spring. Emanating spring waters percolate through the colluvium surrounding the point of discharge and precipitate carbonate cement to produce a breccia (BR), whilst diffuse flow of water into the host sandstone creating carbonate cement and altering the host rock (AHR). (B) Lateral expansion of the cemented breccia results in a relatively impermeable surface which provides a platform for the formation of layered mats (LM) which produce a series of terraces as the mound grows. White-banded veins (WBV) are precipitated by agitated waters that exploit layering within the host rock. (C) Layered mats continue to spread as far as the underlying altered host rock will allow and thicken resulting in further growth of the white-banded veins, which start to penetrate bedding horizons within the layered mats of the mound. (D) During the later stages of growth of the mound supply of CO₂-rich water to the discharge point becomes more episodic. This results in the precipitation brown banded veins (BBV), which crosscut the earlier developed lithofacies. Eventually the spring becomes inactive, and deposition ceases, allowing erosion of the travertine mound to begin.

3.5 Observations from the field

3.5.1 Introduction

The following section focuses on field work carried out in order to characterise travertine morphology and spatial occurrence of mounds along both faults. Travertine deposits, both modern and relict, from both the Little Grand Wash and Salt Wash graben are examined in detail. This characterisation of travertine morphology allows for a close and definite correlation between layered mat and white banded vein facies. This proof of association is important as several mounds within the Salt Wash graben are badly weathered and consist of only white banded vein and altered host rock lithofacies (3.5.2).

3.5.2 Travertine deposits

A total of fifty-six modern and ancient deposits are present in the two field areas (Table 3.2). Each travertine mound was given a unique identifier as shown in Figure 3.12. In the Little Grand Wash one actively precipitating travertine mound, supplied by the Crystal Geyser, and seven ancient deposits occur along a ~3km stretch of the fault (Figure 3.12A). The majority of travertine deposits are on the east bank of the Green River. One small remnant (L2.1- Figure 3.12a) on the western shore of the Green River suggests that there may potentially be further travertine deposits buried underneath the thick stack of river gravels on the inside of the west sweeping meander bend (Figure 3.4). All travertine occurrence is restricted to the eastern limb of the Green River anticline (which may be due to the gravels), unlike the Salt Wash graben where travertine are equally distributed to either side of the anticlinal axis. Along the northern fault of the Salt Wash graben 41 fossil travertine mounds and 6 actively precipitating springs are present (Figure 3.12B). The deposits in this area cover a greater extent of the fault, ~6km along strike, and tend to be smaller and more prone to erosion suggesting they are of a more fragile nature than travertine on the Little Grand Wash.

Field area		SWG	LGW	
Travertine	Total Mounds	47	8	
	Ancient deposits	41	7	
	Modern springs	6	1	
Host rock	Salt Wash Mbr	NE	1	
	Summerville	NE	5	
	Fm Reduced	NE	1	
	Curtis Fm	20	2	
	Reduced	7	1	
Entrada Fm		26	NE	
	Reduced	16	NE	
Age analysis	Total	23	22	
	WBV	22	15	
	Repeats	-	3	
	LM	-	4	
	modern springs	1	3	
Facies Present	LM	23	7	
	AHR	18	-	
	River Gravel	Total	17	4
		LM	15	4
		LM contact	9	4
AHR		2	-	
Dated mounds	Total	22	7	
	LM	15	7	
	AHR	7	-	
	River Gravel	Total	9	4
		LM	9	4
LM contact		7	4	
Non-dated mounds	Total	19	-	
	LM	8	-	
	AHR	11	-	
	River Gravel	total	8	-
		LM	6	-
		LM contact	2	-
AHR		2	-	

Table 3.2: Breakdown of ancient travertine mounds.

Table includes deposits from both the Little Grand Wash fault (LGW) and the northern fault of the Salt Wash graben (SWG). NE equals no exposure of lithology in the field area.

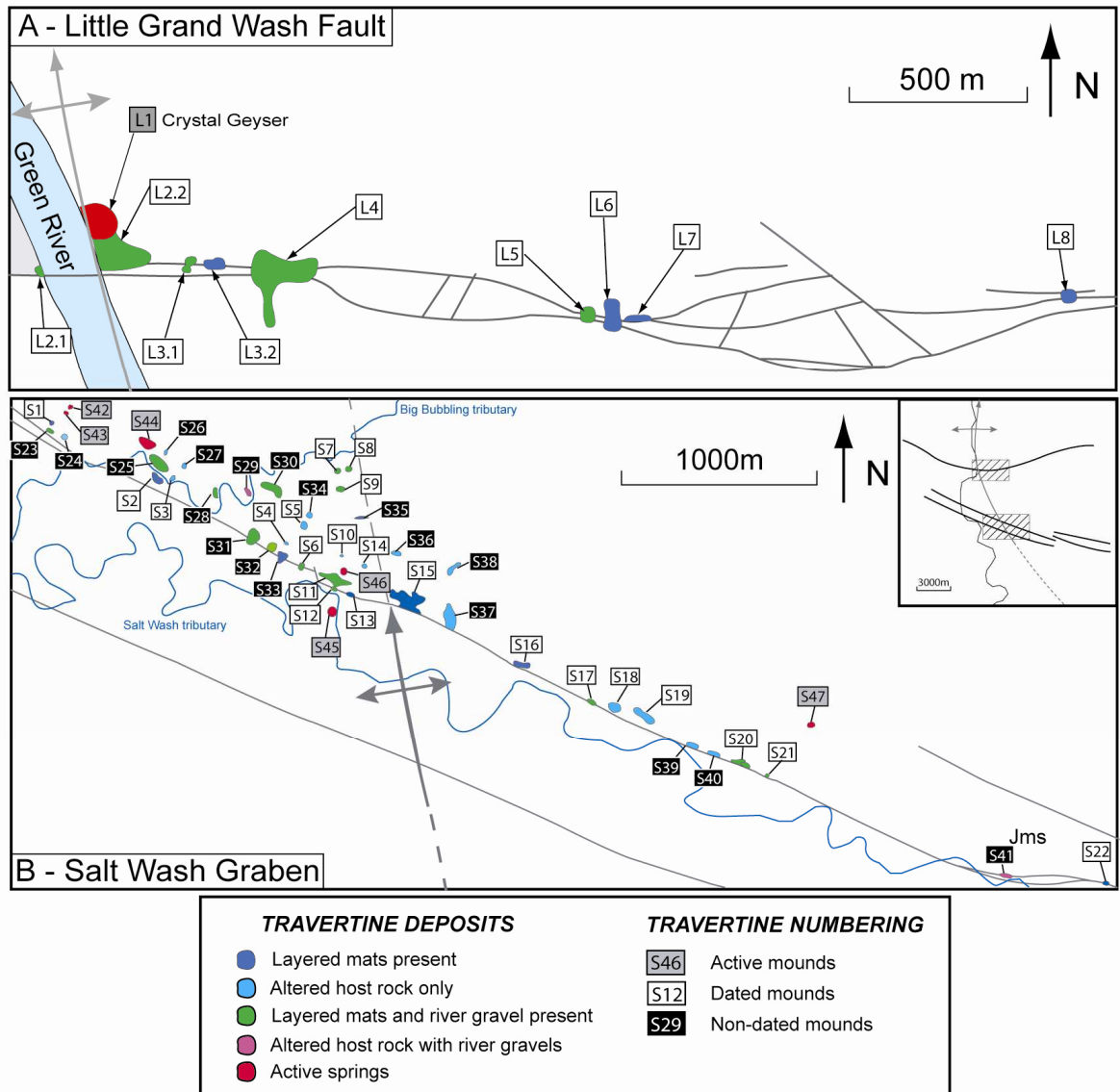


Figure 3.12: The Little Grand Wash and Salt Wash graben field sites.

Maps are based on the geological maps of Dockrill (2006). Only the location of travertine mounds, the surface traces of the respective faults and the location of the Green River anticline are shown. The key shows the colour coded breakdown of the facies present in each mound and also an explanation to the travertine numbering. For a breakdown of the number of travertine that fall into each category see Table 3.2. The inset on the Salt Wash graben map (figure B) shows the two field sites highlighted by dashed boxes. In the Salt Wash area the three main locations of active travertine precipitation are shown by mounds S42, S43 and S44 (The Three Sisters); S45 and S46 (Ten Mile); and S47 (Torrey's). For GPS coordinates of each travertine deposit see Appendix D.



Figure 3.13: The Crystal Geyser (mound L1).

(A) View of the extent of the modern travertine deposit from the top of the Salt Wash bluff looking west. **(B)** Picture, looking north, showing the outward progression of terrace lobe growth from the geyser towards the Green River. Note the multiple hemispherical ponds each complete with pool and raised rim. **(C)** Close up of a large hemispherical pool showing the presence of bacterially formed pisoids up to 4 mm in diameter. **(D)** Lobe downstream of the geyser submerged by runoff of freshly erupted geyser waters. Note that in both **(C)** and **(D)** show horizontally orientated hemispherical rims growing on the steeply sloping edge of a microterrace. **(E)** Runoff along one of the main flow paths of erupted waters- the green pools indicate the presence of green algae. **(F)** The side vent of the Crystal Geyser situated to the north east of the main leakage point. These springs bubble periodically throughout the eruption cycle of the main vent suggesting that they are closely associated.

3.5.3 Actively precipitating travertine

Travertine is being presently formed in several locations in the two field sites. All active travertine precipitation is occurring at the lowest elevation, or base level, of local topography. In the Little Grand Wash there is currently only one actively forming deposit, known as the Crystal Geyser (L1, Figure 3.12A), situated on the east bank of the Green River in the immediate footwall of the Little Grand Wash fault (Figure 3.13). The waters here erupt from an abandoned exploration hydrocarbon well, Glen Ruby #1-X, drilled in 1935 to the base of the Triassic section (TD 801 m) (McKnight, 1940). This site was probably chosen for drilling due to its close proximity to the structural high formed by the 3-way trap and the presence of ancient travertine deposit hinting at past leakage. The geyser is powered by CO₂ charged waters that erupt cold water (up to 18°C) to heights of 10 m over intervals of 4 to 12 hours (Shipton et al., 2005). Drilling records for the well document the thickness of this pre-existing travertine as 21.5 m (Baer and Rigby, 1978). Given that the surrounding landscape is being actively eroded that would imply that precipitation of this mound originally occurred in a deep depression in the landscape. Considering that this mound is proximal to the Green River its initial inception would have to have been below the base level of the river, which is highly unlikely. The 21.5 m recorded in the Glen Ruby # 1-X well therefore is more likely to represent the depth of veins and carbonate cemented altered host rock within the Curtis sandstone beneath the mound.

Eruptions from this geyser have resulted in the development of a large ochre-coloured terrace deposit that is ~70 m wide by 80 m long and ~3 m thick. During geysering events water covers most of the western flank of the mound and eventually drains into the Green River via a series of channels that connect the upper surfaces of down-stepping terrace lobes. Three other springs within 10 m of the geyser effuse periodically throughout geyser eruption and so are closely linked to the plumbing of the geyser. The pools could represent the location of pre-well CO₂ charged springs or could be due to the escape of CO₂ charged waters from the abandoned pipeline at shallow levels (Shipton et al., 2005). Along the trace of the fault in the Green River bubbles highlight intermittent CO₂ leakage from the river bed.

The Salt Wash graben currently hosts six active sites of orange coloured travertine precipitation. These have been reported to be the result of a mix of natural and drilling induced emergence of saturated waters (Shipton et al., 2004). Only one deposit, the Ten Mile Geyser (S45, figure 10B), has evidence of being man-made as it has well casing around its orifice (Figure 3.14E), however no drilling records exist for this location. Torrey's Spring is possibly the result of the exploratory Delany Petroleum Corporation Well #1 drilled in 1949 (Dockrill, 2006). Many of the other deposits have a natural appearance (Figure 3.14) but the small size of the travertine deposits, which suggests a recent onset of precipitation, coupled with the poor exploration records in this area means that a drilling origin can not be ruled out for any of the modern deposits. All sites are formed by CO₂ charged cold water (~15 to 16°C) and are situated in the footwall bar the Ten Mile Geyser (S45, figure 10B), which is situated around 200 m into the hanging wall. The geochemistry of its waters suggests that it penetrates the fault at depth and taps into ground water from the footwall side (Heath et al., 2004).

Active travertine mounds along the northern fault of the Salt Wash graben are generally low, thin and poorly developed in comparison to the Crystal Geyser deposit. Thin salt crusts are common around drier sections of the actively precipitating travertine. The mounds are restricted to three main locations along the northern fault of the Salt Wash graben- Three Sisters, Ten Mile and Torrey's (Figure 3.12B). The Three Sisters to the west of the field area consists of the Big Bubbling spring (S44) and the northern (S42) and southern (S43) Small Bubbling springs (Figure 3.14A-C). Central to the field area, Ten Mile hosts the Ten Mile Geyser (which erupts up to a height of ~1.5 m) within the hanging wall of the fault and Ten Mile Spring (S46, Figure 3.12B) which is located due north of the geyser 100 m into the footwall of the fault. Torrey's spring (Figure 3.14D) is situated ~350 m into the footwall of the fault and ~2,200 m to the east of the anticline (S47, Figure 3.12B).

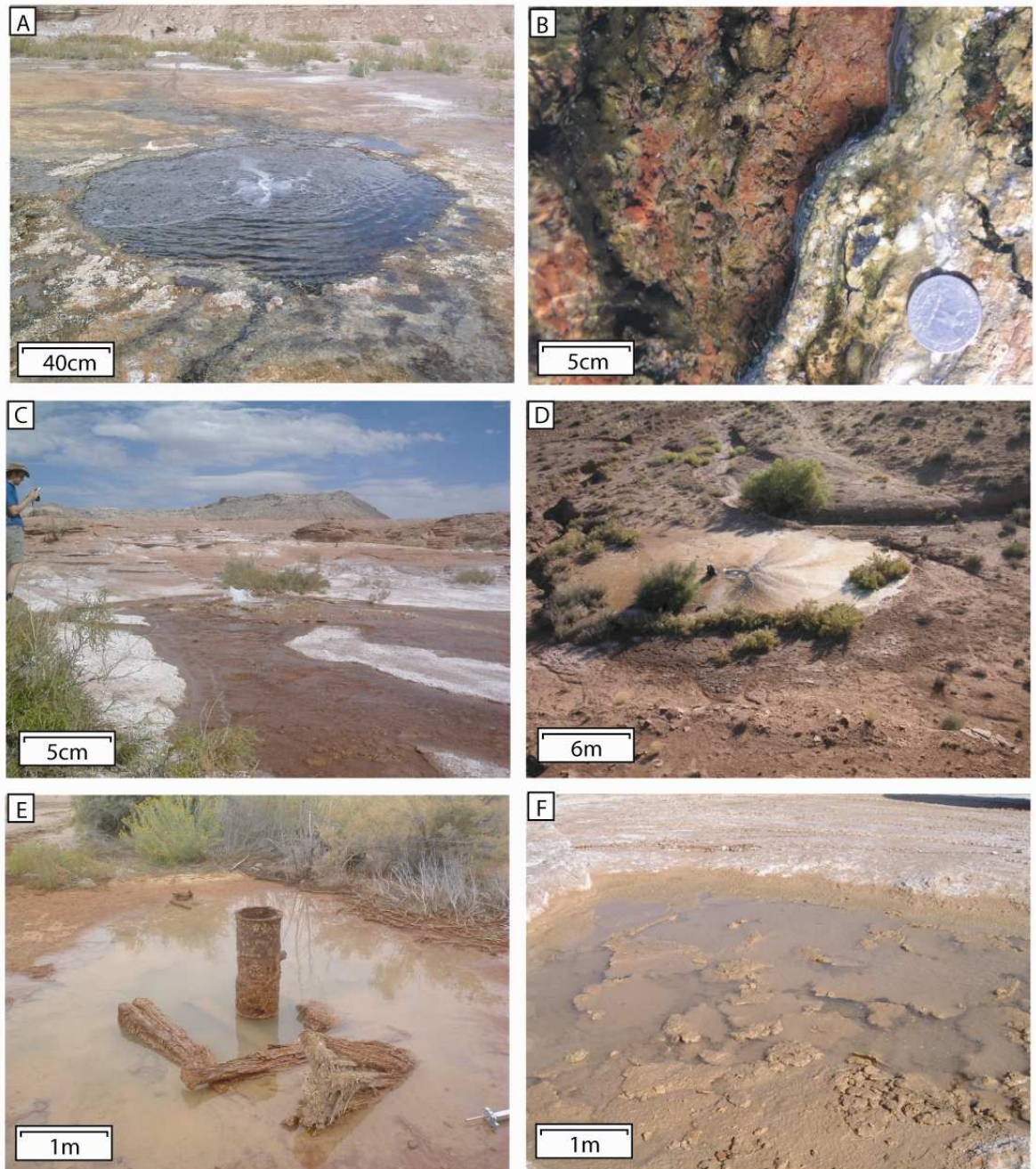


Figure 3.14: Active springs of the Salt Wash graben.

(A) The main pool of the Big Bubbling spring (mound S44) showing the encroachment of light grey salt deposits. **(B)** Close-up of the edge of the Big Bubbling spring showing the presence of both green and red algae in its waters. **(C)** Southern Small Bubbling spring (mound S43) shown during geyser-style eruption of waters. **(D)** Picture taken, looking east, from above Torrey's spring (mound S47) showing extent and circular character of this spring. **(E)** Pool of water and well casing around Ten Mile Geyser (mound S46), this is the only travertine deposit located within the hanging wall of either fault. **(F)** Image of pool supplied by the Ten Mile spring (mound S45) showing the formation of layered mats in the surface waters of the pool. These formations start as small thin crusts and eventually grow to form large plates up to 10 cm thick and a meter in diameter. Once they reach this they become dense enough to sink to the bottom of the pool.

3.5.4 Ancient travertine deposits

3.5.4.1 Ancient travertine occurrence and preservation

Fossil travertine is usually easily distinguishable in the field as the solid carbonate provides a good barrier to erosion and caps high buttes and terraces of local host sandstone that sit proud of the general landscape (Figure 3.15 and Figure 3.16). Along the Little Grand Wash fault mounds form in the immediate footwall, where the Summerville and Curtis Formation sandstones are exposed at the surface, and drape over the fault into the hanging wall. Travertine deposits that occur along the northern fault of the Salt Wash graben are predominantly confined to the footwall rocks of the Curtis Formation and Entrada Sandstone, occasionally draping into the adjacent graben. Of the forty-one ancient mounds on the Salt Wash, only twenty-three have clear evidence of layered mat facies (Table 3.2), with most of these comprising of thin poorly-developed deposits ranging from 0.3 to 1.2 m thick. The remaining eighteen are distinguished from the surrounding landscape by the presence of white banded vein and significantly altered host rock. These mounds are confirmed as travertine by the close association of layered mats and white banded veins in better preserved mounds (Section 3.5.4.2). All seven fossil travertine deposits on the Little Grand Wash fault display evidence of both layered mat and white banded vein facies (Figure 3.15). Mounds in this area tend to be better developed and thicker, ranging from 0.5 to 6 m, than those on the Salt Wash graben, so are therefore more robust and resistant to the effect of erosion (Figure 3.15 and Figure 3.16).

Travertine deposits on the Little Grand Wash fault are all closely associated with the surface expression of the fault (Figure 3.12A). The location of the mounds in this field site appears to be restricted to fault bends and relay zones which have greater fracture intensity in comparison to structurally simpler sections of the fault (Dockrill and Shipton, 2010). This may suggest that the damage zone of the Little Grand Wash fault is creating zones of increased permeability around areas of increased structural complexity for fluid flow to exploit (section 5.3.1.3). Mounds in the Salt Wash graben are more numerous and not restricted to the surface trace of fault, with some occurring a significant distance into the footwall (Figure 3.12B). The more diffuse nature of flow is likely to be due to the highly porous nature of the Entrada Sandstone (Table 3.1; Hood and Patterson, 1984) which is the

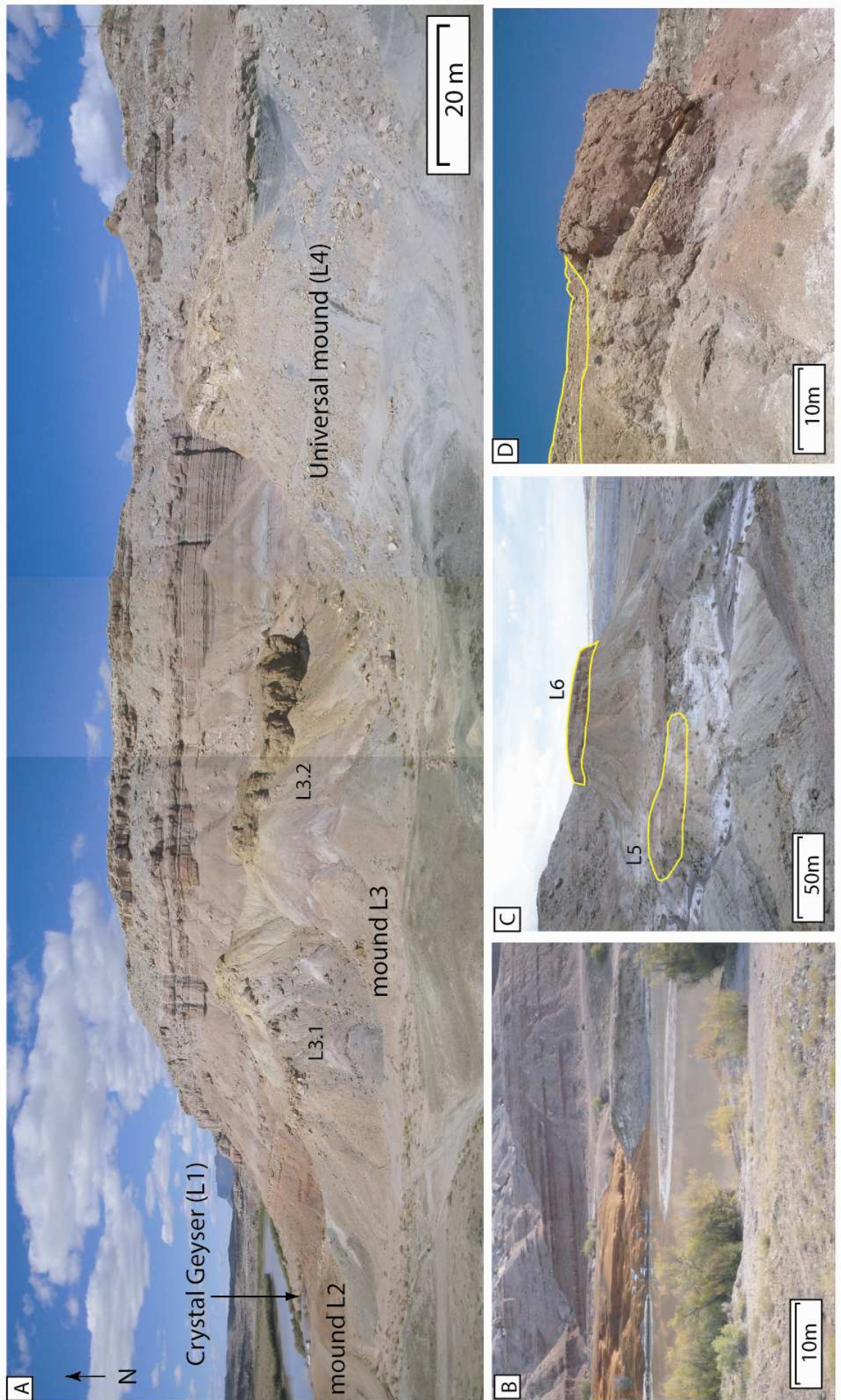
surface lithology in the immediate footwall of the fault. This may be a key factor in the greater spread of travertine in this area and could be one cause of the Salt Wash travertine being smaller and more fragile than their Little Grand Wash contemporaries. Travertine that occur away from the fault, up to 530 m into the footwall, appear to be related to the trace of the Green River anticline. Structural flexure along the axis of the anticline is ruled out as a cause of this association as the anticline has a gentle inter-limb angle of $\sim 172^\circ$. Leakage through exposed aquifer or bedding surfaces that lead away from the fault is a more likely scenario (section 5.3.1.2).

3.5.4.2 Association of layered mat and white banded vein facies

Layered mats are found associated with all travertine deposits on the Little Grand Wash fault. One of the problems encountered in the Salt Wash graben field is the presence of veining and altered host rock without clear evidence of layered mat facies in nearly half of the present mounds (Table 3.2). To interpret these mounds as travertine, which is important for later discussion, the white banded vein present in complete mounds must be demonstrated to be associated with the layered mat facies.

Figure 3.15: Ancient travertine mounds on the Little Grand Wash fault.

(A) Panoramic photograph, looking north, of the western end of the Little Grand Wash field area showing mounds L1 to L4. Note the difference in elevation of the deposits with the younger mounds becoming successively lower, with age increasing from L1 (~ 0 ka), L2 (~ 5 ka), L3 (~ 50 ka) and finally L4 (~ 114 ka). (B) Image taken from the west bank of the Green River looking east. Note the ochre colour of the actively precipitating Crystal Geyser in comparison to the dull brown colour of the ancient mound L2. Parts of the Crystal geyser travertine have been altered from ochre to light grey by submersion under the waters of the Green River during periods of high flow. An island of vein debris in the middle of the river adds further evidence to the association of L2.1 and L2.2. (C) Well developed mounds L5 and L6 (looking east) which demonstrate all travertine facies and are 0.6 and 5 m thick respectively. (D) Picture of mound L8, again looking east, with extent of layered mats, which are 2.5 m thick, highlighted in yellow.



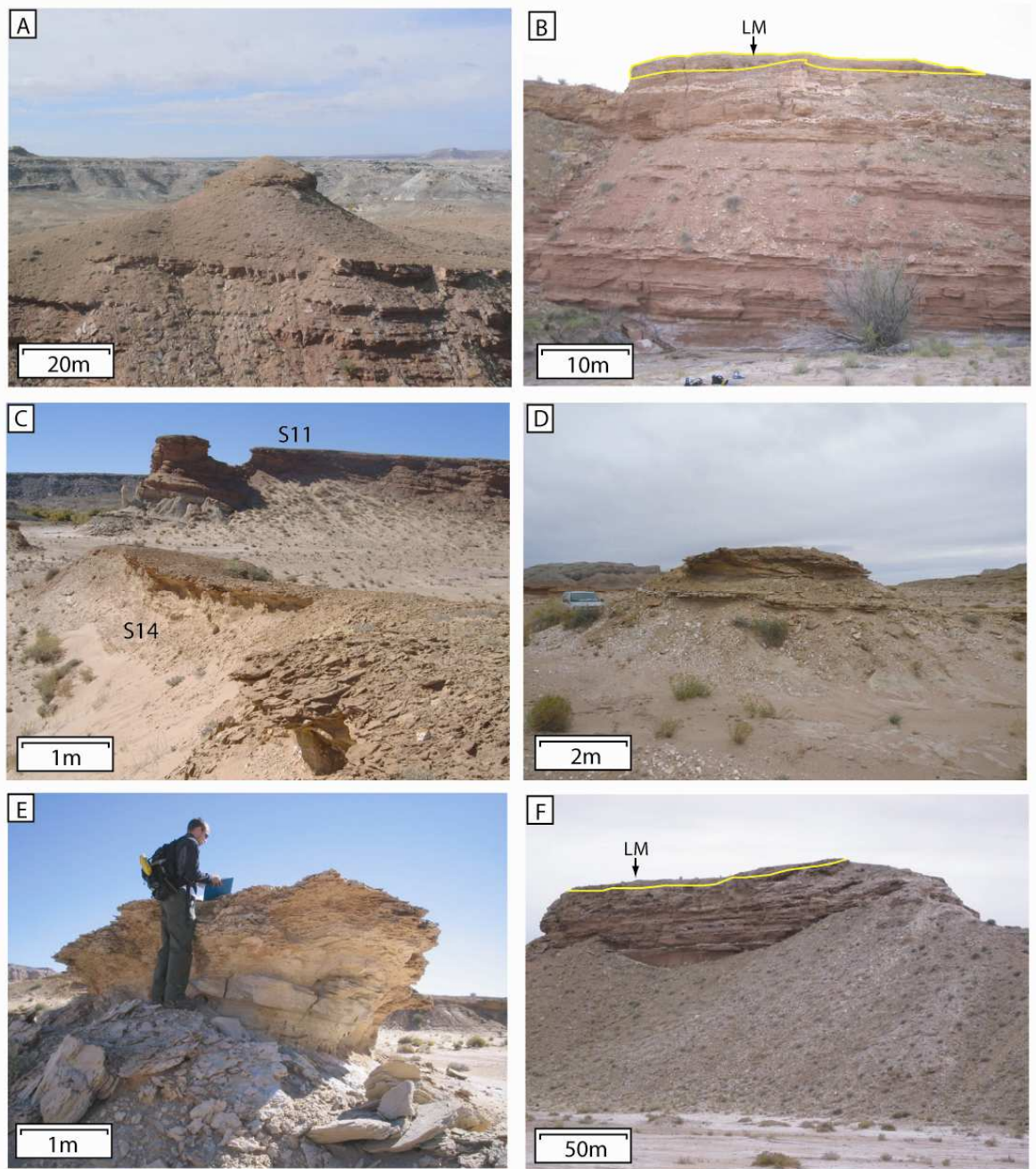


Figure 3.16: Ancient travertine along the northern fault of the Salt Wash graben.

(A) Picture of mound S5, the oldest deposit in the area. This mound is situated on the bluff between the Salt Wash and Big Bubbling tributaries. It stands proud of the flat bluff surface, and like several of the deposits in the area consists of only altered host rock and white banded veins. (B) Northern side of travertine deposit S2. Here veining can be clearly seen running horizontally within the altered host rock beneath the layer mat unit, which is 1 m thick. (C) Image looking south of the very thin and poorly developed mound S14 in the foreground and the prominent S11 in the background. Note the difference in height of the older S11 mound (~93ka) above younger S14 mound (~34ka). (D) Small and poorly developed 0.4 m thick S13 mound looking east. (E) Mound S10, looking east, this mound lacks layered mats and is composed of only white banded veins and well altered host rock (in this case Entrada Sandstone). (F) Image of mound S11 looking east. Despite its large number of horizontally orientated veins running through the host rock up to 9 m below the travertine, its layered mats are only 1 m thick.

In the field several pieces of evidence point to a clear association of layered mats and white banded vein. In the mounds with both facies present the white banded veins are present throughout the layered mats and also the host rock underlying the travertine (Figure 3.9, Figure 3.15, Figure 3.16; section 3.4.7). Numerous mounds across both field areas have carbonate cemented river gravels beneath them (section 4.5). These gravels mainly consist of well rounded clasts of the local country rocks and in several examples clasts of layered mats and white banded vein are also present (Figure 3.17). In two locations on the Salt Wash graben layered mats and white banded vein can be found in close proximity in the same gravel. The gravels preserved within mounds in the Salt Wash graben are fossilised river terraces of minor tributaries, the Salt Wash and Big Bubbling streams, which drain into the Green River to the west. The small pebbles entrained within these gravels suggest that the tributaries are low energy and have a low carrying capacity (section 5.2.1.2). Since it is likely that the clasts of layered mat and white banded vein have not been transported far it makes it likely that those found in close proximity originate from the same mound.

Further evidence is provided by one key locality on the northern fault of the Salt Wash graben. Sample location S21 is like several of the mounds in the Salt Wash graben in that it consists of a butte of altered host rock complete with white banded veins. Unlike the other altered host rock buttes in the area S21 has a large block of layered mat facies 1.5 m thick situated half way down its southern scree slope roughly 5 m from the main mound. The block contains two episodes of layered mat growth, which have different dip angles in their layering, and has a layer of river gravel at its base (Figure 3.17F). The layering of both episodes of layered mat growth is sub-vertical which gives this block a tilted appearance; it is also surrounded by scree derived from the main part of the mound which all suggests that this block has slid down the scree slope from the main part of the mound. However, the hemispherical pool texture has not been well preserved on the surface of the layered mats and as this facies (section 3.4.6.4; Figure 3.13) can form on slopes it is hard to conclusively determine its original orientation so an *insitu* deposit can not ruled out.

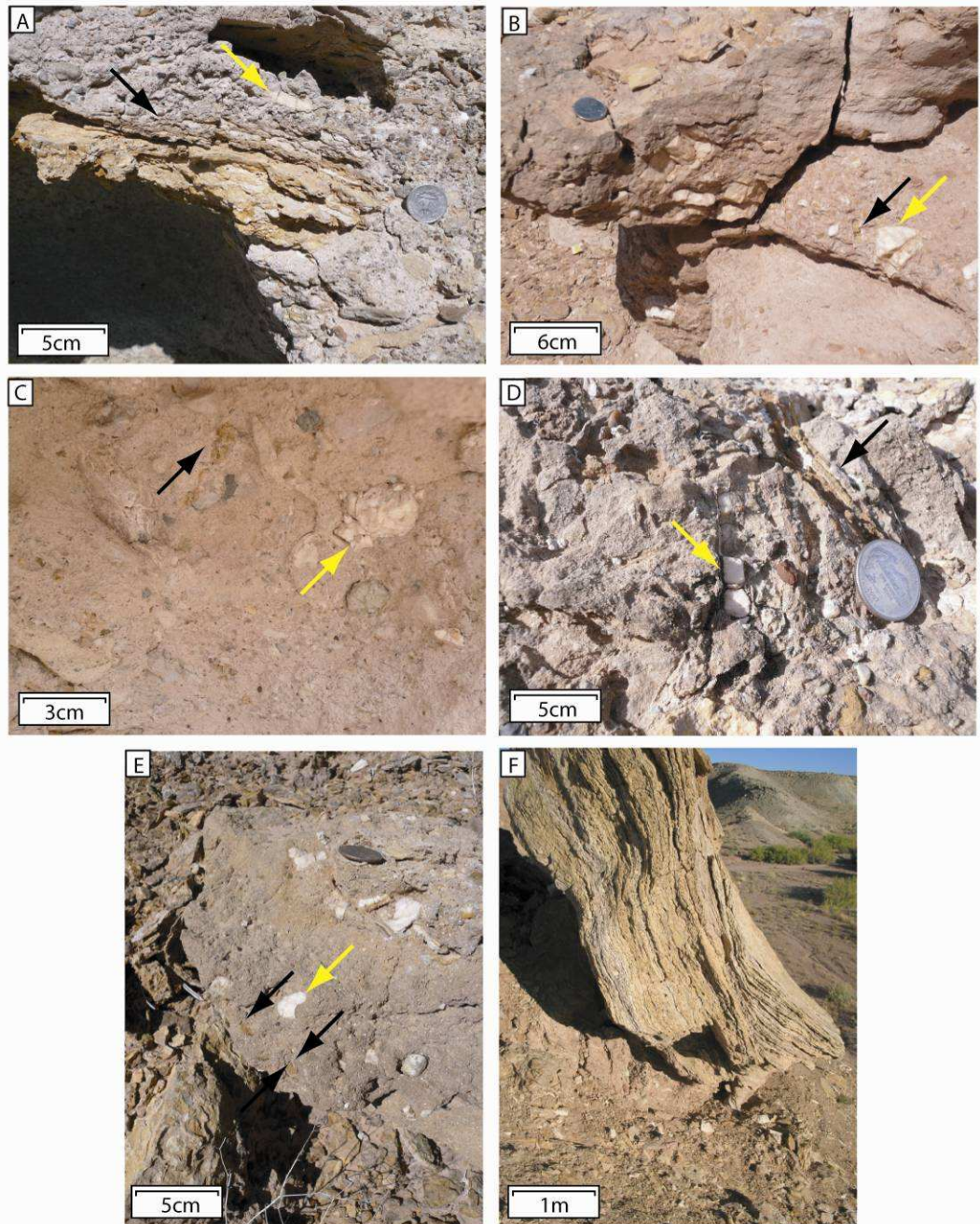


Figure 3.17: Evidence for association of layered mats and white banded veins.

In the images of gravel with clasts of both facies white banded vein and layered mat segments are indicated by yellow and black arrow respectively. (A - E) Evidence of facies in gravels from mounds S31, S17, L4, S29, and S6. Note that mound S29 depicted in (D) is devoid of insitu layered mats so the evidence of this facies within gravel associated with this mound suggests the former presence of layered mats on this mound. (F) Image of detached block from mound S21. Note the two separate episodes of growth which are demonstrated by the two separate dip angles of the layered mat 'sections'.

4 Results of U-series analysis of travertine deposits

4.1 Introduction

Radiometric age analysis of travertine mounds has allowed the timing of CO₂ leakage to the surface along both Little Grand Wash and northern Salt Wash graben faults to be characterised. A total of forty-five samples from both field areas were analysed by U-series dating (Section 1.6) giving a unique data set for investigation of fault related fluid flow later in Chapter 5. Specific problems with U-series dating of travertine are presented in section 4.2. Here the source of uranium present within travertine is considered and the suitability of each travertine facies for U-Th age determination is examined. Section 4.3 discusses in detail the radiometric results with respect to several facets of interest, including; (1) repeat analyses of samples from three separate locations of distinct age in order to check the reproducibility of the analysis; (2) multiple analyses from a single mound in order to determine its lifespan and precipitation rates; (3) dating of separate remnants suspected to comprise the same mound in order to confirm field interpretation; (4) age analysis of layered mat samples in order to determine their suitability for dating and confirm if they are clearly associated with the white banded veins present in the travertine mounds. Spatial variation in $\delta^{234}\text{U}$ of samples, and potential cause of this variation, is discussed in section 4.4. The work carried out within this section provides clues to the potential near-surface fluid flow pathways utilised by the CO₂ charged water creating the travertine.

The travertine U-Th age results allow determination of accurate incision rates in each area; these are presented in section 4.5. Whilst giving the first quantitatively determined incision rates for both sites, this information also permits the calculation of robust estimations of the age of undated mounds along the northern fault of the Salt Wash graben. These ages are used in Chapter 5 to discuss the implications for fluid flow highlighted by the U-series results. In section 4.6 volume estimates of the travertine mounds are presented. This allows for a comparison of travertine deposits, both for individual mounds and total travertine volume, between the two field sites. The results of this section are the basis for calculation of volumes and rates of CO₂ leakage to the surface along the Little

Grand Wash and northern Salt Wash graben faults, which are presented in Chapter 6. The lifespan of each individual mound is also estimated, by combining volume measurements with the minimum lifespan of mound L4 (subsection 4.3.3), which allows for further comparison between the field sites.

The overall results of the above sections are discussed in section 4.7, which also goes into detail on what these results mean for the timing of flow to the surface. Finally, the conclusions of this chapter are presented in section 4.8.

4.2 U-series analysis of travertine deposits

4.2.1 Uranium incorporation into travertine mounds

Uranium is readily transported in ground water mainly as carbonate complexes, whilst thorium hydrolyses readily and precipitates or absorbs on to the matrix material through which the ground water passes (section 1.7.6). Uranium complexes are formed in waters that have passed through aquifers that are capable of contributing Ca^{2+} , CO_3^{2-} , and SO_4^{2-} ions, and which are saturated or supersaturated with respect to calcite, aragonite and/or dolomite (Gascoyne and Schwarcz, 1982). This mainly occurs in areas where the bedrock is a carbonate and ground or surface waters have had extensive opportunity to react with the rock. The dissolved load is controlled by factors such as the temperature, the amount of CO_2 available for dissolution in the water, the presence of other ions which can form stable complexes with calcium and the rate at which water moves through the aquifer (Gascoyne and Schwarcz, 1982).

Surficial spring deposits may be composed of either calcite or aragonite (depending on the molar concentration of Mg^{2+} or SO_4^{2-} , section 3.4.4). Both varieties of calcium carbonate are useable for age determination as all calcium carbonate polymorphs behave similarly with respect to U-series dating (Bischoff and Fyfe, 1968).

4.2.2 Travertine morphologies useful for dating

Travertine mound morphology must be examined in order to determine which travertine facies are suitable for U-Th dating. According to the model of travertine evolution devised by Dockrill (2006), and re-evaluated in section 3.4.7,

mounds are composed of five prominent travertine lithofacies: (1) altered host rock; (2) cemented breccia; (3) layered mats; (4) white banded veins; and (5) brown banded veins. Samples for age determination are selected primarily based on the criteria for U-series analysis outlined in section 1.7.6: they must represent the geological system to be dated, be free of final daughter product during initial formation, and have been a closed system with respect to migration of parent and daughter nuclides since formation.

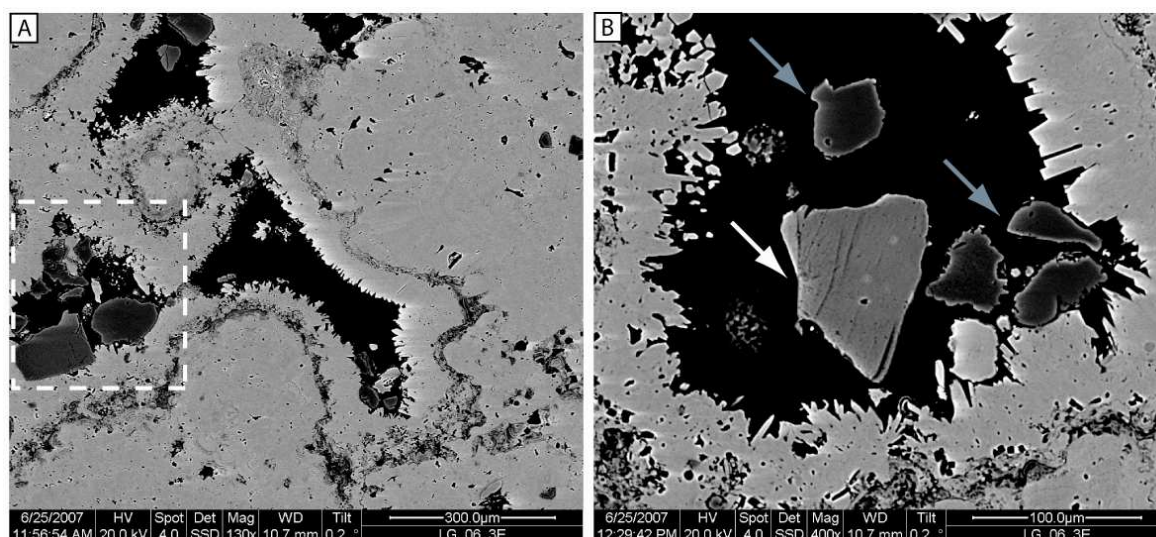


Figure 4.1: EBSD images of layered mats from mound L1.

(A) Shows the shrub like texture of layered mats with micritic calcite crystals radiating outward. Several darker coloured grains, blown in from the surrounding environment, are also present. The white dashed box highlights an example of carbonate overgrowth incorporating these grains into the structure of this layered mat sample. (B) An image of three times increased magnification showing the presence of quartz (grey arrows) and feldspar (white arrow), which carry non radiogenic thorium, within the layered mat.

Carbonate cemented breccia, formed by initial leakage of CO₂ rich fluid to the surface, consists of a such a fine grained clast supported matrix that it is impossible to separate the intergranular carbonate cement from the clasts, which will contain significant detrital ²³⁰Th. Layered mats can prove to be extremely impure. They are generally very porous and permeable because they have been deposited on a mat of vegetation which later decays away, leaving an open framework of casts and moulds (Gascoyne and Schwarcz, 1982). Due to their deposition in an open air environment this facies is prone to detrital contamination by wind, streams, and colluvial transport (Figure 4.1). The extent of this contamination can vary, but since the allogenic material is likely close to secular equilibrium (with respect to [²³⁴U/²³⁸U]) it can be assumed that it carries a significant amount of non-radiogenic ²³⁰Th (section 1.8.3.2). The open, porous

structure and association with algal and cyanobacteria mats can also facilitate sediment trapping. Secondary overgrowths of calcite may occur as calcite-saturated waters continue to percolate through the older travertine deposits, leading to a gradual infill of pore spaces (Gascoyne and Schwarcz, 1982). Another consequence of this relatively open structure is that radionuclides in the U-series may be added or subtracted by water percolating through the rock (Mallick and Frank, 2002).

These components of travertine mound construction are not present in all deposits in the field. Only the most developed mounds that have been eroded to produce to create a clear cross section, such as L4 (section 4.3.3), tend to display the initial breccia stage. Layered mats are more common but are missing from numerous travertine deposits, which have been eroded, along the northern fault of the Salt Wash graben (section 3.5.4).

Brown banded veins represent the latest stage of travertine evolution and consist of thinner bands of aragonite crystals which have been retarded in their growth by numerous iron-rich laminations. This facies is rare across the field areas and the fine layering tends to be quite incohesive with individual crystals easily separating on removal. The fine scale gaps in the boundary between crystals may allow for percolation of meteoric water through the vein especially after exhumation. During their formation episodic fluid flow conditions also created an unstable and alternating environment (Dockrill, 2006). Coupled with the scarcity of brown banded veins these two factors are likely to lead to an open system with respect to migration of nuclides considering the variation in conditions they suggest since the time of precipitation.

White banded veins are common in the field, being present in all ancient travertine deposits. Due to their dense nature, and their formation in fractures and faults (i.e. sub-surface deposition) white banded veins tend to form detritus-free calcium carbonates making samples from this facies ideal candidate for U-Th analysis. This is supported by a study of tectonic movements in Nevada by Szabo et al. (1981) who report dating results from over thirty vein samples that yielded ages in agreement with $^{40}\text{K}/^{40}\text{Ar}$ dating. The fact that this facies consists of pure and clean layers of aragonite means that white banded vein meets all the requirements required for precise U-series dating.

Some mounds only consist of plentiful white banded vein running through altered host rock. In order to confirm these outcrops as true travertine deposits a close association must be demonstrated between the white banded vein and layered mats facies as layered mats conclusively indicate the presence of a fossil mound (section 3.5.4.2). Of the forty ancient samples selected for age determination thirty-seven were of white banded vein facies. A total of three samples from the Little Grand Wash fault consisted of fossil layered mat deposits in order to check its validity for age determination. This work has important implications for locations of travertine accumulation where layered mat facies is abundant but white banded vein facies is absent (such as above the proven CO₂ reservoir at St. Johns, Arizona).

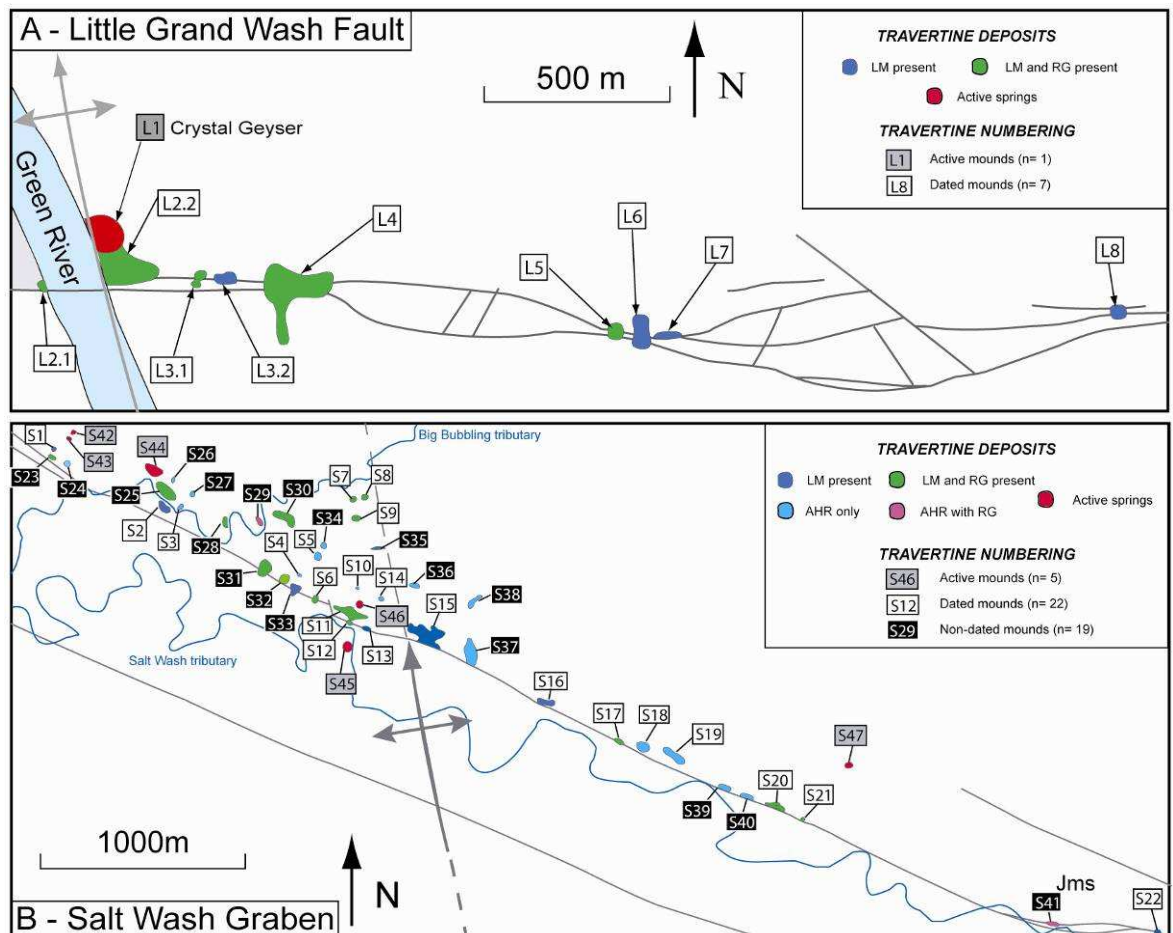


Figure 4.2: Travertine maps of the Little Grand Wash and Salt Wash graben field sites.

Maps (which are adapted from Dockrill, 2006) show the location of mounds, the surface traces of the respective faults and the location of the Green River anticline. The travertine is colour coded to show the breakdown of facies present in each mound. Individual travertine deposits have each been assigned a unique sample identifier which corresponds to the samples numbers shown in Table 4.1 and Table 4.2. For GPS coordinates of mounds see Appendix D.

Mound	Sample	Facies	U- Th age (2 σ with λ)	$\delta^{234}\text{U}(0)$ (2 σ with λ)	Total U (ppm)	Total Th (ppb)	[$^{230}\text{Th}/^{232}\text{Th}$]
L1	LG.06.3E	LM	842 \pm 7	4.594 \pm 0.012	2.263	117.33	2.3
	LG.06.3A	LM*	236 \pm 4	4.410 \pm 0.011	2.682	1.15	86.2
	LG.06.3B	LM*	252 \pm 3	5.114 \pm 0.013	2.237	2.57	36.7
	LG.06.3C	LM*	223 \pm 2	5.355 \pm 0.014	2.316	2.09	44.5
L2.1	LG.06.37A	WBV	5,029 \pm 31	5.118 \pm 0.100	4.539	0.64	2875
	LG.06.37B	LM	8,629 \pm 30	4.366 \pm 0.012	1.655	730	1.5
L2.2	LG.03.50A +	WBV	5,699 \pm 26	3.626 \pm 0.009	6.485	0.39	50459
	LG.03.50A +	WBV	5,060 \pm 4	3.647 \pm 0.009	5.160	0.24	19841
	LG.06.10E	LM	6,927 \pm 22	4.669 \pm 0.012	3.265	236.39	11.1
L3.1	LG.06.8C	WBV	50,890 \pm 390	4.118 \pm 0.018	4.111	1.47	13721
L3.2	LG.06.9D	WBV	49,088 \pm 187	4.421 \pm 0.019	2.160	16.37	499
L4	LG.03.42AD	WBV	113,912 \pm 604	4.012 \pm 0.010	5.076	0.04	905311
	LG.03.42AF	WBV	109,614 \pm 901	5.094 \pm 0.014	4.220	0.06	675748
	LG.03.42AX	WBV	106,526 \pm 544	4.794 \pm 0.011	5.093	0.38	888662
	LG.03.42AZ	WBV	103,172 \pm 1,486	4.896 \pm 0.019	4.754	-	-
	LG.06.7F	LM	114,098 \pm 646	3.716 \pm 0.009	2.556	63.05	13.5
L5	LG.06.5F	WBV	31,217 \pm 297	5.966 \pm 0.033	0.523	13.43	164
L6	LG.03.48F +	WBV	61,274 \pm 504	6.382 \pm 0.024	8.023	0.31	187559
	LG.03.48F +	WBV	56,419 \pm 506	6.268 \pm 0.017	8.962	0.4	170636
L7	LG.06.6C	WBV	75,495 \pm 656	6.257 \pm 0.023	8.299	0.73	93471
L8	LG.03.51Q +	WBV	27,405 \pm 80	7.228 \pm 0.018	5.927	0.64	416542
	LG.03.51Q +	WBV	26,716 \pm 250	7.418 \pm 0.019	7.487	0.08	370026

Table 4.1: Age results of radiometric dating of travertine samples from the Little Grand Wash fault.

Location of mound deposits can be seen in Figure 4.2. Facies acronyms stand for layered mat (LM) and white banded vein (WBV), with LM* signifying samples precipitated from modern waters in the lab. '+' Indicates repeat analysis of a single sample.

Mound	Sample	U-Th age (2 σ with λ)	$\delta^{234}\text{U}(0)$ (2 σ with λ)	Total U (ppm)	Total Th (ppb)	[$^{230}\text{Th}/^{232}\text{Th}$]
S1	SW.06.12E	38,906 \pm 161	2.021 \pm 0.005	3.301	0.15	367166
S2	SW.03.65N	60,188 \pm 443	4.045 \pm 0.011	7.314	-	-
S3	SW.06.14E	29,028 \pm 107	4.345 \pm 0.011	7.052	0.15	139424
S4	SW.06.22A	291,307 \pm 5,594	4.180 \pm 0.042	3.025	3.54	6820
S5	SW.06.16B	413,474 \pm 15,127	6.572 \pm 0.221	2.413	0.11	212447
S6	SW.06.23A	13,068 \pm 59	3.341 \pm 0.009	6.020	4.74	1442
S7	SW.06.17D	100,378 \pm 562	5.365 \pm 0.013	4.909	0.67	62991
S8	SW.06.18C	106,088 \pm 660	5.275 \pm 0.013	4.746	0.02	168935
S9	SW.06.19C	135,135 \pm 1,142	5.212 \pm 0.015	6.245	0.01	828530
S10	SW.06.27A	51,290 \pm 248	4.435 \pm 0.011	3.201	2.99	5102
S11	SW.03.56H	92,792 \pm 1,118	4.840 \pm 0.016	4.702	0.08	2217
S12	SW.03.53K	28,375 \pm 238	5.032 \pm 0.014	0.792	0.24	11154
S13	SW.06.24B	10,797 \pm 42	4.911 \pm 0.012	3.197	49.25	91
S14	SW.06.25C	34,971 \pm 142	5.309 \pm 0.013	4.276	0.41	44315
S15	SW.06.31A	65,085 \pm 334	2.842 \pm 0.008	2.312	7.50	1125
S16	SW.06.29A	57,014 \pm 412	5.497 \pm 0.014	3.985	13.49	1871
S17	SW.06.30B	4,792 \pm 30	3.137 \pm 0.008	1.696	8.15	89
S18	SW.02.36J	112,804 \pm 634	6.778 \pm 0.016	2.387	0.05	462932
S19	SW.06.32A	130,666 \pm 831	6.749 \pm 0.016	2.574	0.36	85363
S20	SW.06.33A	110,000 \pm 634	6.796 \pm 0.016	2.227	0.57	44284
S21	SW.06.34A	116,788 \pm 691	7.154 \pm 0.017	2.140	0.89	28864
S22	SW.06.36A	9,749 \pm 45	6.960 \pm 0.018	2.184	1.80	2174
S45*	SW.06.28A	285 \pm 5	2.833 \pm 0.007	2.218	107.6	2.9

Table 4.2: Age results of radiometric dating of travertine samples from the northern fault of the Salt Wash graben.

All analysed samples are of white banded vein facies bar sample S45 which was a layered mat sample precipitated from modern Ten Mile Geyser waters in the lab. For location of mound deposits see Figure 4.2.

4.3 Discussion of U-series age results

4.3.1 Introduction

A total of forty-five U-series analyses were carried out on samples from both field areas. Results of analyses are shown in Table 4.1 and Table 4.2. The Little Grand Wash fault, with seven distinct ancient travertine mounds and one active deposit, was covered by high resolution sampling. Of the twenty-two analyses from this site four were carried out on layered mat facies, three on modern precipitates from water samples, and fifteen analyses on white banded vein samples from eight distinct mounds (Table 4.1). To assess the reproducibility of travertine ages three samples from this area were used for repeat analysis (Table 4.3). Along the northern fault of the Salt Wash graben forty-one fossil travertine mounds and six actively precipitating springs are present (Section 3.5.2). Twenty-three samples were analysed from the northern fault of the Salt Wash graben (Table 4.2). These comprised one water sample from Ten Mile geyser and the rest from individual ancient mounds in order to gain the best spatial resolution possible for the northern fault of the Salt Wash graben.

4.3.2 Reproducibility

Repeat measurements were carried out on three samples from mounds of distinct age (L2, L6, and L8; Table 4.3) to test that sample selection procedure and subsequent preparation for analysis was sound. Considering the small analytical errors on ages the results demonstrated good levels of reproducibility, with repeat sample ages within a range of 2.5 to 11% of each other (Table 4.3, Figure 4.5). In general small differences in repeat isotopic measurements may reflect natural variation in the sample, variation in the measurement process between analyses, variation inadvertently caused by the person making the measurement, or a combination of these factors (Davis, 2002). New work utilising U-series dating suggests that the main factor in obtaining precision for U-Th dates depends on the samples and not the mass spectrometry (Thompson, 2010). Natural variation within the white banded vein samples is therefore likely to be the main reason for the discrepancies between ages. The coral age result reported in Chapter 2 (section 2.5), which provided a repeat age within analytical error (158.1 ± 2.9 and 153.7 ± 1.6 ka), was produced from a completely dissolved *C.caespitosa* coralite

sample. In contrast, subsamples of individual white banded veins were cut by rock saw (to ~1 g cubes), crushed into a coarse powder, and dissolved in nitric acid for dating (section 1.9.2). Repeat specimens came from adjacent saw-cut cubes, care was taken to sample from the same lamination. It is possible that these samples could have come from a relatively heterogeneous section of the vein, so that the difference in ages of adjacent samples reflects real changes in age of the vein material. Further detailed dating of a single vein would be necessary to constrain the age distribution properly, in particular to confirm if an individual vein lamination has a single age.

During ICP-MS analysis younger samples are more prone to systematic sources of error. This is because ^{230}Th becomes a more difficult measurement due to the low amount of ^{230}Th within the samples. The low ^{230}Th content makes younger samples susceptible to problems with blanks. Any small variation in the blank measurement, which is not corrected for, may cause exaggerated discrepancies in the ages of younger samples. This effect is evident as the repeat of the youngest sample, L2, produced the worst reproducibility. Older samples are less likely to provide good reproducibility as there is an increased chance that the U-Th chronometer has been affected (section 1.7.6), again the effects of this can be seen when comparing samples from travertines L6 and L8 in Table 4.3.

Mound	Sample	U- Th age	2σ (with λ)	%R	%R (2σ)
L2	LG.03.50	5,699	26	11.2	10.4
	LG.03.50	5,060	4		
L8	LG.03.51	27,405	80	2.5	1.6
	LG.03.51	26,716	25		
L6	LG.03.48	61,274	504	7.9	6.3
	LG.03.48	56,419	506		

Table 4.3: Table of repeat U-series analysis.

This table shows the repeat analyses of three samples of distinct age from the Little Grand Wash. The reproducibility of age analysis is shown as a percentage (R%) and represents the difference between the two repeats. Reproducibility including the error envelopes on the ages is also included (%R with 2σ).

4.3.3 Detailed study of travertine L4

Multiple samples were analysed from mound L4 as it is the best preserved mound in the field area and demonstrates clear examples of all of the travertine facies (subsection 3.5.4.1; Figure 4.3). A total of five separate samples were dated from this mound incorporating four white banded vein samples and a single layered mat sample (Figure 4.3). The four vein samples came from three separate veins within the mound with two of the samples coming from the inner and outer edge of the main vein. This was done to gain an understanding of the order of vein precipitation and to find out how long it takes for an individual vein to form. The two samples from the main vein, LG.03.42AF and LG.03.42AD (B and C on Figure 4.3) provided ages of $113,912 \pm 604$ for the outside edge of the vein and $109,614 \pm 901$ for the inner edge giving a time span for of precipitation of $4,298^{+604}_{-901}$. Due to the banded nature of the veins (Figure 3.10) it is likely that vein growth occurs stochastically over several deposition events. Using the ages of the inner and outer edges of this 2.5 m thick vein therefore gives a time averaged precipitation rate of 0.58 mm per year. When errors on the two ages that bracket this vein are taken into account the time averaged precipitation rate ranges from between 0.51 and 0.74 mm per year.

The other two dated white banded vein samples were taken from thin horizontal veins within the transitional zone of the travertine (Figure 4.3). Sample LG.03.42AZ, adjacent to the main vein (D on Figure 4.3), gave an age of $103,172 \pm 1,486$ making it $6,442^{+901}_{-1,486}$ years younger than the main vein. Sample LG.03.42AX from the boundary of the layered mats and transitional zone (A and Figure 4.3) produced an age of $106,526 \pm 175$. This demonstrates that veins higher in the sequence are not always the youngest and that veining searches out areas of weakness in the mound to exploit. Between the oldest and youngest samples from this mound an age difference of $10,740^{+604}_{-1,486}$ years is apparent. This gives a minimum estimate of the lifespan of the deposit and tells us that leakage at a single point on the fault may be active for a minimum of ~11,000 years.

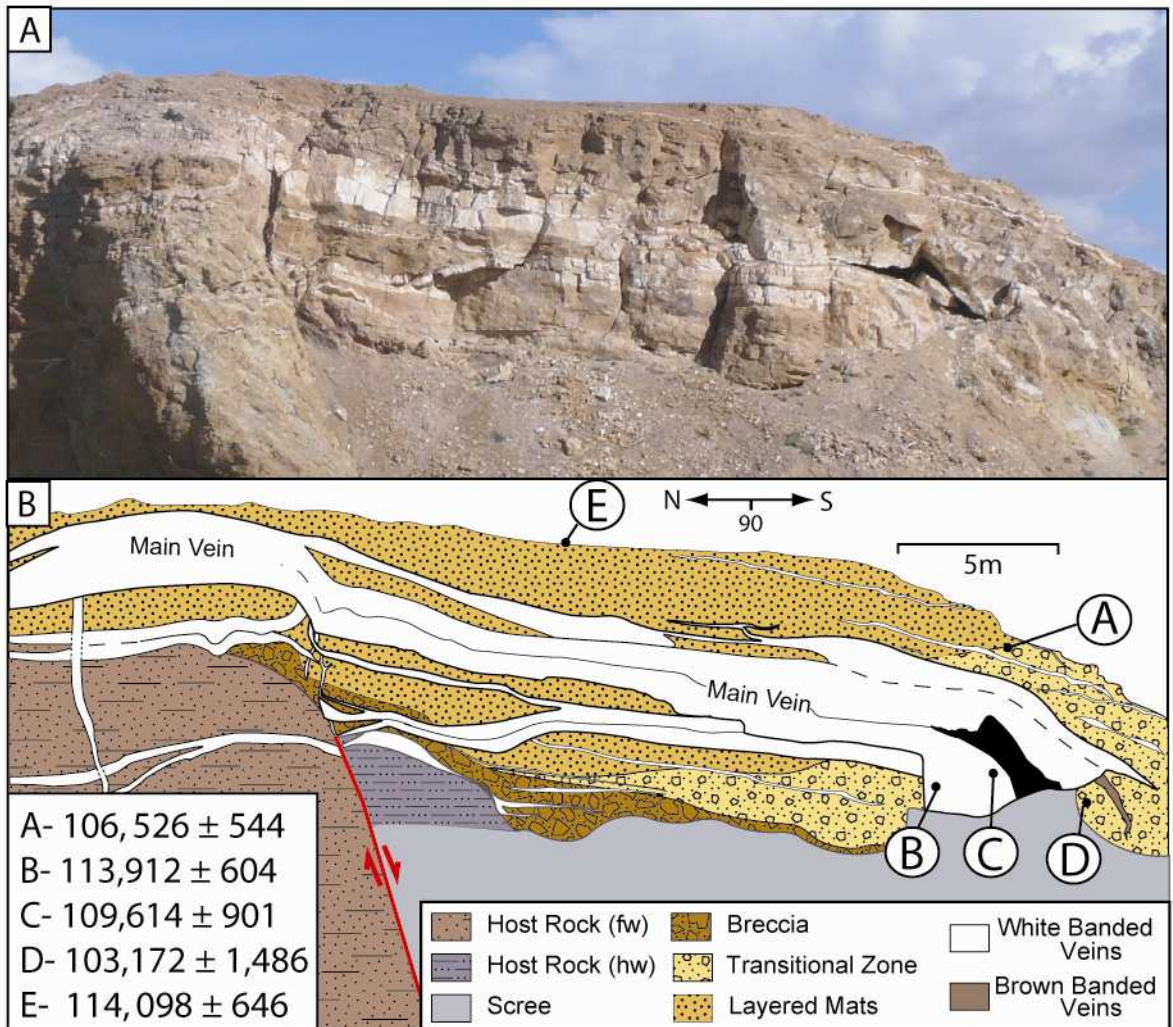


Figure 4.3: Field image and schematic of the L4 travertine mound.

(A) Shows a photograph of this mound taken looking east. (B) Schematic of mound L4 (after Dockrill, 2006) showing location of samples used for U-series analysis. Inlet shows ages complete with error, with A to D representing white banded vein samples (with B and C being from the same vein) and E representing the layered mat sample. Fault is shown in red with the footwall on the left hand side and the downthrown hanging wall to the right.

4.3.4 Age analysis to support field observations

Travertine mounds L2 and L3 both contain two distinct sections which were believed to be correlated due to field relationships. The two segments of L2 are located at the same elevation either side of the Green River. In the middle of the river a small pile of white banded vein chunks is visible between the two, suggesting that both segments may represent the same mound (Figure 4.4B). Age dating confirmed the hypothesis with segment L2.1 giving an age of $5,029 \pm 29$ years and a repeat analysis of segment L2.2 providing ages of $5,699 \pm 8$ and $5,060 \pm 38$ years (giving an average of $5,380 \pm 23$ years). The difference between the age of L2.1 and the average of L2.2 is 6.5% (Table 4.4), which is below the reproducibility shown during the analysis of L2.2 (11%-section 4.3.2). The two sections of mound L3 are only separated by ~10 m and sit at a similar elevation surrounded by the same scree slope (Figure 4.4A). A slight dip in the topography of the scree slope between the segments implies that the centre of a once complete mound may have been removed by erosion. The closely matching age results of these two segments, with L3.1 and L3.2 produce dates of $50,890 \pm 351$ and $49,088 \pm 96$ (average of $49,989 \pm 224$), which are within 3.5% of each other and further suggest that these remnants are part of the same mound.

Mound	Remnant	Sample	U-Th age	2σ (with λ)	Age %	Age % (2σ)
L2	L2.1	LG.06.37A	5,029	31	6.5	6.5
	L2.2	LG.03.50A	5,380	33		
L3	L3.1	LG.06.8C	50,890	390	3.5	2.4
	L3.2	LG.06.9D	49,088	187		

Table 4.4: U-Th ages for testing field observations.

Age results for mounds L2 and L3. The closeness of age analysis from the separate remnants of these mounds is shown as the percentage difference (Age %) between the two ages. Percentage difference including the error envelopes on the ages is also included (Age % with 2σ).

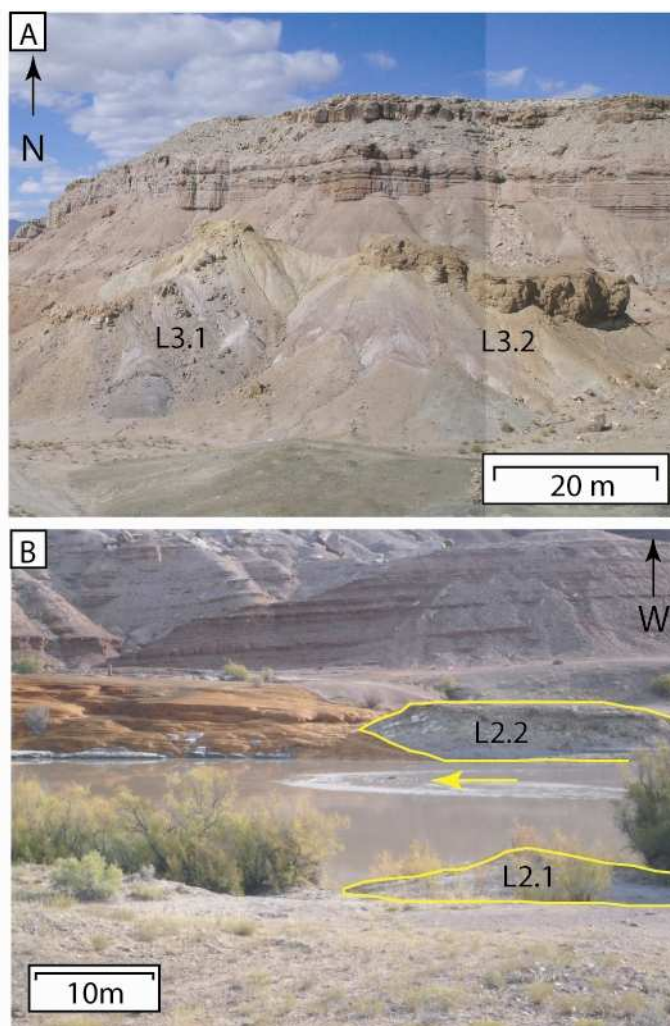


Figure 4.4: Field images of mounds L2 and L3.

(A) The two remnants of travertine deposit L3. (B) The remnants of deposit L2 separated by the Green River. A pile of white banded vein segments, which form a small island when the river level is low, is indicated by the yellow arrow. The location of these deposits is shown in Figure 4.2.

4.3.5 Layered mat analysis

Age analysis of several layered mat samples was carried out to check the feasibility of this facies for U-Th dating and to determine the relationship of layered mats with white banded veins. This latter point is necessary as a key problem with travertine in the Salt Wash graben field area is that in nearly half of the mounds only veining and altered host rock are present and there is no clear evidence of layered mat facies (Table 3.2). To interpret these as the eroded remnants of travertine mounds the white banded vein present in complete mounds must be demonstrated to be associated with the layered mat facies. The supporting evidence from field observations have been discussed previously (Section 3.5.4.2) so the latter part of this section will examine possible geochemical trends which may further support this claim.

4.3.5.1 Suitability of layered mat facies for age determination

The modern formation of the Crystal Geyser travertine (L1) shows us that the hemi-spherical pools of the precipitating layered mats on the surface of the deposit are open to contamination from the surrounding environment and may entrain windblown deposits/debris in their layers. Preparation of samples included an extra stage of hydrogen peroxide addition and in some cases the use of perchloric acid to remove the large amount of organics present.

Mound	Sample	Facies	U-Th age	2 σ (with λ)	Age %	Age % (2 σ)
L2.1	LG.06.37A	WBV	5,029	31	41.8	41.2
	LG.06.37B	LM	8,629	31		
L2.2	LG.03.50A	WBV	5,380	33	22.3	21.6
	LG.06.10E	LM	6,927	22		
L4	LG.03.42AZ	WBV	103,172	1,486	9.6	7.8
	LG.03.42AD	WBV	113,912	604	0.2	-
	average	WBV	108,306	884	5.1	3.8
	LG.03.51	LM	114,098	646		

Table 4.5: Comparison of layered mat and white banded vein results.

Analyses of layered mat and white banded vein specimens from the same mounds, with layered mat results highlighted in yellow. The closeness of age analysis from the two different facies is shown as the percentage difference (Age %) between the two ages. Percentage difference including the error envelopes on the ages is also included (Age % with 2 σ). For mound L4, which has multiple dated samples, the percentage difference in age is shown between the layered mat sample and the youngest, oldest and average of all white banded vein sample results from this mound.

A sample from the modern day L1 mound produced an age of 842 ± 7 years. The Glen Ruby #1-X well that created the Crystal Geyser was drilled in 1935 meaning that age analysis from a 'clean' sample from this mound should range from 0 – 72 years. The radiometric age result of this sample was 842 ± 7 years (Table 4.1). A [$^{230}\text{Th}/^{232}\text{Th}$] of 2.3 for this sample revealed that it had been significantly contaminated with non radiogenic ^{230}Th . As outlined in subsection 1.8.3.2, activity ratios of less than 15 to 20 have been found to significantly affect the age analysis of a sample by making it appear older.

Samples analysed from L2.1 and L2.2 produced ages of $6,927 \pm 14$ and $8,629 \pm 26$ years, which are older than the white banded vein specimens from the same sites by 22.3 and 41.8%. The percentage difference in age between layered mats and white banded veins is between two and four times greater than the repeat percentage demonstrated by L2.2 (section 4.3.2). Again [$^{230}\text{Th}/^{232}\text{Th}$] of 11.1 and 1.5 (Table 4.1) suggests the presence of a significant level of detrital thorium leading to an apparently older age result.

4.3.5.2 Geochemical association of layered mats and white banded vein

As has been determined above, the presence of significant amounts of non-radiogenic thorium within layered mat facies renders this facies inappropriate for age determination. Therefore any comparison of the ages of layered mats and white banded veins from the same mound is not valid. However, the supporting chemistry from the U-Th age analysis technique, specifically the ${}_0\delta^{234}\text{U}$, can be used to compare the uranium content of the formation waters of each facies. On comparing the ${}_0\delta^{234}\text{U}$ of layered mats with white banded veins samples it can be seen that these are similar for the same mound (Figure 4.5). For the modern mound, L1, the results of the travertine precipitated in the field (sample LG.06.3E-Table 4.1) and the average of the travertine samples precipitated in the lab (3A-3C) for $\delta^{234}\text{U}$ are 4.594 ± 0.012 and 4.960 ± 0.013 respectively. The ${}_0\delta^{234}\text{U}$ results of L2 averaged out for each facies gave similar values of 4.517 ± 0.012 for layered mats and 4.130 ± 0.013 for white banded vein. Mound L4 produced an average $\delta^{234}\text{U}$ of 4.699 ± 0.014 for the four white banded vein samples which is higher than the ${}_0\delta^{234}\text{U}$ of 3.716 ± 0.008 for the single layered mat sample analysed. The white banded vein samples for this mound range over a total of 10,740 years which is far greater than the 670 years difference between the oldest and youngest L2 white banded vein samples. On comparison of the oldest white banded vein specimen for L4 and the layered mat specimen, whose ages overlap within error, ${}_0\delta^{234}\text{U}$ results are 4.012 ± 0.002 and 3.716 ± 0.009 . Relatively closely matching ${}_0\delta^{234}\text{U}$ of white banded vein and layered mats within the same mound suggests that white banded vein and layered mats are closely associated components of an ancient travertine mound that precipitated from the same source waters.

4.4 Variation of uranium chemistry between mounds

4.4.1 Introduction

Travertine mounds in the field are relatively rich in uranium compared to normal continental crustal levels (average 1.4ppm). Concentrations of 2-4 ppm are common and values up to 8ppm occur. The validity of U-Th dating on coral specimens is checked using ${}_0\delta^{234}\text{U}$, which in a closed system reflect the composition of seawater that has a known and consistent value, $1.145 \pm 2\%$,

through time (Section 2.5.2). Terrestrial carbonates, such as travertine, cannot be checked in this way as the $\delta^{234}\text{U}$ of groundwater can vary from 0.5 to above 30 (Frolich, 1990). Other checks such as purity of sample and $[\text{}^{230}\text{Th}/\text{}^{232}\text{Th}]$ must be used in this case to confirm the presence of a closed system. White banded veins from the present study provide pure aragonite samples with high $[\text{}^{230}\text{Th}/\text{}^{232}\text{Th}]$ and therefore demonstrate U-Th decay within a closed system. As such, the variable ${}_0\delta^{234}\text{U}$ across the samples can be used to give information on the composition of the fluid with any variation suggesting evolution of fluid through time or spatial discrepancies. The ${}_0\delta^{234}\text{U}$ of the dated samples varies from 3.626 ± 0.009 to 7.418 ± 0.019 in the Little Grand Wash and from 2.021 ± 0.005 to 7.154 ± 0.017 in the Salt Wash graben.

4.4.2 Variation in ${}_0\delta^{234}\text{U}$

The considerable variation of ${}_0\delta^{234}\text{U}$ suggests that the composition of the ground water has changed quite considerably between the travertine deposits. On a plot of ${}_0\delta^{234}\text{U}$ against age of the sample a random scattering of points occurs suggesting that there is no trend with time (Figure 4.6A), ruling out variation of $\delta^{234}\text{U}$ with evolution of fluid composition over the last 413 ka. Plotting ${}_0\delta^{234}\text{U}$ results against the distance from the axial trace of the Green River anticline reveals a spatial signal with ${}_0\delta^{234}\text{U}$ increasing from west to east (Figure 4.6B; C).

This pattern is clearly evident in the Little Grand Wash where a trend line of best fit has an $R^2 = 0.96$. The trend line for the northern fault of the Salt Wash graben has an R^2 of a little under 0.5 as it contains a couple of low lying outliers. The similar ${}_0\delta^{234}\text{U}$ of travertine mounds in close proximity, such as L5 to L7 and S7 to S9 (Table 4.1; Table 4.2; Figure 4.6), further supports a spatial trend in the initial uranium composition of the precipitating fluids.

The increasing ${}_0\delta^{234}\text{U}$ to the east signifies an increase in ^{234}U within the groundwater supplying the travertine mounds. Uranium 234 is a particularly mobile nuclide in aqueous conditions as it is oxidised to a hexavalent state (+6) and preferentially leached from rocks over thorium. In addition alpha recoil, the process of ejection and subsequent decay of the short lived ^{234}Th isotope, can increase the ^{234}U concentration of surrounding waters. Alpha recoil also has the effect of damaging the crystal lattice hosting the ^{234}U making it more vulnerable to leaching than neighbouring atoms (Section 1.7.6).

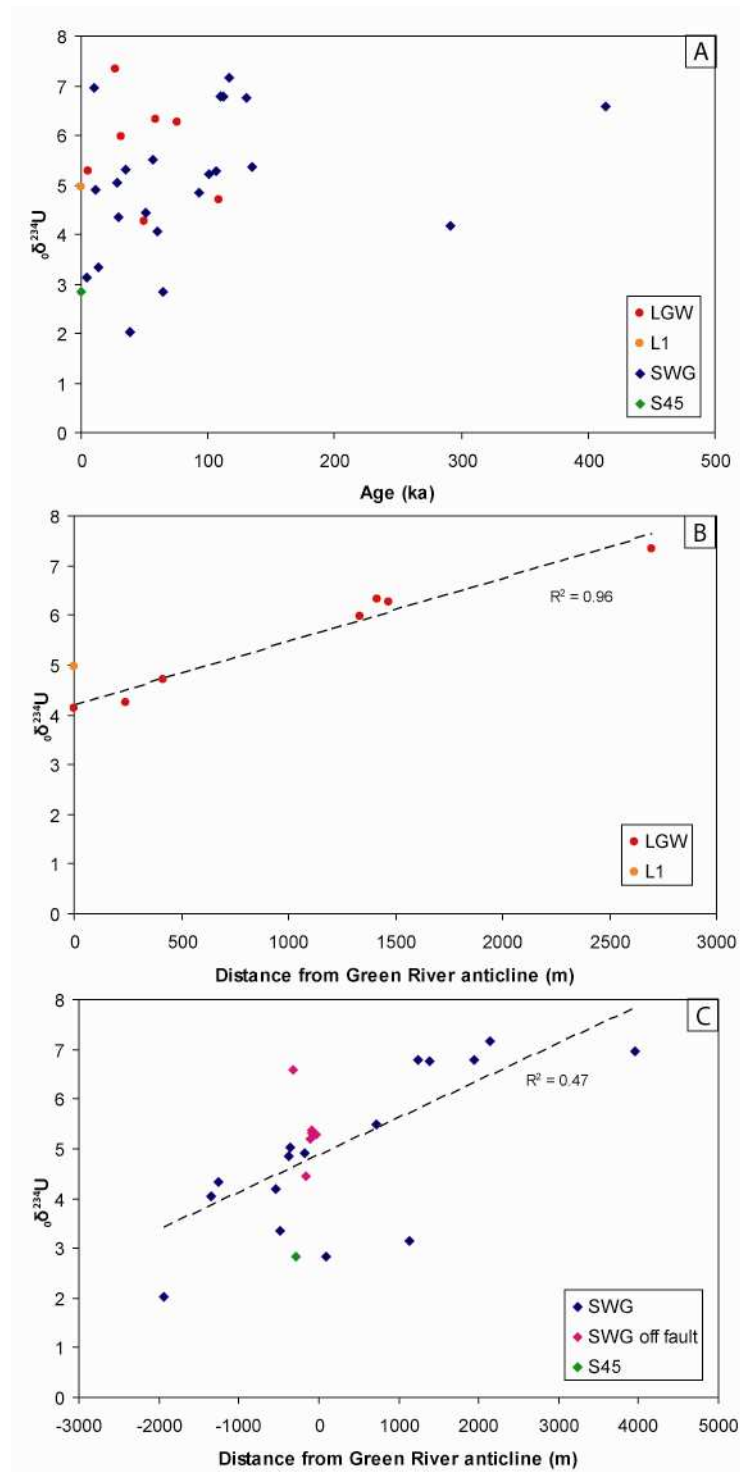


Figure 4.6: Variation of $\delta^{234}\text{U}$ vs. time and space.

(A) $\delta^{234}\text{U}$ against age of sample (ka). Samples from both areas are plotted on the graph with modern waters from mound L1, the Crystal Geyser, and S45, Ten Mile Geyser, shown by orange and green points respectively. (B) Little Grand Wash fault and (C) northern fault of the Salt Wash graben plots showing $\delta^{234}\text{U}$ against distance from the Green River anticline (m) for each field site. Colours for points are the same as with (A) with the addition for a distinction of travertine in the Salt Wash graben that occur away from the fault (pink diamonds).

4.4.3 Spatial trend of $\delta^{234}\text{U}$

Two models are presented for the cause of the increasing trend of $\delta^{234}\text{U}$ from west to east (Figure 4.7). Model A involves mixing of old deep brine water carrying a low $\delta^{234}\text{U}$ and meteoric waters carrying a high concentration of ^{234}U in the Navajo aquifer. Model B is less dependant on mixing and involves increased leaching of ^{234}U above the aquifer as flow paths to the surface increase. Both models imply a source of old brine water from depth with a low $\delta^{234}\text{U}$, possibly close to secular equilibrium ($\delta^{234}\text{U} = 1$), migrating up the faults and into the Navajo aquifer somewhere to the west of the travertine deposits.

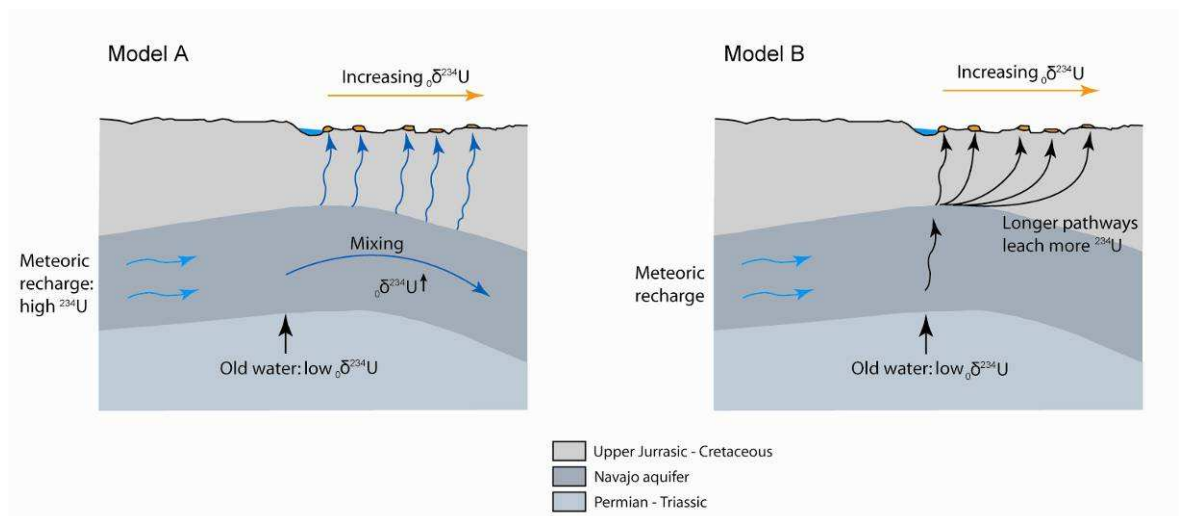


Figure 4.7: Conceptual models for observed variations in $\delta^{234}\text{U}$ chemistry

Cartoon cross section running parallel to the Little Grand Wash fault. Model A involves leaching of ^{234}U by meteoric waters sourced from the San Rafael Swell. In this case mixing with low $\delta^{234}\text{U}$ brine waters (which flow into the Navajo aquifer from depth) is a gradual process from west to east. Multiple breaches through the Carmel Formation top seal allow ground waters of various $\delta^{234}\text{U}$ compositions to migrate to the surface. Model B involves old brine waters with low $\delta^{234}\text{U}$ to migrate from depth straight through the Navajo aquifer to a single leak point in the Carmel Formation caprock. Fluid pathways that travel further to the east are longer and therefore have the opportunity to leach more ^{234}U from the sedimentary sequence that they travel through.

Model A centres on mixing within the Navajo aquifer, which is the main source of the emanating waters that supplied the travertine mounds. The Navajo aquifer, which is at a depth of 600-800 m in the field (Shipton et al., 2005), is charged by meteoric water in the San Rafael Swell where the rocks outcrop ~ 35km west of the field areas. Decreasing potentiometric head in the Navajo aquifer from the San Rafael swell eastwards demonstrates that regional ground water flow is coming from the northwest, approximately parallel to the strike direction of the faults (Hood and Patterson, 1984). Leaching of ^{234}U from the sandstone along this

travel path may be providing meteoric water of high $\delta^{234}\text{U}$ to mix with the influx of low $\delta^{234}\text{U}$ from deep brines into the aquifer close to the field areas. Increased mixing of brine with meteoric water down the regional flow direction to the west should result in an increased meteoric signal as $\delta^{234}\text{U}$ from younger waters becomes increasingly mixed with $\delta^{234}\text{U}$ from older brine waters. Unfortunately I have found no records of the uranium concentration of the sedimentary rocks within this aquifer, though general estimates for sandstones which have uranium in secular equilibrium range from 0.45- 3.2ppm (Levinson, 1980) to 1ppm (Frolich, 1990).

High uranium content has been ascribed to Permian and Triassic rocks in the area such as the Kaibab Limestone of the Permian Cutler formation, Sinbad Limestone of the Moenkopi formation and the Moss Back member of the Chinle Formation (Doelling, 1967; Morrison and Parry, 1988); whilst uranium ore bodies are common in upper Jurassic strata such as the Salt Wash and Brushy Basin members of the Morrison Formation (Buranek, 1942; Trimble and Doelling, 1978; Mohammed, 1986). Uranium ore bodies have also been mentioned in connection to the Navajo in southern Utah (Beltier et al., 2005) and Wingate sandstone at Temple Mountain in the San Rafael Swell (Morrison and Parry, 1988). Considering that Temple Mountain is situated in the south east of the San Rafael Swell, directly between the Swell and the Salt Wash graben, there could potentially be ore bodies present near the source of the meteoric water for the Navajo aquifer. This could provide a highly concentrated source of uranium, up to 3,000ppm (Doelling, 1969), for the water to pass through and leach.

Model B involves an increase in $\delta^{234}\text{U}$ to the east due to interaction of fluid escaping out of the Navajo aquifer with rock it encounters on its way to the surface. This would mean that leakage from the Navajo aquifer is occurring at a single or series of proximal points to the west of the travertine mounds, with more easterly travertine deposits having a higher $\delta^{234}\text{U}$ as a result of the fluid using a longer pathway to reach the surface. These longer pathways give the opportunity for fluid to potentially leach more ^{234}U from sandstones and shales in the layers above the aquifer. The strata between the Navajo aquifer and the surface in the footwalls of the faults include the inter-layered shales and limestones of the Carmel Formation, the Entrada Sandstone (which has a shale rich base) and the Curtis formation sandstone in the Salt Wash graben, whilst the less eroded

sequence of sediments at the Little Grand Wash also includes the Summerville formation. Given the general uranium concentration of sandstone, 0.45-3.2ppm, and concentrations of 2.2ppm for limestone and 4.5ppm for shale (Frolich, 1990) the rocks above the aquifer could provide a plentiful source of uranium from which to leach ^{234}U .

4.4.4 Analysis of modern waters

Three water samples were collected in the field during one eruption cycle of the Crystal Geyser (L1) and from all of the springs in the Salt Wash graben at varying points of the eruption cycle. Of the Salt Wash graben samples the 10 Mile Geyser (S45) water was chosen for analysis because the sample was from the actively flowing spring vent. Crystal Geyser samples comprised of pre, during and post eruption waters. Water was collected using 0.5 litre air-tight bottles. After six months of refrigeration it was found that travertine flakes had precipitated in these bottles (Table 4.1 and Table 4.2). After analysis of the waters on a Quadripole ICP-MS returned values of zero for uranium content, the precipitated travertine was removed from the bottles dried down and analysed on a MC-ICP-MS (Section 1.9.4.3).

Results and descriptions of these samples are given in Table 4.1 and Table 4.2. Ages ranged from 223 ± 2 to 252 ± 3 years for the Crystal geyser (L1) and 285 ± 5 for Ten Mile geyser (S45), giving ages that are older than the true ~ zero age of the precipitated carbonate. As these samples have very low ^{230}Th content these results could be due to blank problems (section 4.3.2). Alternatively these ages could be the result of low $[\text{}^{230}\text{Th}/\text{}^{232}\text{Th}]$. The Ten Mile geyser sample produced an activity ratio of 2.9 and the results of the Crystal Geyser samples ranged between 37 and 86. Although above the 15-20 limit thought to affect age dating (section 1.8.3.2) the Crystal Geyser activity ratios are similar to the *C. caespitosa* sample ($[\text{}^{230}\text{Th}/\text{}^{232}\text{Th}] = 91$) known to have non-radiogenic thorium contamination from the Gulf of Corinth study (section 2.5.4). These activity ratios are also well below the $[\text{}^{230}\text{Th}/\text{}^{232}\text{Th}]$ recorded for white banded vein samples and therefore have higher detrital ^{230}Th present (Table 4.1 and Table 4.2).

Alternatively the age results of the freshly precipitated travertine may provide an age for mobilisation of uranium in the ground waters supplying the geyser. The thorium present is potentially a result of decay of ^{234}U in the water as

it flows from source to site of precipitation, with either the active flow of water keeping the thorium in suspension or the thorium becoming bound in small insoluble particles present in the water (Section 1.7.6.3). If this is the case then the ages provided by the water samples may represent the travel time from source of the waters to deposition of travertine. The waters supplying the springs are 90% meteoric (Wilkinson et al, 2008) and are likely sourced from the San Rafael Swell 35km to the west where the Navajo aquifer outcrops. Combining this distance with the recorded ages provides a flow rate of 3.9 to 4.9×10^{-6} m/s which is a typical rate for a sandstone aquifer (Anderson, 2007).

4.5 Age estimation of un-dated travertine

4.5.1 Introduction

In the field areas ancient travertine mounds cap buttes of varying elevation above the general topography. U-series dating of travertine mounds has shown that older mounds occur at higher elevations than younger mounds (Figure 4.9). This provides a qualitative check on the age dating technique as mounds with common base level should give ages that agree with their stratigraphic order. However due to the differing extents of erosion on each mound, with some missing layered mat deposits, it is hard to find a common point from the mound facies alone that represents base level during precipitation of each mound. In addition to travertine facies numerous mounds in both the Little Grand Wash and Salt Wash graben also contain well cemented ancient river gravel terraces (Figure 4.11). These gravels have been syn-depositionally cemented below the mound by passing bodies of flowing water, providing a key indicator of base level when the travertine was actively precipitated. The slopes of the better-preserved terrace landforms indicate transport directed from the local Morrison slopes which suggests that these terraces are composed of piedmont gravels (Joel Pederson, personal communication; section 5.2.1.2). The immature sediment texture, poor sorting and local composition of clasts suggests that the cemented gravels once belonged to the tributaries of the Green River that drain each field area (Figure 4.8 and Figure 4.10).

Measurement of the elevation of cemented terraces above the current elevation of the nearest drainage allows a calculation of incision rates for individual

mounds, which when plotted together for each field area gives an overall incision rate for the Little Grand Wash (Figure 4.8) and Salt Wash graben field sites (Figure 4.10). All elevation measurements were carried out using a Trimble differential GPS.

4.5.2 Incision on the Little Grand Wash

In the Little Grand Wash four travertine mounds have cemented piedmont gravel from the Little Grand Wash tributary (Figure 4.8, Figure 4.11, Table 3.2). The elevation of these gravels was measured relative to the closest point of the tributary. The Little Grand Wash travertine river gravels are directly related to the Little Grand Wash tributary by palaeo-current directions and the relatively fine size and nature of the clasts present within them. Some locations include finer-grained gravel which is likely to be the result of small run-off channels coming directly from the Morrison cliffs to the north akin to the present day. A series of six river terraces is present on the west bank of the Green River. These terraces generally obscure the fault and possibly any extent of travertine mounds present on this side of the river. The river terraces mainly consist of Green River mainstream gravels stacked one on top of the next, with the occasional piedmont deposit present (Section 5.2.1.2). The clearest example of gravel deposits is provided by the oldest mound, L4, where a large L-shaped 'tongue' ~70 m in length stretches out from the southern end of the mound and then turns west (Figure 4.11). Today the Little Grand Wash tributary has its mouth just ~600 m south of this older remnant (Figure 4.8), as it currently flows from east to west it must have swept to the north of its present location ~114 ka ago to leave these deposits. The elevation of this piedmont terrace is similar to the stratigraphic horizon of the M4 gravel on the west bank of the river so I have labelled it 'P4'. The P4 gravel was right at the palaeo-mouth of the tributary and at the same elevation as the mainstream Green River during its deposition, which makes it a proxy for the mainstream Green River. An incision rate of 0.342 m/ka demonstrated by comparison of the elevation of these terraces against the age of their associated deposit (Figure 4.9) therefore provides an incision rate for the Green River itself in this location.

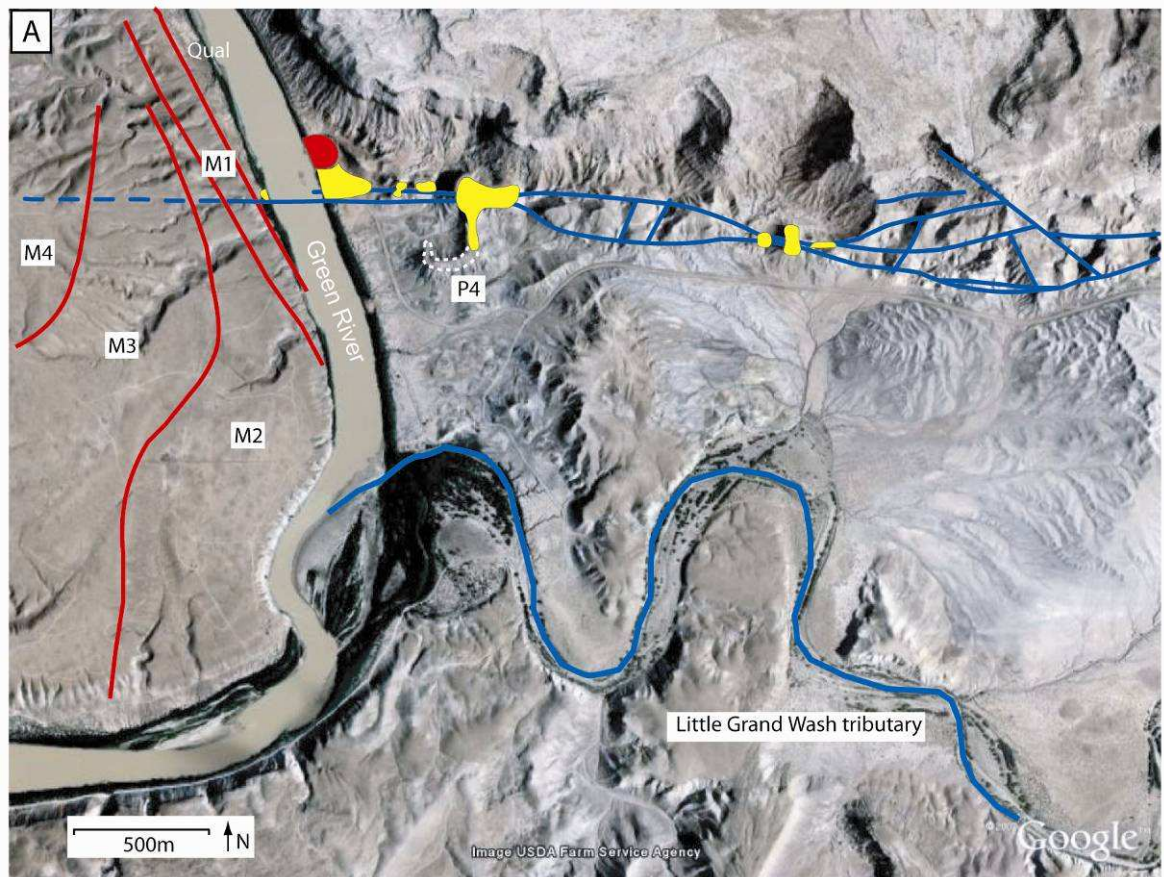


Figure 4.8: Satellite image of the Little Grand Wash tributary.

The image, provided by Google Earth, shows the tributary in relation to the Green River and travertine deposits. The Little Grand Wash tributary is highlighted in blue, ancient travertine in yellow, active travertine in red and the fault in navy blue. Also indicated are the succession of mainstream Green River gravels on the west bank (in red) and the location of the P4 terrace associated with the L4 travertine deposit (white dashes).

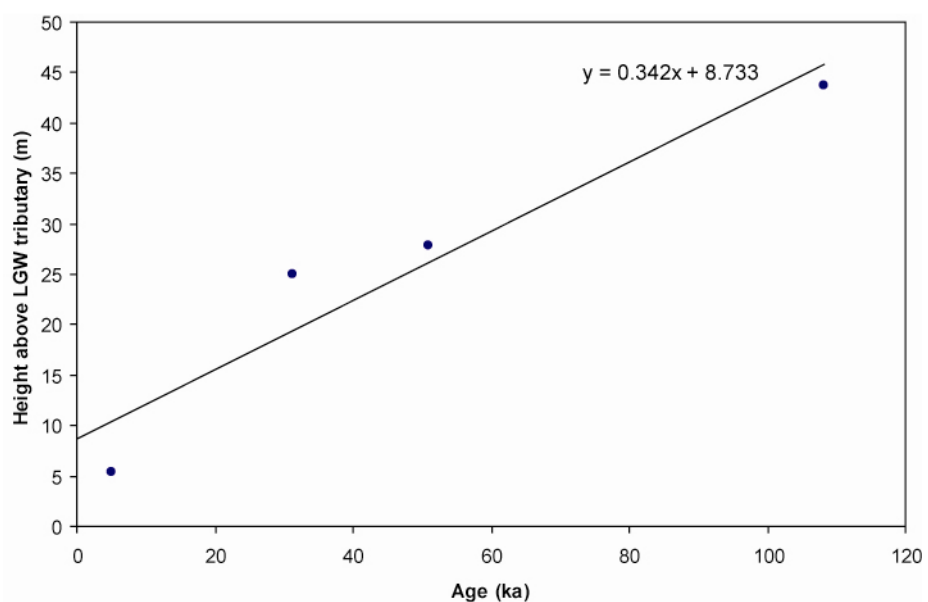


Figure 4.9: Incision rate graph for the Little Grand Wash.

Incision rate for the Green River as recorded by four separate travertine mounds (L2, L3, L4 and L5) along the Little Grand Wash fault.

4.5.3 Incision on the Salt Wash graben

The Salt Wash graben river gravel deposits are related to the small tributaries which run through this field area and drain into the Green River to the west. There are two tributaries, the Salt Wash and the Big Bubbling wash, with the latter a tributary to the former (Figure 4.10). Travertine deposits are related to each stream by their presence within the associated wash. Mounds that occur at greater elevations on the high ground between the two streams are attributed to the most proximal tributary. The closest travertine to the Green River is S1 on the Big Bubbling tributary, over 3 km up the stream channel from the mainstream. Long profiles of these streams are in dynamic equilibrium (section 5.2.1.4.2) indicating that they are graded to the mainstream Green River in the area of travertine deposition (Figure 4.12A). Graded is a term used to describe a stream which has a mouth at the same elevation as the mainstream channel (Charlton, 2008). If the tributary streams here had been unsuccessful in keeping up with mainstream incision, knick points would form along them and show up on the long profiles. As these streams are in equilibrium with the Green River it suggests that differences in elevation between entrained gravels and modern drainage in this field area provide an accurate incision rate that is not solely a minimum estimate. A total of fifteen mounds on the Salt Wash graben have cemented gravel of which nine have been dated (Figure 4.2; Table 3.2, Table 4.2). One of these mounds is not in situ (mound S21, section 3.5.4.2), so of these dated mounds eight can be used to calculate an incision rate for this field area of 0.168 m/ka (Figure 4.12B).

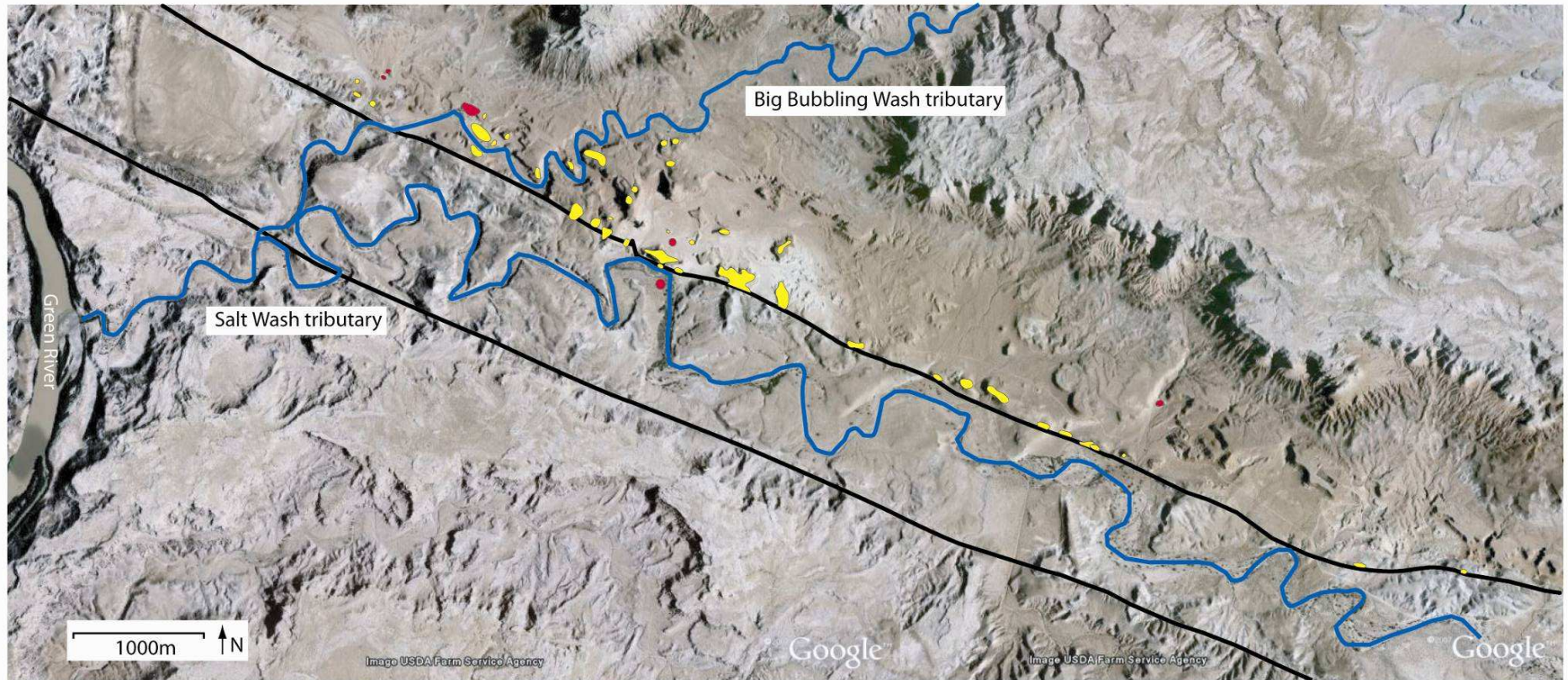


Figure 4.10: Satellite image of the Salt Wash graben tributaries.

The image, provided by Google Earth, shows the tributaries in relation to the Green River and travertine deposits. The Big Bubbling and Salt Wash tributaries are highlighted in blue, ancient travertine in yellow, active travertine in red and the faults in black.

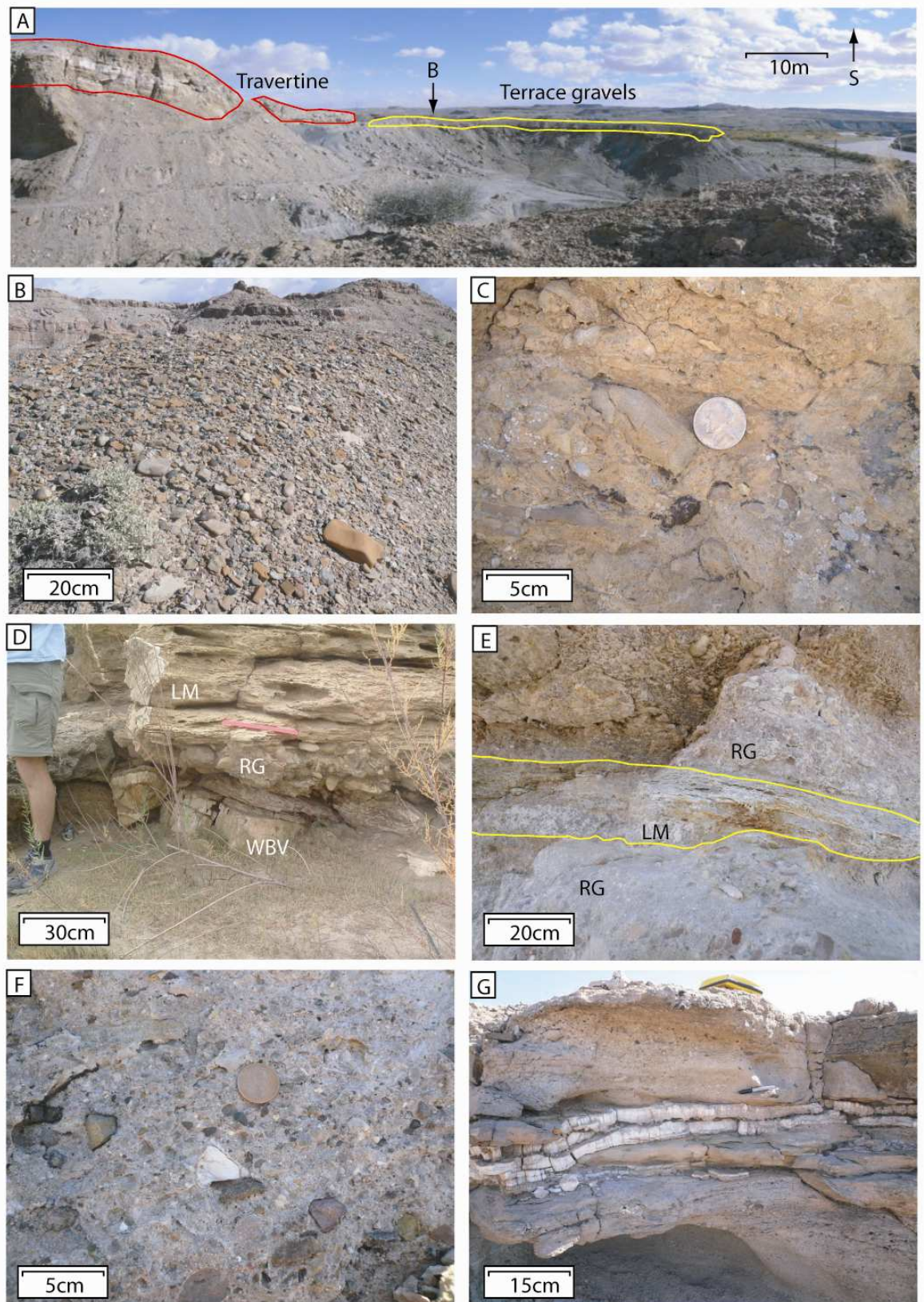


Figure 4.11: River terraces associated with the travertine mounds.

(A) Panoramic view of the L4 travertine mound. (B) Close up of the piedmont gravels on top of the large river gravel tongue that protrudes from L4. (C) Cemented gravel from L3. (D) Close association of layered mats, white banded veins and river gravels found in L2.1. (E) Interlayered gravels and layered mats from L5. (F) Piedmont gravel from the Salt Wash Tributary in mound S32. (G) Gravel that has been cut by carbonate veining in mound S31. For locations of travertine mounds see Figure 4.2.

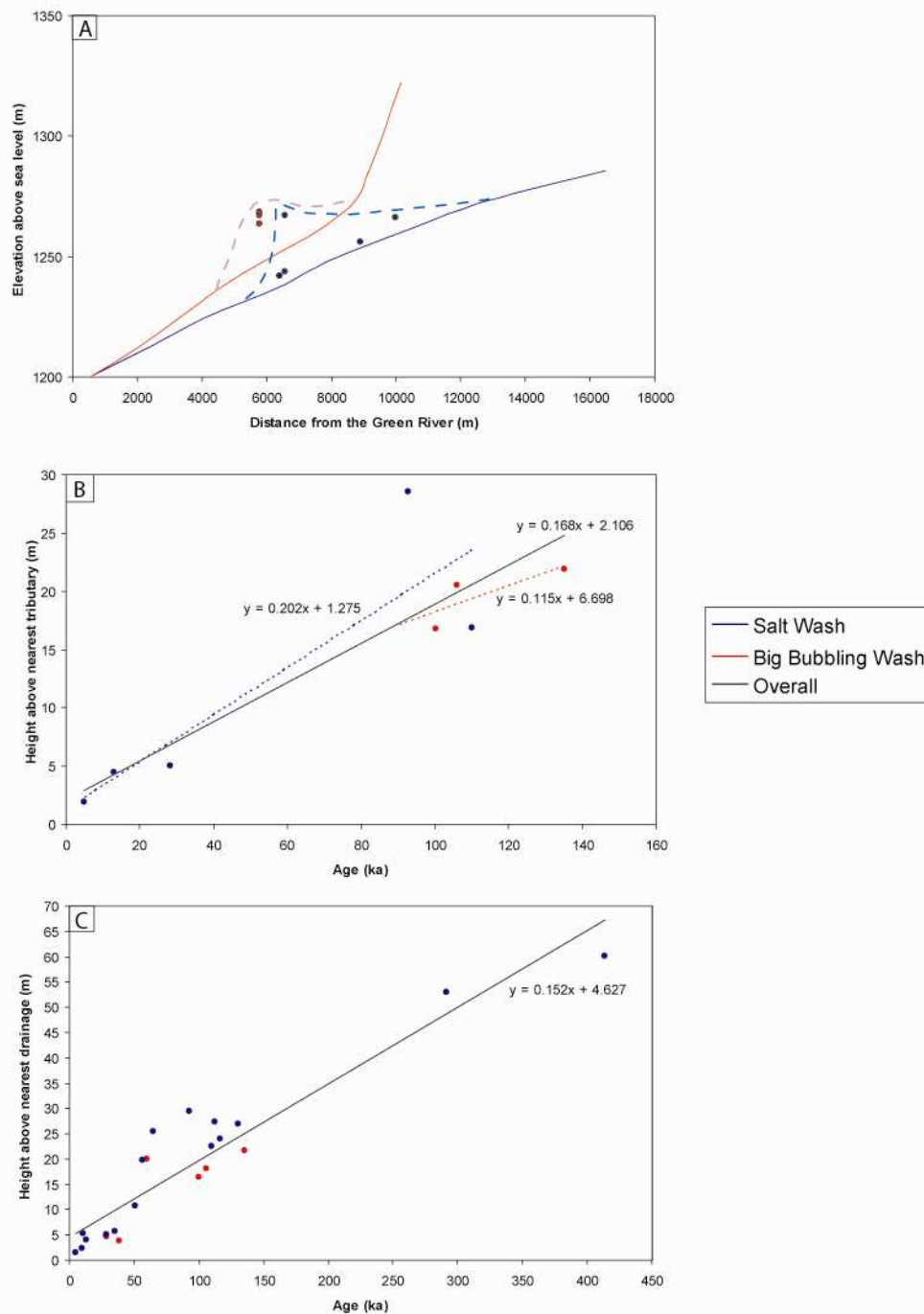


Figure 4.12: Incision rate graphs for the Salt Wash graben.

Key shows the colour coding for both of the tributaries with the Salt Wash represented by blue and the Big Bubbling wash by red in all plots. Overall incision rates are shown by black trend lines. (A) Long profiles of the tributaries. The eight dated mounds complete with gravel are plotted as colour coded squares. Dashed lines show which mounds are related to which tributary and in doing so show the relative surface topography above each tributary. (B) Salt Wash graben incision rate calculated by the elevation of river gravels entrained within travertine deposits. Incisions rates for both washes plus an overall rate are shown. (C) Salt Wash graben incision estimated from elevation of dated mounds alone. This measurement was taken from either the base of layered mats or from the maximum elevation of the peak of the mound (if mound was devoid of layered mats).

4.5.4 Travertine age estimate results

By taking the incision rate of the Salt Wash graben and the elevation of the non-dated mounds above their nearest point of drainage, ages for these mounds were estimated. Elevation of the non-dated mounds was measured from the base of cemented gravel if it was present. Mounds without gravel were measured from either the base of layered mats or the peak of the extent of altered host rock if layered mats were not present. This is a less than ideal measurement but in the absence of layered mats the elevation of the top of altered host rock provides the minimum possible elevation for eroded layered mats.

A plot of estimated elevation against age for all dated mounds provides a similar incision rate to that provided by river gravel erosion (0.152 m/ka, Figure 4.12C). The similar rates of erosion further confirm that travertine mounds along the northern fault of the Salt Wash graben are thin deposits. Age estimates for non dated mounds from both of these incision rates are shown in Table 4.6. These estimates are based on the forced assumption that incision rate has been constant through time. The ages provided calculated from the gravel incision are considered to be more accurate as this incision rate is based on definite evidence of base level during precipitation of ancient travertine mounds.

Figure 4.13 shows a time line of mound occurrence for the Little Grand Wash and northern Salt Wash graben faults. Using age estimates for un-dated mounds from Table 4.6 provided a complete coverage of Salt Wash graben travertine and allowed a more detailed history of fluid flow to be deduced for this area. This allowed for a more complete comparison to be made for the timing of fluid flow to the surface throughout the history of leakage along the Little Grand Wash and northern Salt Wash graben faults (section 4.7.6).

Mound number	Elevation (m)			Age estimate (years)	
	Travertine (T)	Drainage (D)	T - D	Mound incision	Gravel incision
S23	1223.3	1221.7	1.6	10,407	9,342
S24	1231.4	1222.4	8.9	58,980	52,942
S25	1230.3	1228.1	2.2	14,493	13,009
S26	1238.0	1228.1	9.9	65,497	58,792
S27	1238.5	1230.2	8.2	54,209	48,660
S28	1245.2	1234.3	10.9	71,672	64,336
S29	1250.6	1238.9	11.7	76,949	69,072
S30	1261.2	1238.9	22.3	146,979	131,934
S31	1251.1	1237.1	14.0	92,399	82,940
S32	1264.5	1237.1	27.4	180,562	162,078
S33	1269.2	1237.1	32.1	211,700	190,029
S34	1293.0	1238.9	54.1	356,822	320,295
S35	1256.9	1239.2	17.8	117,011	105,033
S36	1273.3	1246.5	26.8	176,937	158,825
S37	1259.5	1246.5	13.1	86,150	77,332
S38	1287.7	1258.6	29.1	191,677	172,056
S39	1270.3	1258.9	11.4	75,059	67,375
S40	1294.8	1282.0	12.8	84,577	75,919
S41	1267.2	1246.9	20.3	133,817	120,118

Table 4.6: Age estimation of non-dated mounds.

All non-dated mounds are located along the northern fault of the Salt Wash graben. Elevation measurements are in meters above sea level and drainage elevation measurements were taken from the nearest tributary to the travertine mound. Age estimates are calculated from the incision rate of 0.152 m/ka for mound incision from Figure 4.12C and 0.168 m/ka for gravel incision from Figure 4.12B.

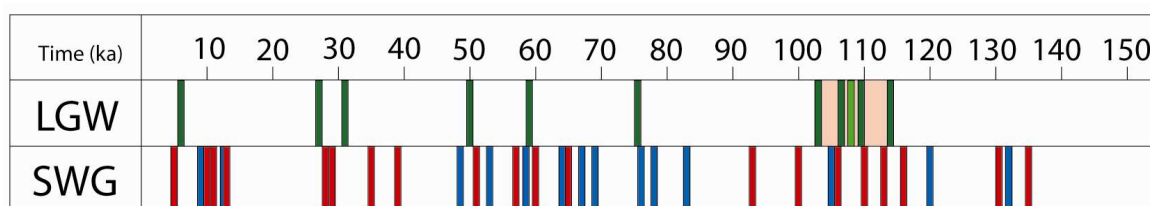


Figure 4.13: Timing of travertine activity.

Coloured bars represent occurrence of individual travertine mounds. Bars are an arbitrary width and analytical errors (which are mainly smaller than the bar widths) are left out for clarity. Dated deposits for the Little Grand Wash fault (LGW) travertine are green whilst mounds from the northern fault of the Salt Wash graben (SWG) are shown in red. Blue bars represent estimated age of un-dated mounds from the Salt Wash graben as calculated from the gravel incision rate (Table 4.6). Beige highlighted section in the Little Grand Wash fault timeline indicates the lifespan of mound L4. The light green bar shows the average age ($108,306 \pm 884$ years) of the four samples dated from this mound.

4.6 Travertine Volumetrics

4.6.1 Introduction

Estimations of the volume of travertine preserved along the footwalls of the Little Grand Wash and northern Salt Wash graben faults provides a tool with which to compare and contrast the travertine deposits of the two different areas. Combination of total travertine volume estimate with the minimum age of mound L4 provides a proxy for all travertine mounds which allows for estimation of minimum life spans of all travertine deposits across both areas.

4.6.2 Volume and lifespan estimates of travertine mounds

Measurement of both thickness and area of travertine deposits allowed for the volume of each mound to be estimated. Within these volume estimations travertine was assumed to have a cylindrical shape. This shape was chosen as it represented the simplest appropriate geometry applicable to all travertine mounds across both field areas. Volumetric calculations of the Little Grand Wash fault travertine had been previously carried out by Dockrill (2006). In these calculations the thickness of the Crystal Geysir travertine was taken from the Glen Ruby # 1-X well record (McKnight, 1940), which was drilled as a wild-cat petroleum well through the mound in 1935 and recorded travertine to a depth of 11 m below the surface. The close proximity of this deposit to the Green River makes it likely that this measurement represents the depth of white banded veins associated with this mound in the host Curtis sandstone (Section 3.5.3). Given the likelihood that this well was spudded into a section of the adjacent ancient mound the same thickness has been attributed to the Crystal Geysir travertine. Thickness, area and volume estimates for the travertine of the Little Grand Wash are shown in Figure 4.14 and Table 4.7.

Volumes for travertine in the Salt Wash graben were calculated from digitised outcrop maps in ImageJ and multiplying with their respective thicknesses measured in the field (Table 4.8). Due to the variables involved an error of 8% was attributed to thickness measurements and 19% attributed to area measurements (which included both field mapping and ImageJ) which provided a total error of $\pm 27\%$ on volume estimations. The depositional thickness of mounds with no layered

mat morphology preserved was estimated by attributing the average thickness of layered mats in more complete mounds to the average area of these mounds, giving a depositional thickness of 0.8 ± 0.07 m of layered mats for every $2,275 \pm 432$ m² of travertine mound. This is based on the forced assumption that the thickness of travertine mound increases with lateral extent as the mound grows, and that the preservation of layered mats facies in the more complete mounds is 100%.

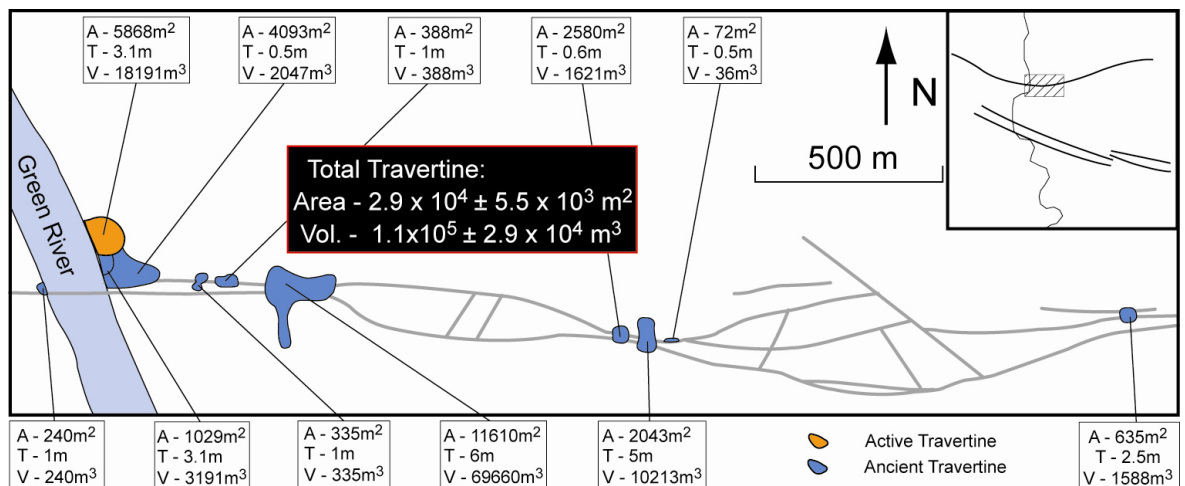


Figure 4.14: Volume estimates for the Little Grand Wash travertine.

Estimated area (A), thickness (T) and volume (V) measurements of travertine in the footwall of the Little Grand Wash fault from Dockrill (2006). Values are from field measurements of Dockrill whilst inset shows the relative location of field area along the fault. Errors on individual deposits, which can be seen in Table 4.7, are left out for clarity. Errors on total measurements are $\pm 19\%$ for area and $\pm 27\%$ for volume.

Mound number	Age (years)	Area (m ²)	Error ($\pm 19\%$)	Thickness (m)	Error ($\pm 8\%$)	Volume (m ³)	Error ($\pm 27\%$)
L1	modern	5,868	1,115	3.1	0.2	18,191	4,912
		240	46	1	0.1	240	65
L2	5,263	4,093	778	0.5	0.0	2,047	553
		1,029	196	3.1	0.2	3,191	862
L3	49,989	335	64	1	0.1	335	90
		388	74	1	0.1	388	105
L4	113,912	11,610	2,206	6	0.5	69,660	18,808
L5	31,217	2,580	490	0.6	0.0	1,621	438
L6	58,847	2,043	388	5	0.4	10,213	2,758
L7	75,495	72	14	0.5	0.0	36	10
L8	27,061	635	121	2.5	0.2	1,588	429
Total	-	28,893	5,490	24.3	1.9	107,510	29,028
Average	-	2,303	437	2.1	0.2	8,932	2,412

Table 4.7: Volume estimates for the Little Grand Wash travertine.

Estimated area, thickness, and volume measurements of travertine along the Little Grand Wash fault. Measurement of the active L1 deposit is shown in blue, whilst multiple measurements from the separate remnants of L2 and L3 are highlighted in green and pink respectively. Area error comes from both mapping and ImageJ interpretation while thickness error is based on potential measurement errors. Volume error is the sum of area and thickness errors. Averages, which further allow for comparison between the field sites, are for ancient travertine only.

Sample set	Mound number	Age (years)	Area (m ²)	Error (± 19%)	Thickness (m)	Error (± 8%)	Volume (m ³)	Error (± 27%)
mounds dated by U-series	S1	38,906	471	89	0.4	0.03	188	51
	S2	60,188	2,229	423	1.0	0.08	2,229	602
	S3	29,028	634	120	0.2	0.02	150	40
	S4	291,307	332	63	0.1	0.01	41	11
	S5	413,474	1,207	229	0.4	0.04	543	147
	S6	13,068	1,013	193	0.5	0.04	507	137
	S7	100,378	833	158	1.0	0.08	833	225
	S8	106,088	864	164	0.6	0.05	518	140
	S9	135,135	1,110	211	1.0	0.08	1,110	300
	S10	51,290	199	38	0.1	0.01	15	4
	S11	92,792	5,612	1,066	1.0	0.08	5,612	1,515
	S12	28,375	612	116	1.2	0.10	734	198
	S13	10,797	911	173	0.4	0.03	364	98
	S14	34,971	534	102	0.2	0.02	106	29
	S15	65,085	12,013	2,282	0.5	0.04	6,006	1,622
	S16	57,014	2,331	443	0.6	0.05	1,399	378
	S17	4,792	1,080	205	0.3	0.02	324	87
	S18	112,804	2,614	497	1.0	0.08	2,545	687
	S19	130,666	4,125	784	1.5	0.12	6,341	1,712
	S20	110,000	2,392	454	0.7	0.06	1,674	452
	S21	116,788	357	68	1.1	0.09	393	106
	S22	9,749	637	121	0.4	0.03	255	69
mound ages estimated from incision rates	S23	9,342	742	141	0.5	0.04	371	100
	S24	52,942	808	154	0.3	0.02	244	66
	S25	13,009	5,230	994	1.0	0.08	5,230	1,412
	S26	58,792	443	84	0.2	0.01	73	20
	S27	48,660	651	124	0.2	0.02	158	43
	S28	64,336	1,215	231	0.9	0.07	1,094	295
	S29	69,072	1,013	193	0.4	0.03	383	103
	S30	131,934	4,607	875	0.9	0.07	4,146	1,119
	S31	82,940	4,236	805	2.0	0.16	8,472	2,287
	S32	162,078	1,896	360	0.5	0.04	948	256
	S33	190,029	1,124	214	2.0	0.16	2,248	607
	S34	320,295	819	156	0.3	0.02	250	68
	S35	105,033	819	156	1.0	0.08	819	221
	S36	158,825	2,251	428	0.8	0.07	1,888	510
	S37	77,332	6,296	1,196	2.3	0.19	14,768	3,987
S38	172,056	1,883	358	0.7	0.06	1,321	357	
S39	67,375	1,567	298	0.6	0.05	915	247	
S40	75,919	1,382	262	0.5	0.04	711	192	
S41	120,118	1,215	231	0.5	0.04	550	149	
modern travertine	S42	modern	493	94	0.2	0.02	99	27
	S43	modern	435	83	0.2	0.02	87	23
	S44	modern	3,787	720	0.5	0.04	1,894	511
	S45*	modern	1,130	215	0.5	0.04	565	152
	S46	modern	1,963	373	0.2	0.02	393	106
	S47	modern	988	188	0.3	0.02	297	80
	Total	-	89,103	16,930	32	2.55	79,809	21,548
Average	-	2,275	432	0.8	0.1	963	260	

Table 4.8: Volume estimates for the Salt Wash graben travertine.

Estimated area, thickness, and volume measurements of travertine on the northern fault of the Salt Wash graben. Mound numbers S23 to S41 have ages estimated from gravel incision rates (subsection 4.5.4), whilst mounds S42 to S47, highlighted in blue, represent modern mounds. Deposits devoid of layered mats and therefore with minimum estimated thicknesses and volumes are highlighted in yellow (see text for details). Averages include ancient travertine of known area and thickness only.

Estimated minimum life-spans of all travertine deposits were calculated by using the measured volume, 69,660 m³, and known lifespan, 10,740⁺⁶⁰⁴_{-1,486} years, of the L4 travertine mound (section 4.3.3). By taking the error on this lifespan from radiometric dating and combining it with error from volume estimates, total error on lifespan estimations equals +32%, -41%. Since these calculations are based on the volume of mounds, poorly preserved travertine deposits give an apparently short lifespan (Table 4.9 and Table 4.10), for instance it is hardly likely that mounds L7, S4 and S10 were active < 10 years. Active deposits are completely intact in both areas which mean that life span estimates may be more applicable to modern travertine. Rates of modern precipitation may differ from ancient mounds however, due to their anthropogenic source (section 3.5.3).

Mound number	Age (years)	Volume (m ³)	± Error (27%)	Lifespan (years)	+ Error (33%)	- Error (41%)
L4	108,306	69,660 ^a	18,808	10,740 ^b	3,544	4,403
L1	Modern	18,191	4,912	2,805	926	1,150
L2	5,263	5,478	1,479	845	279	346
L3	49,989	723	195	111	37	46
L5	31,217	1,621	438	250	82	102
L6	58,847	10,213	2,758	1,575	520	646
L7	75,495	36	10	6	2	2
L8	27,061	1,588	429	245	81	100
Total	-	107,510	29,028	16,576	5,470	6,796
Average	-	12,760	3,445	1,967	649	807

Table 4.9: Lifespan estimates of Little Grand Wash travertine.

Life span calculations for both field areas are based on the measured volume (a) and known lifespan (b) of travertine L4 (section 4.3.3). The active L1 deposit is highlighted in blue. For mounds with repeat and multiple analyses average ages of all analyses are shown (c). Averages quoted include only ancient deposits.

Table 4.10: Lifespan estimates of Salt Wash graben travertine.

All active travertine deposits are termed 'modern' under age and highlighted in blue, with the radiometrically analysed S45 deposit, the Ten Mile Geyser, indicated (*). Travertine deposits that have had layered mats completely removed by erosion and so have estimated volumes are highlighted in yellow. Averages quoted include only ancient deposits.

Sample set	Mound number	Age (years)	Volume (m ³)	± Error (27%)	Lifespan (years)	+ Error (33%)	- Error (41%)
mounds dated by U-series	S1	38,906	188	51	29	10	12
	S2	60,188	2,229	602	344	113	141
	S3	29,028	150	40	23	8	10
	S4	291,307	41	11	6	2	3
	S5	413,474	543	147	84	28	34
	S6	13,068	507	137	78	26	32
	S7	100,378	833	225	128	42	53
	S8	106,088	518	140	80	26	33
	S9	135,135	1,110	300	171	56	70
	S10	51,290	15	4	2	1	1
	S11	92,792	5,612	1,515	865	286	355
	S12	28,375	734	198	113	37	46
	S13	10,797	364	98	56	19	23
	S14	34,971	106	29	16	5	7
	S15	65,085	6,006	1,622	926	306	380
	S16	57,014	1,399	378	216	71	88
	S17	4,792	324	87	50	16	20
	S18	112,804	2,545	687	392	129	161
	S19	130,666	6,341	1,712	978	323	401
	S20	110,000	1,674	452	258	85	106
	S21	116,788	393	106	61	20	25
	S22	9,749	255	69	39	13	16
mound ages estimated from incision rates	S23	9,342	371	100	57	19	23
	S24	52,942	244	66	38	12	15
	S25	13,009	5,230	1,412	806	266	331
	S26	58,792	73	20	11	4	5
	S27	48,660	158	43	24	8	10
	S28	64,336	1,094	295	169	56	69
	S29	69,072	383	103	59	19	24
	S30	131,934	4,146	1,119	639	211	262
	S31	82,940	8,472	2,287	1,306	431	536
	S32	162,078	948	256	146	48	60
	S33	190,029	2,248	607	347	114	142
	S34	320,295	250	68	39	13	16
	S35	105,033	819	221	126	42	52
	S36	158,825	1,888	510	291	96	119
	S37	77,332	14,768	3,987	2,277	751	934
S38	172,056	1,321	357	204	67	83	
S39	67,375	915	247	141	47	58	
S40	75,919	711	192	110	36	45	
S41	120,118	550	149	85	28	35	
modern travertine	S42	modern	99	27	15	5	6
	S43	modern	87	23	13	4	5
	S44	modern	1,894	511	292	96	120
	S45*	modern	565	152	87	29	36
	S46	modern	393	106	61	20	25
	S47	modern	297	80	46	15	19
	Total	-	79,809	21,548	12,305	4,061	5,045
Average	-	963	260	262	86	107	

4.6.3 Volume and number of travertine through time

Cumulative plots of volume and travertine occurrence for both areas are presented in Figure 4.15. The slope of a straight line between any two points on these plots represents the average precipitation rate (for volume) or number of events (mound occurrence) per unit of time for the interval between the two points.

Patterns of flow can be potentially deduced from these plots. If flow to the surface is constant through time then volumes plots should provide lines of near constant gradient, whereas intermittent flow will produce lines with clear changes in gradient. Similarly a relatively constant precipitation rate of travertine through time will produce a straight line through the volume plots whilst alternating precipitation rates, perhaps brought about by climate or salinity variation, will produce a line of more variable gradient. This latter factor may produce a smaller signal on top of flow consistency, as it is unlikely any pattern in precipitation will be noticeable unless flow is constant through time. Variation in precipitation of travertine, as construed from section 4.3.3, ranges from 0.51 - 0.74 mm/y. Changes of this order may affect the volume of travertine at any given time by up to 31%. Even taking all of these potential signals into account, erosion will have the largest influence on these plots because ancient travertine mounds are not completely preserved and therefore represent less than their initial precipitated volume. Erosional affects can be taken into account by comparing volume and occurrence plots for each field site because erosion will have a lesser effect on mound number than volume of mounds. Any changes in rate of volume accumulation can be compared and contrasted with the occurrence of travertine deposits- if number of mounds increases rapidly whilst volume remains relatively constant then it is possible that erosion is having a major effect in the travertine record at that particular time.

As there are only eight mounds in the Little Grand Wash and the oldest is by far the largest, cumulative volume of travertine has a steady gradient through time which may reflect constant flow. Slight pickups occur toward mound L6 at ~60 ka and the currently active Crystal Geyser (L1) travertine. This may hint that in between these larger deposits fluid flow to the surface has not been as strong and smaller mounds have been deposited that are not as resistant to erosion. The cumulative mound profile for this area is relatively constant.

The forty-seven travertine mounds of the northern fault of the Salt Wash graben provide a much larger data set to work with. In the plot of cumulative volume several sharp changes in the gradient of the line allude to periods of higher and lower production of travertine and hence leakage to the surface. Cumulative volume shows a gentle gradient from the start of leakage at ~414 ka up to ~135 ka, a trend that is reflected in the cumulative number of mounds plot. At this stage a sharp increase in total volume occurs, this coincides with a change in gradient in the number of mounds. This change in gradient may highlight an increase in the number of mounds becoming active and the onset of more continual leakage in the Salt Wash graben. Volume of mounds then plateaus from 130 to 120 ka which may reflect a period of non-deposition or erosion could have since removed evidence of mounds from this time period. The rate of volume accumulation remains relatively constant from 120 to 75 ka which may suggest relatively constant flow to the surface. After a minor plateau up to 65 ka, which is during the activity of five separate mounds, a sharp increase in volume then occurs up to ~57 ka. Volume of travertine deposited from ~57 to 13 ka is very low despite ten mounds being deposited during this time period. This may reflect the deposition of small friable mounds that have proved vulnerable to erosion. A sharp rise in total volume then remains until the present day which may be a result of there being lesser time for erosion to take place on these younger mounds.

Closer inspection of the trends just discussed for the northern fault of the Salt Wash graben is provided by Figure 4.15C which shows a direct comparison of the number of mounds and the volumes being precipitated during 10 ka intervals. It should be kept in mind that the numbers provided in this figure are very dependant on the assumptions made during estimation of volumes for the travertine mounds. It is likely that erosion of mounds has a huge influence on these results. However, if erosion has been constant across all mounds in this area, intervals which have large volumes in comparison to the number of mounds may be highlighting periods of increased activity. If this is the case then larger quantities of leakage may have occurred during the interval between 140 and 130 ka and for a more extended period of time between 110 and 70 ka.

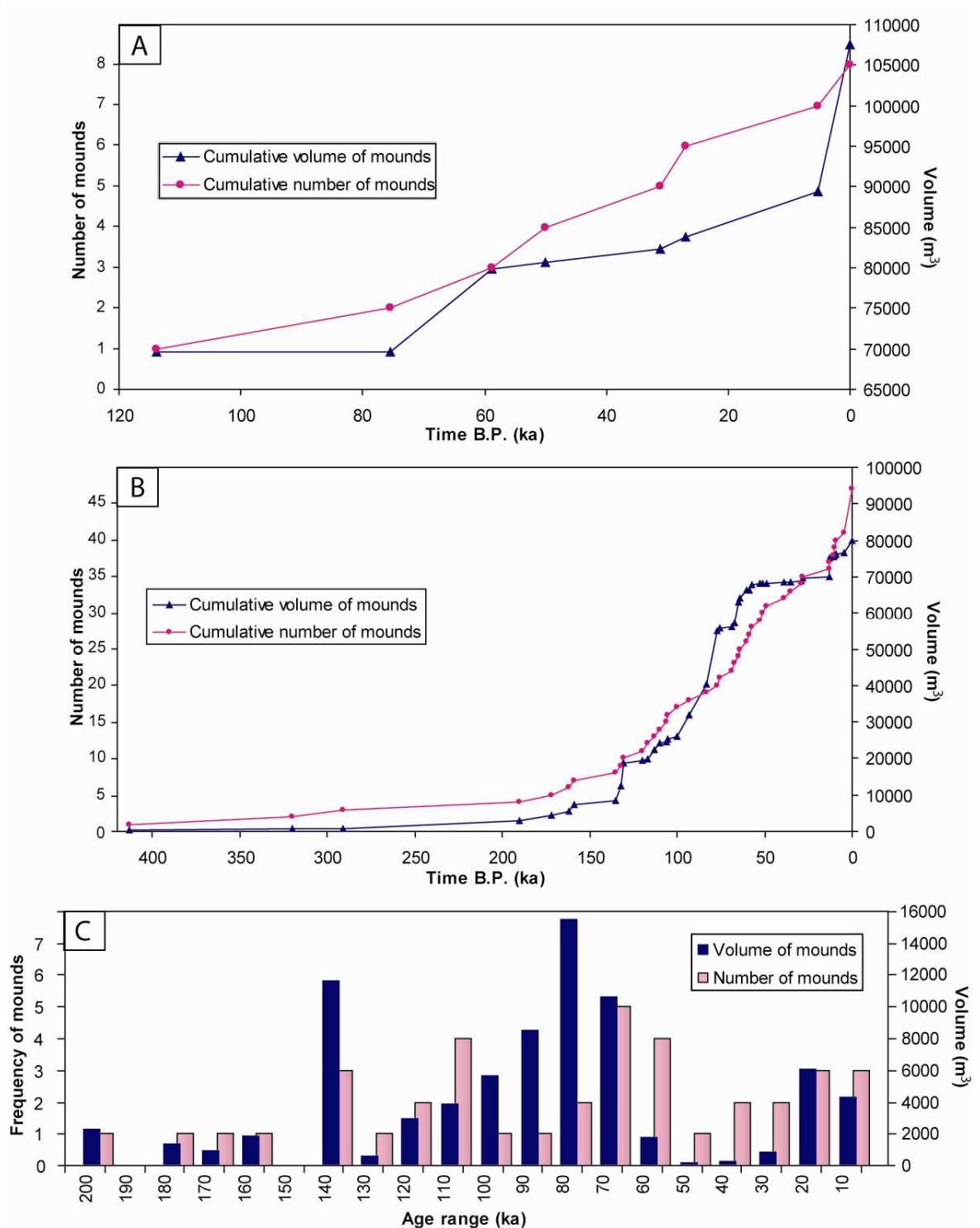


Figure 4.15: Cumulative plots for number and volume of travertine deposits.

(A) Cumulative plot for the Little Grand Wash travertine with time (B.P.) plotted against both number of mounds (left axis) and estimated total volume of mounds (right axis). **(B)** Cumulative plot for mounds associated with the northern fault of the Salt Wash graben, same axis used as for the Little Grand Wash. Y-axis scales do not match so the lines for each aspect are not intimately related, rather gradients on lines are compared and contrasted. It is worth noting that the scale of mound volume for each site is similar whilst the number of mounds along the northern fault of the Salt Wash graben is far greater- this is likely to be a result of more diffuse flow to the surface in this area. **(C)** Bar chart showing both the frequency and volume of travertine deposits on the Salt Wash graben divided into 10 ka time periods. Errors on volume, which are $\pm 27\%$, have been omitted from all three graphs for clarity.

4.7 Discussion

4.7.1 *U-Th age analysis of travertine*

Travertine morphology consists of four separate facies, of which three (breccia, layered mats, and brown banded veins) are unsuitable for U-series analysis due to violation of the criteria desired for accurate age determination and a scarcity of field examples. The white banded vein facies meets these requirements and is abundant in all fossil deposits making it suitable for U-Th dating of individual mounds. Dating of multiple mounds was carried out to gain a good spatial resolution of leakage along the faults through time. All seven mounds on the Little Grand fault were dated at least once to give a complete coverage of this area. Travertine mounds in footwall of the northern fault of the Salt Wash graben are far more common. In this area travertine is not restricted to the fault and occurs up to 530 m into the footwall. Over half of the forty-two deposits have been dated in this area. Good spatial resolution was achieved by dating travertine mounds stretching the length and breadth of the area.

A more comprehensive analysis of travertine from the Little Grand Wash involving a total of twenty-two samples allows for a more intensive investigation of the travertine mounds and the technique used to date them. Repeat age analyses of three mounds of distinct age demonstrate the excellent reproducibility of analysis and prove the robust nature of the preparation and U-series age determination techniques used. Detailed study of a single large and well defined mound involved analysis of five samples. A spread of ~11,000 years on the ages of the samples gives a minimum estimate for the lifespan of this deposit. This also suggests that leakage from a single discrete point on the fault may be active for a minimum of 11,000 years.

Dating of the inner and outer edges of the main vein present in this mound gave an age difference of 4,300 years which translates into a time averaged precipitation rate of 0.6 mm per year. Ages from veins above and below this main vein demonstrate that separate veins do not get younger up sequence, with veins seemingly exploiting the areas of weakness in the layered mat horizons.

Layered mats theoretically provide poor samples for dating. Analyses of this facies from two separate mounds of very distinct age were carried out to

determine if this was the case. The main motivation behind this was the lack of white banded veins but abundance of layered mats in other field areas of interest to the investigation of CO₂ leakage such as St. Johns, Arizona. Though it was confirmed that U-Th dating of layered mats alone produces dubious results, the comparison of layered mats with white banded veins from the same mound produced valuable findings. Closely matching $\delta^{234}\text{U}$ of white banded veins and layered mats suggest these facies are closely associated components of an ancient travertine mound. These geochemical results back up field observations and help to provide a sound case for confirming eroded mounds in the Salt Wash, devoid of layered mats, as legitimate travertine deposits.

4.7.2 Implications for determination of incision rate

River terraces are geomorphologically important because they and their associated deposits provide information about the sedimentological, hydrologic and erosional history of a river channel. As such they can provide a key to understanding the effect of base level change on landscapes and provide important information on incision rates when they can be numerically dated. The occurrence of fossil stream terraces within several of the travertine mounds in the Little Grand Wash and Salt Wash graben coupled with the U-Th age of their host travertine deposits allows quantitative constraint of the incision rate over tens of thousands of years in these areas. A rate of 0.169 m/ka for the Salt Wash graben agrees well with the findings of Dethier (2001) who calculated a regional incision rate of 0.15 m/ka. The Little Grand Wash produces a rate of 0.342 m/ka which is twice that of the Salt Wash graben. This is likely to reflect the incision rate of the Green River which agrees well with the work of Garvin et al. (2005) and Marchetti et al. (2005) who found incision rates of 0.4 and 0.43 m/ka from measurements downstream on the Colorado and Fremont rivers.

Based on the assumption that travertine age is proportional to the height of mound above present day base level, the calculation of incision rate on the Salt Wash graben allows ages of the remaining nineteen undated travertine deposits to be estimated. Previous studies used regional erosion rates to estimate the age of deposits along both faults (Baer and Rigby, 1978) with resulting maximum age estimates ranging from 190,000 to 200,000 years. This is an over-estimate for the Little Grand Wash and underestimates for the Salt Wash graben, but the present

study has a better understanding of incision rates in these areas due to both geomorphologic interpretation and radiometric dating.

4.7.3 Volumetric comparison of Little Grand Wash and Salt Wash graben travertine deposits

Thickness, area, and volume estimates for each mound in the Little Grand Wash are shown in Figure 4.14 and Table 4.7, and results from the Salt Wash graben are shown in Table 4.8. A summary table of total and average volumes is shown below in Table 4.11. For the calculation of volumes the shape of travertine mounds was treated as cylindrical. This is because this is the simplest geometry to attribute to the travertine mounds which grow horizontally during leakage of CO₂ charged waters to the surface. This method assumes that the travertine is equally thick across its area and so may overestimate the volume of relict mounds. However, this is counteracted by the fact that ancient travertine mounds are weathered, and so are missing potentially significant volumes of original material; it also doesn't account for subsurface veining, which in some cases is extensive and comprises a large volume of carbonate.

The total volume for travertine along the Little Grand Wash fault is 107,510 ± 29,028 m³ and the total volume of travertine along the northern Salt Wash graben fault is 79,809 ± 21,548 m³. A similar volume of travertine is precipitated along each fault (Figure 4.16). This suggests that a similar volume of CO₂ has leaked to the surface in each area. However it should be noted that the preservation potential of mounds in the Salt Wash graben is far less than that of the Little Grand Wash (subsection 3.5.4.1). The seven ancient mounds present in the Little Grand Wash show recognisable preservation of both veining and layered mat facies. A total of forty-one travertine mounds are present in the Salt Wash graben, with eighteen of these mounds lacking layered mat preservation.

The largest mound along the Little Grand Wash fault, travertine L4, at 69,660 ± 18,808 m³ is an order of magnitude larger than the largest fully measured travertine in the Salt Wash graben, S15, at 6,006 ± 1,622 m³ (Table 4.7 and Table 4.8). These two mounds have identical mapped areas (11,610 m² ± 2,206 to 12,013 ± 2,282 m²) so the volume difference may be due to the length of activity, with L4 being active for significantly longer and therefore producing a much thicker deposit. This trend is also seen when comparing the averaged dimensions of

ancient travertine across the two areas. Travertine along the Little Grand Wash fault is on average 2.1 ± 0.2 m thick, $2,303 \pm 437$ m² in area, and $8,932 \pm 2,412$ m³ in volume; whilst mounds complete with layered mats along the northern fault of the Salt Wash graben give values of 0.8 ± 0.07 m, $2,275 \pm 432$ m², and 963 ± 260 m³ for thickness, area and volume respectively. The smaller ratio of area to volume in the Salt Wash graben further suggests that mounds on the Little Grand Wash may have been active for longer or are more resistant to erosion. A comparison of vein thickness in deposits across the two areas, with the L4 mound's main vein of 2.5 m being five times greater than the thickest vein of mound S11 (0.5 m), suggests that Little Grand Wash travertine have a longer lifespan, providing that precipitation rates are constant across all mounds.

		Area (m ²)	Error (± 19%)	Thickness (m)	Error (± 8%)	Volume (m ³)	Error (± 27%)	Lifespan (years)	+ Error (33%)	- Error (41%)
LGW	Total	28,893	5,490	24.3	1.9	107,510	29,028	16,576	5,470	6,796
	Average	2,303	437	2.1	0.2	8,932	2,412	1,967	649	807
SWG	Total	89,103	16,930	32	2.55	79,809	21,548	12,305	4,061	5,045
	Average	2275	432	0.8	0.07	963	260	262	86	107

Table 4.11: Summary of travertine volumes and lifespan.

Totals and averages of travertine in both the Little Grand Wash fault and the northern fault of the Salt Wash graben. Sources of error are provided in section 4.6.1.

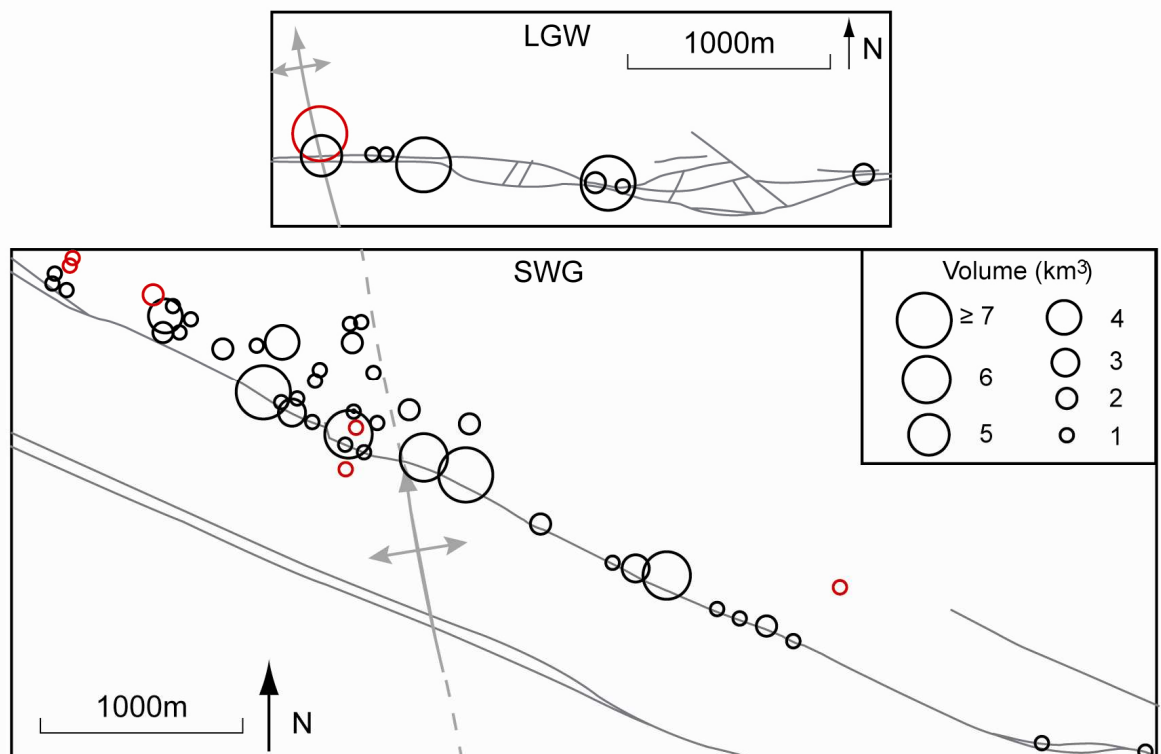


Figure 4.16: Travertine volume maps.

Maps show volume of travertine along the Little Grand Wash fault and the northern fault of the Salt Wash graben. Inset on the Salt Wash graben map shows the legend of mound volumes. Red circles represent active deposits. Both maps are to the same scale

4.7.4 Actively precipitating travertine

Active precipitation of travertine in along the northern fault of the Salt Wash graben forms relatively thin layered mat crusts with estimates of total thickness of these deposits ranging from 0.2 – 0.5 m (Table 4.8). This is in contrast to the Crystal Geyser travertine which may be up to 3 m thick (Table 4.7) and has a clearly higher volume of fluid flowing to the surface. Though all of the active springs in both areas may be man-made they may be analogous to the precipitation of the ancient mounds as ancient deposits along the northern fault of the Salt Wash graben are also significantly thinner than deposits along the Little Grand Wash fault. The concentrated nature of modern flow shown by L1 in comparison to the more diffuse flow of the active Salt Wash graben springs may also reflect the more diffuse nature of flow to the surface throughout the fluid flow history of the northern Salt Wash graben fault. Actively precipitating mounds in the Salt Wash graben with the exception of the Big Bubbling spring (mound S44) have life span estimates of fewer than 87 years which would place their maximum age within the last 100 years, contemporaneous with exploration in the area. This further suggests that the six active springs of the Salt Wash graben are likely to have been caused by anthropogenic drilling.

4.7.5 Pattern of flow to the surface

High resolution U-series dating of travertine mounds on the Little Grand Wash fault and northern fault of the Salt Wash graben allows for further investigation into the pattern of fluid flow. With each mound there is a distinct change in location of leakage to the surface along the extent of travertine deposition on both faults. The following section will discuss possible temporal and spatial trends in the travertine data which may lead to an explanation of the observed location of mounds in the field sites and give an insight into the fluid flow pathways in the subsurface.

4.7.6 Timing of fluid flow as recorded by U-series results

A complete record of fluid flow to the surface through time exists for both field sites (Figure 4.17). As can be seen from the time lines of travertine occurrence there are gaps present between travertine on the Little Grand Wash

fault while the travertine of the northern fault of the Salt Wash graben is more numerous and more continuous with time (Figure 4.15). Gaps between mounds on the Little Grand Wash fault are up to 32 ka in length between the two oldest mounds; L4 and L7 (Figure 4.17B). From 75 ka to the present day timing of mounds alters between longer gaps of 17, 19 and 22 ka and shorter gaps in deposition of 9 and 4 ka. The forty one mounds of the northern fault of the Salt Wash graben provide a record of nearly constant leakage up until 135 ka before large gaps start occurring between deposition of mounds. Over this time there are at least four recognisable gaps between apparent periods of constant leakage. These gaps, mainly lasting in the region of 10 ka, occur between 13-28 ka, 39-49 ka, 83-93 ka and 120-130 ka. Further back than 135 ka and up to 413 ka there are gaps as large as 101ka present between the seven travertine mounds deposited in this time frame. On closer inspection of both areas over the same time frame it can be seen that there is a potential overlap of travertine activity across the Little Grand Wash fault and the northern fault of the Salt Wash graben with what appears to be four distinct periods of activity (Figure 4.17B).

4.7.6.1 Statistical Analysis of timing of travertine deposition

Although there initially appears to be a correlation between the two areas, a more detailed statistical analysis has been carried out to confirm if there are any trends in the timing of the travertine deposits, or if what we are seeing is a random pattern of occurrence. Figure 4.18 shows logarithmic plots of the empirical survivor function (ESF) for both field areas. The points in each of these plots represent the percentage of intervals between travertine occurrences longer than the specified number of years (along the x-axis). If events occur randomly in time the ESF will be close to exponential in form, whilst departures from randomness will appear as deviations from the straight line form of the plot. The two larger time gaps (of 93 and 101 ka) between deposition of travertine over 200,000 years old on the northern Salt Wash graben fault show a deviation from a straight line plot and give the entire data set an $R^2 = 0.73$ with respect to the best fit exponential trend line. Of the forty intervals present between mound precipitation thirty-eight are 29 ka or less, and if the two oldest time gaps are left out, these plot as a straight line with an $R^2 = 0.90$, which suggests a random pattern of deposition with respect to time over at least the last ~135 ka. The Little Grand Wash ESF has an R^2 value of 0.95 when compared to an exponential trend line.

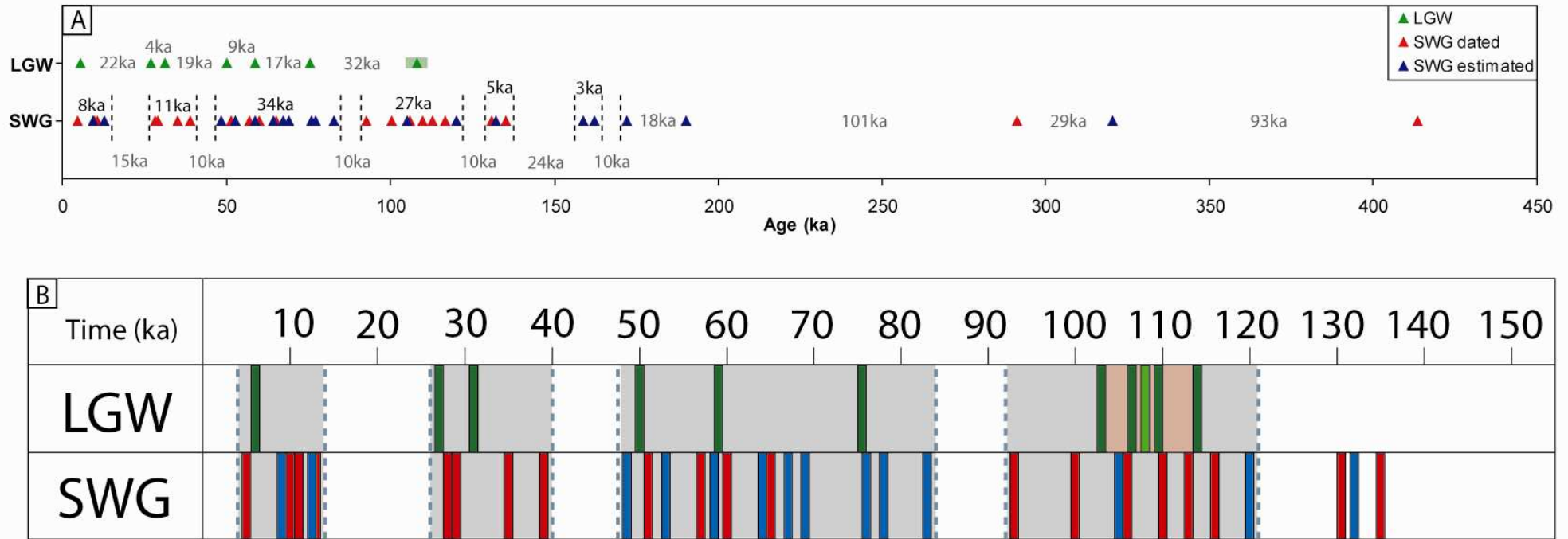


Figure 4.17: Timing of travertine occurrence for both field areas.

(A) Total timelines for the Little Grand Wash and Salt Wash graben fault travertine. Lengths of gaps in deposition are signified by grey text. In the Salt Wash graben grey numbers are used up until ~175ka to show times of quiescence between periods of more continual flow. Black numbers show the length of time represented by these periods of nearly continual activity. (B) Comparative timelines for the entire history of the Little Grand Wash fault. Colour code for different travertine the same as in Figure 4.13. Areas of potential overlap of timing of precipitation in each area are highlighted by grey boxes.

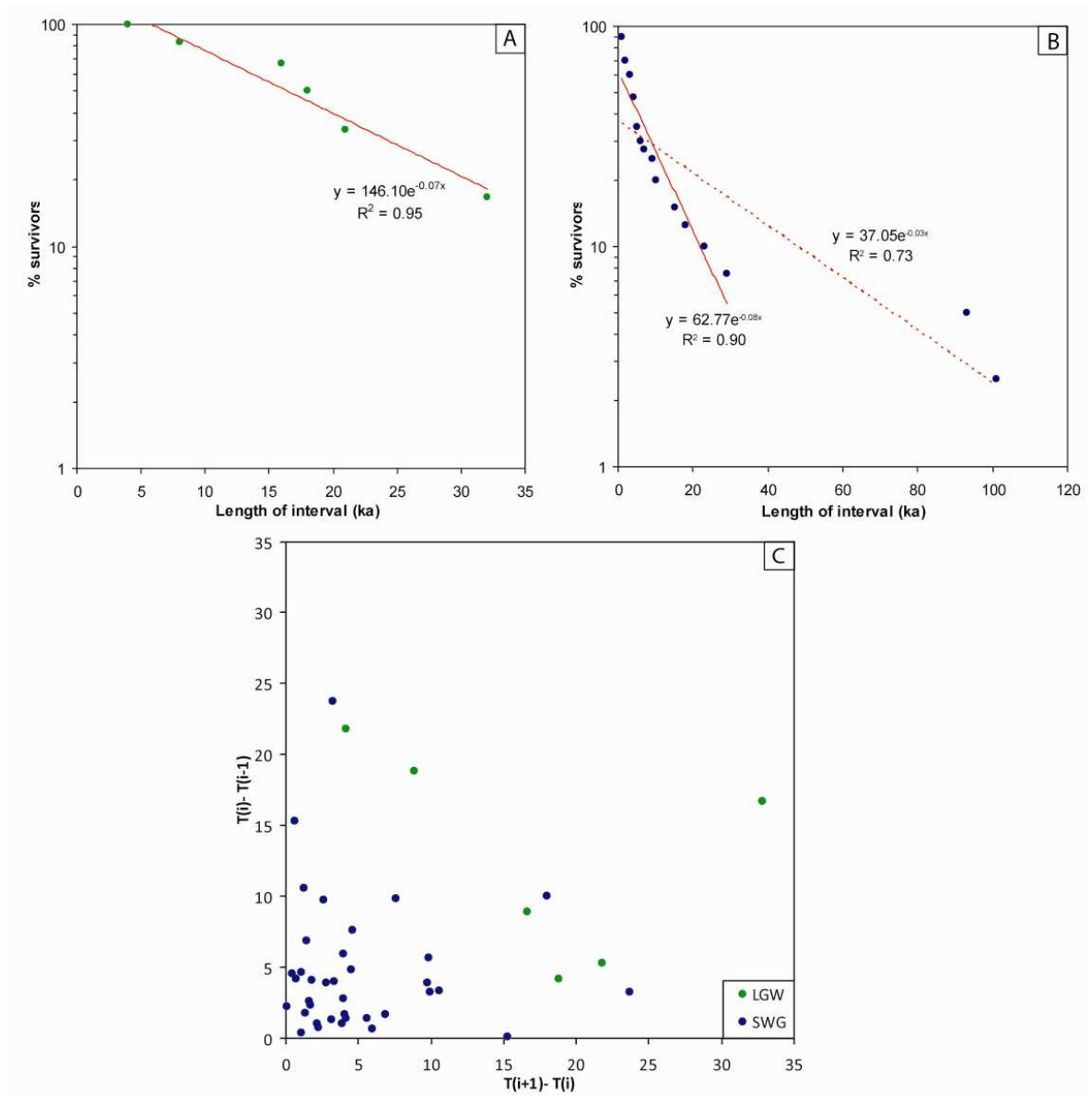


Figure 4.18: Statistical analysis of mound timing.

(A) Empirical survivor function (ESF) plot for the Little Grand Wash fault travertine deposits. An exponential line of best fit is also plotted in red with R^2 value. **(B)** ESF plot for mounds of the northern fault of the Salt Wash graben. Exponential lines of best fit are shown for both the total data set and for time gaps of 29 ka or less between successive travertine mounds. **(C)** Scatter diagram of serial correlation of successive intervals between mound occurrences for both field sites. The degree of correspondence between the length of an interval and the length of the immediately preceding interval is shown by plotting $x_i = t_{i+1} - t_i$ against $y_i = t_i - t_{i-1}$ where t_i is the time of occurrence of the i th event.

A further statistical analysis known as a Serial Correlation was carried out to compare the length of time between successive intervals (Figure 4.18C). This scatter diagram reveals the tendency for intervals to be followed by intervals of similar length. A scatter diagram with a relatively high concentration of points near the axis and a large dispersal of points is typical of a random series of events. Intervals between occurrences of Salt Wash graben travertine are typical of this random distribution with almost 50% of points falling close to the axis and a large dispersal of points. For Little Grand Wash intervals however, while showing a large dispersal, have no points close to the axis due to the large time gaps between deposits.

4.7.6.2 Gaps in the record

The above statistical analysis suggests a distinct lack of periodicity in the deposition of travertine mounds in the Little Grand Wash and Salt Wash graben. However these analyses should be treated with caution as the travertine record for both field areas is incomplete. We have no constraint on how long each dated mound was active for as only one mound, the L4 deposit from the Little Grand Wash, has multiple dates. The age results of samples from this mound, ranging from 113.9 ± 0.6 to 103.1 ± 1.4 ka, provide only a minimum estimate for the life span of the mound. It is also hard to use the time span and size of this mound to provide time span estimates for all of the other mounds in this study. This is due to the varying preservation potential of each individual mound. As some mounds have been eroded more than others, it is difficult comparing size of mound to gauge the length of activity. For the northern fault of the Salt Wash Graben there is a more continuous record of leakage up to ~200 ka along this fault before large gaps appear between mound occurrences. The poor preservation of several mounds, especially the oldest present, suggests that it is possible that some travertine deposits have become completely removed by erosion. The large gaps recorded between later mounds may reflect periods of time where travertine has not been preserved rather than not been precipitated. The lack of data points in the Little Grand Wash travertine makes it easy to find a trend in that data. Although mounds are better developed and more robust with concerns to erosion it is possible that several mounds may be present on the west bank of the Green River buried beneath the relict river terraces. Alternatively any travertine once

present on that side of the river, along the western limb of the anticline, could have been completely removed by the river.

4.7.7 Spatial relationships of travertine deposits

Travertine mounds in both areas are restricted to short stretches of the faults centred near the axial trace of the Green River anticline. U-series analysis of the travertine may allow an insight into the layout and structure of fluid flow pathways supplying these leakage sites in the subsurface. Both age results of travertine deposits and the supporting geochemical results provided by $\delta^{234}\text{U}$ are discussed below with reference to potential structure of leakage pathways.

4.7.7.1 Relationships from U-Th age analysis

Figure 4.19 shows the radiometric age results of travertine in both areas in a simplified geological map and as plots of age against distance from the Green River anticline. This feature was chosen as it is common to both field areas. The results for the Little Grand Wash fault show that travertine age decreases away from each side of the oldest mound, L4 (Figure 4.19A). This suggests that leakage to surface in this area may have spread out from a central initial point. Mounds L5, L6, and L7 are meters apart and occur in same link point between fault limbs. The three distinct ages of these mounds, which range over ~45 ka, and their three distinct elevations suggests that pathways may be becoming re-used throughout the leakage history of this fault.

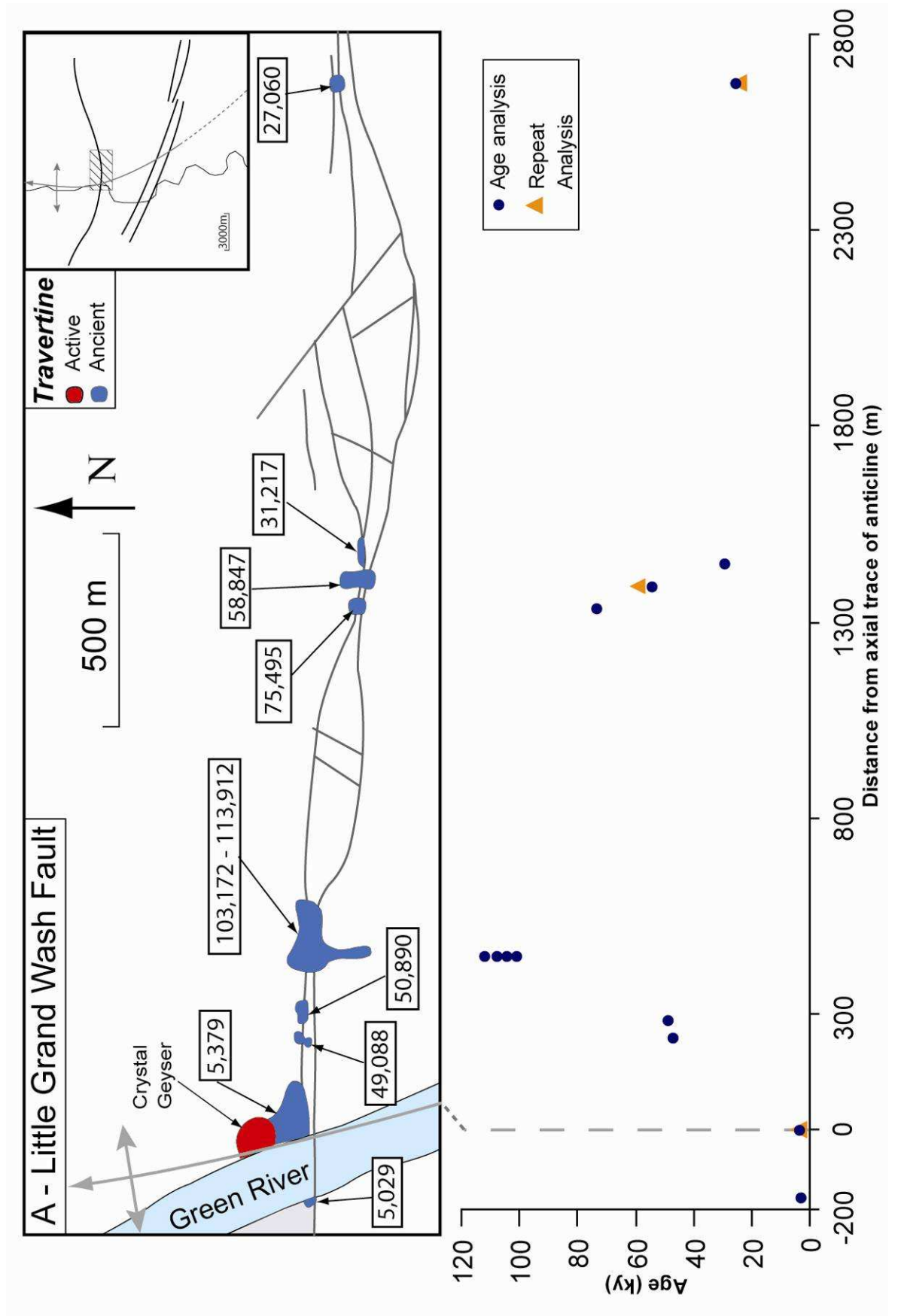
Of the 41 ancient mounds on the Salt Wash graben a total 22 were dated while estimates of the non-dated mounds have been provided by using a local calculated incision rate (Section 4.5.4). The results from these analyses and calculations show a more complex picture than the Little Grand Wash (Figure 4.19B). Similar to the Little Grand Wash fault initiation of leakage occurs centrally with the oldest deposits occurring near to the trace of the Green River anticline. Although the timing of initiation of leakage gradually decreases with time from this central point to both the west and east, like the Little Grand Wash, younger mounds are not restricted to the outer edges of this progression and occur throughout the total extent of travertine deposition. Figure 4.19B confirms the close association of travertine mounds occurring away from the fault with the trace of the Green River anticline. When age estimates of non-dated mounds are

included in the plot of age against distance from the axial trace of the anticline the story doesn't change. Estimated mounds generally fit into this sequence of the initiation of travertine deposit getting younger away from the anticline (Figure 4.20).

4.7.7.2 Relationships from $\delta^{234}\text{U}$

Two speculative models were put forward in section 4.4.2 in order to try to explain the observed spatial pattern of $\delta^{234}\text{U}$ of dated travertine mounds rising to the east of each field area. Model A involved mixing of old deep brine water carrying a low $\delta^{234}\text{U}$ and meteoric waters carrying a high concentration of ^{234}U in the Navajo aquifer, and multiple leakage points in the caprock above the aquifer. Model B was based on brine migrating through the aquifer to a single leakage point in the caprock to the west of each field site. Increased $\delta^{234}\text{U}$ to the east in this case would be a function of pathways increasing in length from the single leak point and having greater opportunity to leach ^{234}U from the lithologies above the aquifer.

The close association of travertine with fault traces and more specifically with points of increased structural complexity in the Little Grand Wash suggest that upward migrating fluids are taking advantage of discrete areas of high permeability within the fault zones. It is unlikely therefore unlikely that upwelling fluid will have the chance to interact significantly with rock in the 600 to 800 m of strata between the surface and the Navajo aquifer. Model B also implies minimal mixing of meteoric and deep brine waters with the $\delta^{234}\text{U}$ of the brine water being maintained during migration of deep waters through the Navajo aquifer. Evidence from stable isotopes of δD and $\delta^{18}\text{O}$ from modern day springs occurring in the field areas suggest a deep brine contribution of 10-20% mixed with a meteoric component of 80-90% in the source waters of the springs (Wilkinson et al., 2008). This suggests mixing of the two varieties of waters with a significant component of meteoric water, which favours Model A. It is therefore likely that $\delta^{234}\text{U}$ concentration in the meteoric waters is having a significant effect on the $\delta^{234}\text{U}$ recorded in the ancient travertine mounds with an increased meteoric signal to the west as incoming regional ground water mixes with water within the three way trap provided by the Green River anticline and the Little Grand Wash and northern Salt Wash graben faults.



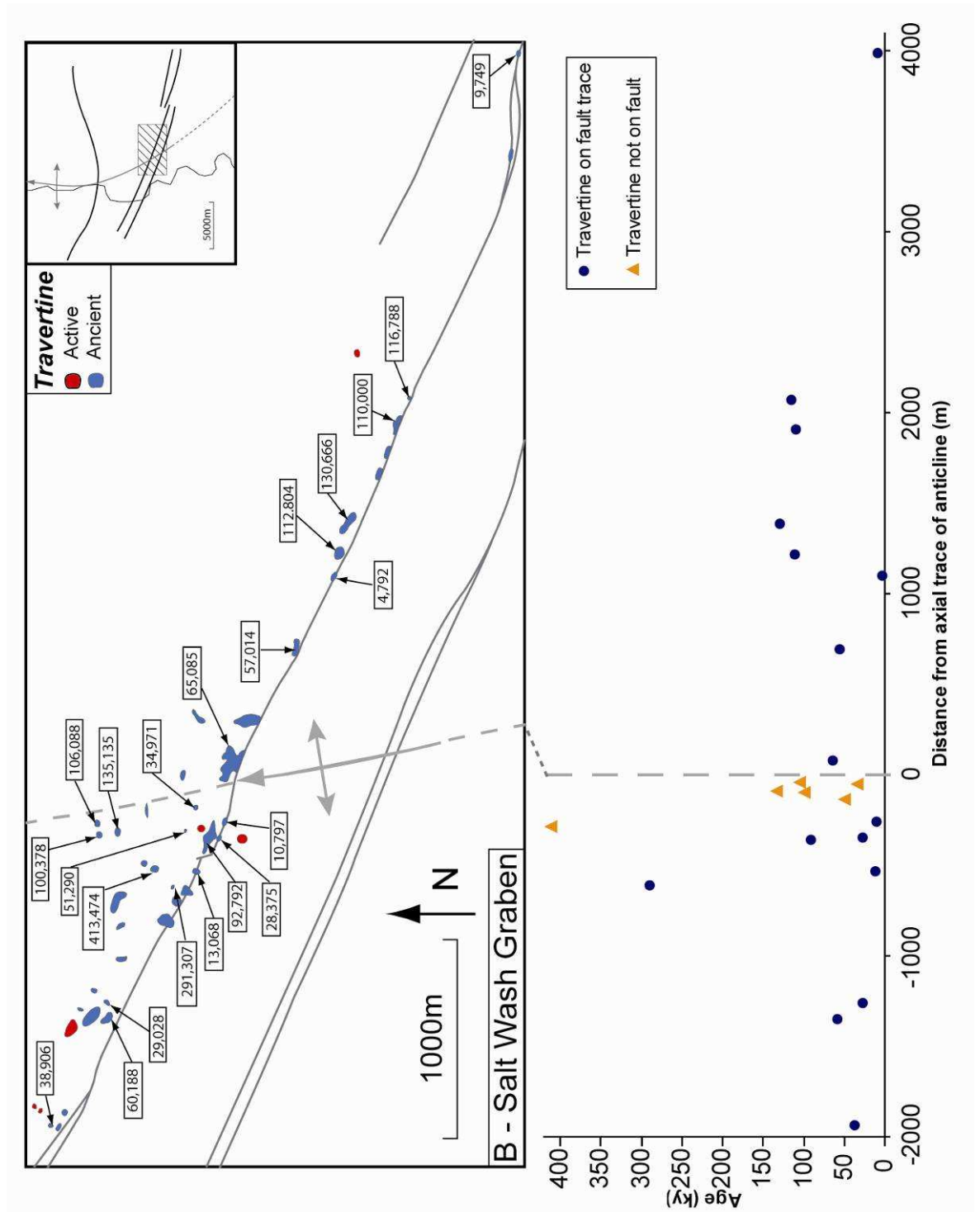


Figure 4.19: Age maps and distance plots of U-series results.

(A) and (B) show simplified geological maps showing only travertine mounds, faults, and Green River anticline. Results of U-Th dating are shown in white boxes with error omitted for clarity. The plots below the maps show results plotted as age against distance from the Green River anticline. Error on the ages, which is often smaller than the size of the points, is omitted for clarity. For the northern fault of the Salt Wash graben all travertine mounds that are located over 50 m away from the mapped fault trace are classed as 'off fault' travertine.

Further evidence for Model A is the horizontal distance of 35 km from the start of the source meteoric waters to the Green River anticline, which is almost sixty times greater than the vertical distance between the aquifer and the surface. This provides a greater opportunity for the leaching of readily soluble ^{234}U from the sandstone present in the Navajo aquifer. The potential presence of uranium rich ore bodies, with concentrations of up to 3,000 ppm, near the source of this water provides a uranium rich source from which to leach further ^{234}U .

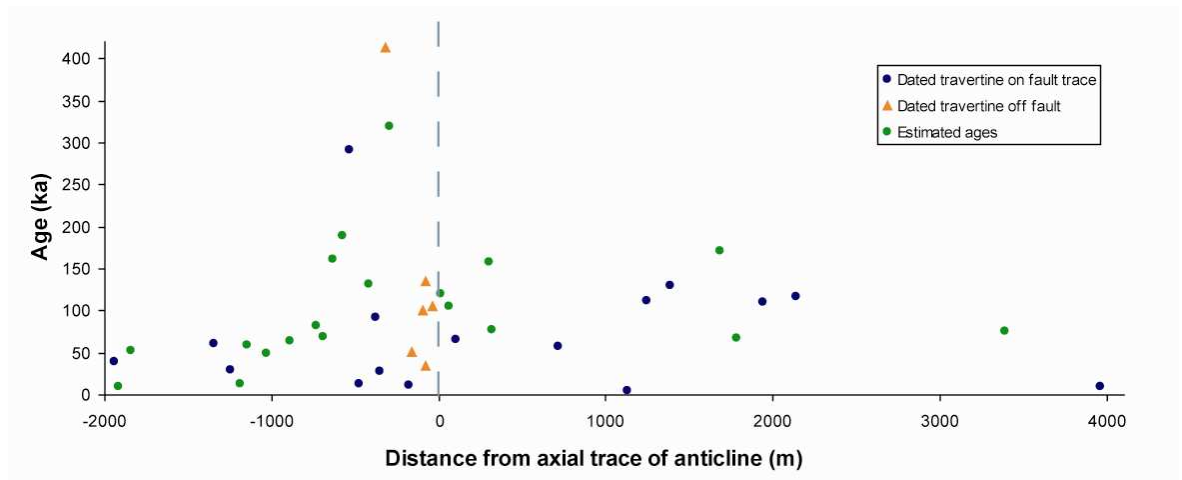


Figure 4.20: Age distance plot for the Salt Wash graben including estimated ages.

Estimated ages of un-dated mounds (calculated from incision rate) along the northern fault of the Salt Wash graben are indicated by green circles. Analytical errors on ages are generally smaller than the point on the plot and so have been omitted for clarity.

4.8 Summary: Lessons from U-Th dating

U-series dating of travertine deposits along the Little Grand Wash Fault and the northern fault of the Salt Wash Graben provide a unique data set with which to study fault related fluid flow. Subsurface formed white banded veins within these deposits provide pristine samples for U-Th analysis as they are precipitated in a

closed system. The surface layered mats facies of travertine mounds provide poor samples for dating as they are prone to introduction of non-radiogenic nuclides and so form in an open system environment. This is confirmed by the low [$^{230}\text{Th}/^{232}\text{Th}$] present in samples analysed from this facies. The supporting $\delta^{234}\text{U}$ chemistries of layered mat samples matches that of white banded vein samples from the same mound indicating that they are formed from the same spring waters. Coupled with observations from the field confirm their close association with white banded veins. This allows for well weathered mounds, devoid of layered mats, to be validated as travertine deposits.

Study of the interaction between uplift and erosion is a major theme of geology (Pederson et al., 2002), but understanding of their interplay is often limited by a lack of quantitative data. The data set obtained in this study coupled with the presence of relict river terraces allows for local incision rates to be calculated in each field site. This can provide further information into the study of incision of rivers in the area and uplift of the Colorado Plateau. Calculation of incision rates in the Salt Wash graben has also allowed for the age estimation of non-dated mounds in this area to provide a complete coverage of travertine.

The location of mounds on the Little Grand Wash faults appears to be clustered around areas of intersection between different fault strands. This suggests that flow to the surface is located along discrete vertical pathways in the fault. This may be due to increased fracture density at these points of intersection, but without knowledge of fault structure at depth this is hard to conclude. The proximal occurrence of three mounds of distinct age ranging over 45,000 years suggests that fluid flow pathways can be repeatedly reused over time scales of tens of thousands of years. From the onset of leakage 114,000 years ago leakage points have spread from a central point decreasing in age towards the extremities of travertine occurrence. It may be the case that once travertine mounds reach the end of their lifespan that new leakage spreads to the closest available high permeability pathway up the fault.

Age results for the northern fault of the Salt Wash graben, similar to the Little Grand Wash, show that initiation of leakage spreads from a central point near the Green River anticline. However, unlike the Little Grand Wash, younger deposits do not solely form progressively further out from this central point and occur throughout the area covered by travertine precipitation. Deposits also occur

away from the fault trace but are always closely associated with the anticlinal axis. The greater number of travertine in the Salt Wash graben and their less restricted locations, in comparison to the Little Grand Wash, suggests that there is a more distributed pattern of flow. Leakage away from the fault may be due to fracturing of the caprock away from the fault due to structural flexure at the crest of the anticline. Alternatively diffuse flow may be due to leakage through the exposed aquifer unit of the highly porous Entrada Sandstone. These ideas are further discussed in Chapter 5 which goes into further detail on the implications that the results presented in this chapter have for fluid flow and leakage to the surface.

What is clear in both areas is that flow to the surface does not follow a constant direction throughout leakage history. Mound locations change to both the east and west along each fault repeatedly through time. The oldest deposit occurs at the centre of travertine extent in each area, with initiation of leakage spreading out from this central point. Timelines of travertine occurrence for both areas suggests that fluid flow may not have been constant through time and that there may have been several gaps of non-deposition in the record. However, when estimated ages are included for the northern fault of the Salt Wash graben and the likely lifespans of mounds are taken into account then it can be seen that a nearly constant record of fluid flow exists for this fault over the last ~120 ka. It should also be remembered that the effects of erosion are likely to be having a large influence and some mounds may have been completely removed from the record. Statistical plots show that there is no temporal trend in the history of travertine precipitation and that timing of mounds appears to be random. Increasing $\delta^{234}\text{U}$ from west to east across both the Little Grand Wash fault and the northern fault of the Salt Wash graben suggests a spatial trend in the leaking waters supplying travertine formation at the surface. This is likely to be due to mixing of ^{234}U rich meteoric water coming in from the San Rafael Swell to the west and brine water with low $\delta^{234}\text{U}$ leaking into the Navajo aquifer from the Permian White rim sandstone at depth. The closely matching $\delta^{234}\text{U}$ of nearby travertine deposits that are separated in age by 1,000's of years confirms a spatial pattern in source waters. The results of U-series dating provide an excellent record of travertine precipitation history which clearly shows that fluid flow pathways to the surface are switching throughout both time and space.

5 Implications for fluid flow

5.1 Introduction

The history of palaeo-fluid flow preserved in ancient travertine deposits along the northern fault of the Salt Wash graben and the Little Grand Wash fault show a record of switching of leakage of CO₂ rich waters to the surface over the last 100- 400 ky. Mound deposition is spread over an along-strike distance of 2.5 km on the Little Grand Wash fault and 6 km on the northern Salt Wash graben fault. The location of leakage along each fault has switched repeatedly through time, with some travertine deposits appearing kilometres away from the previous leakage site. Particular locations have also been reoccupied after extended periods of time, with flow sometimes returning after several other leakage events elsewhere.

Potential causes of switching can be split into external and internal factors. External factors, which are discussed in section 5.2, are events outwith the fault system, such as seismic triggering and climatic control, which can have an influence on the system's hydrology. If external factors are playing a role in the switching of fluid flow pathways then it is possible effects should be seen on both faults simultaneously. In section 5.3 the direct influence of internal factors on the fluid flow history of the Little Grand Wash and northern Salt Wash graben faults will be considered. Fault structure, fluid flow properties and mineral precipitation are all internal factors which have the potential to affect fluid flow. Because internal factors are dependant on an individual fault, the effects will not be correlated between sites.

5.2 External factors

5.2.1 *Seismic activity*

Two varieties of seismic activity are considered within this section: activity of the two fault systems in question and hydrological change seismically triggered by large scale seismic activity on distant faults. Seismic activity has been known to affect hydrological systems for at least 2000 years (Esposito et al., 2001). Hydrological changes, such as dramatically changing water level and spring

discharge, which follow major earthquakes, depend on the style of faulting with the most significant response associated with slip on normal faults (Muir-wood and King, 1993) like those in the present study. Changes observed at the time of earthquakes suggest that earthquake-induced stress is the cause of hydrological variation (Elkhoury et al., 2006). Changes in the static stress field and the dynamic stress from seismic waves are both possible causes for seismically induced stress.

Static stress change within the crust surrounding a fault is generated by offset on the fault. The strain involved has the same signal as the first motion on seismograms, and can include both extension and compression. Brittle rock, sediment and soil become permanently deformed at shear strains from 10^{-4} to 10^{-3} MPa with even greater strains of 10^{-2} MPa and above leading to complete failure (Manga and Wang, 2007). Deformation of porous solids in response to static stress can instigate change in pore pressures and allow pore fluids to flow (Manga and Wang, 2007).

An induced change in permeability caused by the shaking motions of seismic waves is known as dynamic stress change. As seismic waves produce spatial variation in strain, they also result in spatial variation in pore pressure. This leads to pore pressure oscillations which can induce temporary increases in effective permeability. The magnitude of this increase scales with the amplitude of pore pressure oscillation (Liu and Manga, 2009). As permeability recovery following dynamic stressing occurs as the inverse square root of time, permeability change can persist well after the stress perturbation (Elkhoury et al., in press). This recovery suggests that a reversible mechanism such as clogging/unclogging of fractures causes the permeability increase.

Static and dynamic stresses increase with seismic activity of an earthquake but decay differently with distance, r , from the seismic event (Stein and Wysession, 2003; Felzer and Brodsky, 2006). Static stresses decrease as $1/r^3$ whereas dynamic stresses, which follow a standard empirical relationship between surface wave amplitude and magnitude, dissipate more gradually as $1/r^{1.66}$ (Manga and Wang, 2007).

Several attempts to model the hydrological effects of different styles of earthquakes have been proposed (Muir-wood and King, 1993). Most have been concerned only with saturated pores in the protolith; however, recent work has attempted to address the presence of water filled fractures. These play a key role

in hydrology as they open and close throughout earthquake cycles (Renard et al., 2000; Petit et al., 1999).

Elkhoury et al. (in press) experimented with dynamic stress on dry *in-situ* fractured sandstone samples by forcing deionised water through the resulting fractures during steady and oscillating pore pressure. Experimental conditions set the dynamic stress at 10^{-2} to 10^{-1} MPa. They found that pore pressure oscillations induced an increase in the effective permeability of the samples of up to 50% which persisted well after the stress perturbation. From these experiments Elkhoury et al. (in press) suggest that recovery of permeability following dynamic stressing occurs as the inverse square root of time (i.e. the magnitude of permeability recovery is inversely proportional to the square of the travel time from the dynamic stress source). The permeability recovery indicated that a reversible mechanism, such as clogging/unclogging of fractures by particles produced by the initial fracturing of the sandstone, caused the permeability increase.

In a series of contemporary experiments Liu and Manga (2009) investigated the evolution of permeability in saturated fractures within sandstones in response to dynamic stress. They also added silt sized particles to some fractures to assess the role of mobile particles. Liu and Manga (2009) found that permeability decreased after shaking and that fracture apertures decreased within the samples. Fractures with added particles showed a larger change in permeability suggesting compacting and trapping of the mobile particles effectively clogged the sample, particularly at the narrowest constrictions along flow paths.

Although changes in pathway have not been investigated, these experiments can perhaps give clues to the behaviour of discrete channels of fluid flow in response to seismic stress. The experiments of Elkhoury et al. (in press) involved fracturing under dry conditions and so perhaps are analogous to fracturing and failure of sealing lithologies, such as the Carmel Formation above the Navajo aquifer. The experiments of Liu and Manga (2009) were carried out using completely saturated fractures so could be taken to represent an active fluid flow pathway. In both cases the effects of unblocking and blocking of pathways is enhanced by the presence of loose particles. Clogging by compaction and trapping of particles in sections of pathways resulted in a decrease in permeability, whilst remobilisation of particles was found to produce two competing effects. The removal of blockages created permeability by opening up pathways; however, if

the particles moved away from regions where they were maintaining the width of a pathway then the pathway contracted and permeability was decreased.

The following subsections will go into detail on possible earthquake activity on the Little Grand Wash and northern Salt Wash graben faults and then go onto discuss seismic triggering and compare the palaeoseismic record of distant faults with switching of pathways on the faults in the present study.

5.2.1.1 Earthquake activity on the Little Grand Wash and northern Salt Wash graben faults

The Little Grand Wash and Salt Wash graben faults are listed on the USGS Quaternary fault index as 'not active' (USGS and UGS 2007, Hecker, 1993). However, there is history of seismicity in the local area. In the nearby Canyonlands region, 80km due south of Green River, over 150 events were recorded between 1979 and 1987 (Wong and Humphrey, 1989). The largest of these was M 1.8, so nowhere near enough to induce surface rupture (McCalpin, 1996), and the poorly constrained focal depths appeared generally deep (15 to 25km). Microearthquakes have also been observed near the Shay Graben faults, the only faults to display Quaternary displacement in the Canyonlands region. Again however, the exact location and cause of these minor seismic events is unclear (Wong and Humphrey, 1989).

The main piece of palaeoseismic evidence that would suggest recent seismic activity on the Little Grand Wash and Salt Wash graben faults would be the presence of a surface rupture. Surface ruptures can be instigated by five separate modes of faulting, ranging from coseismic slip to steady creep (Sibson, 1983). The mode that occurs during earthquakes depends primarily on the speed of its occurrence, or characteristic rise time, which is defined as the time for 90% of the slip to occur at a point on the fault (Sibson, 1983). Bonilla (1988) reclassifies Sibson's five modes of faulting into two all encompassing definitions; coseismic slip in which rupturing occurs suddenly with a rise time of a few seconds; and seismic creep in which rupturing occurs gradually with a rise time of minutes to days. Surface rupture for coseismic slip events has only been observed in historic earthquakes above a moment magnitude (M_w) of 5 (McCalpin, 1996), while seismic creep events have been reported to show surface rupture for earthquakes with M_w of 2.5 or greater (Bonilla, 1988).

Shipton et al. (2004) state that the structural relationship between the Little Grand Wash and northern Salt Wash graben faults and their travertine deposits are consistent with recent fault movement offsetting the surface. This is based on field observation that some of the travertine mounds appeared to be nestled within a hanging wall half-graben, which they attribute to syn-depositional movement along the faults. They find that the thickness of mound L4 is greater in the hanging wall of the fault and suggest that the Little Grand Wash fault may be cutting a pre-existing deposit.

5.2.1.2 Geomorphological constraint on fault movement

Detailed field investigation coupled with radiometric dating of deposits in the present study provides new insights into the faults and their associated travertine mounds. Direct contacts between travertine mounds and the fault are often obscured by scree slopes of angular travertine clasts or fine-grained fault gouge. Despite this, several mounds across both areas have a clear contact between their base and both the footwall and hanging wall sides of the faults. This allowed for potential offset within the mounds to be observed. River terrace deposits from the Little Grand Wash fault and long profiles of the tributary streams of the northern fault of the Salt Wash graben were also utilised in order to provide a further geomorphological constraint for movement of the Little Grand Wash and northern Salt Wash graben faults.

5.2.1.3 Constraining movement on the Little Grand Wash fault

5.2.1.3.1 Evidence from travertine deposits

All travertine mounds in the Little Grand Wash area straddle the fault trace with no evidence of being offset. A schematic of the oldest L4 mound straddling the Little Grand Wash fault is shown in Figure 5.1. The layering of the travertine itself shows no offset, though a slight fault scarp exists in the host rock either side of the fault. This scarp is likely to be a pre-travertine erosional feature due to the relative rock hardness of the Brushy Basin Member sandstone in the footwall and the softer and more easily erodible Mancos Shale Member in the hanging wall of the fault.

5.2.1.3.2 Evidence from river terrace deposits

River terraces are formed and preserved as a stream changes activity between incision, lateral planation and alluviation (Reading, 1978). These changes are commonly thought of in terms of balance between the driving forces of available stream power and the resisting forces that must be overcome to transport the sediment load. River gravels deposited by the Green River, like those deposited on the west bank in the Little Grand Wash area are termed mainstream (M) gravels (Charlton, 2008). The more minor gravels deposited from the tributary streams of main rivers are termed piedmont (P) deposits (Charlton, 2008). Piedmont terraces are less mature, have a finer grain size, and are composed only of poorly sorted clasts of local outcropping rock.

The river terraces on the west bank of the Green River in the Little Grand Wash are also not offset by the fault. Field mapping led to the determination of six separate ancient mainstream channels of the Green River stacked upon one another (Figure 5.1A and C). These were numbered according to stratigraphic age ranging from the most recent, M1, ~1.5 m above the present day river level, to the oldest, M6, ~55 m in elevation above the present day river level (Figure 5.2). The deposits are dominated by imbricated small pebbles, interspersed with the occasional sand lens. Exposures of the M5 terrace in a quarried gravel pit and along big N-S gullies show that this terrace has a planar basal contact on top of the fault and is undisturbed (Figure 5.1D). If the fault was moving at even a mild pace (e.g. a time averaged slip rate of 0.005-0.01 mm/yr would produce a total offset of between 0.5-1 m for the last 100 ky) the M5 gravel would show evidence of dip down into and towards the fault, or would be bent upward as it approached the fault due to drag and downward movement in the hanging wall (McCalpin, 1996). The gently sloping land surface of local hill slope piedmont gravel and gully deposits coming down from the Morrison bluffs immediately to the north out onto the M5 gravel is undeformed and shows no sign of a fault scarp. Piedmont slopes of small and weak drainage systems such as this would not be able to denude or destroy a scarp over time. There is no evidence of a break in vegetation or gullying following the fault trace. These geomorphological indicators provide further solid evidence of negligible movement on the Little Grand Wash fault.

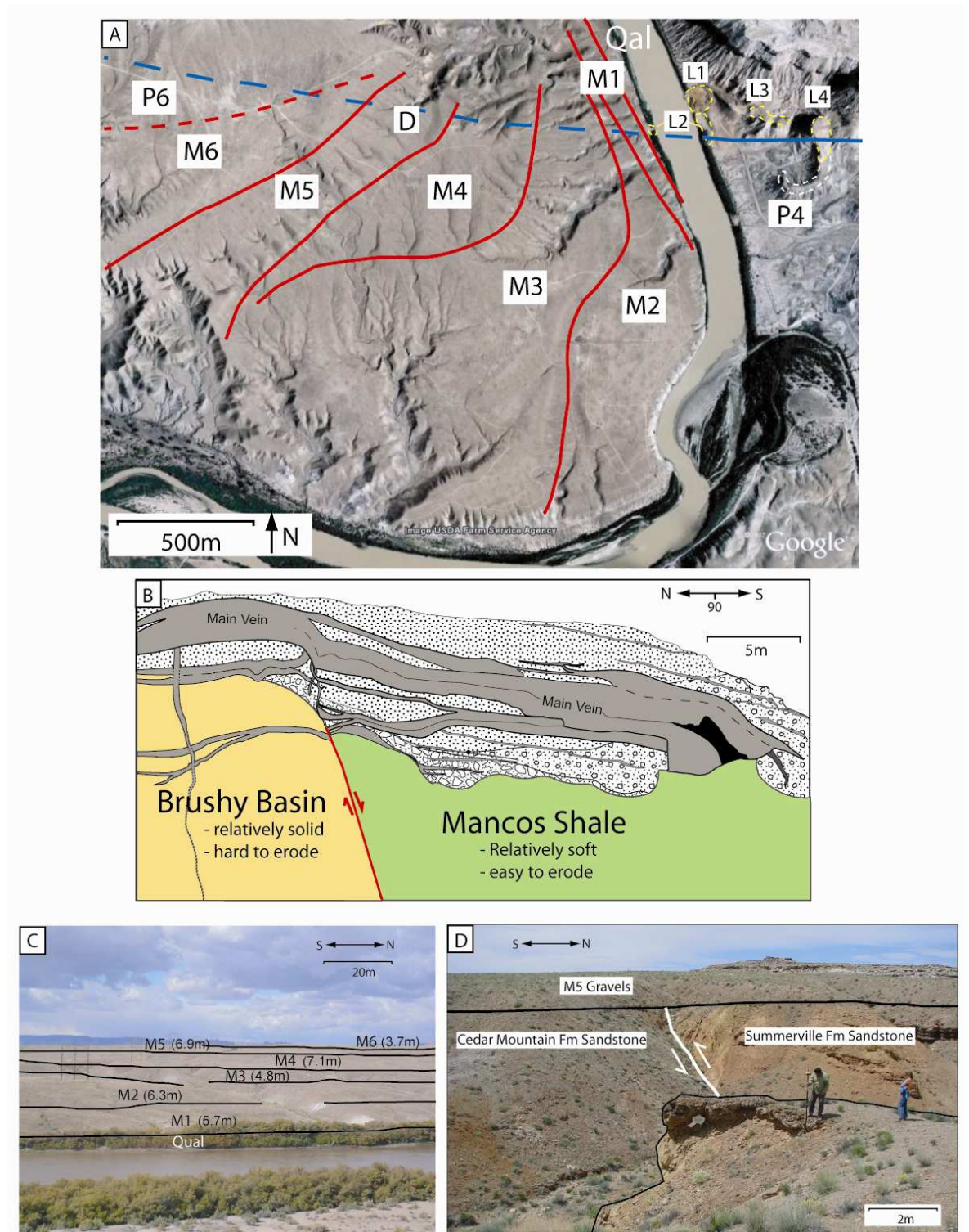


Figure 5.1: Evidence for lack of recent movement on the Little Grand Wash fault.

(A) Location map (base taken from Google Earth) showing Holocene river terraces present on the west bank of the Green River as mapped by myself and Joel Pederson. Mainstream terraces are labelled M1 to M6, and piedmont gravels P4 and P6. Travertine mounds L1, L2, L3 and L4 are highlighted with gravel P4 protruding from L4. Letter D shows the location of figure (D). (B) Schematic of mound L4 (after Dockrill, 2006) showing the lack of disruption of travertine layers and reason for apparent scarp of host rocks. (C) View of terraces looking west from edge of P4 with thickness of each terrace in brackets. (D) Closer investigation of the M5 river terrace showing no offset across the fault. Location of picture shown in (A).

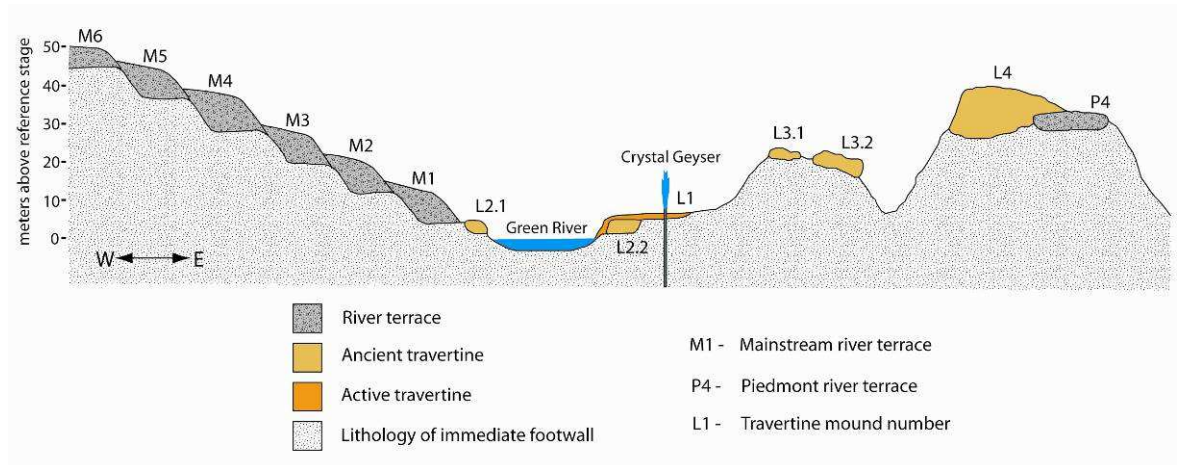


Figure 5.2: Sketch cross section of the geomorphology of the Little Grand Wash.

Section is shown in the plane of the Little Grand Wash Fault. Immediate footwall lithology in this section of the fault, Curtis Formation and Summerville Formation, are grouped together as emphasis is on surficial Quaternary deposits.

5.2.1.4 Constraining movement on the northern Salt Wash graben fault

5.2.1.4.1 Evidence from travertine deposits

Mound S12 occurs right on the banks of the modern day Salt Wash graben tributary. This mound appears to have two distinct lobes of layered mats with an older orange coloured section occurring on top of the footwall side of the fault and a grey section covering the hill slope from the fault down to the tributary (Figure 5.3A). The angle of rim pools of the layered mats on the surface and the presence of stalactites on the grey section confirm that it is insitu (Figure 5.3B). This segment of the mound abruptly stops at the fault where a ~2 m section of the footwall is exposed. Altered host rock comprises ~0.5 to 1 m of this vertical wall along the extent of the mound with the remaining thickness made up of orange layered mats. The grey colouring of the lower section may hint that it is a different age, however this 'bleaching' of layered mats is visible at the modern Crystal Geyser (L1) at points where solidified layered mats has been submerged for presumably extensive periods of time beneath the Green River (Figure 3.15). The colouration difference is therefore likely to be a result of the submergence of this section of the mound under the surface waters of the Salt Wash graben tributary during precipitation of the mound.

As previously discussed (section 3.5.4.2) mound S21 has no insitu layered mats. However the altered host rock here sits at an angle of roughly 45° across the top of the fault and there is no offset in the white banded veins suggesting no

fault movement for the lifespan of this mound (Figure 5.3C). The fault is also visible beneath travertine deposit S33. Similar to L4 in the Little Grand Wash this mound has a thicker extent of travertine in the footwall of the fault (Figure 5.3D). Again there is a fault scarp present but the undisturbed nature of the layering suggests this is a pre-mound erosional feature and indicates that there has been no movement on the fault since the formation of this mound.

5.2.1.4.2 Evidence from stream profiles

A river is said to be in equilibrium when the driving and resisting forces acting upon it are balanced such that neither aggrades or incises and takes its characteristic long term profile (Griffiths et al., 1996). Tell tale signs of fault movement can be picked up by sharp disturbances or 'knick points' in the long profile of a river. Knick points highlight locations in a river where there is a sharp change in channel gradient, such as a waterfall or lake, resulting from different rates of erosion above and below the knick point.

The long profile of the Big Bubbling Wash, which crosses the fault between mounds S24 and S25 (Figure 4.2), provides further evidence of recent quiescence of the northern fault of the Salt Wash graben (Figure 5.3E). The steady gradient of its profile shows no evidence of a knick point and therefore no evidence of a sharp change in channel slope. Due to the small size of this stream it is unlikely that incision across the fault would be strong enough to remove any evidence of fault slip and resultant scarp at the surface.

5.2.1.5 Qualitative and quantitative estimates of fault quiescence

Several travertine mounds that straddle the faults in both areas show no evidence of being offset. Radiometric dating of some of these mounds therefore gives minimum estimates for the time since last activity on the two faults. In the Little Grand Wash area the oldest and most prominent L4 mound shows a clear contact with the fault trace, age analysis of this deposit suggests that this fault has not moved for at least ~114 ka (L4 study, section 4.3.3). U-series age determination of travertine S21, which straddles the northern fault of the Salt Wash graben confirm there has been no fault movement for a minimum of ~116 ka (section 4.3). Based on incision rate calculation, the age estimate of the non-dated S33 mound in the Salt Wash graben extends this period of fault inactivity to around 190 ka (section 4.5.3).

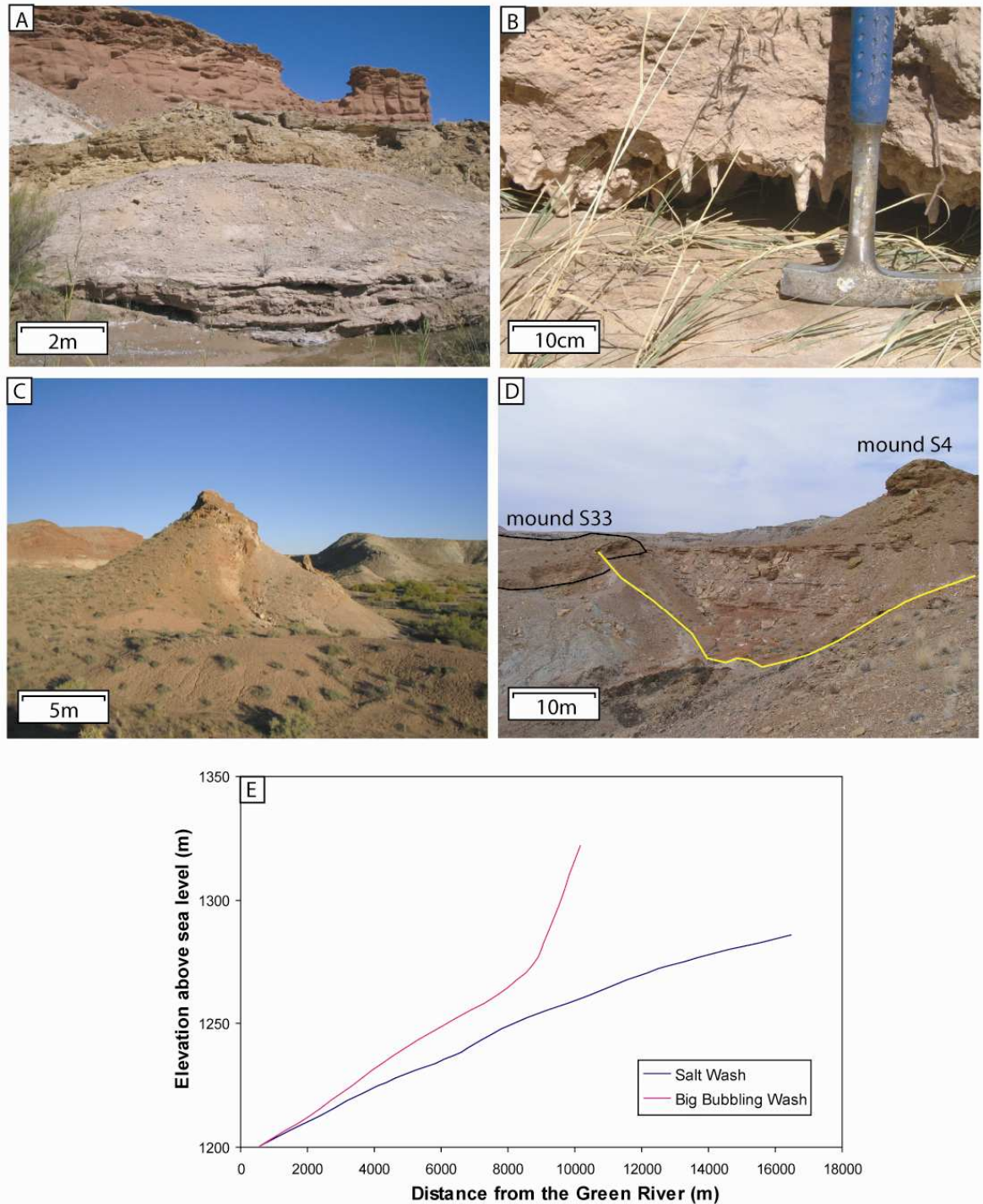


Figure 5.3: Evidence for lack of recent movement on the northern Salt Wash graben fault.

(A) Image of mound S12 taken looking north showing the orange segment of the mound situated in the footwall and the grey lobe protruding out from the fault. (B) Base of the grey lobe from this mound demonstrating stalactites. (C) Mound S21 looking west, showing the tilt of travertine and the isolated block that has slide part way down the scree slope on its northern side. (D) Image of mound S33 with the fault highlighted in yellow. Similar to mound L4 a thicker section of travertine occurs in the hanging wall. (E) Long profiles of tributaries associated with the northern fault of the Salt Wash graben.

Further qualitative evidence against fault movement in the Little Grand Wash comes from a thick sequence of six separate river terraces comprising of gravels deposited by the Green River. Here the second oldest terrace, M5, has a basal contact with the fault trace and shows no sign of offset. Stratigraphical correlation of the younger M4 terrace deposit with piedmont gravel (P4) of similar elevation entrained within mound L4 suggests that terrace M5 is older than any travertine deposit in this location (Figure 5.2). By taking the elevation of this deposit and applying the calculated incision rate for the Little Grand Wash area (section 4.5.2) the age of terrace M5 is estimated to be 137 ka, which further increases the minimum estimate of quiescence on the Little Grand Wash fault. In the Salt Wash graben area the long profile of the Big Bubbling Wash, which runs over the fault has a smooth gradient and shows no sign of any knick points. The small scale of this wash coupled with a long profile that is in equilibrium provides further support for a recent lack of movement at the surface along this fault.

However, it should be noted that seismic activity has been reported to occur with no evidence of surface rupture. Archaeological and historical records indicate a number of destructive earthquakes during Roman times which suggest a 2,000 year history of large scale seismic activity along the Pamukkale Range Fault, Turkey (Hancock and Altunel, 1997). No significant surface rupture or related travertine deposition occurred during this time (Uysal et al., 2007). So, it is not possible to rule out seismic activity at depth that has affected the hydrology of the faults but not instigated surface rupture.

5.2.1.6 Hydrological changes induced by seismicity on other faults

5.2.1.6.1 Introduction

Seismic activity on distant faults can potentially alter the hydrology of inactive fault zones. Localised earthquakes and fluctuations in geyser and spring systems associated with large earthquakes on distant faults have been well recorded across the United States (e.g. Rowland et al., 2008; Rubenstein et al., 2009; Manga and Rowland, 2009). Sustained change in ground water pressure, often an order of magnitude larger than can be explained by static stress change, can be attributed to distant earthquake activity (Brodsky et al., 2003). This effect is produced by the interaction of seismic waves with aquifers, which can produce sustained changes in pore pressure 100s of kilometres from an earthquake (King et al., 1999). The distance involved with many of these triggering events makes it

likely that dynamic rather than static stress change is the key factor. This is because static displacement decays more rapidly with distance from the earthquake (Stein and Wysession, 2003; Felzer and Brodsky, 2006). The redistribution of pore pressure by seismic triggering can potentially generate crustal deformation (Brodsky, 2006; Johnston et al., 1995) which has implications for the alteration of fluid flow pathways.

Previous work on regional scale seismic triggering suggests that seismic waves generate pore pressure changes in geothermal areas that in turn generate changes in hydrology (Hill et al., 1993; Stark and Davis, 1996). For hydrological systems to be affected by seismically induced pore pressure changes they generally need to meet three separate criteria; (1) have low matrix specific storage, (2) contain fractures or faults, and (3) have a source of material available for clogging (Brodsky et al., 2003). The Little Grand Wash fault and the northern fault of the Salt Wash graben meet all three criteria. Specific storage, the volume of fluid a unit volume of aquifer releases under a unit decrease in head (Fetter, 2001), is not well recorded for strata in the field areas. Hood and Danielson (1981) do present a generalised value of 1×10^{-3} for the Navajo sandstone which is at the upper end of aquifer specific storage values. Being the most permeable aquifer unit in the field (Table 5.1) it is very likely that the rest of the strata have lesser values. Faults are prominent features of both field sites whilst the presence of numerous travertine deposits demonstrates the abundance of calcium carbonate, which is a potential clogging agent.

Due to the poor seismic record and lack of evidence for seismic activity in the Little Grand Wash fault and Salt Wash graben it is hard to say whether permeability changes were generated on these faults in response to activity on distant faults. The hydrological regimes in question however meet the criteria listed above so it is not inconceivable that pore pressures within these systems were affected by seismic activity tens of kilometres distant. In the following sections the stress state of the faults will be discussed in order to determine if they have the potential to be affected by distant activity. Occurrences of induced seismicity will then be examined, focusing on Yellowstone National Park. Finally a review is undertaken of the timing of distant regional seismic events and their potential effects on the Little Grand Wash and northern Salt Wash graben faults.

Unit	Boyle's Law Porosity (%)	Calculated Porosity (%)	Permeability (Millidarcies)	Permeability (m ²)	Average thickness (m)	Area (km ²)
Entrada Sandstone	-	26.4	-	-	-	-
Navajo Sandstone	17.7	19.5	534.5	5.28 x 10 ⁻¹³	125	3,700
Kayenta Formation	19.6	21.4	500	4.93 x 10 ⁻¹³	-	-
Wingate Sandstone	20	21	340	3.56 x 10 ⁻¹³	122	3,780
Moss Black Member	-	14.3	-	-	-	-
Sinbad Limestone	8.2	-	-	-	-	-
Kaibab Limestone	8.6	-	-	-	-	-

Table 5.1: Permeability and porosity of strata present in the field.

The Navajo sandstone, Kayenta Fm, and Wingate sandstone make up the main aquifer supplying the springs in the field areas- the Navajo aquifer. Also included is data from the Entrada Sandstone, one of the surface lithologies of the Salt Wash graben, and Permian and Triassic strata. The Moss Black member is a conglomerate of the Chinle Fm, whilst the Sinbad limestone is a 10-15 m thick section of limestone from the Moenkopi Fm. The Kaibab limestone is late Permian. Data collated from Hood and Patterson (1984). Included in the table is the Boyle's law porosity of some of the strata. This measurement is carried out on cored rock samples and determined by injection of a gas, usually air or helium, into a porosimeter. Boyle's law, expressed by the equation $P_1V_1 = P_2V_2$, states that under conditions of fixed gas quantity and constant temperature the product of the pressure and volume stay constant.

5.2.1.6.2 Stress orientation of the Little Grand Wash and northern Salt Wash graben faults

The permanent and dynamic stress changes inferred to trigger earthquakes are usually orders of magnitude smaller than the stresses relaxed by the earthquakes themselves, implying that triggering occurs on critically stressed faults (Hill et al., 1993; Gomberg et al., 2004). It is therefore important to determine whether the Little Grand Wash and northern Salt Wash graben faults are optimally primed for failure. This can be achieved by looking at the orientation of the faults and comparing this to the ambient stress field for the surrounding region (Sibson, 1985; 1990). The contemporary seismicity of the Colorado Plateau is typified by widely distributed earthquakes of small to moderate magnitude, the largest of which have been observed to have a M_w of 5-6 (Wong and Humphrey, 1989). Very few of these events can be associated with geologic structures and so appear to be associated with the reactivation of pre-existing faults that lack surficial

exposure. Predominance of nearly vertical maximum principal stress indicates that normal faulting is the dominant style of seismic slip within the plateau (Wong and Humphrey, 1989). This is supported by the work of several further researchers whose collated work around the Colorado Plateau is shown compiled as part of the World Stress Map (Figure 5.4).

The present day state of stress in the Colorado plateau is characterised by a uniform northeast to southwest trending extension (Wong and Humphrey, 1989). This is demonstrated by the dominance of northwest to north-northwest striking normal faults within the Colorado Plateau (Figure 5.4). The Little Grand Wash fault (striking west-east) and northern fault of the Salt Wash graben (striking northwest – southeast) are therefore optimally oriented for failure and are potential candidates for seismic triggering.

5.2.1.6.3 Yellowstone case study

The recent effects of earthquakes on the Denali fault, Alaska (2002) and Landers fault zone, Mojave Desert, California (1992), on geyser activity at Yellowstone National Park are well documented. Numerical simulation of geyser systems by Ingebritsen and Rojstaczer (1993, 1996) suggest that their existence depends on a combination of rock properties, and thermal and hydrological conditions; and also intimate that the deeper parts of geyser conduits are likely to consist of anastomosing fracture networks. Within these conditions eruption frequency is highly sensitive to the intrinsic permeabilities of geyser conduits and their surrounding rock matrix, and the pressure gradients within the system.

The findings of Ingebritsen and Rojstaczer (1993, 1996) show that the geyser system at Yellowstone can be used as an analogue for the hydrological systems in the present study because fluid flow in both instances is dominated by a highly fractured medium containing highly pressurised multiphase fluids. While the phases at Yellowstone consist of steam and liquid, there is potentially a range of phases present in the Little Grand Wash and northern Salt Wash graben fault cases, with liquid, gas and supercritical fluid in various combinations a possibility. Unlike the field areas in the present study, in which carbonate is the main precipitate, fractures in hydrothermal areas are clogged by rapid precipitation of silica. Similarly though, loosening of these mineral deposits can reopen existing fractures and alter permeability, thus changing fluid flow pathways.

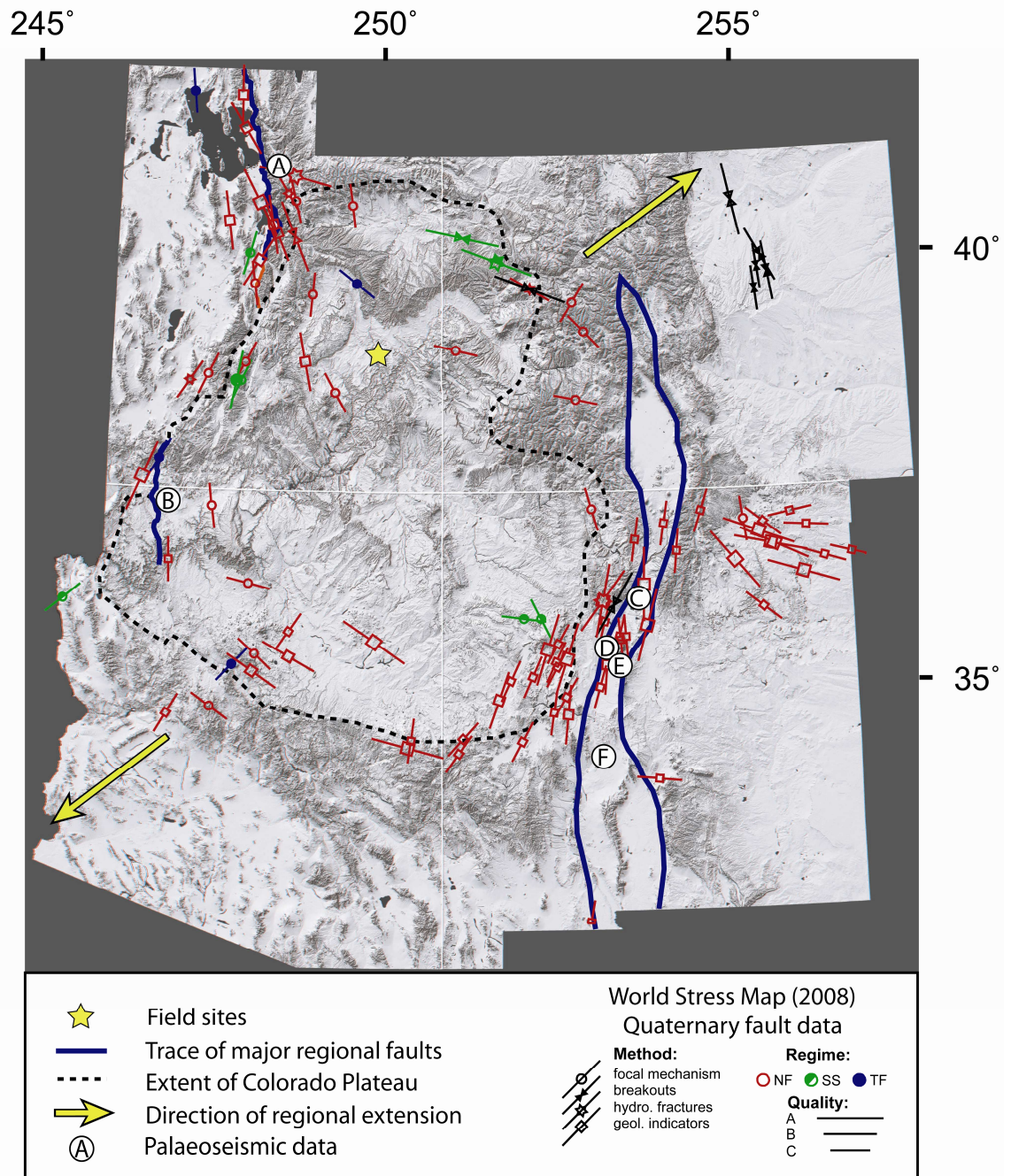


Figure 5.4: Data from World Stress Map and Location of major regional faults.

Image is a 3D topographic image of the states of Utah, Colorado, Arizona, and New Mexico (SAHRA, 2007) with data from the World Stress Map (USGS and UGS, 2007; Heidbach et al., 2008) compiled from various researchers. The yellow star marks the location of the field areas whilst the black dashed outline marks the boundary of the Colorado Plateau (Pederson et al., 2002). Dated sections of faults mentioned in the text are signified by lettering; A- Wasatch Fault; B- Hurricane fault, C- Parajito fault, D- Calabacillas fault, E- Hubbell Spring fault, F- La Jencia fault. Faults C-F are situated within the Rio Grande Rift. Fault traces are from the works of Lund et al., 2002; Chang and Smith, 2002; McCalpin, 2005; McCalpin, 2000; Personius and Mahan, 2003; and Machette, 1986. Quality of stress data record from the World Stress Map is ranked according to the scheme introduced by Zoback and Zoback (1989), and Zoback and Zoback (1991), and refined and extended by Sperner et al. (2003). Groupings of this scheme refer to the orientation of the maximum horizontal compressional stress (S_H) and are accurate to within $\pm 15^\circ$ for 'A' quality, $\pm 20^\circ$ for 'B' quality and $\pm 25^\circ$ for 'C' quality.

Geysers periodicity has been observed to be sensitive to small strains (of 0.01 to 1 microstrain) in the Earth and so can potentially be influenced by seismicity, caldera resurgence and deflation, Earth tides, barometric pressure, availability of meteoric recharge and wind (Ingebritsen and Rojstaczer, 1996). In a field study of Upper Geysers Basin, Yellowstone, Rojstaczer et al. (2003), found most of these aspects do not have any influence on eruptive periodicity. No statistically significant evidence of Earth tide or atmospheric-pressure influence was observed, leading to the conclusion that geysers periodicity was insensitive to deformation on the order of less than 20-100 nanostrain. This suggests that in order for geysers periodicity to respond to seismic activity an earthquake event must be create a strain signal greater than this range of values.

The Denali earthquake, associated with a surface rupture of 340km and a M_w of 7.9, was one of the strongest strike-slip events to be observed in North America over the last 150 years (Eberhart-Phillips et al., 2003). Evidence of induced seismicity in response to this event was recorded up to 3,385 km from the epicentre (Gomberg et al., 2004). More than 200 small earthquakes were triggered within 18 hours in Yellowstone, 3,100 km south-east of the epicentre. Subsequently more than 1,000 earthquakes were recorded over the course of a week, with earthquake swarms occurring simultaneously close to different major geysers basins (Husen et al., 2004). These tremors, ranging from M_w 0.5 to 3.0, could not be located accurately enough to determine the epicentre or depth of their origin (Smith, 2004). Coupled with this triggered seismicity, the alteration in the eruption cycle of several geysers was observed within hours of main shock. It is likely that these events were induced by the arrival of large amplitude surface waves which caused dynamic stresses of up to ~470 nanostrain (Husen et al., 2004).

The Landers earthquake, an M_w 7.3 right lateral strike-slip event, occurred on the 28th of June 1992 in the Yucca Valley, South California. This was the largest seismic event to occur in California for 40 years and was accompanied by an M_w 6.1 foreshock and M_w 6.2 aftershock (Hauksson et al., 1993). The main event produced surficial offsets of up to 6 m and a rupture length of 85 km (Sieh et al., 1993), though it is reported that over 100 km of the sequence was ruptured if concealed faults are also taken into account (Hauksson et al., 1993). Seismic activity 1,250 km to the north-east at Yellowstone was found to be triggered by the main event (Hill et al., 1993). This was the most distant associated activity and

occurred in a small cluster 15 km north-west of the Yellowstone caldera within the Yellowstone National Park. Static stress changes calculated for elastic models of the earthquake, by Hill et al. (1993), appear to be too small to have caused this triggering. The authors of this study propose that large dynamic strains associated with seismic waves emanating from the main shock may have triggered this further and far reaching seismic activity. Stark and Davis (1996) suggest the Landers event may have been particularly efficient at generating remotely triggered swarms throughout the western United States because of its size and shallow focal depth, which would promote large surface waves.

It should be noted that changes in geyser activity at Yellowstone have not been restricted to these two seismic events. Significant changes in eruption patterns have also been observed following large regional (<200 km) earthquakes, such as Hebgen Lake, Montana, (M_w 7.5, 17th August, 1959) and Borah Peak, Idaho, (M_w 7.3, 28th October, 1983). The Borah Peak event, which has been estimated to have produced a static strain of 100 nanostrain (Okada, 1992), was observed to alter the interval between eruptions at Old Faithful geyser. Rojstaczer et al (2003) suggest that this response was due to dynamic ground motions affecting in the physical state of the geysers leading to, at least temporarily, alteration in local permeability.

The Denali and Landers events were also observed to affect locations closer to the field sites in the present study. Stark and Davis (1996) report minor activity in response to the Landers earthquake at Geysers geothermal field in California, which is an identical distance from the main shock as the Little Grand Wash fault (760 km to 763 km). This event also triggered an earthquake swarm near Cedar City in south-west Utah, 490 km from the epicentre and only 290 km from the Little Grand Wash fault. More than sixty earthquakes were triggered here with at least seven of them felt locally in the Hurricane fault zone (Hill et al., 1993). It has also been suggested that the Denali event triggered small quakes in northern Utah, occurring near little-known hot springs along the Wasatch fault (University of Utah Science Daily release, 2004), which is only 265 km from the Little Grand Wash fault. While changes in geyser periodicity appear synchronous with major earthquakes in the examples outlined above, it is important to note that identification of tectonically induced changes in permeability requires seismic events to be synchronous with a period of otherwise relative quiescence in geyser eruptive variability (Rojstaczer et al., 2003).

5.2.1.6.4 Potential sources for triggering of seismicity at the Little Grand Wash and Salt Wash graben faults

As seismic triggering on distant hydrological systems is well documented and the Little Grand Wash and northern Salt Wash graben faults are optimally orientated within the present day Colorado Plateau stress regime, potential sources capable of triggering variation in hydrology along these faults were investigated. Due to the far reaching distance of the recorded affects of the Denali and Landers events, it is conceivable that any major earthquake within ~3,000km may potentially have had an influence on the permeability of fluid flow pathways in the Little Grand Wash and northern Salt Wash graben faults. Due to time constraints the investigation of potential triggers focused on the palaeoseismic history of large active fault zones within ~500 km of the field sites. The three key fault zones within this proximity were identified, all of which were known to have hosted large seismic events in the recent past: the Rio Grande Rift in New Mexico, the Hurricane Fault in south-west Utah and the Wasatch Front in northern Utah (Figure 5.4, Figure 5.5). All of these faults have a normal sense of slip and strike ~ north to south, and so are typical of faults in the northeast - southwest extensional regime of the Colorado Plateau. The Hurricane fault and Wasatch front are both situated within a prominent north-south trending zone of earthquakes within the western United States interior known as the Intermountain Seismic Belt (ISB). This zone marks an intraplate extensional regime extending 1,300km from Montana to Northern Arizona (Smith and Sbar, 1974; Chang and Smith, 2002).

Dynamic stress change was found to be the trigger of seismicity of the two examples discussed above (Section 5.2.1.6.3). It should be noted that this mechanism should be enhanced in directions where rupture directivity focuses radiated energy (Gomberg et al., 2004). For the palaeo-earthquake examples highlighted in this section it is impossible to deduce the direction of the energy released from the events, therefore it is hard to say for certainty which, if any, has the most potential for triggering permeability changes on the Little Grand Wash and northern Salt Wash graben faults.

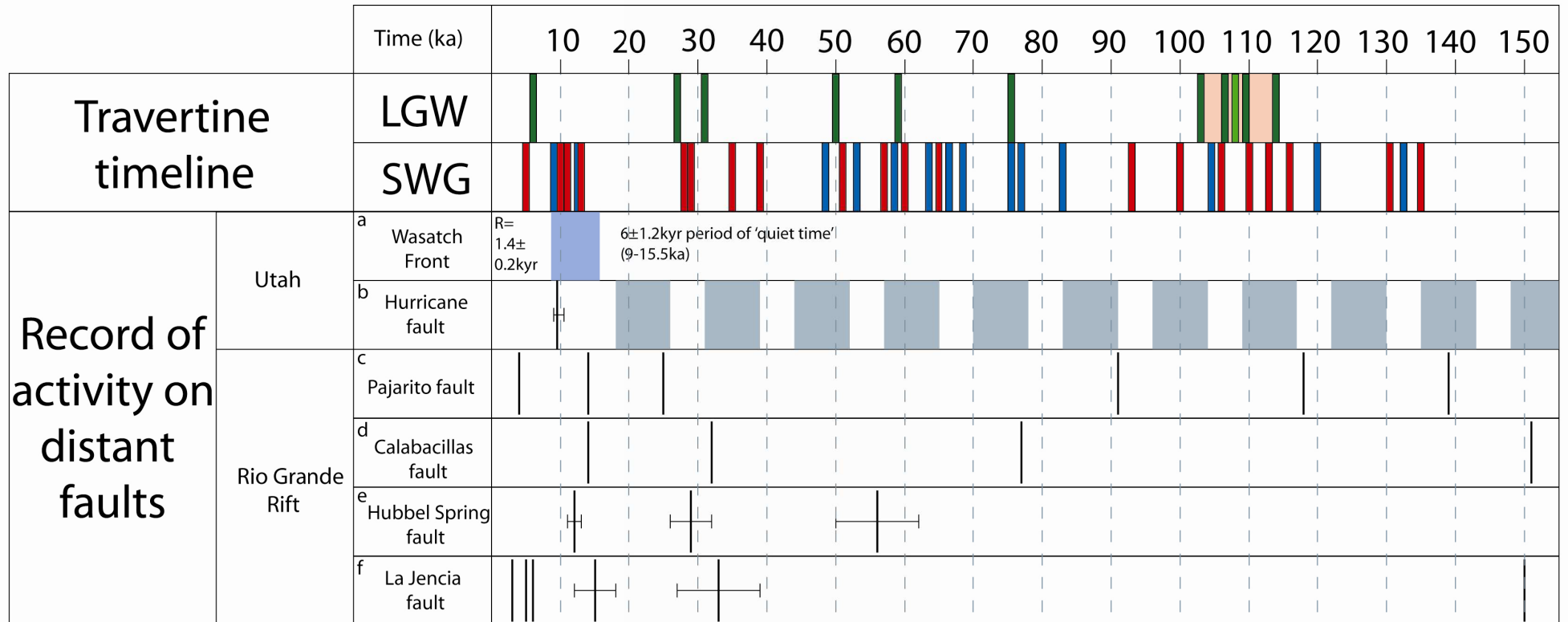


Figure 5.5: Timeline of travertine occurrence against regional seismic activity.

The top two rows demonstrate the occurrence of travertine in the Little Grand Wash and Salt Wash graben. U-Th dated mounds (the errors of which are smaller than the width of the bars) shown as red bars and age estimated mounds from the northern fault of the Salt Wash graben shown as blue bars. The four separate ages from mound L4 are shown with the area between them shaded to show the life span of the mound and with a light green bar to show its average age. Seismic activity segment of the figure shows dated and speculated seismic events that have occurred on distant faults. (a) Data from Chang and Smith (2002) and McCalpin and Nelson (2001). (b) Data from Lund et al. (2002), Lund et al. (2007), and Amoroso et al. (2004). (c) Data from McCalpin (2005). (d) Data from McCalpin (2000). (e) Data from Personius and Mahan (2003). (f) Data from Machette (1986). For details on dating techniques used in each case see Appendix C and locations of the faults see Figure 5.4

The top two rows demonstrate the occurrence of travertine in the Little Grand Wash and Salt Wash graben. U-Th dated mounds (the errors of which are smaller than the width of the bars) shown as red bars and age estimated mounds from the northern fault of the Salt Wash graben shown as blue bars. The four separate ages from mound L4 are shown with the area between them shaded to show the life span of the mound and with a light green bar to show its average age. Seismic activity segment of the figure shows dated and speculated seismic events that have occurred on distant faults. (a) Data from Chang and Smith (2002) and McCalpin and Nelson (2001). (b) Data from Lund et al. (2002), Lund (2007), and Amoroso et al. (2004). (c) Data from McCalpin (2005). (d) Data from McCalpin (2000). (e) Data from Personius and Mahan (2003). (f) Data from Machette (1986). For details on dating techniques used in each case see Appendix C and locations of the faults see Figure 5.4

It is hard to draw correlations between the timing of activities on these distant faults and switching of fluid flow along the Little Grand Wash and northern Salt Wash graben faults because the palaeoseismic record is sparse and inaccurate (Figure 5.5). The records of each distant fault and the dating techniques used to deduce past activity is presented in Appendix C. Information gained from the historical record is far too recent to provide an accurate estimate of the complete seismic cycle, especially in this case when time scales in the order of 100,000's of years are desired. Sparseness of the record is a result of the time period involved because relatively few age dating techniques can accurately deal with late Pleistocene to Holocene deposits, and even then particular materials required for each dating technique must be present.

Over the distant faults taken into consideration a wide variety of techniques were implemented in order to determine past seismic events. Only one radiometrically determined event, from ^{13}C on the Hurricane fault, is published (Amoroso et al., 2004). The rest of the data are either from qualitative techniques that involve large errors on age such as thermo and infrared stimulated luminescence, or quantitative techniques like the soil development index (Harden, 1982) and geologic observations.

The absence of radiometric ages is not surprising for these faults as radiometrically datable materials such as charcoal or volcanic ash are not often preserved in critical surface exposure or in excavations dug specifically for dating

purposes (Machette, 1986). Of the published luminescence analysis, ages are either provided as approximations with no error (McCalpin, 2000; McCalpin, 2005) or as rounded ages with up to 20% error (Personius and Mahan, 2003). Movement of fault scarps in the literature for these distant faults are often estimated from offset of stratigraphy (Chang and Smith, 2002) or the juxtaposition of soils with faulted sediments (Machette, 1986; McCalpin, 2005). The technique used to date this later aspect; the soil development index (Harden, 1982) has many variables and can only provide an estimate of age of scarp forming events. The huge inaccuracy of these techniques, excluding the single radiometric date, makes them poor methods to compare and correlate events across numerous faults.

5.2.2 Climatic Effects

A second possible external influence on the switching of pathways along the Little Grand Wash and northern Salt Wash graben faults is climate. Relatively warm and cold periods during the history of the area will have had a direct influence on precipitation rates which in turn could potentially affect water table height and supply of water to the springs that deposit the travertine mounds. In order to compare the travertine mounds in this study to any climatic information we must be certain that the mounds can potentially reflect climatic cycles.

If change in ground water discharge is not the result of seismic activity then spring-deposited travertine growth could potentially reflect climatic fluctuation as travertine has been reported to represent effectively wetter periods than the present (Livnat and Kronfeld, 1985). Past climate records, stretching back tens of thousands of years are well established on a global scale, with δD data from the Vostok ice core and $\delta^{18}O$ record from SPECMAP (Winograd et al., 1992; Lorius et al., 1985). However the climatic record for this region and indeed the Colorado Plateau in general is sparse over the time frame of travertine deposition in this study. Dendrochronology, the science of tree-ring dating, on conifers from the El Malpais National Monument, New Mexico, has produced an accurate short term record of rainfall for the last couple of thousand years (Grissino-Mayer et al., 1997). Beyond this record one must rely upon various studies that may lack precision but nevertheless can provide some information to the past climate of the Colorado Plateau.

5.2.2.1 The past climate of the Colorado Plateau

Situated between the Rocky Mountains to the east and north, and the Basin and Range to the west and south, the Colorado Plateau is a unique physiographical province (Figure 5.4). It presently straddles the transition between summer-wet and summer-dry climatic regimes to the south and north-west respectively (Anderson et al., 2000). This coupled with the topographic diversity has led to the production of diverse environments and plant communities. The palaeo-ecological record of the plateau is poorly known, but there are numerous potential sources for analysis. Records are mainly split into two varieties, both of which provide a record of the last ~35 ka; stratigraphic deposits and animal traces.

Stratigraphic deposits mainly come from high elevation locations (>2,200 m) and include sediments from lakes, bogs, alluvium, and caves. From 34-30 ka depositional hiatuses in lake deposits indicate a dry period of minimal rainfall (Anderson, 1993). Water levels in lakes were higher than present day between ~30-24 ka suggesting a wetter climate, whilst temperature records also indicate a cooler climate (3-4°C colder than present). Change in vegetation recorded between 18 and 14 ka indicates a drop in temperature to a colder climate (5°C cooler than present), with near modern vegetation being established by 12.4 ka.

Animal traces, such as pack-rat middens and bat guano, are common at low elevations (<2,200 m). Changes of vegetation found within middens suggest a full glacial climate between 27.5 and 17 ka (Long et al., 1990; Thompson et al., 1990). This agrees well with radiocarbon dates of rock varnish in the Sierra Nevada, California (Dorn et al., 1987). Late glacial type vegetation became dominant between ~18 to 14 ka. Finally, increasing temperature and increased rainfall between ~14 to 10 ka instigated a transitional period toward modern vegetation occurred (Jackson et al., 2005). Isotopic $\delta^{13}\text{C}$ and δD values recorded in guano from the Grand Canyon confirm this pattern of warming through to the early Holocene until ~9 ka (Wurster et al., 2008). Decrease in both isotopic values around 8 ka suggests a rapid change in atmospheric circulation and a cooler and dryer climate.

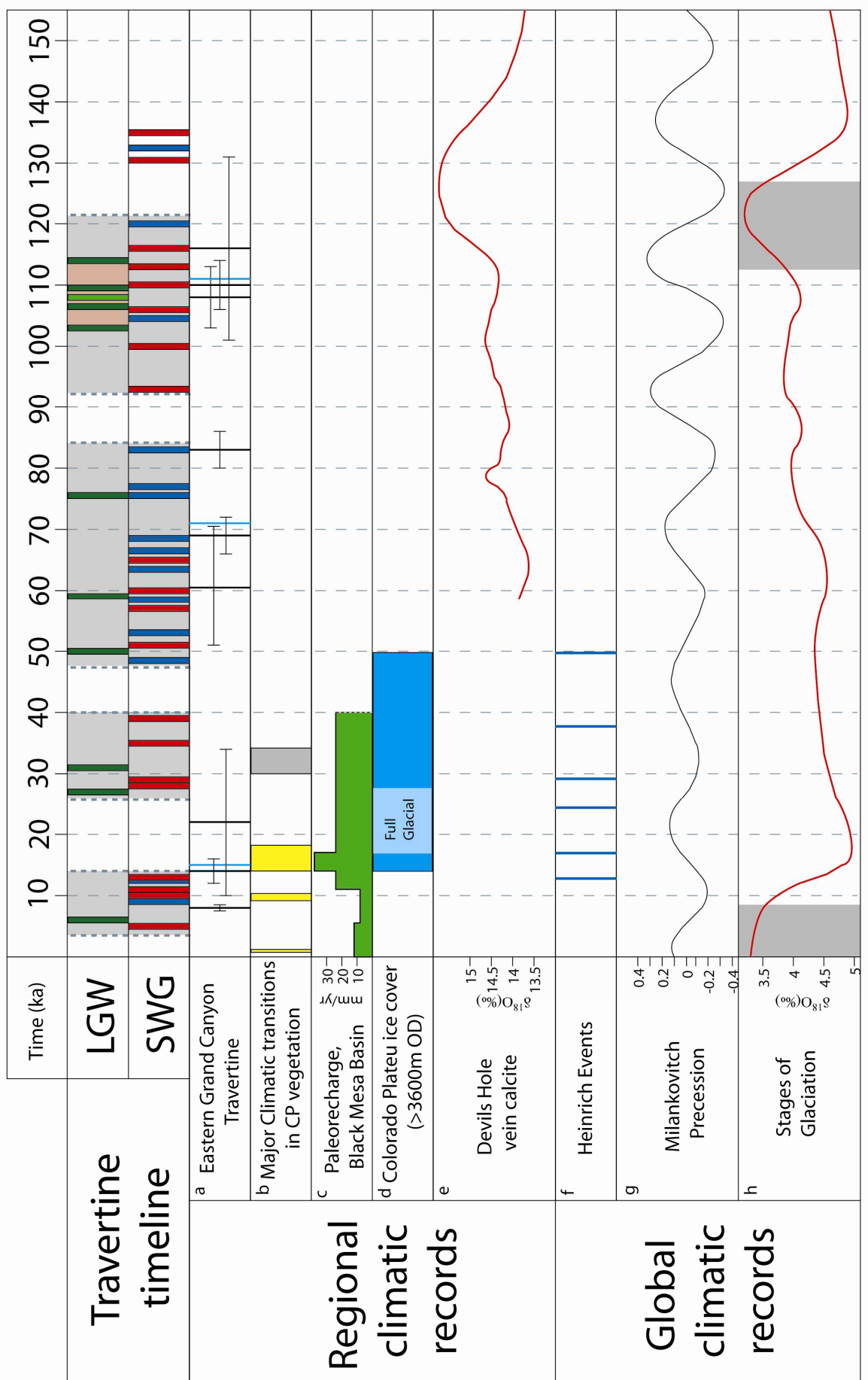
Anderson (2000) suggests that the highest elevations of the Colorado Plateau (above 3,600 m) were probably ice covered for much of the duration of the last Ice Age (from ~110 to 13 ka). These changes in atmospheric circulation are

the result of the size and position of the Laurentide ice sheet, which covered much of Canada and the northern United States during this time (Bartlien et al., 1998; Dyke et al., 2002). Simulation models by COMAP (Kutzbach et al., 1993) between ~18 and 14 ka suggest that the polar jet stream reached ~20° south of its present position. Coupled with stronger inshore upper level winds along the west coast these conditions produced colder winters and summers than present, and greater winter precipitation. The warming of the climate since this time can be attributed to northward shift of the jet stream as continental ice sheets retreated (Thompson et al., 1993; Shuman et al., 2002).

A further climatic record available in the Colorado Plateau comes from measurement of palaeo-recharge. This measurement reveals variability in spring discharge, which has been reported to respond to precipitation trends on multi-year time scales (King et al., 1994). Palaeo-groundwater-flow records from Black Mesa, northern Arizona, suggest that between 31 and 11 ka recharge rates were higher than today, with the maximum pulse of 2-3 higher than today occurring between 17 and 14 ka (Zhu et al., 1998) (Figure 5.6). This coincides with evidence for retreating ice sheets seen elsewhere (section 5.2.2.1). Numerical simulations of ground water flow executed by these authors suggest that thousands of years are required for water levels to fully respond to changes in recharge. It is therefore possible that any climatic record recorded by spring deposited travertine may be delayed in relation to changes in climate.

Figure 5.6: Timeline of travertine occurrence against climatic records.

Timeline includes both regional and world-wide records. Colour coding of travertine occurrence in the Little Grand Wash and Salt Wash graben areas is the same as in Figure 5.5. Grey boxes highlight potential overlap of timing of precipitation in each field area, after Figure 4.17. (a) Eastern Grand Canyon travertine data from Szabo (1990). This information is included as the occurrence of mounds is attributed to period of increased relative wetness. The source of error on younger ages is not discussed in Szabo (1990), while samples with age errors in excess ± 10 ka are calculated from isochron plot ages using data from both acid soluble and acid insoluble derived residue fractions. Blue lines represent the average age of each group of travertine provided by Szabo (1990). (b) Data from Anderson (1993) and Jackson et al. (2005). The yellow represent key changes in vegetation on the Colorado Plateau whilst the grey box highlights dry period indicated by lake sediments. (c) Data from Zhu et al. (1988). (d) Data from Anderson et al. (2000). (e) Data from Winograd et al. (1992). (f) Data from Rahmstorf (2003). Heinrich events are caused by a ~1,470 year cycle in dramatic climate variation. (g) Milankovitch precession is included as the gaps between deposition of several mounds in the Little Grand Wash fall close to the precession cycle period of ~21.6 to 25.7 ky (generally 23 ky). (h) Data from Lisieki and Raymo (2005). This information is a section of the climate record constructed by these authors using benthic $\delta^{18}\text{O}$ records from 57 globally distributed sites, the grey bars indicate interglacial periods.



5.2.2.2 Comparison with regional and global climatic records

Figure 5.6 shows a timeline comparing the occurrence of travertine on the Little Grand Wash and northern Salt Wash graben faults with both regional and global records. If climate is having an effect on the switching of these travertine mounds then it would be likely that a similar pattern of deposition/precipitation will be seen in the Little Grand Wash and Salt Wash graben field areas, and with spring deposits elsewhere in the region.

A study on travertine deposits by Szabo (1990) from the Grand Canyon produced thirteen travertine U-series dates, of which nine cover a similar timescale to the mounds in the present study. Szabo (1990) divides these nine dated mounds into three distinct groups which he attributes to being controlled by long-term fluctuations in the regional climatic pattern, especially in periods of increased effective wetness. As can be seen from Figure 5.6 at first glance there appears to be a potential overlap of the mounds in the present study with the groups of Szabo (1988). However, the youngest group of Szabo (1990) spans a 'gap' in the potential overlap of precipitation between the Little Grand Wash and Salt Wash graben field sites. Plus the timing of travertine mound precipitation in the present study occurs throughout the predicted dry spells of Szabo's travertine groupings. It is also apparent that travertine deposition has occurred throughout a period of arid conditions in the region as highlighted by dried out lake sediments (Jackson et al., 2005).

Further to a lack of a trend with local climate records, the statistical analysis carried out in section 4.7.6.1 showed no evidence of periodicity in either area. This random distribution of travertine precipitation through time should rule out climatic influence which tends to have a periodic pattern due to the influence of Milankovitch cycles such as obliquity and precession (Martinson et al., 1987). However, for any climate signal to be apparent in the travertine it must be remembered that the mound will reflect a climatic signal of the precipitation supplying the mound, which, as highlighted above may take thousands of years to travel from its source (Zhu et al., 1998). Analysis of lab precipitates from modern waters from both areas may represent the travel time of the meteoric water supplying the springs from its source ~35 km to the west (section 4.4.4). The ages provided by this analysis ranged from 223 ± 2 to 285 ± 5 years. This apparent time-lag is small enough to quickly demonstrate any climatic signal and so seems

to further suggest that climate is having little influence on the timing of travertine deposits.

Figure 5.6 demonstrates the lack of correlation between fluid flow history on these faults and available climate records. This finding further backs up the results of statistical analysis from Section 4.7.6.1, which shows the timing of travertine deposition at the surface to be random.

5.3 Internal forcing factors

5.3.1 Fault structure and fluid flow effects

In this section the internal features of faults will be examined in order to investigate their potential influence on the spatial and temporal distribution of travertine mounds along the Little Grand Wash and northern Salt Wash graben faults. The following subsections will deal with three main aspects; variation in fault structure, variation in fault permeability and potential fluid flow regime. As part of these subsections structural control on spring location, maintenance of fracture permeability, and the effect of CO₂ on fluid flow will be discussed.

5.3.1.1 Variation in fault structure

Despite its importance, vertical fluid flow in faults is still not completely understood (section 1.3). The generally accepted three component fault zone model, discussed in section 1.3.2, views faults as comprising a generally low permeability core, surrounded by a generally high permeability damage zone of fractured rock that grades into undamaged protolith (Chester and Logan, 1986b; Antonellini and Aydin, 1994; Caine et al., 1996). Faults have been demonstrated to be highly heterogeneous and have complex permeability structures whose properties can vary both spatially and temporally (Smith et al., 1990; Forster and Evans, 1991; Bentley, 2008; Wibberley et al., 2008). Fluid outflow from faults occurs most commonly at areas of high fault propagation and interaction which forms sites of elevated stress termed breakdown regions (Curewitz and Karson, 1997). This concentration of stress can lead to active fracturing and continual reopening of fluid-flow conduits, permitting long lived flow despite potential clogging of fractures due to mineral precipitation (section 5.3.2).

5.3.1.2 Structural setting of springs

Modelling and field studies of fault related springs suggest that spatial variation in permeability strongly influences spring location (Rowland et al., 2008). Curewitz and Karson (1997) suggest six specific structural settings within fault zones which can instigate low permeability and provide ideal locations for springs; (1) fault terminations; (2) fault overlaps or double tip interaction; (3) 'locked' fault intersections; (4) 'slipping' fault-intersections; (5) fault traces; and (6) asystematic with respect to the fault (Figure 5.7). Examples of these regimes can be found throughout the central part of the western U.S. Both ambient and hydrothermal fault related fluid flow within southern Utah and the Basin and Range province of north-west Nevada are reported to be preferentially associated with areas of fault intersection, overlap and termination (Fossen et al., 2005; Faulds et al., 2006; Hintz et al., 2008).

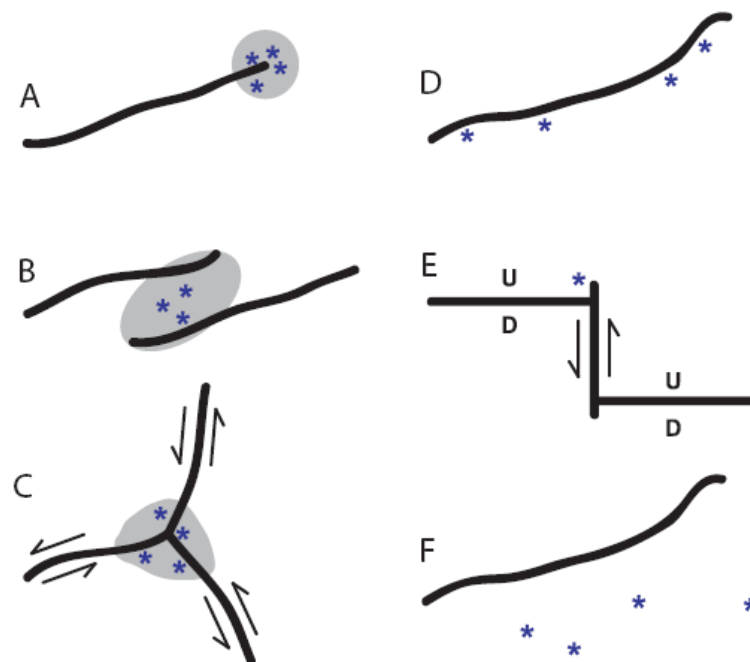


Figure 5.7: Structural settings of springs associated with faulting.

Stars indicate the location of springs in each setting with breakdown regions highlighted by shading. (A) Fault tip, (B) Fault tip interaction area, (C) Locked fault, (D) Fault trace, (E) Slipping fault intersection, (F) Asystematic. Settings A-C dynamically maintained, D-E kinematically maintained. After Curewitz and Karson (1997) and Anderson and Fairley (2008).

In the present study ancient and modern travertine deposits along the Little Grand Wash and northern Salt Wash graben faults are mainly located in the immediate footwall. Fault traces mark the intersection of fault planes with the Earth's surface and can show the topographic expression of an active fault or deep levels of an inactive fault exposed by erosion. In addition to occurring on the fault trace travertine mounds in the Salt Wash graben occur significant distances away (up to 530 m) from the fault. These deposits fall under the asystematic regime of Curewitz and Karson (1997) as they are not closely associated with the northern Salt Wash graben fault trace. The host rock for these mounds is the highly porous Entrada Sandstone (Table 5.1). It is likely that this exposed aquifer unit is providing high permeability conduits for fluid flow away from fault. This theory is supported by the close proximity of travertine deposits to reduced host sandstone which suggests previous fluid flow (Dockrill and Shipton, 2010).

5.3.1.3 Variations in fault permeability

Previous work carried out to characterise permeability variations within fault zones is sparse (Lopez and Smith, 1996). Concentration of flow through areas of structural complexity is demonstrated by work on an active fault zone in the Great Basin extensional province in Idaho by Fairley et al., (2003), Fairley and Hinds (2004a; 2004b), and Anderson and Fairley (2008). Although active, the faults described in this area are analogous to those in this study as they are all normal dip-slip faults with a predominantly low permeability fault zone. Springs are found above a relatively few, spatially discrete, high permeability channels. Variation in temperature of both springs and soil in the area of the Idaho faults highlight the presence of these channels. Temperature in this case was treated as a proxy for permeability, as the two are roughly proportional, at least over a limited range (Fairley et al., 2003; Fairley and Hinds, 2004b). Variogram modelling, indicator kriging and Gaussian simulation allowed for a geostatistical analysis and the production of a composite image of the temperature distributions emanating from the discharge of hydrothermal fluids along the faults (Anderson and Fairley, 2008). As permeable pathways in hydrothermal systems are generally maintained by fracturing (Hintze et al., 2008), high temperature areas were postulated to correspond to areas of increased fracture propagation. Even with this advanced information on fault structure and fluid flow in comparison to the present study, Anderson and Fairley (2008) found this data to still be insufficient to uniquely

determine the structural setting of the springs. They base their final conclusion on the observed distribution of temperatures, which is consistent with the location of the study area in a fault tip-line region or a releasing step within an obliquely slipping fault interaction area (Anderson and Fairley, 2008).

5.3.1.4 Maintenance of fracture permeability

Fault slip can give rise to anisotropic permeability as bands of fault gouge and cataclasite develop into highly fractured conduits of rock parallel to the fault zone (Scholtz and Anders, 1994; Dockrill, 2006; Wibberley et al., 2008). This mechanism may create fracture permeability along irregular fault surfaces and promote the channelling of fluid flow vertically up the fault zone to the surface (section 1.3.2.3).

The permeability of fluid flow channels in faults can be maintained by one of two main mechanisms- 'dynamic' or 'kinematic' (Figure 5.7, Curewitz and Karson, 1997). Fracture permeability maintained by kinematic systems is limited to the immediate vicinity of the fault and depends on active slip of the fault to re-open pre-existing fracture networks. Of the structural setting discussed earlier (section 5.3.1.2) Curewitz and Karson (1997) state that slipping fault intersection and fault trace regimes are maintained by this system. Dynamic maintenance of fluid flow pathways is dependant on continued fault propagation or interaction. As this system leads to stress concentration and fracturing away from the fault it is usually associated with the fault propagation, fault interaction and locked fault intersection regimes (Curewitz and Karson, 1997).

The location of spring deposits along the normal faults in the present study is mainly indicative of a fault trace structural regime. As highlighted above this regime is mainly associated with kinematic fracture maintenance, which relies on continual fault movement. However, as discussed previously (section 5.2.1.1) both geomorphological and radiometric evidence suggests there has been no movement on the faults in this study for at least 190 ka, ruling out this method of pathway maintenance. Evidence for stress build up in dynamically maintained cases can include microearthquake swarms, aftershock concentrations and arrays of microfaults and fractures (Curewitz and Karson, 1997). Historical records of activity on both faults are poor and the subsurface structure of the faults is poorly understood, as such there are no specific data for stress build up on either fault.

Due to the evidence against recent movement on these faults (section 5.2.1.2) and the lack of evidence for continual fracture propagation it is unlikely that the fluid flow pathways in this study are being dynamically maintained. There must be some other mechanism at play which allows for maintenance of the fluid flow pathways in static fault conditions. Fracture analysis along the Little Grand Wash fault demonstrate higher fracture density around relay zones than in structurally simpler sections of the fault (Dockrill and Shipton, 2010). Travertine mounds on the clay rich host rocks of the Summerville and Morrison Formations are also restricted to fault bends and relay zones. Both of these observations suggest that permeability pathways are preferentially associated with more structurally complex sections of the fault (Dockrill and Shipton, 2010). It is possible that irregularities on the fault plane are creating small pressure shadows with small shear strain in comparison to the rest of the fault (Gartrell et al., 2003). Relief of shear strain around these zones of structural complexity may allow for the maintenance of fracture width within them and lead to the promotion of fluid flow.

5.3.1.5 Potential fluid flow regime

Fluid flow patterns can be affected by both pressure and temperature gradients and the permeability of the rocks encountered by the fluids (Xu et al., 2003). Mathematical and numerical models constructed by Lopez and Smith (1995; 1996) to map permeability space provide four possible fluid flow regimes within a fault zone: conductive, advective, steady convective and unsteady convective. The regime present in a particular fault zone depends on the permeability of both the protolith and the fault zone components. Conduction can only occur at low fluid velocities because molecule motion in the fluid becomes less random and more directed by higher fluid flow rates. Further increase in velocity of fluid flow leads to an advective regime in which fluid flow in the protolith is directed towards the fault plane and fluid is discharged vertically at the fault trace. As the fault zone becomes more permeable convective circulation is established. This can take one of two forms which depend on the permeability of the fault zone. Steady convection dominates at lower permeabilities and can establish a large scale steady flow pattern whereas unsteady convection creates smaller more chaotic fluid flow cells at high velocities. Lopez and Smith plot the relationship of these regimes in a base diagram of country rock permeability against fault rock permeability (Figure 5.8).

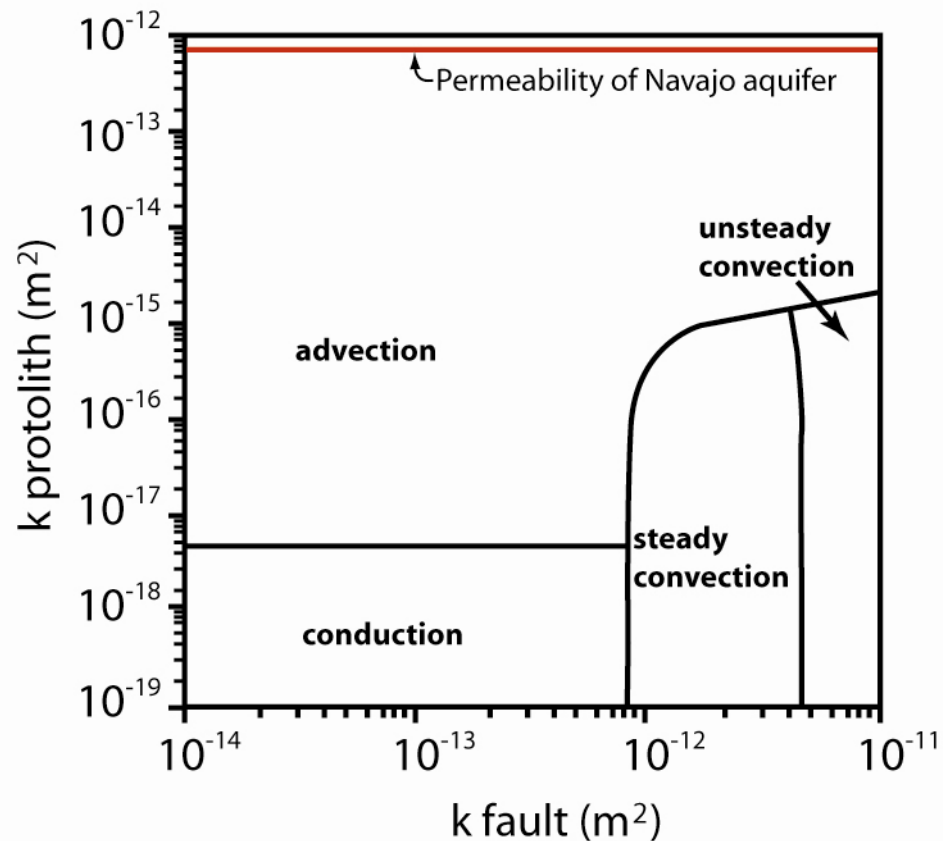


Figure 5.8: Plot of protolith against fault permeability for fluid flow regimes

Figure expanded from the base case of Lopez and Smith (1995). The four different regimes are shown constrained by the range of permeabilities of the protolith and fault that support them. The permeability of the Navajo aquifer is shown by the red line. Boundaries between the regimes can vary with length, depth and width of the fault zone. Even with changing the parameters of the fault zone, the Navajo aquifer always plots in the advective regime.

The average permeability of the Navajo aquifer, the main source of waters to the springs in both the Little Grand Wash and Salt Wash graben (Section 3.4.2), is $4.5 \times 10^{-13} \text{ m}^2$ (Table 5.1, Figure 5.8). When this is plotted against the base diagram of Lopez and Smith (1995) it occurs in the advective regime for all fault permeabilities. This may form a good approximation of the fluid flow regime in the Little Grand Wash and northern Salt Wash graben faults as Lopez and Smith (1995) state that as permeability is the dominant factor, results plotted in permeability space can provide general guidance in anticipating large scale hydrologic features of a fault zone. However, solely taking the permeability of the Navajo aquifer as the bulk protolith value provides only an idealised homogeneous case when in reality vertical fluid flow up the Little Grand Wash and northern Salt Wash graben faults encounters a series of stacked aquifers separated by impermeable limestone and clay rich shales. The fact that both faults in the present study demonstrate evidence of heterogeneous permeability along strike

(Dockrill and Shipton, 2010) adds further complications to any generalisation of fluid flow regime. In a second paper Lopez and Smith (1996) do add anisotropic fault permeability to their fluid flow model by altering vertical permeability with respect to horizontal permeability. However, permeability variation in either of these orientations is not modelled or discussed.

For heterogeneous faults with isotropic permeability the location of springs in the advective regime is determined by the large scale alignment of higher permeability zones in the dip direction of the fault. This alignment of higher permeability zones can be defined in terms of connected pathways along which the permeability is everywhere greater than the effective permeability of the fault zone (Silliman and Wright, 1988; Lopez and Smith, 1996). A combination of the spatial variation in permeability, the depth of the fault zone and the spatial distribution of fluid input from the country rock could form a control on the spacing between springs at the trace of a fault zone. Smaller lengths between permeable pathways lead to more diffuse flow, with closely spaced discharge sites having a relatively lower rate of groundwater discharge. The travertine of the northern fault of the Salt Wash graben may reflect this pattern as their locations are more tightly spaced in comparison to Little Grand Wash fault travertine (Figure 4.2), they are generally smaller and thinner than the Little Grand Wash travertine (section 4.7.3) and they are also the result of more diffuse flow to the surface due the porous Entrada Sandstone host rock (section 5.3.1.2).

5.3.1.6 The effect of CO₂ on fluid flow

The fluid flowing to the surface of the field areas is rich in CO₂ therefore it is crucial to take into account the effects that the various forms of CO₂ could be having on the fluid flow system. Three different phases of CO₂: aqueous, liquid and gas can be present in several different combinations in a water-CO₂ system above freezing point (Figure 5.9). At typical subsurface conditions of temperature and pressure, CO₂ is always less dense than aqueous fluids, therefore buoyancy forces will tend to drive CO₂ upward towards the land surface whenever increased vertical permeability is available in areas of increased fracture density (Agosta et al., 2008; Pruess, 2005).

An analogue for CO₂ migration in a fault associated hydrological system is provided by the modelling of Pruess (2003; 2005) which investigates CO₂ injection

into a geological disposal reservoir. Pruess implements numerical modelling of an idealized homogeneous fault zone with the simple assumption that leakage from the primary storage reservoir will cause the CO₂ to be present at a constant overpressure in a small subvolume of the fault zone. The parameter of upward CO₂ migration through permeable formations is input at rates so small so as to cause negligible disturbance of the *in-situ* pressure and temperature conditions of a typical crustal setting (i.e. a hydrostatic gradient of ≈ 10 MPa/km, and a geothermal gradient $\approx 30^\circ\text{C}/\text{km}$). Geothermal gradients measured near the study sites provide a mean of 27.8°C and reflect this typical value (Reitler et al., 1979; Smouse, 1993; Nuccio and Condon, 1996).

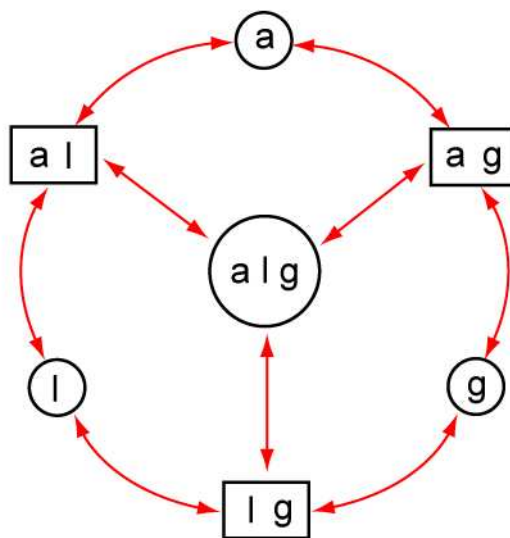


Figure 5.9: Possible phase conditions of two component water- CO₂ systems.

Figure adapted from Pruess (2005). Letters stand for; a- aqueous, l- liquid CO₂, g- gaseous CO₂. There are a total of seven separate phase combinations including three single phase states (circled), three two –phase states (in squares) and a three-phase state (large circle in middle).

The timescale of these models is up to ~ 1 ka, which is two orders of magnitude shorter than the fluid flow history of the Little Grand Wash and northern Salt Wash graben faults. As discussed above in section 5.3.1.5 neither of these faults are as simple as an idealized homogeneous fault zone as they are heterogeneous with respect to vertical permeability and cut through stacked aquifers and caprocks of widely variable permeabilities. This model also does not explain the behaviour of CO₂ migration pathways through fracture dominated caprock. Nonetheless, the models of Pruess are based on numerical simulations of the behaviour of water-CO₂ mixtures in permeable media under typical temperature and pressure conditions, and therefore can provide insights to what happens during leakage of a CO₂ charged system through a permeable pathway.

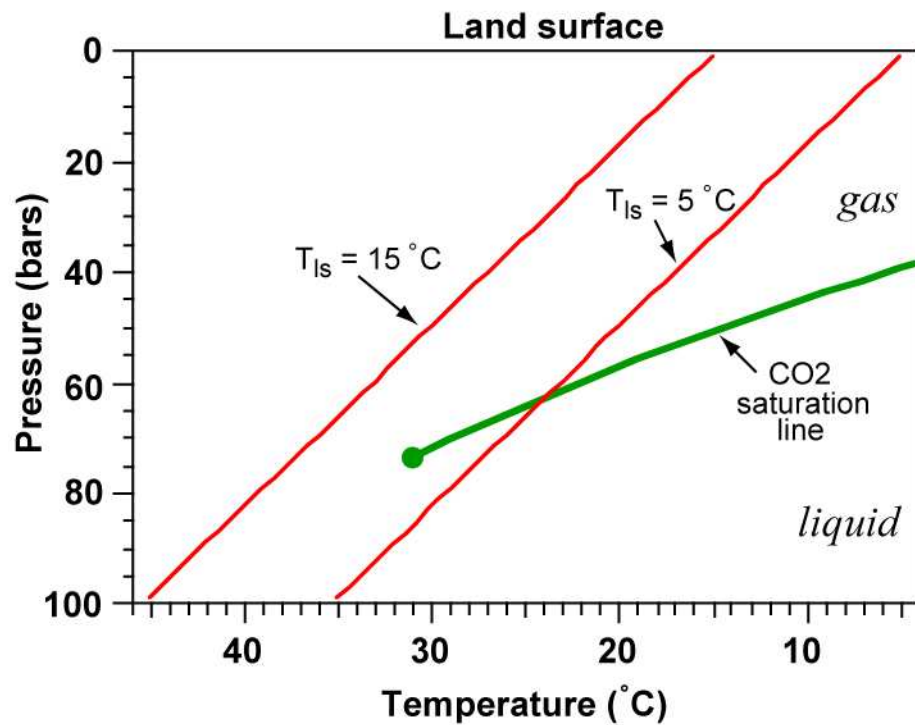


Figure 5.10: CO₂ saturation line and fluid pressure- temperature profiles for a setting with typical geothermal profile.

Figure altered from Pruess (2005). The red lines show hydrostatic profiles for surface temperatures of 5°C and 15°C. As can be seen the profile for 15°C does not pass through the CO₂ saturation line so flow is continual to the surface. For the profile of 5°C the saturation line is reached at a depth of ~630 m. At this point two phase flow become three-phase (see text) and fluid mobility drops impeding flow to the surface.

When temperature at the land's surface is increased to 15°C in the model of Pruess (2005) the hydrostatic profile of rising CO₂ does not pass the saturation line (Figure 5.10). This migration negates the liquid phase meaning that CO₂ can pass from supercritical to gaseous conditions without a phase change. Absence of a 3-phase zone in this case means there is no region of severely reduced fluid mobility; therefore no resistance to up-flow of CO₂ occurs (as seen in the early stage T1 of Figure 5.11). This is especially apparent near the centre of flow where phase interference had been the most severe during modelling of a surface temperature of 5°C. As a consequence to this less plume broadening was observed and CO₂ fluxes to the land surface had a more pronounced and persistent maximum flux above the CO₂ leakage point. Variation in mobility of upwelling fluids caused by changes in ambient temperature at the surface suggests that climatic variation may have a direct effect on the evolution of pathways. As discussed in section 5.2.2.2 however there is no climatic signal evident in the travertine deposits of the Little Grand Wash or northern Salt Wash graben faults.

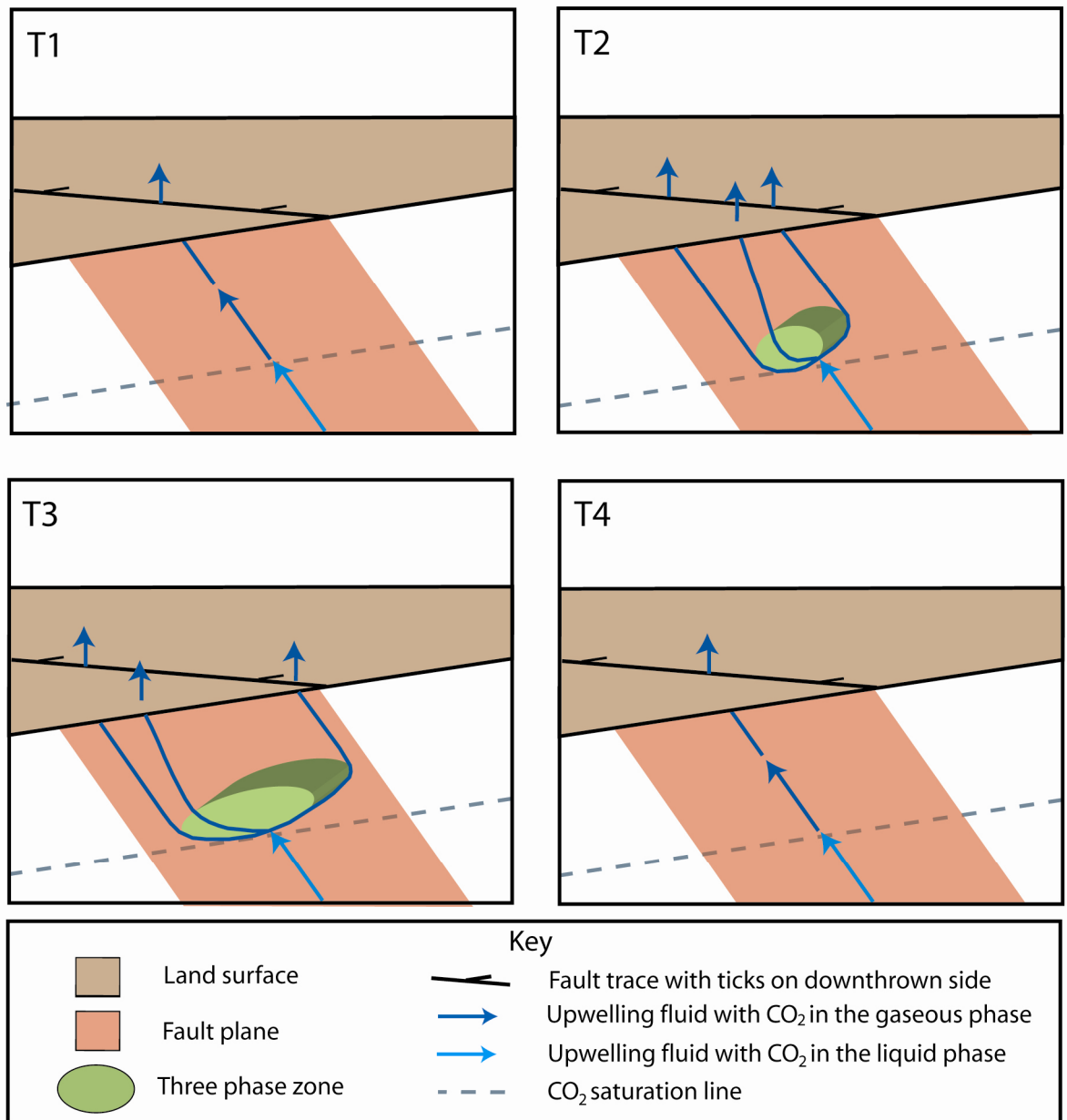


Figure 5.11: Flow through time for CO₂ rich fluid

Figure based on a hydrostatic profile with surface temperature of 5°C. T1- Flow is uninterrupted to the surface. CO₂ is initially present as the liquid phase in the upwelling fluid and boils into the gaseous phase as it reaches the CO₂ saturation line at a depth of roughly 630 m. T2- As latent heat is absorbed by the phase change process and Joule-Thompson effect cause further cooling which interrupts phase change from liquid to gaseous CO₂ and a third phase, aqueous CO₂, results creating a three phase zone. As the size of this three phase zone increases the interference between the separate phases strongly reduces fluid mobility and flow is impeded. T3- With time this three phase zone increases further and gives rise to lateral plume broadening. An increased volume of upwelling fluid gets diverted around the three phase zone and leads to more dispersed pattern of leakage at the surface. T4- Eventually this diversion of flow reduces the flux of CO₂ and cooling rates in the three phase zone. This allows temperatures to recover, and boiling of liquid phase CO₂ resumes. CO₂ flux is increased and more focused as thermodynamic conditions return to a two phase system.

In these conditions, modelled with a surface temperature of 5°C, CO₂ migrating from depth will remain in the liquid phase until it reaches the CO₂ saturation line (which is at temperature/pressure conditions of 31.04°C and 7.4 MPa- Vargaftik, 1975), where it boils into gas (Figure 5.10). This transition causes a large increase in volume and decrease in viscosity (Pruess, 2005). If this process occurs at a finite rate, it will cause formation temperatures to decline as latent heat is absorbed by the phase change process. Additional temperature decline occurs from Joule-Thompson cooling as the gaseous CO₂ depressurizes and expands as it migrates toward the surface. As there is always an aqueous phase present, the region with liquid-gas CO₂ conditions becomes a 3-phase zone. Due to temperature decline from Joule-Thompson cooling and associated condensation effects, the volume of this 3-phase zone increases with time. Interference between the separate phases leads to a decrease in the relative permeability of each phase and strongly reduces fluid mobility. As a consequence, up-flow in the CO₂ charged system is impeded locally in the three phase zone reducing flow rate in the vertical direction and slows advancement of the liquid CO₂. This gives rise to lateral plume broadening and over time an increasing fraction of the up-flowing CO₂ is diverted sideways around the zone giving rise to dispersed CO₂ discharge at the land surface. This diversion of flow reduces the flux of CO₂ and cooling rates in the 3-phase zone, allowing temperatures to recover by heat conduction from the wall rocks, causing liquid CO₂ to boil away. This will cause thermodynamic conditions to return to a two-phase system (aqueous-gas), increasing fluid mobility and CO₂ flux. The result is a temporal trend in 3-phase conditions which leads to a periodicity in CO₂ flux and fluid flow to the surface (Figure 5.11).

Leakage rates within these models may be affected by phase change of CO₂ as density is much lower for the gaseous than for the liquid state. A transition to gaseous conditions greatly increases the buoyancy forces and could accelerate fluid leakage, as well as causing a rapid increase in fluid pressures at shallower levels. This increase in fluid pressure would inevitably lead to an increase in the ambient pore pressure of the system. Build up of pore pressure is limited by the least principal stress plus the tensile strength of the pathway hosting rock (Nur and Walder, 1992). If this limiting stress level is exceeded hydrofracture may occur creating short lived but significant pathways for upward migration of fluid. This is accompanied by a short episode of fluid expulsion or pressure pulse followed by a

drop in pore pressure and sealing of the system. After another build up period, hydrofracture can once again occur, taking advantage of pre-existing fractures creating a periodic pattern in permeability of the pathway and leakage to the surface. Dimensional analysis of Nur and Walder (1992) estimates that these 'pulses' of migrating fluid can last for $10^3 - 10^5$ years which is more than adequate for the maximum duration of travertine deposits in the Little Grand Wash and Salt Wash graben.

5.3.2 The potential effects of mineral precipitation

Mineral precipitation is very efficient at filling fractures and void spaces. Significant mineral precipitation may occur over hundreds of years and lead to a reduction of permeability in fractures, inhibiting fluid circulation, and ultimately block discharge in the absence of any physical mechanism of permeability maintenance (Sibson, 1987; Anderson and Fairley, 2008; Eichhubl et al., 2009). The abundance of calcium carbonate in the waters leaking to the surface in along the Little Grand Wash fault and the northern fault of the Salt Wash graben is clear to see in the field with the presence of numerous travertine mounds in both locations. As these waters are rich with respect to calcium carbonate they provide a large volume of mineralising agent for the potential clogging of subsurface pathways.

5.3.2.1 Mineralisation observed in the field

Fluid pathways can become blocked by the precipitation of carbonate through degassing of fluid migrating from depth. Upon blockage of a pathway the upwelling fluid finds the next point of least resistance and flows to the surface along that pathway until it becomes blocked and so on. An indicator of mineralisation driven switching could therefore be a continuous fluid flow history along the Little Grand Wash fault and the northern fault of the Salt Wash graben. The timelines for the history of mound occurrence (e.g. Figure 5.6) demonstrate gaps in deposition between deposits which initially suggests that there have been periods of time where there has been no fluid flow to the surface. However, the gaps in the record have been discussed previously in section 4.7.6.2, and it is possible that they are actually due to one of the following factors:

- It is unsure how long each travertine mound has been active for as radiometric ages provide only a single point in time during which each dated mound was active.
- An estimated minimum lifespan is available for mound L4, but the preservation of other mounds varies and so it is difficult to use the size of a mound to estimated length of activity.
- Possible that mounds have been completely eroded away meaning that gaps in the record may reflect periods non-preservation rather than non- precipitation.

If the gaps in the time line truly reflect time intervals of non-leakage at the surface then they could potentially be explained if it takes an extended period of time for up-welling fluid to find and exploit a new pathway once a previous pathway has become completely blocked by mineral precipitation.

Investigation of travertine deposits in the northern Salt Wash graben fault field site gives insights to where mineralised blockage of pathways to the surface may be occurring. If the blockage was occurring near the surface then flow of CO₂-charged waters to the surface would be diverted around a particular leakage point but would remain localised to the blocked pathway due to the highly permeable host rocks of the Entrada Sandstone and Curtis Formation. This would give rise to nearby or subsidiary mounds of slightly younger age than the original spring deposit. There is only one location in the Salt Wash field site where there is evidence of similarly aged mounds in close proximity- mounds S7 and S8 (Figure 4.2). These two deposits are $100,378 \pm 562$ and $106,088 \pm 660$ years in age and separated by a distance of ~ 20 m. Despite there being several other locations where separate mounds are found within 20 m of each other there is no further evidence of similarly aged mounds next to one another. The overall trend therefore suggests that any potential blockage of pathways is likely to be happening below the Entrada Sandstone and in the fault-associated damage zone fractures within the low permeability shales and limestones of the Carmel Formation which caps the Navajo aquifer.

5.3.2.2 Previous work on precipitation

Published work looking at precipitation rates of veins has mainly focused on silica; however some of these findings along with work carried out on calcite can be applied to the present study. The amount of vein precipitation from a given volume of fluid can be influenced by several factors including; pressure, ambient geothermal gradient, initial saturation state, flow velocity, activity coefficients of ions, relative concentrations of dissolved components, the presence of reaction inhibitors, and in the specific case of calcite veins, P_{CO_2} (Xu et al., 2003; Lee and Morse, 1999)

Analogues for natural precipitation can be found in the work of Lowell et al. (1993) who use analytical models to look at isolated fractures in hydrothermal up flow zones and the effects of silica precipitation within them. Temperature was kept constant, both spatially and temporally, during this modelling in order to investigate the effects of both fluid flow velocity and saturation state of waters with respect to silica. Whilst constant temperature is not realistic in the hydrothermal systems that Lowell et al. (1993) are considering it may be an appropriate assumption for the system in the present study which is of a normal geothermal gradient. Precipitation rate was found to be mainly driven by degree of fluid supersaturation with respect to silica which in turn was found to be dependant on the average velocity of fluid flow as this controlled the flux of silica to the site of precipitation. For high flow velocities, large fracture widths, or slow reaction kinetics the dissolved silica gradient is diminished and no precipitation occurs.

5.3.2.3 Precipitation rates

Calcite is a common vein-filling mineral in rocks; however, due to a lack of data from subsurface fracture systems and an incomplete understanding of the kinetics of vein-filling, the fluid volumes and timescales required for calcite vein formation are hard to predict (Morse and Mackenzie, 1993). Lee and Morse (1999) try to resolve this situation by looking at the time and fluid volume necessary to form calcite veins in a synthetic situation. Their long term experiments, carried out at constant pressure and temperature conditions, were conducted to simulate calcite precipitation in veins at various flow velocities and initial solution saturation states with respect to calcite. The results showed that the solution to calcite volume ratio dramatically decreased with increasing solution saturation state for a

constant flow velocity. This indicates that extremely large volumes of fluid are required to precipitate calcite at low saturation states.

When veins develop by fracture-channelled flow, the velocity of fluid flow must be fast enough to prevent uneven flow distribution along a fracture and the fluid has to be slightly saturated with respect to calcite with natural veins typically having solution to calcite volume ratios of $10^5 - 10^6$ (Lee et al., 1996). Factors such as solution carrying capacity, the rate constant k and vein size can all influence the solution to calcite volume ratio (Lee et al., 1996). Taking these factors into account Lee and Morse (1999) suggest that timescales for vein precipitation for a given flow velocity may vary by an order of magnitude and so estimate precipitation rates of $10^2 \pm 1$ years for cm-scale veins and $10^4 \pm 1$ years for meter-scaled veins. This range of estimated time scales agrees with work carried out by Fisher and Brantley (1992) who suggest that mm scale crack-seal veins can develop over 10^2 to 10^4 years.

In the present study the inner and outer edges of a 2.5 m thick vein from mound L4 were sampled and dated in order to determine the length of time required for its precipitation. The radiometric age results demonstrated that the vein had been precipitated over $4,298^{+604}_{-901}$ years (Section 4.3.3). This timescale, which is of the order of 4.3×10^3 years, agrees within error to the estimates of Lee and Morse (1999) for meter scale veins. The time averaged rate of precipitation of this vein, 0.51- 0.74 mm/year, may therefore represent a good approximation of the length of time required to completely seal fractures within the Carmel Formation and force up-welling CO_2 charged waters to find an alternative route to the surface.

5.4 Summary: The likely causes of switching

Upon looking at the aspects discussed above it is clear that there may be a number of interacting factors having an effect on the switch of fluid flow along the Little Grand Wash and northern Salt Wash graben faults. An in-depth look at the climatic history of the surrounding region reveals evidence of distinct periods of temperature change causing intermittent periods of relative wetness. Work by Szabo (1988) suggests that travertine mounds deposited in the Grand Canyon reflect this climatic signal. Plots of the timing of travertine mounds in the present study against various regional and global climate records show that the timing of

travertine in both field sites does not seem to be concurrent with observed changes in the climate. As evidenced from other studies (Winograd et al., 1992; Zhu et al., 1998) time-lags in climatic signals due to the length of time required for meteoric waters to travel from their source in the San Rafael Swell to the site of precipitation some 35km to the east could potentially cause this discrepancy. However, even taking this into consideration, results of statistical analysis on the history of travertine deposition along both the Little Grand Wash and the northern fault of the Salt Wash graben do not show any evidence of periodicity in the timing of mounds. As no periodicity in travertine deposition exists and there appears to be no correlation between travertine mounds and major climatic events, this external forcing factor is completely ruled out as a cause of switching of pathways.

Seismic activity on the Little Grand Wash and northern Salt Wash graben faults also appears an unlikely cause as radiometric and geomorphological evidence suggest there has been no surface rupturing on the Little Grand Wash fault for a minimum of ~ 137 ka and on the northern fault of the Salt Wash graben for at least ~190 ka. However, evidence from Yellowstone and the Geysers geothermal field demonstrate that large scale earthquakes can alter the hydrological systems up to 3,100 km distant. In order for these systems to have been affected the stress change resulting from seismic events must have been greater than 20-100 nanostrain (Rojstaczer et al., 2003). Elastic models of the Denali earthquake show that the resulting static stress change would have been too small to exceed this threshold and cause any triggering effects (Hill et al., 1993). Large amplitude surface waves from both the Denali and Landers earthquakes are therefore most likely cause of triggering as they instigated dynamic stresses of up to 470 nanostrain (Hill et al., 1993; Rojstaczer et al., 2003; Husen et al., 2004).

As both the Little Grand Wash fault and the northern fault of the Salt Wash graben are optimally orientated for failure in the present day ambient stress field of the Colorado Plateau they are potential candidates for seismic triggering. As such the timing of travertine mound deposition was compared to the palaeoseismic record of several major faults in the local region (Figure 5.5). However, due to the poor availability of dateable materials the palaeoseismic record for each of these faults has a real paucity of data extending back over the timeframe of travertine deposition.

Although it is hard to draw any correlation between earthquake events on these faults with switching of travertine location along either the Little Grand Wash or northern Salt Wash graben faults, seismic triggering is not ruled out as a potential cause. This is because of the sheer distance that the effects of seismic events can reach. It is very possible that earthquakes on faults outwith the 500 km radius of distant faults investigated in the present study could have created enough dynamic stress change for alteration of the hydrological systems in question, provided the seismic event's radiated energy was focused in the direction of the Little Grand Wash and northern Salt Wash graben faults.

The structure of the Little Grand Wash and northern Salt Wash graben faults are no doubt playing a sizeable role in at least the formation of fluid flow pathways. Areas of increased fracture density around fault bends and relay zones create regions of relatively high permeability which provide sub-vertical channels for migrating fluid to reach the surface. As permeability pathways are preferentially associated with more structurally complex sections of fracture interaction active pathways to the surface have potentially been maintained by zones of low shear strain in relation to the rest of the fault plane.

Fluid flow effects may be a major factor in pathway switching especially with the hydrological systems in question being rich in CO₂. Numerical modelling of fault related fluid flow regimes has been carried out by Lopez and Smith (1995; 1996). Permeability is the dominant factor in these models, so results plotted in permeability space should provide guidance in anticipating the large scale hydrologic features of fault zones such as the Little Grand Wash and northern Salt Wash graben faults. When the Navajo aquifer is plotted on Lopez and Smith's (1995) base diagram of country rock permeability against fault rock permeability it plots in the advective regime for all fault permeabilities. The same result occurs when the Navajo is plotted on the updated anisotropic version (Lopez and Smith, 1996) which has vertical permeability four times greater than horizontal permeability.

However, it should be taken into consideration that although the Navajo is the main source for the springs in the present study, the geological stratigraphy of the field area is far too complex for a singular bulk value of protolith permeability to be considered for accurately predicting a fluid flow regime to the surface. Comparisons of the fluid flow system in the present study, and indeed any system,

therefore require consideration of the site specific conditions for both the protolith and fault zone. In the case of the Little Grand Wash and northern Salt Wash graben faults variability in protolith values is due to the presence of strata of varying thickness (ranging from ~ 10-150 m for each unit- section 3.3.1) and composition (ranging from shales to sandstones- section 3.3.2). For the faults themselves the physical properties of the fault zone, such as width, depth and slip, and their effect on the heterogeneity of the faults permeability need to be known. This is discussed and speculated in sections 3.2 and 4.7.5 for the Little Grand Wash and northern Salt Wash graben faults, however far more detail and further measurement is required in order to give a conclusive answer on the fluid flow regime taking place.

The various phases that fluid can take on in a water- CO₂ system can play a key part in migration of the fluid to the surface. Numerical simulations by Pruess (2003; 2005) suggest that CO₂ leaking along heavily permeable pathways from deep accumulations may demonstrate cyclical behaviour. As upwardly migrating liquid CO₂ reaches the CO₂ saturation line and it boils into gas leading to an increase in volume plus a decrease in viscosity. The resulting cooling of the Joule-Thompson effect and phase interference between liquid, aqueous and gaseous CO₂ results in a strong reduction of fluid mobility. CO₂ flux above the original leakage point declines and up-welling fluid is diverted around the 3-phase zone creating new leakage points at the surface. Diversion of flow allows temperatures to recover in the 3-phase zone, which leads to a reestablishment of two-phase flow to the original leak point. The simulation timescales of Pruess (2003; 2005) are two orders of magnitude shorter than the fluid flow history recorded along the Little Grand Wash and northern Salt Wash graben faults, however they are long enough to provide an insight into the localised switching of pathways between mounds of similar age (i.e. <10,000 years). Above the CO₂ saturation line increased pore pressure caused by the build up of gaseous CO₂ may lead to hydrofracture of any blockage and the re-activation of mineralised pathways. Given the normal pressure and temperature conditions demonstrated by measurement from near the field sites (section 5.3.1.6) it is likely that the local CO₂ saturation line will be at a similar depth, ~630 m, to that used in the simulations of Pruess (2003; 2005). As the depth of the Navajo aquifer is between 600 – 800 m (Shipton et al., 2005) it is likely that the Carmel Formation will be

below the CO₂ saturation line and that hydrofracture by this method is therefore an unlikely mechanism in the present study.

Precipitation effects could also have a significant influence in the switching of pathways by clogging viable pathways to the surface and forcing upwelling fluid to find alternative routes. The histories of travertine deposition in both field sites do not show a continuous record of flow to the surface, however gaps in the timelines may be due to one or a combination of: preservation issues, uncertainties around the lifespans of deposits or the removal of mounds from the record by erosion. Alternatively these gaps may be explained if it takes considerable periods of time (up to 1,000s of years) for up-welling fluid to establish a new pathway to the surface. Work by Lee and Morse (1999) and Fisher and Brantley (1992) suggest that calcite veining can completely infill fractures on time scales of $10^{2 \pm 1}$ to $10^{4 \pm 1}$ years. Radiometric dating of the inner and outer edges of the main vein of travertine mound L4 from the Little Grand Wash supplies an age of $4,298^{+604}_{-901}$ years, which agrees with this range. The calculated lifespan of $10,740^{+3,544}_{-4,403}$ years from multiple radiometric age analysis of this deposit may provide an analogue for how long it can take for pathways to become completely blocked by mineralisation at depth within the Carmel Formation. This is a minimum estimate for the lifespan of L4, so it is likely that this mound was actually active for longer than this timeframe. However, as L4 is by far the largest mound in the field, even with taking erosional affects into consideration, its lifespan can be taken to be the maximum possible age of all other travertine deposits across both field areas and therefore the longest timeframe required to block pathways by mineralisation.

From the reasoning above there are realistically three separate mechanisms for switching of fluid flow pathways along the Little Grand Wash and northern Salt Wash graben faults: mineralisation, 3-phase interference and dynamic strain. In order to determine which of these factors was the most likely the timing between switching of successive travertine deposits was plotted against the distance between these successive mounds for both field areas (Figure 5.12). Upper limits of each mechanism were deduced and plotted onto the graphs in order to highlight zones in which they may be having an affect. The limits of the 3-phase interference zone were based on the distance of displacement of CO₂ flux to the surface from the longest running model of Pruess (2003). Mineralisation was deemed to influence switches of any distance as it is solely a 'switching off' mechanism. An upper time limit is placed on this zone by the minimum lifespan of

mound L4 plus its positive error (14,069 years – sections 4.3.3, 4.6.2). As dynamic strain is an external influence it is possible that any section of the hydrological system in either field site could be affected, therefore this mechanism is deemed capable of causing a switch in pathway of any length or any distance.

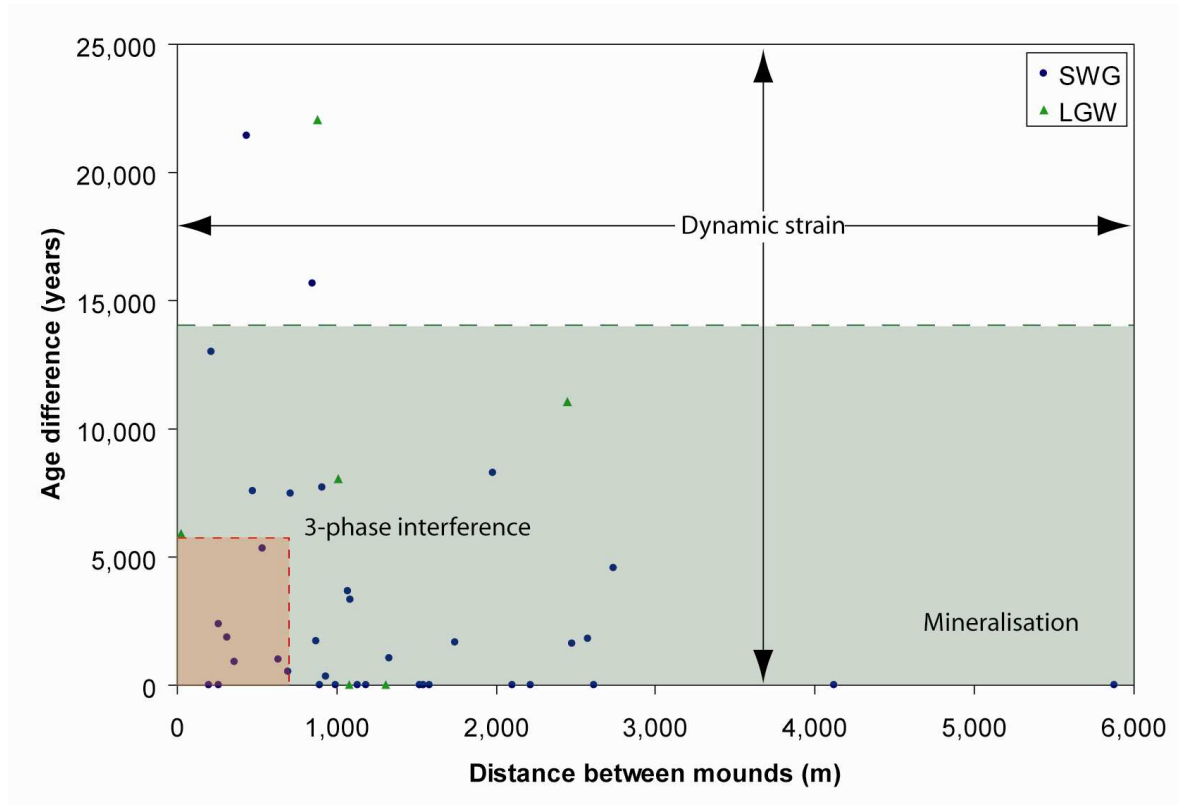


Figure 5.12: Plot of potential switching mechanisms.

Plots of the age difference between successive travertine deposits against the distance between them. Each deposit was given the same maximum lifespan (i.e. the lifespan plus the positive error) as the longest lived mound in each field area (14,069 years from L4 and 3,593 years from S37- section 4.6.2) in order to provide an estimate of the smallest possible time-gap between deposition of successive mounds. Lifespans that overlapped were given an age difference of zero. The potential mechanisms that may have instigated the switching of pathway to the surface are shown by colour coded zones. The red and green zones highlight the potential reach of influence of 3-phase interference and mineralisation respectively (note that these overlap in the bottom left corner). Dynamic strains, which are triggered by distant seismic events, are capable of causing a switch in pathway of any length or any distance. Demonstration of how these switching events can occur and possible examples of each are given in Figure 5.13. For clarity two switches of pathway from the northern fault of the Salt Wash graben have been omitted from the plots. These gaps are both >93ka and so plot solely in the dynamic strain regime.

Figure 5.12 shows that 3-phase interference is having a minimal effect on the pathways of the Little Grand Wash fault, but may be playing a decisive role along the northern fault of the Salt Wash graben. Eight possible switches between leakage points at the surface at this site occur within this zone. Examples include the switch sequences from mounds S7 - S35 - S8 and S2 - S28 - S26. The

difference in the potential role of 3-phase interference in each field area is not surprising. This is because the flow to the surface in the Little Grand Wash will be restricted to damage zone fractures due to the presence of several low permeability sealing units between the Navajo aquifer and the surface. The northern fault of the Salt Wash graben is less restricted as once flow has penetrated the sealing Carmel Formation it only has to pass through the Entrada Sandstone, and unconfined aquifer unit, to reach the surface.

As it is solely a 'switching off' mechanism mineral precipitation is the simplest method to explain changes in flow to the surface and it is likely to be the main cause of switching between mounds less than ~10 ka apart. This is shown by Figure 5.12 which shows that most of the switches in both field areas fall within this zone. Switches with zero time gap (when lifespans are taken into consideration) between precipitation of one mound and the next suggest periods of ~ continual flow to the surface and are the most likely to have been caused blockage of pathways due to mineralisation.

Dynamic strain can affect any switch shown by fluid flow pathways in both field areas. What is interesting from Figure 5.12 is that there are several switches in pathway outside of the zones of precipitation and 3-phase interference which implies that four of the switches on the northern Salt Wash graben fault and one of the switches on the Little Grand Wash fault are likely to be the result of triggering by dynamic seismic strain. This suggests that for these switches dynamic strain isn't only unblocking mineralised fractures associated with the current leakage of CO₂ charged ground waters, but is creating new pathways for the present fluid flow system. It is possible therefore that induced seismicity may be able to further rupture tight fracture sets or previous episodes of veining with the caprocks (which are not associated with the current fluid system) of the Little Grand Wash and northern Salt Wash graben faults.

Though it should be noted that the zones only provide guidelines on what mechanisms could be causing the switching of pathways the fact that there is potentially a difference in the dominance of mechanism in each field area highlights an important point. Most modelling of fluid flow and fault systems looks at ideally homogenised faults within a single, usually permeable media or protolith. As discussed above this is not representative of natural systems which will show significant variation in structure and permeability. The case presented here shows

that the behaviour of fluid flow switching in a system confined to damage zone fractures, the Little Grand Wash fault, and a system leaking through an unconfined aquifer and perhaps analogous to previous modelling attempts, the northern fault of the Salt Wash graben, may be different. This means that a large number of previous simulation and modelling on fault systems are inappropriate for cap rock failure within systems of more complicated stratigraphy. The present study also provides an insight as to how fracture controlled permeability can evolve in space and time and shows that fluid flow pathways can switch along multiple locations on faults, therefore demonstrating that leakage through sealing lithology doesn't necessarily have to be restricted to a single point.

Figure 5.13: Methods for switching of fluid flow pathways.

Conceptual models for switching of pathways via mineral precipitation, 3-phase interference and dynamic strain. (A) Precipitation of calcite within the damage zone fractures of the Carmel Formation, the sealing lithology of the Navajo aquifer, can lead to blockage of fluid flow pathways at depth and abandonment of travertine precipitation at the surface. As shown from Figure 4.19 leakage starts at a central point around the axis of the Green River anticline and spreads outwards in both directions along strike of the faults with time. This is consistent with the central point of the anticline supporting the thickest accumulation of CO₂ charged ground water and therefore the greatest head. (B) Phase interference between gaseous, aqueous and liquid CO₂ within the up-welling groundwaters can lead to a zone of low fluid mobility around the CO₂ saturation line due to the temperature drop associated with the boiling of liquid CO₂ and the Joule-Thompson effect. This can divert flow of up-welling fluid to the surface. Drop in flow to the centre of the zone of phase interference allows temperatures to recover and the 3-phase zone to dissipate, allowing for fluid flow to resume along the original pathway. Eventually the pathway will become blocked by mineralisation within the Carmel Formation. A possible example of this method of switching is shown by mounds S7, S8 and S35 (Figure 4.2B) along the northern fault of the Salt Wash graben. (C) Dynamic strain, induced by dynamic waves from distant seismic events can lead to the unblocking of mineralised pathways and the re-establishment of former fluid flow pathways. This can allow once abandoned sites to become re-activated at the surface. Mounds L5, L6 and L7, which all occur within ~50 m of each other along the Little Grand Wash fault (Figure 4.2A) demonstrate that fluid flow pathways may become re-used.

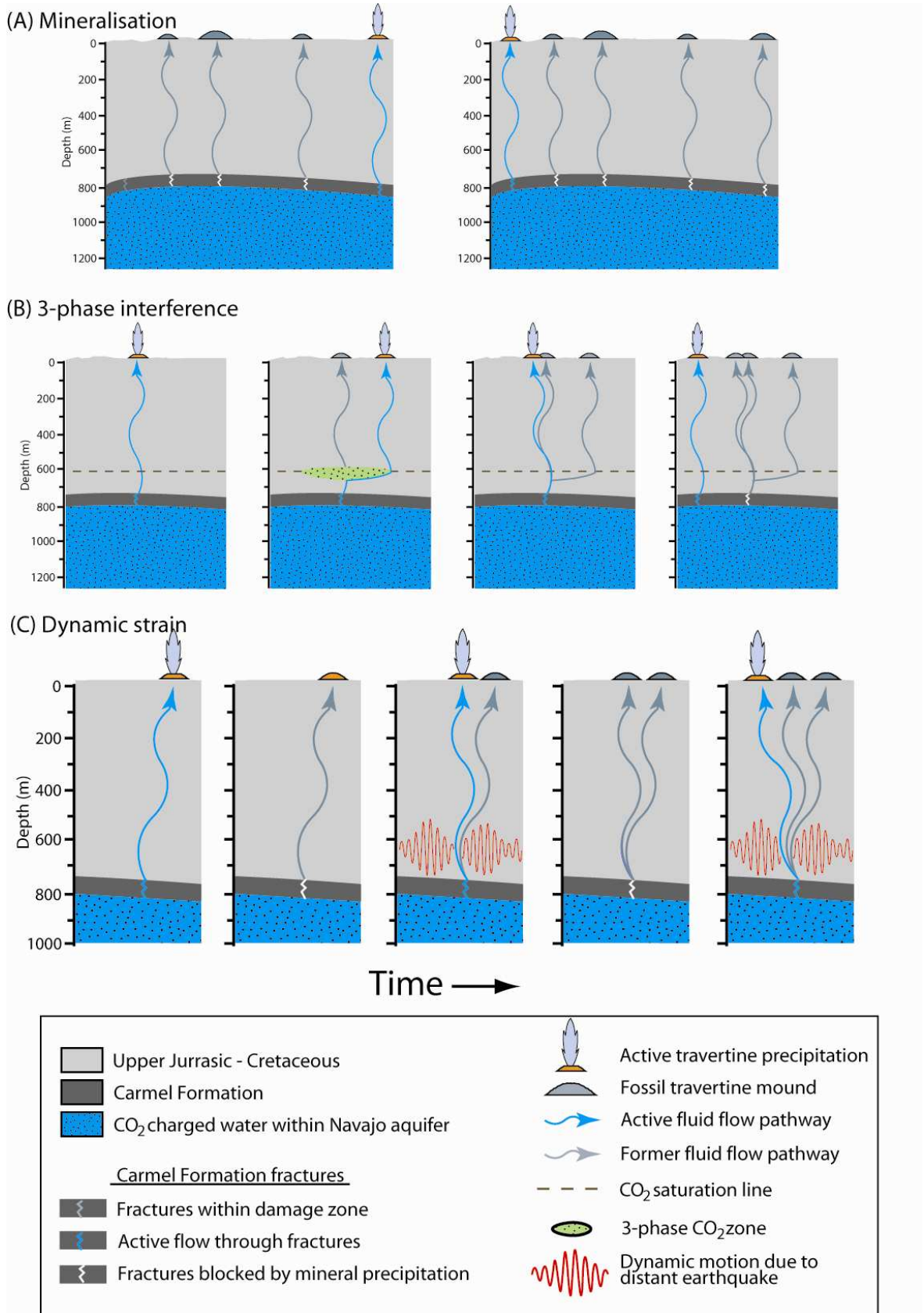


Figure 5.13: Methods for switching of fluid flow pathways.

6 Calculation and risk assessment of CO₂ leakage

6.1 Introduction

Dating and measurement of the physical dimensions of travertine deposits along both the Little Grand Wash and northern Salt Wash graben faults has allowed approximate values for proportion and rate of CO₂ leakage to the surface to be determined for both field sites. These values come with an appreciation of the large errors involved with the estimation of the volume of travertine deposits (which include area and thickness measurement- section 4.6). This chapter will demonstrate the necessary calculations in section 6.2 before going on to discuss the results for both the faults in the present study and their implications for anthropogenic storage sites in section 6.3 . Finally, to conclude, section 6.4 will form a risk assessment of the leakage along the Little Grand Wash fault and the northern fault of the Salt Wash graben and go on to present general findings applicable to the consideration of leakage in anthropogenic CO₂ storage sites.

6.2 Quantity and leakage rates of CO₂

6.2.1 Total volume of leaked CO₂

To convert the volumes into CO₂ mass leaked to the surface, a series of basic calculations need to be conducted (Dockrill, 2006). Firstly, the total mass of travertine along each fault is calculated by:

$$M_{CaCO_3} = \rho_{CaCO_3} V_{CaCO_3}$$

Equation 6.1

Where ρ_{CaCO_3} equals the average density of calcium carbonate (2,800 kg/m³) and V_{CaCO_3} is the total volume of travertine. The total proportion of CO₂ within this mass is calculated as follows;

$$M_{CO_2} = M_{CaCO_3} \left(\frac{MM_{CO_2}}{MM_{CaCO_3}} \right)$$

Equation 6.2

Where MM_{CaCO_3} is the mass of travertine, MM_{CO_2} is the molar mass of carbon dioxide (44 g) and M_{CaCO_3} is the molar mass of calcium carbonate (100.1 g). The total mass of CO₂ that has leaked to the surface along each fault is calculated by:

$$M_{TCO_2} = \frac{M_{CO_2}}{X_{CO_2}}$$

Equation 6.3

Where M_{CO_2} is the mass of CO₂ precipitated in the travertine and X_{CO_2} is the proportion of CO₂ leaked to the surface that is precipitated as travertine. Geochemical modelling using measured water chemistry from the Crystal Geysers by Heath (2004) suggests that approximately 10% of leaked CO₂ is precipitated while the remainder is either vented as a free gas into the atmosphere or retained in solution. This value is based on the assumption that no free phase CO₂- gas is present and that there is no calcite in solution, which may be appropriate due to the likely hood of the Navajo aquifer being below the CO₂ saturation line. Heath (2004) used Phreeqc 2.8 to model the solution, which was equilibrated with respect to calcite and atmospheric CO₂ ($P_{CO_2} = 10^{-3.5}$ atm). Although no errors on this estimate are provided a sensitivity of $\pm 5\%$ (equal to an error of $\pm 50\%$) on Heath's (2004) X_{CO_2} is applied to the results of the present study in order to produce a likely range for fixation of CO₂ during precipitation of travertine mounds.

The results of these calculations for total and modern leakage in both field areas are presented in Table 6.1 and Figure 6.1. Also included within these results are the leakage estimates of mound L4 and for the last ~113 ka of the northern fault of the Salt Wash graben, which was calculated to provide further comparison between the two field sites. The estimated total amount of CO₂ to have leaked (taking $X_{CO_2} = 10\%$) along the Little Grand Wash and Salt Wash graben faults since the precipitation of the oldest remaining travertine deposits each area is $1.3 \times 10^6 \pm 3.6 \times 10^5$ tonnes and $9.8 \times 10^5 \pm 2.7 \times 10^5$ tonnes respectively. For the last ~113 ka the total CO₂ to have leaked from the Salt Wash graben is $7.4 \times 10^5 \pm 2 \times 10^5$ tonnes, a total that is just over half of the volume of CO₂ leaked from the Little Grand Wash fault over the same time period. Indeed the total amount of CO₂ leaked from mound L4, $8.6 \times 10^5 \pm 2.3 \times 10^5$ tonnes on the Little Grand Wash fault is greater than this. These conservative estimates of leakage, due to all ancient mounds having been eroded to a varying degree, may be demonstrating that less

CO₂ has been leaked to the surface in the Salt Wash graben or, as discussed previously in the thesis, that erosion may have had a greater affect on travertine along the northern fault of the Salt Wash graben (sections 3.5.4.1 and 4.7.3).

In order to give a maximum value, and test the two theories above, worst case scenarios for proportion of leakage in both field areas were estimated by attributing each mound across the two field areas with the same dimensions as that of the largest mound in each area (L4 and S37). The results of these calculations, which are presented in Table 6.2, were deduced by considering every ancient mound to have the same dimensions as that of the largest deposit in each field area. The results of this scenario produced a total leaked mass of CO₂ almost five times greater than the minimum estimate for the Little Grand Wash fault ($6.2 \times 10^6 \pm 1.7 \times 10^6$ tonnes) and over seven times that of for the northern fault of the Salt Wash graben. ($7.4 \times 10^6 \pm 2 \times 10^6$ tonnes). These estimates of maximum volumes of leakage show that the Salt Wash graben could have leaked a greater mass of CO₂ into the atmosphere over its entire history than the Little Grand Wash fault. However, when only the last ~113 ka of Salt Wash graben leakage ($5.3 \times 10^6 \pm 1.4 \times 10^6$ tonnes) is compared to the Little Grand Wash it can be seen that for the same timescales of worse case leakage scenario that the Little Grand Wash has still leaked a larger amount of CO₂.

Larger scale leakage on the Little Grand Wash fault is also reflected by the amount of CO₂ leaked from currently active travertine spring deposits. The mass of CO₂ leaked from the Little Grand Wash ($2.2 \times 10^5 \pm 6 \times 10^4$) is over five times greater than that of the northern fault of the Salt Wash graben ($4.1 \times 10^4 \pm 1.1 \times 10^4$), despite there only being one site of active leakage there in comparison to six. This may be an unfair comparison as mound L1, the Crystal Geyser, is definitely the result of anthropogenic drilling as evidenced by drilling records of the Glen Ruby #1-X exploration well (section 3.4.5). Though it is not totally certain whether all of the active Salt Wash graben deposits are man-made or natural, the presence of well casing around mound S45, the Ten Mile Geyser, and the low estimated lifespans (<87 years) of the rest of the deposits suggests that are all the result of exploration drilling (section 4.7.4). Nevertheless drilling records for any of these sites are non-existent so total depths and the stratigraphy they intercept is unknown.

		Little Grand Wash fault			Northern fault of the Salt Wash graben		
		Total	L4	Modern springs	Total	Last ~113ka	Modern springs
Volume (m ³ ± 27%)		107,510 ± 29,028	69,660 ± 18,808	18,191 ± 4,912	79,809 ± 21,548	60,030 ± 16,208	3,333 ± 900
Mass (tonnes ± 27%)		301,028 ± 81,278	195,048 ± 52,663	50,935 ± 13,752	223,465 ± 60,336	168,084 ± 45,383	9,333 ± 2,520
CO ₂ mass (tonnes ± 27%)		132,320 ± 35,726	85,735 ± 23,149	22,389 ± 6,045	98,227 ± 26,521	73,883 ± 19,948	4,102 ± 1,108
CO ₂ leaked (tonnes ± 27%)	10%	1,323,200 ± 357,264	857,354 ± 231,486	223,889 ± 60,450	982,265 ± 265,212	738,831 ± 199,484	41,022 ± 11,076
	5%	2,646,400 ± 714,528	1,714,708 ± 462,971	447,778 ± 120,900	1,964,531 ± 530,423	1,477,662 ± 398,969	82,044 ± 22,152
	15%	882,133 ± 238,176	571,569 ± 154,324	149,259 ± 40,300	654,844 ± 176,808	492,554 ± 132,990	27,348 ± 7,384
Leakage rate (tonnes/yr ± 27%)	10%	11.6 ± 3.1	79.8 ± 21.6	3,153 ± 851	2.4 ± 0.6	6.5 ± 1.8	578 ± 156
	5%	23.2 ± 6.3	159.7 ± 43.1	6,307 ± 1,703	4.8 ± 1.3	13.1 ± 3.5	1,156 ± 312
	15%	7.7 ± 2.1	53.2 ± 14.4	2,102 ± 568	1.6 ± 0.4	4.4 ± 1.2	385 ± 104
Area (m ² ± 19%)		28,893 ± 5,490	11,610 ± 2,206	5,868 ± 1,115	89,103 ± 16,930	68,175 ± 12,953	8,796 ± 1,671
Lifespan (years ± 31% -42%)		13,842 ^{+4,568} -5,675	10,740 ^{+3,544} -4,403	71	11,876 ^{+3,919} -4,870	8,741 ^{+2,845} -3,584	86 ⁺²⁸ -35
Flux (g/m ² /day ± 46%)	10%	1.10 ± 0.51	18.84 ± 8.67	1,472 ± 677	0.07 ± 0.03	0.26 ± 0.12	180 ± 83
	5%	2.20 ± 1.01	37.68 ± 17.33	2,945 ± 1,355	0.15 ± 0.07	0.53 ± 0.24	360 ± 166
	15%	0.73 ± 0.34	12.56 ± 5.78	982 ± 452	0.05 ± 0.02	0.18 ± 0.08	120 ± 55
Flux- switching on/off	10%	9.06 ± 4.17	-	-	2.54 ± 1.17	3.40 ± 1.56	-
	5%	18.13 ± 8.34	-	-	5.09 ± 2.34	6.79 ± 3.13	-
	15%	6.04 ± 2.78	-	-	1.70 ± 0.78	2.26 ± 1.04	-

Table 6.1 CO₂ leakage and flux estimates.

Totals are derived from the calculations of equations 6.1 – 6.4. Every value based on the volume of deposits is attributed with a ±27% error, whilst flux is attributed a total error of ± 46% as it is calculated from volume of CO₂ leaked (±27%) and the area of deposits (±19%). Leaked CO₂, CO₂ leakage rate and CO₂ flux are all presented with the estimation of Heath (2004) for CO₂ precipitated within travertine mounds ($X_{CO_2} = 10\%$) and also with a sensitivity of ±5% on this value. Flux was considered for switching on/off of leakage at the surface by taking into account the sum of all the mound lifespans in each field area and using this value for time in the flux calculation. This value is therefore the time averaged flux for the minimum length of time of travertine production through out the history of leakage.

		LGW	SWG	SWG last 113ka
Volume (m ³ ± 27%)		505,811 ± 136,569	608,821 ± 164,382	431,605 ± 116,533
Mass (tonnes ± 27%)		1,416,271 ± 382,393	1,704,699 ± 460,269	1,208,494 ± 326,293
CO ₂ mass (tonnes ± 27%)		622,537 ± 168,085	749,318 ± 202,316	531,206 ± 143,426
CO ₂ leaked (tonnes ± 27%)	10%	6,225,366 ± 1,680,849	7,493,181 ± 2,023,159	5,312,062 ± 1,434,257
	5%	12,450,732 ± 3,361,698	14,986,360 ± 4,046,317	10,624,120 ± 2,868,512
	15%	4,150,244 ± 1,120,566	4,995,453 ± 1,348,772	3,541,373 ± 956,171
Leakage rate (tonnes/yr ± 27%)	10%	55 ± 15	18 ± 5	47 ± 13
	5%	109 ± 30	36 ± 10	94 ± 25
	15%	36 ± 10	12 ± 3	31 ± 8
Area (m ² ± 19%)		87,138 ± 16,556	266,932 ± 50,717	191,380 ± 36,362
Lifespan (years ^{+31%} / _{-42%})		75,251 ^{+23,328} / _{-31,605}	93,443 ^{+28,967} / _{-39,246}	68,396 ^{+21,203} / _{-28,726}
Flux (g/m ² /day ± 46%)	10%	1.72 ± 0.79	0.19 ± 0.09	0.67 ± 0.31
	5%	3.44 ± 1.58	0.37 ± 0.17	1.35 ± 0.62
	15%	1.15 ± 0.53	0.12 ± 0.06	0.45 ± 0.21
Flux- switching on/off	10%	2.60 ± 1.20	0.82 ± 0.38	1.11 ± 0.51
	5%	5.20 ± 2.39	1.65 ± 0.76	2.22 ± 1.02
	15%	1.73 ± 0.80	0.55 ± 0.25	0.74 ± 0.34

Table 6.2: Worst case scenario for leakage and flux of CO₂.

To determine the worst case scenario figures for leakage from ancient travertine every mound was attributed with the same volume and area of that of the largest deposit of each area, L4 (69,660 ± 18,808 m³/ 11,610 ± 2,206 m²) and S37 (14,768 ± 3,987 m³/ 6,296 ± 1,196 m²). Intermittent flux is calculated by superimposing the lifespans of mounds L4 and S37 on the rest of the travertine mounds from the Little Grand Wash and northern Salt Wash graben fault field sites respectively.

6.2.2 Leakage rates and Flux

The estimates of CO₂ mass leaked to the surface along the Little Grand Wash and northern Salt Wash graben faults carried out above enables calculation of leakage rates and flux for both ancient and modern travertine deposition. The maximum travertine age for each field site combined with the calculated mass of leaked CO₂ gives a time averaged leak rate of 11.6 ± 3.1 tonnes/year and 2.4 ± 0.6 tonnes/year for each fault, while taking only the last 113 ka for the northern fault of the Salt Wash graben, a timescale which matches the total length of activity for the Little Grand Wash fault, a leak rate of 6.5 ± 1.8 tonnes/year is apparent (Table 6.1, Figure 6.1). Taking the worse case scenarios into account the Little Grand Wash fault (55 ± 15 tonnes/year) and the last 113 ka for the northern fault of the Salt Wash graben (47 ± 13 tonnes/year) produce similar results (Table 6.2). This suggests that natural leakage in both areas may have progressed at a similar rate over time.

The leakage rate of mound L4 was estimated as radiometric dating of multiple samples provided a minimum lifespan for this deposit (section 4.3.3). This individual mound provides a CO₂ leakage rate of 79.8 ± 21.6 tonnes/year which is

eight times more than the time averaged leakage rates for all mounds over the last 114 ka along the Little Grand Wash. As the total represents the leakage rate for the entire lifespan of a deposit it may provide a good estimate of actual leakage rate during natural travertine deposition. This would suggest that individual mounds represent leakage rates that can vary widely from the overall leakage of the faults.

Modern leakage rates are far in excess of the leakage rates provided by ancient deposits (Figure 6.1). Mound L1, the Crystal Geyser, produces a leak rate of $3,153 \pm 851$ tonnes/year, whilst the combined total for the six active mounds of the northern fault of the Salt Wash graben gives a rate of 578 ± 156 tonnes/year. As this latter rate is far in excess of the worse case scenario for the northern Salt Wash graben fault and that calculated from the ancient L4 mound it further suggests that these deposits are man-made in nature.

An alternative measurement of CO₂ leakage commonly used in risk assessment is flux (Oldenburg and Unger, 2005). Flux is a measure of the rate at which CO₂ passes out of the ground per unit area;

$$FLUX = M / A / t$$

Equation 6.4

Where M is the leaked mass of CO₂, A is the area of emission at the surface defined by the areal extent of travertine deposits and t is the total duration of leakage. The time averaged CO₂ flux over the entire histories of the Little Grand Wash and northern Salt Wash graben faults are 1.1 ± 0.5 and 0.07 ± 0.03 g/m²/day respectively. Over the last 113ka, flux for the northern fault of the Salt Wash graben increases to 0.26 ± 0.12 g/m²/day. As the flux values for each area are time averaged values they represent an underestimate due to the forced assumption that all travertine sites were active after initiation. Additionally, the fact that the cross-sectional area of the vent at each mound will be smaller than the total mound area makes these values lower bounds to the total time-averaged flux.

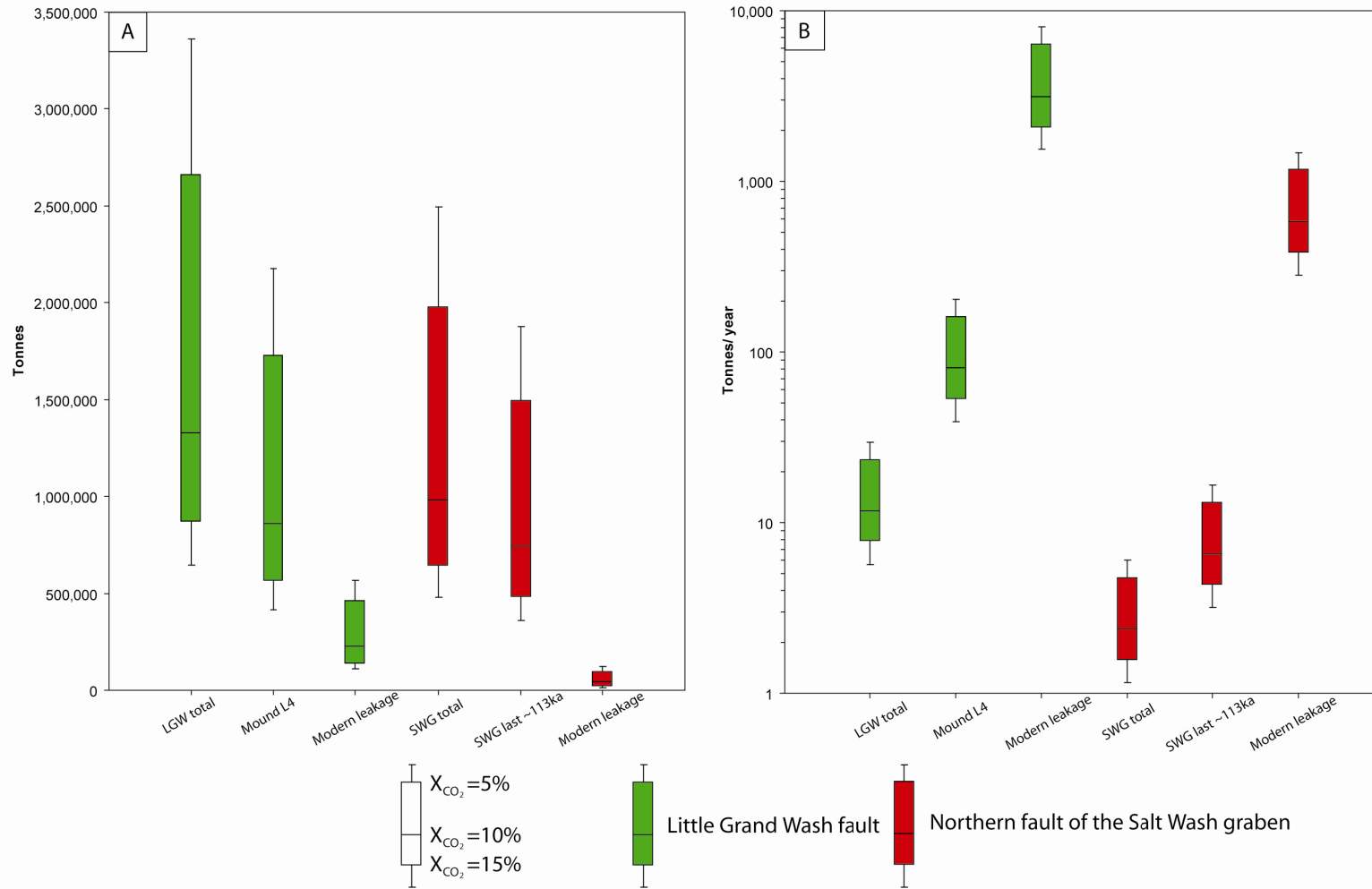


Figure 6.1: Plots of total leakage and leakage rates.

For both plots data from the Little Grand Wash fault is shown in green and data from the northern fault of the Salt Wash graben in red. (A) Plot of total leakage. (B) Plot of leakage rates. Note that the y-axis is logarithmic in scale in order to show all rates.

By taking the sum of all the estimated lifespans of travertine in each area an appreciation of flux during only periods of travertine deposition can be obtained. This is shown in Table 6.1 as the flux value for the switching on and off of leakage to the surface (as the totalled lifespans are less than the recorded history of leakage along each of the faults), and results in an increase flux value for both field sites. In the worst case scenario for leakage shown in Table 6.2 these switching on and off flux values are severely reduced because the summed lifespan of all the mounds (which have all been attributed with the same lifespans of that of the longest lived travertine deposits) in this scenario are far greater than the sum of estimated lifespans in Table 6.1. Perhaps a far more useful tool in this case for flux during the precipitation of natural travertine deposits is the CO₂ flux result for mound L4, 18.8 ± 8.7 g/m²/day. The estimated CO₂ flux of modern springs along both the Little Grand Wash ($1,472 \pm 677$ g/m²/day) and northern Salt Wash graben (180 ± 83 g/m²/day) faults provide an indication of the present day flux values and are again far greater than the flux calculated from the ancient deposits (Table 6.1).

6.3 Discussion

6.3.1 Comparison with other leakage rate estimates on LGW

A contemporary study using aerometric measurements to quantify the mass of CO₂ emitted from the Crystal Geyser estimated a discharge rate from 48 hours of observation of ~12,000 tonnes of CO₂ per year (Gouveia et al., 2005). The discrepancy between this estimate and the values found in the present study could be down to various factors. The leakage rates within the present study have used a value of 10% from the modelling of Heath (2004) for the proportion of CO₂ leaked that is precipitated within the travertine mounds. It is possible that this could be an over-estimation. When a sensitivity of 50% is taken into consideration for Heath's (2004) results and the amount of leaked CO₂ considered to be captured by travertine deposition is lowered to 5% then a leakage rate of $6,307 \pm 1,703$ tonnes/year is resultant for mound L1 (Table 6.1). However, this is still half the rate found by Gouveia et al. (2005) so other effects must be taken into consideration. There is also evidence that suggests not all the CO₂ migrating to the surface comes from discharge of the Crystal Geyser. Soil flux measurements from along the Little Grand Wash fault showed anomalies above background

coinciding with the fault trace (Allis et al., 2005). The highest flux, >700 g/m²/day CO₂, which translates to >256 tonnes/year from this single point, was located on an outcrop of L2 close to the active L1. Supporting evidence for leakage of gas to the surface comes from the observation of gas bubbles along a ~50 m stretch of the Green River from the fresh travertine below the geyser to the remnant of mound L2 on the opposite shore.

Alternatively the rate found by Gouveia et al. (2005) may be an over-estimation as the sampling of the Crystal Geyser was only carried out over 48 hours. It is possible that this was a particularly active 48 hours in comparison to the long term or even yearly average. Clarification of this difference could potentially be solved through more in-depth monitoring and measurement of emissions of the Crystal Geyser over a longer time period, say several months to a year, to gain a more accurate estimate.

6.3.2 Comparison with other natural CO₂ sources

Despite the relatively high modern leakage rates outlined in section 6.2.2 the impact of CO₂ leakage to the surrounding environment of both the Little Grand Wash and Salt Wash graben is minimal. To put this leakage into perspective, the various flux measures are presented in Table 6.3 in comparison to flux rates reported from other sedimentary basins, geothermal fields and observation of other natural sources of CO₂ emission.

The Mátraderecske field, situated in northern Hungary, leaks gas with 95% CO₂ content from a strongly weathered Eocene andesite aquifer from a depth of ~500m (Streit and Watson, 2004). Leakage to the surface mainly occurs vertically through fault conduits in the overlying Eocene and Oligocene clays and sands, and the CO₂ is thought to originate either from nearby deep polymetallic copper-zinc mineralisation (Pearce et al., 2002) or from volcanic CO₂ (Streit and Watson, 2004). The CO₂ in this field is leaking from a largely unconfined aquifer unit with sections of missing local sealing lithologies that allows gas to escape directly (Pearce et al., 2002). The average CO₂ flux to the surface in the area is 235 - 470 g/m²/day (Pearce et al., 2002).

	Source	CO ₂ flux (g/m ² /day)	Reference
This study	Little Grand Wash fault	1.1 ± 0.5	Minimum total leakage
		1.7 ± 0.8	Maximum total leakage
18.8 ± 8.7		Mound L4 leakage	
1,472 ± 677		Modern leakage	
Northern Salt Wash graben fault		0.3 ± 0.1 ^a	Minimum total leakage
		0.7 ± 0.3 ^a	Maximum total leakage
		180 ± 83	Modern leakage
Natural CO ₂ reservoirs with seals	Farnham Dome	0.5- 3.7	Allis et al. (2005)
	Springerville- St.Johns	4 ± 4 (poorly vegetated)	Allis et al. (2005)
10.2- 24.5 (highly vegetated)			
Natural CO ₂ reservoirs without seals	Mátraderecske basin	235- 470	Pearce et al.(2002)
	Rapolano fault	2.3- 3,076	Morner and Etiope (2002)
	Rekjanes geothermal field	6,849	Fridriksson et al. (2006)
Other natural CO ₂ sources	Great Plains- semi arid grassland	0.5- 6.9	Frank et al. (2002) Lee et al. (2006)
	Forest floor	8 - 76 ^b	Janssens et al. (2001) Drewitt et al. (2002)
	Mammoth Mountain tree kill	1,521 ^b	Benson and Hepple (2005)
	Fumerole activity	259 - 1,020 ^b	Vodnik et al. (2009)

Table 6.3: CO₂ flux measurement comparisons.

Table showing comparison of CO₂ flux results from the present study and those found for various CO₂ sources in previous works. (a) Flux shown for total leakage of the northern fault of the Salt Wash graben is for the last ~113ka. (b) Flux estimates converted from μmol/m²/s format to g/m²/day format for the purpose of comparison.

The Rapolano fault forms the eastern border of the Siena-Radicofani basin in Tuscany. This is one of the most vigorous CO₂ leakage sites in Italy due to the highly permeable Pliocene sandstones and high CO₂ pressure gradients due to a deep geothermal reservoir (Etiope et al., 2005). Leakage of CO₂ is unconfined in this area as confining Pliocene clay caprocks found elsewhere in the Siena-Radicofani basin are absent (Etiope et al., 2005). The source of the CO₂ is thought to be sourced from low enthalpy geothermal fluids (Etiope and Lombardi, 1995; 1997). Similar to the present study, previous leakage of CO₂ to the surface is evidenced by ancient travertine deposition in the form of a 150m long ridge along the fault at Terme S. Giovanni (Etiope et al., 2005). CO₂ flux from this fault is of the order of 2.3 – 3,076 g/m²/day (Morner and Etiope, 2002) whilst leakage rates solely from gas vents is estimated to total ~ 7,900 tonnes/year (Etiope et al., 2005).

The Reykjanes geothermal area is the western most system in Iceland's western neo-volcanic zone. CO₂ emissions from this area are localised around 3-5 elongated north-south trending fault zones which are all thought to support a right

lateral strike-slip sense of motion (Fridriksson et al., 2006). Degassing of mantle-derived magma at a depth of 1,000 – 1,200 m is the sole source of CO₂ in the area (Ármansson et al., 2005). The area is devoid of any sealing units as the stratigraphy between the CO₂ source and the surface consists of hyaloclastites and highly permeable Holocene lavas (Fridriksson et al., 2006). Three general pathways; soil diffuse degassing, steam vent discharge and gas bubbling through heated pools; are responsible for CO₂ emissions in the Rekjanes area (Ármansson et al., 2005). The combined leakage of CO₂ to the surface from these pathways is 5,060 tonnes/year, which relates to a flux of 6,849 g/m²/day (Fridriksson, 2006).

The flux measurements from the above sites are generally far greater than the estimated time averaged flux from the faults in the present study (Table 6.3). It should be noted that CO₂ leakage is happening on a far larger scale at these sites due to the lack of confining caprocks above the CO₂ sources. Further to this the Rekjanes geothermal area and the Rapolano fault both display enhanced CO₂ fluxes across wide areas as the leaking CO₂ is actively being produced directly and indirectly via magmatic sources. Despite the unconfined nature of the leakage and the continual supply of CO₂ displayed by the sites above it is interesting to note that the flux rates (235 to 6,849 g/m²/day) and leakage estimates (~5,060 to 7,900 tonnes year) are of the same magnitude to that of modern day anthropogenic leakage at the Crystal Geyser ($1,472 \pm 677$ g/m²/day and $3,153 \pm 851$ tonnes/year) on the Little Grand Wash fault (Table 6.3).

At maximum and minimum time averaged flux rates of 1.1 ± 0.5 to 1.7 ± 0.8 g/m²/day for the Little Grand Wash and 0.3 ± 0.1 to 0.7 ± 0.3 g/m²/day for the Salt Wash graben for the last ~113 ka, natural leakage along these faults is comparable to natural flux from vegetated areas. An individual flux of 18.8 ± 8.7 g/m²/day for the lifespan of mound L4 is still less than CO₂ background soil flux recorded from highly vegetated areas above effectively sealed natural CO₂ reservoirs at Farnham Dome, Utah, and Springerville - St. Johns, Arizona, and towards the lower end of flux levels recorded from forest floors (Table 6.3). However, it must be emphasised that the flux measurements are calculated assuming the entire mound area rather than the vent area (which cannot be measured for the majority of the ancient mounds), so these are lower bounds.

Modern anthropogenic leakage since the drilling of exploration wells in each area is much higher at $1,472 \pm 677$ g/m²/day for the Little Grand Wash fault and 180 ± 83 g/m²/day for the northern fault of the Salt Wash graben. Despite these relatively high leak rates, comparative with fumerole activity and tree kill (Table 6.3), there appears to be no plant mortality around any of the leak sites; in fact slightly enhanced growth of salt tolerant plants is actually evident at some modern leakage sites because of the increase in water at the surface in this desert environment (Shipton et al., 2005). In addition there are no reports of human casualty in the local historical record in relation to CO₂ leakage at the Crystal Geyser even though the area has been popular with locals and tourists since 1935 (Shipton et al., 2005). This all suggests that CO₂ leakage, even with the relatively high modern rates, along both the Little Grand Wash and northern Salt Wash graben faults poses no threat to the local ecosystem or human activity.

Before using examples from natural accumulations in order to gain data to predict possible outcomes of long term anthropogenic storage, the difficulties in comparing different CO₂ accumulations should be appreciated. This is highlighted by the examples used in this section because each location has different sources and volumes of CO₂, with some leakage sites still being driven by active, present-day production of CO₂ at depth. The geology and pressure gradients are also different in each case, with the presence or lack of competent seals and depth of CO₂ reservoir both having huge effects on leakage rates and flux. It is therefore important to note that each of these cases are likely site-specific. For a true appreciation of leakage potential in future engineered storage sites, good base line data are essential, for instance; reservoir volume, pressure gradients, porosity, permeability and mechanical strength of potential pathways (caprock failure, damage zone failure, wellbore failure), natural in-place CO₂ volume and generation.

6.3.3 Implications for anthropogenic storage sites

In order to meet global demand for reduction of CO₂ emission several geological storage projects have been implemented and many more planned in order to investigate the suitability and effectiveness of CO₂ capture and storage for cutting CO₂ emissions into the atmosphere whilst allowing for the continued use of fossil fuels. By comparison of the Little Grand Wash and northern Salt Wash

graben fault systems with current anthropogenic storage sites the leakage rates found within this chapter can be placed further into context. Three main examples, the Sleipner, Weyburn and Gorgon projects, will be used within the following section to discuss the possible implications of the leakage rates calculated from the present study. These three have been chosen due to the availability of data and their different geological situations. In order to discuss potential leakage in better detail for these examples the leakage rates calculated above can be considered as end member analogues for caprock failure and well bore failure for total and modern leakage rates respectively. Since the initiation of leakage, migrating CO₂ charged waters have used fractures within impermeable sealing lithologies in the damage zones of the two faults- this makes the calculated total leakage rates an ideal representation of leakage via caprock failure above a CO₂ storage reservoir. Although storage site may have been chosen in areas where fractures within caprock are deemed unlikely, such as those thought to be devoid of faulting, there may be previously undetected structural heterogeneities within the reservoir that only become apparent after injection. There is also the possibility of overpressuring depleted reservoirs during injection and inciting hydrofracture of once competent sealing lithologies. As modern leakage of mound L1, the Crystal Geyser, is far greater than the active mounds along the northern fault of the Salt Wash graben and it is definitely attributed to anthropogenic drilling- the leakage rates calculated from this deposit are treated as a proxy for catastrophic well failure.

The Sleipner field, located in the North Sea and operated by Statoil, is used to store CO₂ separated from natural gas production at the Sleipner West facility in Stavanger, Norway. Since 1996 around 1 million tonnes of CO₂ have been injected into the base of an off-shore saline aquifer, and by the end of 2008 almost 11 million tonnes had been stored (Hermanrud et al., 2009, Chadwick et al., 2009). The storage reservoir being used, the Utsira Formation is a 200-250 m thick massive sandstone formation located at a depth of 800-1000 m beneath the seabed (Chadwick et al., 2004; Zweigel et al., 2004). This is a similar depth and thickness to the Navajo aquifer supplying the springs in this study. Taking the worst case scenario for total leakage from the Little Grand Wash, it would take $18,298 \pm 4,940$ years for every 1 million tonnes of CO₂ injected to escape from the storage reservoir and $201,278 \pm 54,345$ for the storage reservoir to become completely emptied via caprock failure of the sealing lithology. Taking modern

leakage rates, it would take 317 ± 86 years for every Mt CO₂ injected or $3,488 \pm 942$ years for the entire reservoir to come up a single well that failed in the style of the Crystal Geyser.

The Weyburn oilfield, situated in Saskatchewan Canada, is currently being subjected to CO₂ injection for enhanced oil recovery (EOR). Injection was initiated in the year 2000 and is expected to continue in phases until 2015 (Preston et al., 2005). Currently 5,000 tonnes of CO₂ are injected per day and taking into consideration the full length of the project it is expected that 20 million tonnes will be stored in the Weyburn reservoir. The injected CO₂ is anthropogenically sourced and transported via pipeline from a coal gasification plant in Beulah, North Dakota 320 km to the southeast. The CO₂ is injected into unconformably capped Midale Beds reservoir, which consists of Mississippian-aged shallow marine carbonates 1,300-1,500 m below the surface. CO₂ injection is carried out to increase recovery of heavy oil from about 35% to 50% (Cantucci et al., 2009). Recycled CO₂ accompanying produced oil is re-captured and re-injected into the reservoir in an attempt to permanently store the anthropogenic CO₂ in the subsurface (Jensen et al., 2009). The Weyburn site currently has a total of 963 active and 146 abandoned wells within the oilfield. Although most of the estimated 20 million tonnes of total stored CO₂ should be sequestered in left behind heavy oil, it is still worth noting that if one of the many active wells failed or one of the abandoned wells was reactivated by some means (e.g. corrosion) then it would take 1.6 ± 0.4 years to leak back a days worth of injected CO₂, or as little for $6,342 \pm 1,712$ years for the total intended stored CO₂ to leak back to the surface. Should caprock failure occur above the reservoir at some point it would take 91 ± 25 years for a days worth of injection and $365,961 \pm 98,809$ years for the total stored CO₂ to leak from the reservoir.

The Gorgon project, operated by Chevron with ExxonMobil and Royal Dutch Shell as stake holders, is a Liquefied Natural Gas (LNG) development currently under development offshore of the northwest coast of Australia and is due to be operational within the next five years (Cook, 2009). The goal of this project is to tap into 40 trillion cubic feet of natural gas reservoirs within the Jansz and Gorgon fields to supply gas to the Western Australian domestic market (Reidy, 2008). Liquefaction for easier subsequent transport is carried out on the remote Barrow Island which is over 1,200 km from Perth, the nearest logistical

staging point (Flett et al., 2009). Up to 14% of the gas transported to Barrow Island from the reservoirs is CO₂, which has to be removed as CO₂ becomes solid and can damage equipment during the LNG process. The CO₂ will be injected into the sandstones and siltstones of the 500 m thick Dupuy Formation at the northern end of Barrow Island 2,300 m beneath the surface. The Dupuy Formation is a saline aquifer overlain with a thick shale caprock seal, and is intersected by the Barrow Island fault at the Southern end of the island. It is planned that a total of 125 million tonnes of CO₂ will be injected into the Dupuy aquifer over the lifetime of the project at a rate of 3.3 million tonnes per year (Cook, 2009). Although the CO₂ will be injected at a depth of 2.7 to 3 km (and so will behave as a super-critical fluid) well away from the fault, should the CO₂ manage to reach the fault and leak through fractures in the caprock at any point during active storage then using the rates from this study it would take $60,384 \pm 16,304$ years for a years worth of injection to escape. Should leakage occur at some point in the future after completion of the project it would take a total of $2,287,255 \pm 617,559$ years for the stored CO₂ to completely leak to the surface. However, should the injection well or any sealed exploration wells in the area fail then leakage for a years worth of injected CO₂ would take only $1,046 \pm 283$ years or $39,640 \pm 10,703$ for complete escape of the planned total of CO₂ to be stored.

6.3.4 Monitoring and verification of leakage

The perfect reservoir and trap rarely exist; with most reservoirs capable of leaking to some degree- monitoring of anthropogenic storage sites during and after completion of CO₂ injection is therefore vital in order to confirm the durability of specific sites and the feasibility of CO₂ storage in geological media as a whole. Although monitoring is obviously already a key component of current and planned storage projects the leakage results from the faults in the present study may provide further information which can help aid the monitoring process and provide further guidance as to what to look out for in terms of potential leakage patterns. There is a range of monitoring techniques currently in use for CO₂ storage projects (Chadwick et al., 2007) the following paragraphs discuss the efficiency of some of the main processes, which are applied remotely, in the subsurface or from the surface, in light of the findings of the present study.

Time lapse gravity and seismic profiles of storage sites are two methods that have been commonly implemented to provide a detailed characterisation of CO₂ bodies, or plumes, and the evolution of the geology of storage reservoirs and caprocks in response to stored CO₂ (Arts et al., 2004a; 2004b; 2008; Riddiford et al., 2005; Juhlin et al., 2007; Loseth et al., 2009). For offshore storage sites, such as Sleipner, 4D seismic can be utilised for monitoring. However, this process is relatively expensive and is hard to implement for onshore storage sites due to problems with changing weather, soil humidity and contact conditions (Michael et al. in press). 4D gravity is a cheaper monitoring method which works well for quantitative estimates of CO₂ saturation in the subsurface (Arts et al., 2004a). This method requires a detailed understanding of the geology surrounding the storage site and a well characterised model for the entire geological system (Michael et al., in press). The scale of these methods provides a problem for the channelled and discrete leakage of CO₂ that is evident in the present study. Seismic scan lines have a resolution on a scale of 10's of meters which may miss even meter scale heterogeneities in structures such as faults and would certainly overlook the discrete pathways in this study which are likely to be of sub-meter scale. Microseismic monitoring is a possible way to increase resolution but this would involve an increased number of monitoring wells in close proximity (Teanby et al., 2004) which may be impractical due to the scale of a storage project or inhibitive expensive to operate.

Methods that rely on monitoring wells in addition to injector wells such as temperature and pressure profiling, geophysics and tracer fingerprinting have also been investigated for use in monitoring (Prevedel et al., 2009). 4D vertical seismic profiling and pulsed neutron logging are just two examples of geophysical methods (Muller et al., 2007; Daley et al., 2008) which allow for quantitative tracking of CO₂ plumes. Geophysical methods such as these run into problems when application to commercial scale projects with larger CO₂ plumes are considered as the transmission distance between injection and monitoring wells may become too big to provide desired levels of resolution for monitoring (Chadwick et al., 2009). Fingerprinting of stored CO₂ with non-reactive elements such as noble gases (Gilfillan et al., 2008; Lafortune, 2009) can allow for the verification of CO₂ break through at monitoring wells and in various environments between the storage horizon and the ground surface (Stalker et al., 2009). The sheer number of wells required in these methods to provide a good coverage of leakage monitoring

above a CO₂ storage site could again be impractical and costly. In addition the geology of the storage site would have to be intimately known so that specific locations where leakage is more likely to occur can be highlighted and monitored more intensively.

Monitoring of CO₂ leakage at the ground surface is non-invasive and can vary from technologies as diverse as soil flux measurement to satellite imagery. Soil flux has been discussed in previous sections of this chapter. Work by Allis et al. (2004) show CO₂ soil fluxes above proven CO₂ reservoirs including the field areas within the present study. Ordinary soil flux above Farnham Dome suggests that there may not be any leaking CO₂, however normal fluxes are also generally found above St.Johns and both the Little Grand Wash and northern Salt Wash graben fault sites which all have evidence of leakage in the shape of travertine deposits. Anomalous flux levels are found next to clear examples of leakage at active travertine sites but the flux measurements elsewhere along the fault do not highlight any major leaking of gaseous CO₂ to the surface. Satellite imagery, such as Interferometric Synthetic Aperture Radar (InSAR) had been proven to show increases in surface elevation in the order of 5 mm/year above CO₂ injection wells (Mathieson et al., 2009; Onuma and Ohkawa, 2009). This method may have application for detecting forced increases in volume of shallower reservoirs due to increased pore pressures instigated by injection, which may lead to either failure of the injection well or hydrofracture of caprocks. However any possible variations in surface deformation brought about by discrete channel of leakage to the surface, such as demonstrated by the leakage patterns in the present study would be so small that they would be hard to distinguish from background variations.

Leakage of onshore storage reservoirs will lead to CO₂ release directly into the atmosphere. For offshore storage reservoirs, or reservoirs with large lakes above possible leakage, additional monitoring techniques may be required. If overlain by water it is possible that CO₂ could dissolve upon leaking and then eventually discharge into the atmosphere by diffusion (Nihous et al., 2005), these steady leakage events would need to leave evidence of gas-release pockmarks on the seafloor large enough to pick up or geophysical surveys or subsurface pathways at a detectable scale for seismic survey (Ligtenberg, 2005; Cartwright et al., 2007) in order to be detected. If the leakage took place in water deep and cold enough then it may form hydrates on the seafloor or large supercritical bubbles of

CO₂ which should be detectable from the monitoring of pH (Shitashima, 2008). For sufficiently high leakage rates CO₂ may bubble through the water column and be discharged directly into the atmosphere (Benson and Hepple, 2005). As well as monitoring for pockmarks and pipes in this case satellite or aerial surveillance may be able to detect bubble streams to the surface.

From the above discussion it can be seen that although several different technologies exist that can be used to monitor CO₂ leakage from a number of different angles, however, taken in isolation these technologies are inadequate for full scale monitoring of an anthropogenic CO₂ storage site during injection or after completion of the project. Taking the footprints of leakage only for the immediate area of travertine deposition surrounding the faults ($\sim 2.3 \times 10^6$ and $\sim 6.9 \times 10^6$ m² for the Little Grand Wash and northern Salt Wash graben faults) in the present study it is evident that travertine only covers between 1 to 1.5% of each area. This number is even smaller when considering the well failure analogue of modern leakage which is between 0.1 to 0.3%. Taking these leakage patterns ground penetrating methods such as 4D seismic simply do not have the resolution to confidently detect leakage along discrete channels of high permeability. Detection techniques that require multiple intrusive monitoring wells also produce problems as without a large quantity of wells through out the storage reservoir it would be hard to detect leakage pathways. By introducing more wells more potential channels of leakage are also being introduced to a storage reservoir. This could be countered by having a detailed knowledge of the surrounding geology of the reservoir so a few key site of likely leakage can be identified and less wells need to be used. Surface based detection methods such as soil flux may be complicated by relatively high natural CO₂ fluctuations within the biosphere and atmosphere, plus again a detailed geology must be known, especially of subsurface structures, so that measurement can be concentrated above likely areas of leakage.

6.4 Leakage risks for storage sites

Calculation of total leakage and leakage rates of CO₂ from the Little Grand Wash and northern Salt Wash graben faults and an analysis of monitoring techniques allows for conclusions to be drawn for risk assessment of the leakage of CO₂ in the present study, which may have important implications for

consideration of leakage in anthropogenic storage sites. Assessing the risk of CO₂ leaking from a storage site and the consequences of this leakage are of paramount importance to ensure that a geological storage reservoir is both safe and effective. All of the information available to a project must be used systematically in order to identify the sources of potential CO₂ leakage and estimate the probability and magnitude of leakage.

6.4.1 Site characterisation

Both engineered and natural systems can be a very complex association of the geology of the reservoir unit and the stratigraphy surrounding it, structural features, groundwater flow regimes, fluid phase characteristics and varying well types. A detailed knowledge of the properties of each of these factors and the interaction between them should be known. Although it is desirable to select storage reservoirs that are structurally homogeneous it is hard to find areas completely devoid of faulting. Increasing formation pressures due to the injection of CO₂ can potentially open fractures and cause slip on faults that exist in the reservoir (Wiprut and Zoback, 2000; Streit et al., 2005). As this can potentially lead to the formation of highly permeable conduits for leakage of CO₂ it is especially important that any potential fault slip is identified. This can be achieved by geomechanical modelling providing that the frictional strengths of both the fault and protolith are known (Streit and Hillis, 2003). Firstly the state of stress, including stress orientation and magnitude, should be determined for all faults to determine if they are optimally orientated for failure within the ambient stress regime of the reservoir area. An analysis of pre-injection slip tendency on any present faults can then be carried out. If the faults are favourably orientated for reactivation the maximum sustainable pore fluid pressure that can be sustained during injection without reactivating the existing faults or inducing new fractures in sealing lithologies within the reservoir can be estimated (Streit and Hillis, 2003).

The determination of factors that may affect the storage of CO₂ should not stop at the planning stage, but rather should continue through to the completion of injection. This is supported by the findings of continual site characterisation of the Weyburn reservoir, which despite being subjected to numerous investigations of hydrological, geological and geochemical factors during the planning and early implementation phase from 2000 - 2004 (Khan and Rostron, 2004; Preston et al.,

2005; Cantucci et al., 2009) is still being built upon by new work resulting from the latest phase which focuses on continual injection and monitoring. Use of additional wells has allowed for further information on hydrology and connectivity of Mississippian aquifers and the variably thick anhydrite and dolostone zones that cap the reservoir to be implemented into previous fluid flow models investigating long term fluid behaviour in the Midale Formation aquifer (Jensen et al., 2009). Continual characterisation is also important as features that may have originally gone undetected, such as subsurface and subseismic scale faulting, may be present and interact with the reservoir during the desired lifespan of storage to allow leakage.

6.4.2 Escape scenarios

As geological CO₂ storage is a developing technology there is currently a lack of knowledge from which to extract historical data on all leakage risks. However, this should not stop potential storage sites from attempting to have as great an appreciation as possible for escape scenarios from the storage reservoir. In order to achieve this an analysis of features, events and processes (FEP) can be carried out (Arts and Winthaege, 2005). Features are the physical characteristics of a system that can change with time such as rock, hydrogeological and CO₂ properties. Events are discrete occurrences influencing a system such as seismic activity, climate change and future drilling activities. Processes identify the physics of a change within a system such as diffusion of CO₂, dissolution of minerals and groundwater chemistry. The FEP's identified for the present study are presented in Table 6.4.

Some of these aspects have been discounted throughout this thesis; however, they were all taken into consideration for possible leakage scenarios and studied thoroughly in order to constrain the likelihood that they were having an effect on the Little Grand Wash and northern Salt Wash graben fault systems. For example fault activity and climatic changes have been found to be playing a minimal role, if any at all, on the leakage of CO₂ charged water along these fault systems (section 5.4). The present study also demonstrates that the above factors can vary through time and therefore may not be constant. This is especially important to consider when attempting to forecast the behaviour of reservoirs once storage projects have been completed.

FEPs identified for LGW and SWG systems	
Features	Permeability of Navajo aquifer Permeability of Summerville Fm caprock Permeability of faults Integrity of Summerville Fm caprock Ground water flow Transport pathways Presence of separate CO ₂ phases
Events	Earthquakes (static and dynamic stress change) Triggered Seismicity Climatic events Exploration drilling activity
Processes	Groundwater chemistry Colloid transport Unsealed or damaged boreholes

Table 6.4: FEP analysis for the faults in this study.

6.4.3 Risk assessment and lessons for anthropogenic storage

In order for storage sites to be deemed safe and effective it must be proven that they can store captured CO₂ on the order of thousands of years. The scale of the total volume of CO₂ leaked from the Little Grand Wash and the northern Salt Wash graben fault systems ($10^5 - 10^6$ tonnes) is of a similar scale to the desired volumes of storage for small to medium scale anthropogenic sites. The worst case scenario for total leakage rates for these two systems over the lifespan of Little Grand Wash leakage is 55 ± 15 and 47 ± 13 tonnes/year and the modern day leakage rates of active precipitation is $3,153 \pm 851$ and 578 ± 156 tonnes/year. These two separate leakage rates provide analogues for leakage via caprock rock failure and for catastrophic wellbore failure as they represent the leakage of the natural systems and of anthropogenic exploration.

The time averaged flux of CO₂ for both field areas, even for the scenario of switching on and off of leakage through time, is within the rates of flux demonstrated by areas of natural vegetation. Salt tolerant plants thrive around active precipitation sites and there have thus far been no reports of human casualty in relation to CO₂ release at the most active leakage point, the Crystal

Geysers. It is therefore apparent that leakage of CO₂ along the Little Grand Wash and northern Salt Wash graben faults, even at the relatively high modern rates, has no adverse effect on the local environment. It should also be noted that of the total CO₂ leaked to the surface ~10% is immediately sequestered within travertine deposition. This provides a relatively stable storage facility of this fraction of leaked CO₂ although eventual erosion of mounds may lead to its eventual release into the atmosphere.

Although the leakage at the Little Grand Wash and Salt Wash graben field sites has had no short term effect on the environment surrounding the sites, the radiometric dating of travertine mounds suggests that leakage has been consistently occurring for time periods spanning 100,000s of years. The recognition of this potentially constant leakage and the rates of leakage calculated for the present study give important information on the effects of two different kinds of leakage, caprock failure and well failure, on potential storage sites. Taking the calculated leakage rates and applying them to large scale anthropogenic storage sites such as Weyburn or Gorgon, which plan to capture up to 125 million tonnes of CO₂ during their lifespans, reveals that for caprock failure complete leakage of these reservoirs will take place over timescales of 10⁵-10⁶ years. For catastrophic failure of a single well complete leakage of these reservoirs could occur over as little as 10³ – 10⁴ years.

These figures suggest that monitoring should focus on leakage via well failure as the rates of leakage for caprock failure are so minimal that they are unlikely to compromise the net storage of a reservoir over the desired effective storage timescales. This is an important result for monitoring purposes as caprock failure could occur at any location of structural heterogeneity, which may or may not have been characterised in the potential storage site, and could support variable or switching leakage pathways over multiple locations through time, like those found in the present study. Even for potential storage sites of high borehole density the locations of abandoned wells are likely to be well documented and so high risk leakage sites should be readily identifiable and monitored intensely during and post injection of CO₂.

Several monitoring techniques should be used in order to give the best possible means with which to detect any leakage. The variety of monitoring techniques suited for a particular site can be determined from a FEP analysis of all

the possible leakage scenarios. For example in the present study the key feature of leakage to the surface is the integrity of the Summerville Formation caprock. Chapter 5 discussed in detail the possible causes of switching of the leakage pathways through time and found that new leakage pathways may be instigated by either mineral precipitation of other more high permeability fractures or dynamic stress induced by distant earthquakes refracturing calcite mineralised blockages or rupturing tighter low permeability fracture sets. Of the monitoring techniques described in section 6.3.4, only microseismics would be able to detect the non-surface rupturing seismic waves from distant earthquake events, whilst none would be able to detect mineralisation at depth which would lead to a new leakage pathway. For monitoring of borehole failure detection of leakage is much easier as simple pH detectors could be utilised. This places further onus on active and abandoned wells as not only do they present the highest risk for leakage and are easier to monitor due to their known locations, the requirements for monitoring them are much simpler than for caprock failure.

Leakage of any kind is not desirable for anthropogenic CO₂ storage sites. If monitoring successfully detects leakage then remediation will need to be carried out in order to abate emissions into the atmosphere. Several remediation techniques are available depending on the type of leakage encountered. For the present study for example remediation of leakage from the storage reservoir and leakage from wells would have to be addressed. For remediation of leakage from the storage reservoir the pressure in the storage formation, the Navajo aquifer could be reduced (Benson and Hepple, 2005). This could be achieved by removing water from the reservoir or by injecting water or brine above the leakage point and increasing the upgradient pressure. This would help to stop the leaking by reducing the pressure gradient driving the CO₂ charged water out of the Navajo aquifer and allowing pressure build-up on fractures within the Summerville Formation to dissipate which may allow them to close.

Attempted remediation for the leakage from the abandoned wells could follow one of several methods, such as the injection of heavy mud or cement, developed for the repair of wells in the oil and gas industries (Benson and Hepple, 2005). Alternatively research from the geotechnical industry has demonstrated that biological remediation of groundwater contamination can be effective (Warren et al., 2001; Ferris et al., 2004). These studies show that ureolytic bacteria can

rapidly precipitate calcite during the hydrolysis of urea. Sampling of waters during field work (section 4.4.4) and subsequent analysis has confirmed the presence of urea hydrolysing bacteria at all active leakage locations (Vernon Phoenix, personal communication). If also present at depth at the bases of the abandoned wells all that would be required would be the injection of urea to instigate calcite formation and blockage of the borehole. This technology may provide a better and more long term solution to the blockage of wells at CO₂ sequestration sites as heavy mud is only a short term solution and cement is susceptible to degradation by factors such as sulphate attack, mechanical fatigue, leaching and carbonation (Preston et al., 2005).

7 Concluding remarks and suggestions for future work

7.1 Conclusions

The conclusions resulting from the work carried out within this thesis span a wide range of topics from radiometric dating, to geomorphology, and to vertical fluid flow in faults but come together to provide information about quantities and rates of leakage of CO₂ from geological reservoirs. As the geological reservoirs in this study provide natural analogues for anthropogenic storage sites, the conclusions gained from this study have important implications for the engineered storage of CO₂. The following general conclusions have resulted from this study.

- Preliminary work carried out in the Gulf of Corinth, Greece, allowed for an evaluation of the U-series dating technique on *C. caespitosa* and for a slip rate of the South Alkyonides fault segment to be calculated. The resultant coral ages do not closely match sea level highstand ages. The $\delta^{234}\text{U}$ values of samples do not match that of seawater and get progressively larger with age. This shows that *C. caespitosa* samples form an open system with respect to ²³⁴U decay, a trend that appears throughout the published literature. Despite this trend previous works have neglected the anomalous chemistries and simply correlated the U-Th of coral the nearest sea level highstand. However, *C. caespitosa* specimens do not produce robust samples for U-series dating and can not be used in solitude for highstand correlation. A detailed investigation into the accuracy of sea level curves and of growth depth of *C. caespitosa* produced sizeable areas of uncertainty around sea level highstand age, which allows for coral of initially non-matching ages to be correlated to highstands. This information may allow coral specimens in future work to be correlated to highstand with more confidence. For the present study it allowed a slip rate to be calculated, which showed that slip rate has increased from 290 - 175 ka to 175 - 125 ka in agreement with the results of Roberts et al. (2009).
- There are a total of fifty-four currently active and fossil travertine deposits associated with the Little Grand Wash and northern Salt Wash graben

faults. All travertine mounds are located within the footwall of the faults and the geochemistry of modern spring waters are significantly different to north and south of each fault (Heath et al., 2009), demonstrating that the two faults are acting as barriers to across-fault fluid flow. The ancient travertines of the Little Grand Wash fault appear to be associated with areas of increased structural complexity, such as fault bends and relay zones. This suggests that fluid flow is being channelled sub-vertically up discrete pathways of relatively high permeability in the damage zone of the fault. Travertine deposits associated with the northern fault of the Salt Wash graben are not solely restricted to the trace of the fault due to the presence of unconfined aquifer units at the surface. This may explain the greater number of travertine deposits and more diffuse flow pattern shown by this area. All travertines that occur away from the fault are closely associated to the axial trace of the open, shallowly north-plunging Green River anticline.

- Travertine is a terrestrial carbonate deposit formed by the emergence of CO₂-rich groundwaters at the surface from a combination of abiotic (de-gassing) and biotic (bacterially mediated) effects. The travertine in this study is composed of five distinct lithofacies, four of which are unsuitable for U-Th age dating as they form an open system with respect to decay of ²³⁴U or are prone to detrital contamination which introduces non-radiogenic ²³⁰Th to potential samples. The white banded vein facies provides excellent samples for U-Th dating as it meets all the desired criteria for geologically useful chronometers and is abundant in all fossil mounds. Dating of all travertine deposits along the Little Grand Wash fault indicates that this fault has facilitated the leakage of CO₂-charged waters for at least 113,912 ± 604 years, whilst dating of over half the mounds along the northern fault of the Salt Wash graben suggests that leakage has occurred for at least 413,474 ± 15,127 years.
- The increasing $\delta^{234}\text{U}$ of dated samples from west to east indicates that the main source of ²³⁴U in the waters is likely to be leaching from the sandstone units of the Navajo aquifer as meteoric water travels from its source, in the San Rafael Swell 35 km to the northwest, to the location of precipitation in the field sites. This further backs up previous work which suggests that the source of the springs is mainly meteoric with a small contribution of brine

(Heath et al., 2009; Wilkinson et al., 2008; Kampman et al., 2009). The model of spatial pattern that best suited this scenario further suggests that pathways are emanating from several different locations of fracturing in the Navajo aquifer's caprock, the Carmel Formation.

- Detailed dating of a single mound (deposit L4) shows that leakage points at the surface may be active for a minimum of $10,740^{+604}_{-1,486}$ years. This suggests that when fluid flow pathways are channelled through discreet zones of relatively high permeability in the damage zone of a fault they may naturally last for at least this amount of time before they become inactive. The dating of the inner and outer edges of the main vein from the same deposit gave a time average precipitation rate of 0.51 to 0.74 mm/y. This rate agrees with previous work on fracture sealing vein precipitation (Fisher and Brantley, 1992; Lee and Morse, 1999) and therefore may represent a good approximation of the length of time required to completely seal fractures within low permeability sealing lithologies, such as the Carmel Formation, above sub-surface aquifer units.
- Because some mounds along the northern fault of the Salt Wash graben are completely devoid of layered mats, U-Th dating of this facies was carried out in order to quantitatively determine how closely they are associated with white banded veins. Ages for layered mats from Little Grand Wash travertine were up to 41.2% older than white banded veins from the same mound. This coupled with the high $[^{230}\text{Th}/^{232}\text{Th}]$ of layered mat samples rendered this facies inappropriate of dating purposes. However, relatively closely matching $\delta^{234}\text{U}$ of white banded vein and layered mats from the same mound indicate that they were formed from the same waters and geochemically prove their intimate association. The mounds of the northern fault of the Salt Wash graben that are devoid of layered mats are therefore confirmed as travertine deposits.
- The presence of carbonate-cemented river gravels within travertine mounds allowed for the calculation of local incision rates. These provided results of 0.342 mm/y for incision of the Green River in the Little Grand Wash and 0.158 mm/y for the incision of Green River tributaries in the Salt Wash graben. The former rate provides a further data point for river incision rates across the Colorado Plateau and can therefore contribute to studies on the

uplift of this province. The latter allowed for the ages of un-dated mounds along the northern fault of the Salt Wash graben to be estimated and therefore extended the data set for study of patterns of fluid flow to the surface.

- Study of relict terraces of the Green River in the Little Grand Wash and long profile of the Big Bubbling tributary in the Salt Wash graben coupled with radiometric dating of travertine mounds rules out recent movement on both faults. The un-offset nature of dated travertine along the Little Grand Wash and northern fault of the Salt Wash graben confirms there has been no surface offset for at least $113,912 \pm 604$ and $116,788 \pm 691$ respectively on these faults. Determination of incision rates for each area allowed age estimates to be made for river terrace M5 in the Little Grand Wash and the un-dated S33 mound in the Salt Wash graben which further stretches back evidence of quiescence on the Little Grand Wash fault to $\sim 137,000$ years and on the northern fault of the Salt Wash graben to $\sim 190,000$ years.
- Radiometric dating coupled with estimated ages (from incision rates) of travertine along the Little Grand Wash and northern Salt Wash graben faults show that the locations of fluid flow to the surface have switched repeatedly through time. Along the Little Grand Wash fault timing of leakage decreases away from a central point proximal to the axial trace of the Green River anticline. This suggests that initial leakage occurs from the structural high of the three-way trap provided by the juxtaposition of the Green River anticline with the Little Grand Wash fault. The northern fault of the Salt Wash graben demonstrates a similar pattern; however, unlike the Little Grand Wash fault younger deposits do not solely occur with progressive distance from the initial central leakage point but crop up throughout the area covered by travertine precipitation. The proximal occurrence of three mounds of distinct elevation and age, ranging $\sim 45,000$, suggests that fluid flow pathways can also be repeatedly re-used over time scales of tens of thousands of years.
- Estimation of travertine volumes, by using thickness and area measurements, allowed the deposits of the Little Grand Wash and the northern Salt Wash graben faults to be compared. A similar volume of travertine has been deposited along each fault with the Little Grand Wash

fault having a total volume of $1.1 \times 10^5 \text{ m}^3$ and the northern fault of the Salt Wash graben having a total volume of $0.8 \times 10^5 \text{ m}^3$. Comparison between individual mounds in both areas shows that the average area of travertine is similar ($2,303 \pm 437 \text{ m}^2$ for the Little Grand Wash and $2,275 \pm 432 \text{ m}^2$ for the Salt Wash graben). However, there is a distinct difference in the average thickness of mounds with Little Grand Wash deposits being over twice as thick ($2.1 \pm 0.2 \text{ m}$ in comparison to $0.8 \pm 0.1 \text{ m}$) which also leads to Little Grand Wash travertine having a greater average volume ($8,932 \pm 2,412 \text{ m}^3$ in comparison to $963 \pm 260 \text{ m}^3$). The fact that some of the northern Salt Wash graben travertine mounds are devoid of layered mats facies initially suggests that they may be less resistant to erosion. The comparative thickness of white banded vein between the two largest deposits in each area (with L4 measuring 2.5 m in comparison to 0.5 m of S11) also indicates that travertine along the Little Grand Wash fault have a longer lifespan. It is therefore likely that the effects of erosion are similar in both areas and it is the initial smaller volume of Salt Wash graben travertine that makes it easier to be completely removed by erosion.

- The switching of leakage points at the surface through time is likely to be the result of three separate forcing mechanisms: mineralisation, 3-phase flow interference and dynamic strain alteration by distant earthquake events. Mineralisation is the simplest mechanism as it solely provides a 'switching off' effect and is likely to be the main cause of pathway switching events less than 10 ka apart but don't permit the re-using of pathways. 3-phase interference has a minimal effect on pathways of the Little Grand Wash fault but may play a decisive role along the northern fault of the Salt Wash graben. This is because flow to the surface in Little Grand Wash fault is restricted to the damage zone (due to the presence of several low permeability sealing units in the stratigraphy), while flow in the northern fault of the Salt Wash graben only has to penetrate a single sealing lithology (the Carmel Formation) before migrating to the surface through unconfined aquifer units. Seismically induced changes in dynamic strain have far reaching affects and so can potentially cause any of the switches between leakage points. Analysis of the time between successive leakage events suggests that at least five observed switches are the result of this mechanism, this means that it is creating new pathways for fluid flow either

by rupturing tight fracture sets or previous episodes of veining within the caprocks.

- The work within the present study demonstrates that the behaviour of fluid flow switching in a system confined to damage zone fractures, the Little Grand Wash fault, and a system leaking through an unconfined aquifer, the northern fault of the Salt Wash graben, may be different. This means that a large number of previous simulation and modelling on fault systems, which look at ideally homogenised faults within a single, usually permeable media, are inappropriate for cap rock failure within systems of more complicated stratigraphy. The present study also provides an insight as to how fracture controlled permeability can evolve in space and time by showing that fluid flow pathways can switch along multiple locations on faults and demonstrating that leakage through sealing lithology doesn't necessarily have to be restricted to a single point.
- The total volumes of CO₂ to have leaked from the Little Grand Wash and northern Salt Wash graben faults are estimated as $1.3 \times 10^6 \pm 3.6 \times 10^5$ and $9.8 \times 10^5 \pm 2.7 \times 10^5$ tonnes respectively. The worst case scenario for each area, calculated by attributing the dimensions of the largest mound in each area to every other travertine, gave a total leaked volume of $6.2 \times 10^6 \pm 1.7 \times 10^6$ tonnes for the Little Grand Wash fault and $7.4 \times 10^6 \pm 2 \times 10^6$ tonnes for the northern fault of the Salt Wash graben. If leakage for the northern fault of the Salt Wash graben is only considered over the same timescale as leakage along the Little Grand Wash fault then the total CO₂ leaked equals $5.3 \times 10^6 \pm 1.4 \times 10^6$. This suggests that for the same timescale a similar volume of CO₂ has been leaked from each fault.
- Calculation of time averaged leak rates for the worst case scenario of leakage along the Little Grand Wash and northern fault of the Salt Wash graben faults produced 55 ± 15 and 47 ± 13 tonnes/year respectively. Leakage rates for actively precipitating travertine (which are the result of oil exploration drilling) are estimated to be $3,153 \pm 851$ tonnes/year for the Little Grand Wash fault and 578 ± 156 tonnes/year for the northern fault of the Salt Wash graben. If these fault systems are treated as analogues to current anthropogenic storage sites then the total and modern leakage rates from the Little Grand Wash fault can be taken as analogues for

leakage via caprock failure and catastrophic wellbore failure respectively. Taking the calculated leakage rates and applying them to large scale storage sites such as Weyburn or Gorgon, which plan to capture up to 125 million tonnes of CO₂ during their lifespans, reveals that for caprock failure complete leakage of these reservoirs could take place over timescales of 10⁵-10⁶ years if similar along-fault pathways exist at these sites. For catastrophic failure of a single well complete leakage of these reservoirs could occur over as little as 10³ – 10⁴ years.

- The relatively high modern rates of leakage appear to have no adverse effects on the local environment and there is no historic evidence of human fatality as a result of release of CO₂ from active sites. However, the radiometric dating of travertine suggests that leakage has been consistently occurring for time periods spanning 100,000's of years. If CO₂ is allowed to leak from anthropogenic storage sites over these time scales then the net storage of these sites will be compromised. Monitoring of storage sites is therefore very important. The results of this study emphasise that monitoring should focus on areas where well failure is possible as this is the largest risk with concerns to leakage. This is a positive result for monitoring as the locations of active and abandoned wells are likely to be well documented for potential storage sites (especially offshore). This means high risk leakage sites should be readily identifiable and can be monitored closely during and post injection of CO₂. The results of this study also demonstrate that the physical characteristics of a storage system, such as rock, hydrological and CO₂ properties, can vary through time. This is especially important to consider when attempting to forecast the behaviour of reservoirs once storage projects have been completed.

7.2 Future work

Several topics for further work emerged throughout the multiple topics that are addressed within this thesis. However, if the multiple lines of enquiry could be further pursued then some of the themes discussed could become better developed and provide a greater insight into the causes of switching of fluid flow pathways and understanding of CO₂ leakage. Detailed below are several

suggestions for future work that would build on the results found in the present study.

7.2.1 Future work at the Utah field sites

- Further U-Th dating of travertine deposits could be carried out in order to achieve a full coverage of ages for the un-dated mounds of the northern fault of the Salt Wash graben. This would allow a more confident history of travertine occurrence, and therefore leakage to the surface, to be developed. It would also confirm whether the incision rate calculated in the present study provided a good method for estimation of ages. Dating of multiple samples from a range of individual mounds would also allow travertine lifespan estimations to be further developed and provide a true basis for comparison across the Little Grand Wash and northern Salt Wash graben fault travertine.
- It is speculated within this thesis that U-Th ages obtained from travertine precipitated in the lab from water samples may record the time taken for the precipitating groundwaters to migrate from their source. Further dating of spring waters by more conventional groundwater dating techniques could provide a check on this speculation and determine its merit. One such technique is ^{14}C dating which utilises the ratio of radioactive atmospheric ^{14}C to dissolved ^{12}C acquired by meteoric water as it percolates through soil and rock its way to an aquifer. The ~50 ka age limit of this technique (Frolich, 1990) should be more than adequate to date the travel time of the waters in question.
- Though layered mats in general provide poor samples for dating due to their open system behaviour with respect to decay of ^{234}U decay, dating of a layered mat sample from the oldest deposit along the Little Grand Wash, mound L4, produced a result that was within 5.1% of the average age of the deposit. Whilst the difficulty of calculating a single value of $[\text{}^{230}\text{Th}/\text{}^{232}\text{Th}]$ to correct for the presence of non-radiogenic ^{230}Th , due to the variable possible sources, has been documented (Garnett et al., 2004) the closeness of the age of the layered mat sample and white banded vein samples from L4 leaves room for further investigation. If a solution could be found then dating of travertine in areas where only layered mat facies is

present, such as above the proven CO₂ reservoir at St. Johns in Arizona (Figure 7.1), could potentially be carried out.

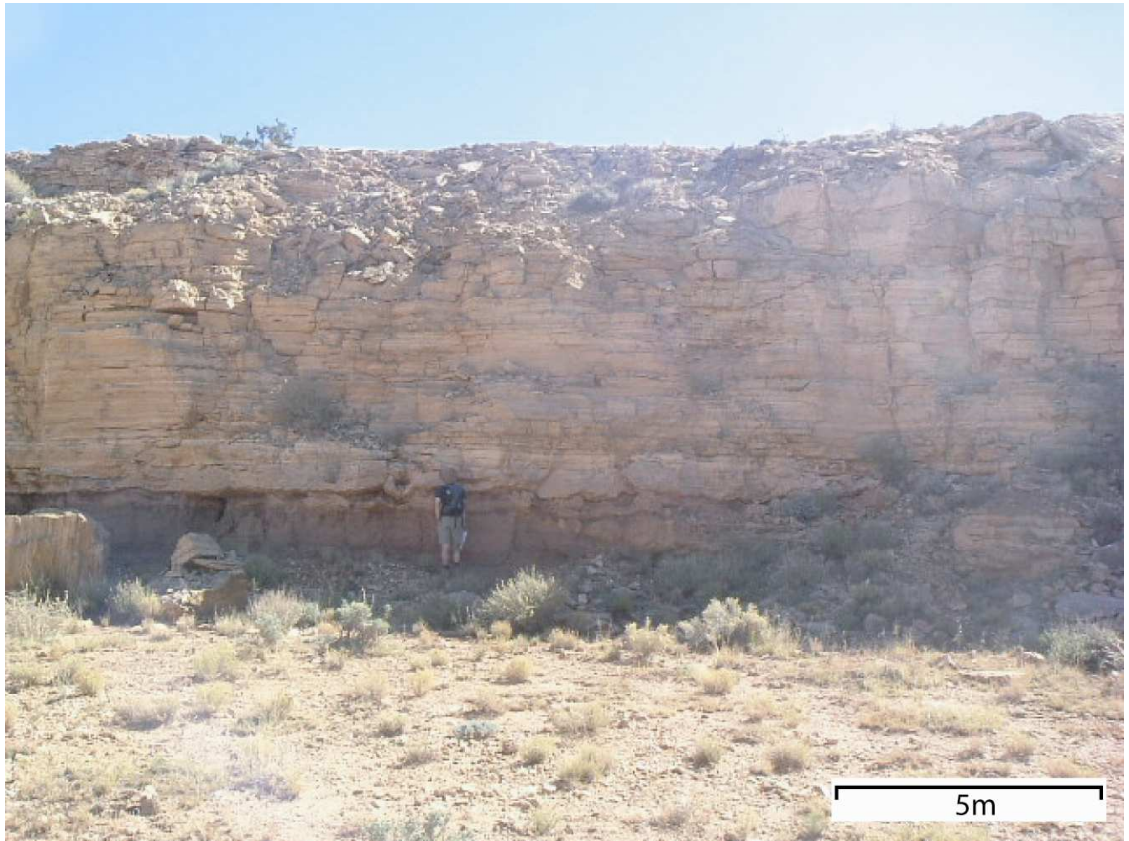


Figure 7.1: Travertine deposit from the St.Johns area.

- Dating of the river gravels associated with mounds and deposited in terraces by the Green River on its western shore bank in the Little Grand Wash by luminescence techniques, such as optically stimulated luminescence, would aid incision rate studies for these areas and provide further quantitative evidence for the minimum period of non-movement on the Little Grand Wash fault. For gravels associated with travertine mounds it could also possibly provide a further dating technique with which to confirm the validity of U-Th ages.
- Further information on the causes of switching between points of leakage could be achieved with more detailed field investigation of the presence of brown banded vein facies in travertine mounds. This rare facies was only noted in a handful of mounds as it wasn't particularly being sought out in this study. The focus of field work was the locations of the mounds and determining the presence of layered mats and gravels. As brown banded vein facies consists of alternating layers of aragonite and iron-rich

laminations it represents fluctuations in fluid flow and the terminal stages of travertine mound development. Their presence would indicate that flow to a mound slowly switched off and would rule out the mechanisms of triggered dynamic strain and 3-phase flow, which should instigate relatively rapid switching off of pathways, for switching between that particular leakage point and the next.

- Further developed statistical analysis which combines position (in relation to the fault) and timing of travertine mounds would allow for a greater understanding of the pattern of leakage which would lead to better determination of the causes for switching between pathways. Despite posing this idea to several statisticians and asking for aid at the 2009 EAGE Faults and Top Seals conference no one has been able to aid me in developing such a statistical test for the data provided by the travertine in this study.
- Better characterisation of the sub-surface geology of the field sites would potentially allow for an accurate depth of the Navajo aquifer and the volume of CO₂ at depth to be determined. The top of the Navajo aquifer is currently thought to be at a depth of ~ 600 to 800 m (Shipton et al., 2005) but no accurate measurements exists for the depth of this aquifer in either of the field areas. Knowledge of the depth of this aquifer would allow for better determination of the possible phases of CO₂ present within in and provide further information on the viability of 3-phase interference for switching of pathways. A conservative estimate of 0.6 to 6.3 million tonnes for the total CO₂ storage capacity of aquifers within the aquifers sealed by the Little Grand Wash fault was produced by Dockrill (2006). However, this was based on the assumption that CO₂ is present as a free gas within the aquifers. Subsequent work on the geochemistry of the groundwaters by Wilkinson et al. (2008) suggests that there is no free gas present at depth. Work in this study, given the normal geothermal profile of the local area, agrees with this finding as the CO₂ saturation line (at a depth of ~ 600 m) will be above the Navajo aquifer. Attempted characterisation of the subsurface geology has been attempted using seismic lines- however these yielded no results due to poor coupling with the host rock (Peter Vrolijk,

personal communication). Geophysical surveys may be a good option for these locations due to the simple stratigraphy.

- Better sub-surface characterisation of faults would provide more information on the potential pathways that CO₂-charged waters are using to reach the surface. Measurement of pore fluid pressures and the normal and shear stresses acting upon the Little Grand Wash and northern Salt Wash graben faults would allow for an analysis of fault slip tendency to be carried out which would accurately determine if these faults are primed for failure. Stress data could be measured by obtaining image logs and analysing the orientation of borehole breakouts and integrating information from density logs over depth, while pore pressures could be measured using drill stem or repeat formation tests (Streit and Hillis, 2003).
- Further and long term monitoring and measurement of emissions of the Crystal Geyser (mound L1) would allow for more detailed active leakage rates to be determined. This would allow for better estimation of how long it would take for anthropogenic storage reservoirs to become completely depleted in the event of catastrophic wellbore failure. The best method for this would be aerometric measurements, such as carried out by Gouveia et al. (2005), carried out over a time period spanning several years.

7.2.2 Future work on CO₂ leakage in general

- Formation of a database containing detailed baseline data of all naturally leaking CO₂ storage sites would provide a good source of reference when attempting to predict long term integrity of potential anthropogenic storage sites. The problem at the moment is that each natural location has a specific set of conditions particular to that site. Good baseline data for numerous natural locations; including aspects such as local geology and stratigraphy, knowledge of local stress field and presence of structural features, volumes and source of CO₂, and depth and pressure gradient of the reservoir; could provide a valuable source of information for a range of conditions. This data can then be combined (using multivariate statistics) to provide statistically significant predictive tools which can then be applied to predictions for anthropogenic sites.

- Field scale experiments where CO₂ is injected into a reservoir and tracked back to the surface would allow leakage rates to be better constrained. This could be achieved by finger-printing injected CO₂, and measuring the time it takes to return to the surface; or by close investigation of the fate of injected CO₂ via a monitoring technique such as seismic surveys. Finger-printing could be achieved by addition of un-reactive components, such as perfluorocarbon tracers or noble gases, to any injected CO₂ (Smith, 2004; Gilfillan et al, 2008). A project utilising finger-printed CO₂, sponsored by the U.S. Department of Energy, is currently underway at West Pearl Queen field in south-eastern New Mexico (Pawar et al., 2006). In this case perfluorocarbon tracers are being used and monitored for by capillary absorption tube samplers at the surface (Smith, 2004). Seismic surveys are also currently in use to monitor the movement of plumes from the CO₂ injected at the Sleipner field (Baines and Worden, 2004; Arts et al., 2008); however the resolution is not good enough to provide accurate leakage rates through the reservoir.
- Greater appreciation of errors on CO₂ leakage and flux estimates are crucial for inputs to modelling, site safety cases and estimation of any leakage impacts. Future work on CO₂ leakage should follow the examples set by this thesis in attempting to show all possible sources of error and including these in the final results. Currently most published work either provides rough estimates or show no errors on measurement whatsoever. In addition, standardised units of measurement for leakage and flux of CO₂ should be used across the globe. At the moment several different measurement units are used which makes it hard to compare results between sites.
- Any injected CO₂ will eventually leak within geological timescales. Therefore a greater understanding of the impact of CO₂ leakage to the surface must be obtained in order to understand the potential risks and consequences of leakage from storage reservoirs. This has economic implications for companies injecting CO₂ as they must weigh up the financial implications of storage of CO₂ versus how long it is likely to be competently stored for.

- Additionally further work must be done to establish the role of local CO₂ emissions to both the atmosphere and the local environment. The case in the present study demonstrates a scenario where there is no detriment to the local environment due to leakage of CO₂. However, it must be remembered that leakage in this case is in a desert environment with very little cover and therefore easy dispersion by the wind. Salt tolerant plants, which thrive in this environment, take advantage of the presence of water at the surface to flourish. In lush environments where forests and greater plant coverage is present plant mortality may occur. If CO₂ was leaking into an environment of little wind or into a well shielded area then deadly plumes of CO₂ may accumulate at the surface. This has been demonstrated at sites such as the Rapolano fault in Italy (Etiope et al., 2005), so it is paramount that great care is taken to assess the potential hazards in the specific environment above an anthropogenic storage site.

Appendix A

Standard data for uranium and thorium analyses

A-1 Uranium standards

U010			
Certified $^{234}\text{U}/^{238}\text{U} = 0.00005466 \pm 51$			
Date	$^{234}\text{U}/^{238}\text{U}(\text{e})$	%SE	2SE
28-Feb-07	0.00005436	0.0682	0.00000007
22-Mar-07	0.00005452	0.1045	0.00000011
14-May-07	0.00005472	0.0618	0.00000007
27-Feb-09	0.00005430	0.0609	0.00000007
27-Feb-09	0.00005431	0.0552	0.00000006
27-Feb-09	0.00005423	0.063	0.00000007
27-Feb-09	0.00005431	0.0602	0.00000007
27-Feb-09	0.00005437	0.0548	0.00000006
27-Feb-09	0.00005422	0.0461	0.00000005
27-Feb-09	0.00005439	0.0686	0.00000007
	Mean	% SD	2 SD
	0.00005437	0.273	0.00000015

U030-A			
Certified $^{234}\text{U}/^{238}\text{U} = 0.0002866 \pm 6$			
Date	$^{234}\text{U}/^{238}\text{U}(\text{e})$	%SE	2SE
28-Feb-07	0.0002868	0.0555	0.00000032
22-Mar-07	0.0002877	0.0582	0.00000033
14-May-07	0.0002872	0.0379	0.00000022
2-Mar-09	0.0002862	0.0594	0.00000034
2-Mar-09	0.0002857	0.0428	0.00000024
2-Mar-09	0.0002866	0.0567	0.00000032
2-Mar-09	0.0002863	0.0515	0.00000029
2-Mar-09	0.0002864	0.0406	0.00000023
	Mean	% SD	2 SD
	0.0002866	0.215	0.00000006

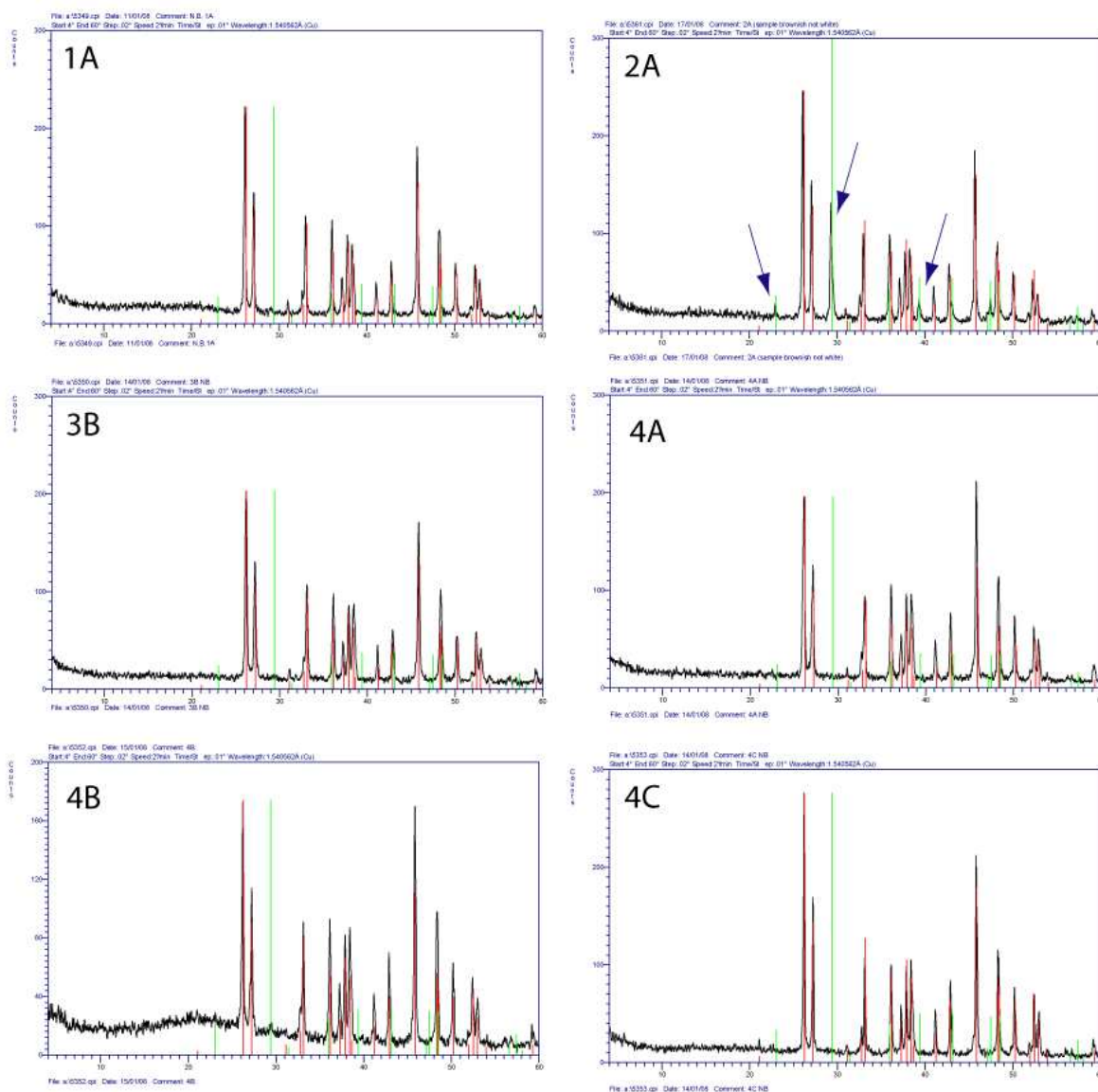
A-2 Thorium standards

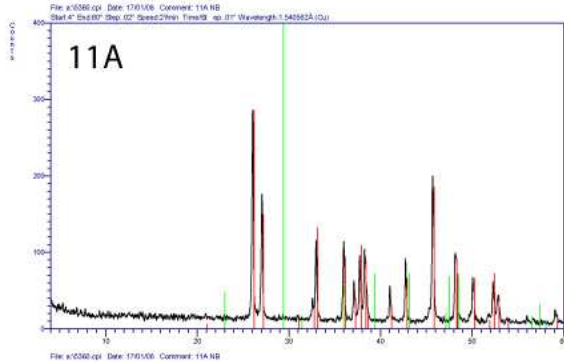
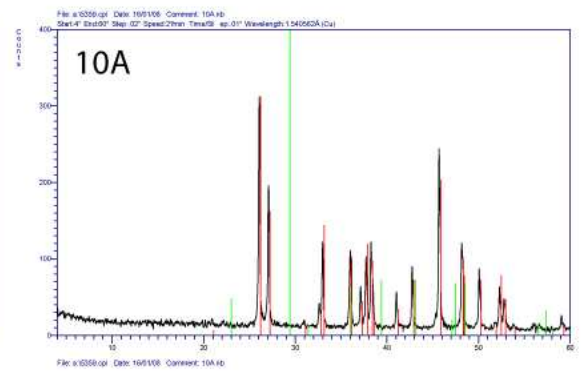
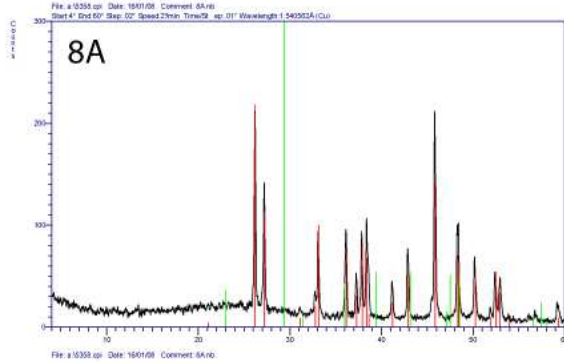
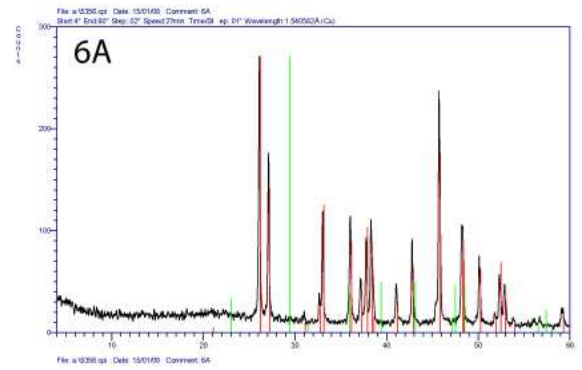
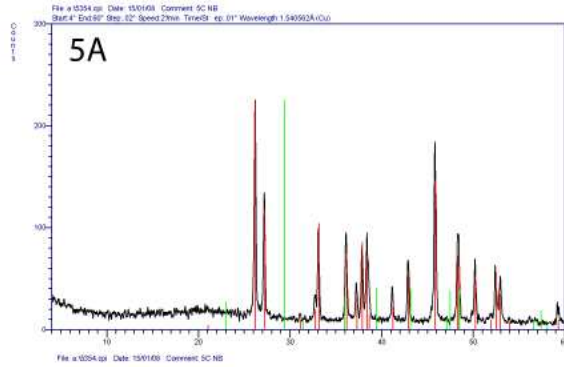
IRMM-035		
Certified $^{230}\text{Th}/^{232}\text{Th} = 0.00001148 \pm 8$		
Date	$^{230}\text{Th}/^{232}\text{Th}(e)$	2SE
10-Mar-06	0.00001131	0.00000004
10-Mar-06	0.00001125	0.00000005
10-Mar-06	0.00001134	0.00000005
10-Mar-06	0.00001143	0.00000005
10-Mar-06	0.00001136	0.00000004
19-Apr-06	0.00001142	0.00000005
19-Apr-06	0.00001142	0.00000003
21-Apr-06	0.00001128	0.00000004
21-Apr-06	0.00001131	0.00000002
21-Apr-06	0.00001136	0.00000005
24-Apr-06	0.00001128	0.00000005
25-Apr-06	0.00001128	0.00000005
25-Apr-06	0.00001129	0.00000004
	Mean	2 SD
	0.00001133	0.00000012

IRMM-036		
Certified $^{230}\text{Th}/^{232}\text{Th} = 0.00000311 \pm 8$		
Date	$^{230}\text{Th}/^{232}\text{Th}(e)$	2SE
10-Mar-06	0.00000316	0.00000002
10-Mar-06	0.00000310	0.00000003
10-Mar-06	0.00000300	0.00000003
10-Mar-06	0.00000306	0.00000002
10-Mar-06	0.00000306	0.00000002
19-Apr-06	0.00000305	0.00000002
19-Apr-06	0.00000304	0.00000002
21-Apr-06	0.00000307	0.00000002
21-Apr-06	0.00000304	0.00000002
21-Apr-06	0.00000308	0.00000003
24-Apr-06	0.00000306	0.00000002
25-Apr-06	0.00000303	0.00000002
25-Apr-06	0.00000309	0.00000002
	Mean	2 SD
	0.00000306	0.00000008

Appendix B

XRD results of *C.caespitosa* samples





— Calcite marker
— Aragonite marker

Appendix C

Seismic record of major regional faults

C-1 The Hurricane fault

The Hurricane fault is one of the longest and most active of several large, late Cenozoic, west-dipping normal faults within the 150 km wide structural and seismic transitional zone between the Colorado Plateau and Basin and Range physiographic provinces (Lund et al., 2007). The fault comprises six segments, and is 250 km long stretching from Cedar City, Utah, to south of the Grand Canyon, Arizona (Figure 2). Displacement on the fault is over 2,500 m in Utah, where it cuts into the Colorado Plateau (Lund et al., 2002). Palaeoseismic investigations have recently been carried out by the Utah Geological survey in order to assess the seismic hazard of the Hurricane fault in response to construction and population boom in south-western Utah and nearby areas of north-western Arizona and south-eastern Nevada (Lund et al., 2002; 2007). No ages of seismic events resulted from this study, though a long term slip rate of 0.44 to 0.57 mm/yr was calculated, decreasing to <0.01 - 0.35 mm/yr in the late Pleistocene and Holocene. This slowing of slip rate on the Hurricane fault, which is thought to have begun more than 350 ka, suggests that fewer surface-faulting earthquakes have been generated in more recent geologic time. A single radiocarbon date for activity on this fault, from the central Shivwits section, of 9300^{+1070}_{-430} ka has been produced by Amoroso et al. (2004). They go on to suggest that a further two rupture events occurred between 15 and 78 ka, and state that the penultimate event was likely to have been ≤ 10 (e.g. equal to or less than the time since the most recent event), and provide a recurrence rate of 9 to 15 ky for M 7.0-7.2 events. The Earth Science Association, 1982 (as reported by Lund et al., 2002) state a recurrence rate of 1 to 10 ky for large surface faulting earthquakes (M 7.5) for the entire Hurricane fault, based on historical seismicity and existing geologic data.

C-2 The Wasatch Front

The Wasatch Front consists encompasses the 370 km long N-S trending Wasatch fault and surrounding faults in central Utah. Some of the highest extensional slip rates in the Western U.S. (1-2 mm/yr for the Holocene) come from the Wasatch fault zone (Machette et al., 2000). The main fault consists of 6-10 individual segments of which at least 6 have shown activity during the Holocene, with the youngest surface rupturing about 600 years ago on the Provo segment (Hecker, 1993). Ages and locations of the Wasatch fault palaeoseismic data imply 17 single or 11 multisegment ruptures in the past 5.6 ky (Chang and Smith, 2002). McCalpin and Nishenko (1996) suggest an average recurrence interval of 350 years for $M > 7$ earthquakes on the fault for this time period. They prefer the multi-segment model because historically most of the large normal faulting earthquakes within the ISB have been multisegment ruptures. The most recent paleoearthquake investigation on the Wasatch fault, the 1999 'mega trench' is reported by McCalpin and Nelson (2001). This deep trench exposed 26m of vertical section across a 30 m wide zone containing two sub-parallel scarps of the Salt Lake City (SLC) segment. The study revealed a 6.0 ± 1.2 ky period of no scarp-forming earthquakes, suggesting fault inactivity between ~ 9.0 and 15.5 ka. This period corresponds to the unloading of the hanging wall during the desiccation of Lake Bonneville; the lake was at its highest about 15.5 ka ago and dropped almost 1,000 feet by 9 ka. This quiescence is four to five times longer than the average $M6.6$ earthquake recurrence of 1.4 ± 1.2 ky for the last 5.6 ky of this segment suggested by Chang and Smith (2002) by using seismic, geologic and geodetic observations. This magnitude is used as it is the commonly used minimum-threshold magnitude of surface-ruptured earthquakes in the Basin and Range province (de Polo, 1994).

C-3 The Rio Grande Rift

The Rio Grande Rift (referred to as RGR for the rest of this appendix) is an east tilted half graben stretching north from Mexico, near El Paso, Texas through New Mexico into central Colorado (Keller and Baldrige, 1999). It is dominated by large-displacement normal faults that form a prominent footwall uplift comprising the Sandia, Manzanita and Manzano Mountains east of Albuquerque in north-central New Mexico (Personius and Mahan, 2003). Most Quaternary faults in the

rift have low slip rates (<0.2 mm/yr, but commonly 0.01-0.02 mm/yr), consistent with occurrence of primarily low- to moderate-magnitude earthquakes that have been recorded or felt historically in New Mexico (Machette, 1998). Average slip rates on the most active faults in the rift are commonly <0.1-0.2 mm/yr, which may be typical of faulting in extensional regimes of the Western U.S. (Wong and Humphrey, 1984). The palaeoseismic record for the RGR is much better than that of any other faults investigated here as scarp forming events have been recorded on several segments. The following paragraphs provide a brief discussion of published work from some of these segments in order of north to south.

C-4 The Pajarito fault

The Pajarito fault is located on the western margin of the RGR in north-central New Mexico. McCalpin (2005) provides data from a total of 14 trenches along this complex fault zone, with two on the main fault scarp and the rest from minor subsidiary faults. These two main trenches provide evidence of 7 events and 8 scarp forming events respectively. Only one event (~25 ka) seems to have been record in both trenches. Dates are from radiocarbon and luminescence analysis on disturbed soils, and from also using the soil development index (SDI) of Harden (1982). McCalpin (2005) does state however that event horizons are inefficiently preserved to identify and date paleoearthquakes with confidence. This preservation issue is mainly due to overprinting of the homogeneous colluvium with other strong textural soil horizons. This perhaps explains why only one event is record across both main scarp trenches.

C-5 The Calabacillas fault

A 40 km long east dipping normal fault, trending N-S and located on the western edge of the Llano de Albuquerque. Palaeoseismic data is provided from OSL analysis of offset aeolian sands by McCalpin (2000) of samples from a 27 m high east facing fault scarp. The four ages provided by this study, 14, 32, 77 and 151 ka are approximations and no errors are supplied.

C-6 The Hubbell Spring fault

A 16m wide faults zone located on the eastern margin of the RGR. Personius and Mahan (2003) suggest there have been four large surface rupturing

earthquakes at this location. Using displacements and rupture lengths they postulate the palaeomagnitude of these earth quakes to be 6.8-7.1. Three of the suggested four events have been dated successfully, at 56 ± 6 , 29 ± 3 and 12 ± 1 ka, by a combination of thermoluminescence and infrared-stimulated luminescence. Given numerous assumptions (and a precision on TL of 5-20%, Forman et al., 2000 reported in Personius and Mahan, 2003) incorporated into these analyses rounded ages and 10% errors were used to estimate probable ages. The authors estimate the oldest event to have occurred 92 to 244 ka.

C-7 The La Jencia fault

The La Jencia fault is a 35 km long major basin-marginal fault that bounds the west edge of the RGR as reported by Machette (1986). This fault consists of 6 segments that have produced a minimum of 5 separate scarp forming events between 3 to 33 ka, though this is potentially 6 if movement along the different segments is non-synchronous. These events over an interval of about 30 ka produce an average recurrence interval of between 6 and 7.5 ka. The SDI appears to have been used to date these younger events, though this is not stated in the text. The author suggests previous events based on offset of stratigraphy at 150 ka and 500 ka, with the event at 150 ka has being supported by colluvium dating. Machette calculates the magnitude of these events as M_W 6.9-7.1 based on the length of rupture and amount of surface offset. No explanation of errors is provided.

The palaeoseismic record for the mid-western United States is sparse and inaccurate. Information gained from the historical record is far too recent to provide an accurate estimate of the complete seismic cycle, especially in this case when time scales in the order of 1000s of years are desired. Sparseness of the record is a result of the time period involved because relatively few age dating techniques can accurately deal with late Pleistocene to Holocene deposits, and even then the particular materials required for each dating technique must be present. Radiometrically datable materials such as charcoal, bone, and volcanic ash are not often preserved in critical surface exposure or in excavations dug specifically for dating purposes (Machette, 1986). Movement of fault scarps are often estimated from offset of stratigraphy, more specifically the juxtaposition of soils with faulted sediments. Soils are ubiquitous in surficial deposits, and their degree of development can reflect their age- to this end Harden (1982) developed the soil

development index (SDI) for use as a tool in age determination of seismic events. It is an index based on several soil characteristics which help to differentiate between young poorly developed soils of recently eroded sites, and older well developed soils associated with more geomorphologically stable landforms. The SDI may provide a valuable tool in the estimation of earthquake recurrence for faults with no dateable material but with so many variables involved and the inaccuracy of ages reported from this technique, such as seen in Machete (1986) and McCalpin (2005), it is not a great method to compare and correlate events across numerous faults.

Appendix D

GPS reference points for travertine mounds

All GPS information is given as UTM grid values using the NAD83 datum. In Appendix D-2 travertine mounds are colour coded as followed: white- ancient mounds complete with layered mats; yellow- ancient mounds devoid of layered mats; blue- actively precipitating travertine mounds.

D-1 The Little Grand Wash fault

Mound number	Easting	Northing	Elevation (m)
L1	574908	4310256	1216.0
L2.1	574906	4310218	1214.1
L2.2	574764	4310185	1213.0
L3	575098	4310171	1236.5
L4	575312	4310125	1252.4
L5	576014	4310071	1233.7
L6	576137	4310078	1262.3
L7	576187	4310073	1257.3
L8	577230	4310106	1265.6

D-2 The northern fault of the Salt Wash graben

Sample set	Mound number	Easting	Northing	Elevation (m)
mounds dated by U-series	S1	576564	4302980	1223.3
	S2	577070	4302710	1248.7
	S3	577161	4302655	1234.8
	S4	577710	4302377	1290.0
	S5	577818	4302463	1289.1
	S6	577829	4302231	1242.0
	S7	577984	4302753	1263.4
	S8	578054	4302733	1267.1
	S9	578088	4302621	1268.5
	S10	578012	4302329	1244.9
	S11	577999	4302165	1267.3
	S12	578026	4302115	1243.7
	S13	579344	4301589	1255.9
	S14	578168	4302300	1249.4
	S15	578567	4302251	1264.6
	S16	578893	4301798	1272.5
	S17	579344	4301589	1265.9
	S18	579458	4301583	1281.5
	S19	579639	4301511	1281.9
	S20	580142	4301282	1271.8
	S21	580154	4301266	1276.3
	S22	582015	4300744	1287.2
mound ages estimated from incision rates	S23	576570	4302938	1225.6
	S24	576625	4302932	1231.4
	S25	577161	4302655	1234.8
	S26	577147	4302818	1238.0
	S27	577208	4302736	1238.5
	S28	577349	4302554	1236.2
	S29	577534	4302629	1250.6
	S30	577702	4302624	1261.2
	S31	577643	4302420	1264.5
	S32	577473	4302234	1251.1
	S33	577740	4302316	1273.8
	S34	577867	4302512	1283.0
	S35	578116	4302593	1267.2
	S36	578275	4302319	1261.8
	S37	578686	4301909	1273.3
S38	578275	4302319	1261.8	
S39	579864	4301383	1287.7	
S40	579979	4301336	1270.3	
S41	581468	4300855	1297.6	
modern travertine	S42	576550	4302983	1220.3
	S43	576629	4303009	1221.3
	S44	577074	4302843	1228.1
	S45*	577979	4301924	1268.0
	S46	578040	4302260	1242.8
	S47	580451	4301510	1271.2

References

- Adamson A. W. (1990) *Physical Chemistry of Surfaces*. John Wiley & Sons, Inc.
- Agosta F., Mulch, A., Chamberlain, C.P., and Aydin, A. (2008) Geochemical traces of CO₂-rich fluid flow along normal faults in central Italy. *Geophysical Journal International* **174**, 758-770.
- Alcaraz-Pelegrina J. M. and Martínez-Aguirre A. (2007) U/Th dating of carbonate deposits from Constantina (Sevilla), Spain. *Applied Radiation and Isotopes* **65** (7), 798-804.
- Allan A. S. (1989) Model for Hydrocarbon migration and entrapment within faulted structures. *AAPG Bulletin* **73**, 803- 811.
- Allis R., Chidsey, T., Gwynn, W., Morgan, C., White, S., Adams M., and Moore, J. (2001) Natural CO₂ Reservoirs on the Colorado Plateau and Southern Rocky Mountains: Candidates for CO₂ sequestration. *DOE/NETL: 1st National Conference of Carbon Sequestration. Proceedings Volume*.
- Allis R. G., Moore, J., and White, S. (2004) Reactive Multiphase behaviour of CO₂ in Saline Aquifers beneath the Colorado Plateau, pp. 15. University of Utah.
- Allis R., Bergfield D., Moore J., McClure K., Morgan C. D., Chidsey T. C., Heath J. E., and McPherson B. (2005) Implications of results from CO₂ flux surveys over known CO₂ systems for long-term monitoring. *DOE/NETL: 4th Annual Conference on Carbon Capture and Sequestration. Proceedings Volume*.
- Ambraseys N. N., and Jackson J. A. (1990) Seismicity and associated strain of central Greece between 1890 and 1988. *Geophysical Journal International* **101** (3), 663-708.
- Amiel A. J., Miller, D.S., Friedman, G.M. (1973a) Distribution and nature of incorporation of trace elements in modern aragonitic corals. *Sedimentology* **20** (1), 47-64.
- Amiel A. J., Miller, D.S., Friedman, G.M. (1973b) Incorporation of uranium in modern corals. *Sedimentology* **20**, 523-528.
- Amoroso L., Pearthree P. A., and Arrowsmith J. R. (2004) Paleoseismology and Neotectonics of the Shivwits Section of the Hurricane fault, North-western Arizona. *Bulletin of the Seismological Society of America* **94** (5), 1919-1942.
- Anderson K. and Bows A. (2008) Reframing the climate change challenge in light of post-2000 emission trends. *Philosophical Transactions of the Royal Society A: Mathematical, Physical and Engineering Sciences* **366** (1882), 3863-3882.
- Anderson L. J., Osbourne, R. H., Palmer, D. F. (1983) Cataclastic rocks of the San Gabriel fault-An expression of deformation at deeper crustal levels in the San Andreas fault zones. *Tectonophysics* **98**, 209-251.
- Anderson M. P. (2007) Introducing Groundwater Physics. *Physics Today* **60** (5), 42-47.
- Anderson R. S. (1993) A 35,000 Year Vegetation and Climate History from Potato Lake, Mogollon Rim, Arizona. *Quaternary Research* **40** (3), 351-359.
- Anderson R. S., Betancourt J. L., Mead J. I., Hevly R. H., and Adam D. P. (2000) Middle- and late-Wisconsin paleobotanic and paleoclimatic records from the southern Colorado Plateau, USA. *Palaeogeography, Palaeoclimatology, Palaeoecology* **155**, 31-57.
- Anderson T. R. and Fairley J. P. (2008) Relating permeability to the structural setting of a fault-controlled hydrothermal system in southeast Oregon, USA. *Journal of Geophysical Research* **113**.
- Andreani M., Gouze, P., Luquot, L., Jouanna, P. . (2008) Changes in seal capacity of fractured claystone caprocks induced by dissolved and gaseous CO₂ seepage. *Geophysical Research Letters* **35**.
- Antonellini M. A., and Aydin, A. (1994) Effect of faulting on fluid flow in porous sandstones: petrophysical properties. *AAPG Bulletin* **78**, 355-377.
- Anzalone E., Ferreri V., Sprovieri M., and D'Argenio B. (2007) Travertine as hydrologic archives: The case of the Pontecagnano deposits (southern Italy). *Advances in Water Resources* **30** (10), 2159-2175.

- Ármansson H., Fridriksson T., and Kristjánsson B. R. (2005) CO₂ emissions from geothermal power plants and natural geothermal activity in Iceland. *Geothermics* **34** (3), 286-296.
- Arts R., Eiken, O., Chadwick, A., Zweigel, P., van der Meer, B, and Kirby, G. (2004a) Seismic monitoring at the Sleipner underground CO₂ storage site (North Sea). In *Geological Storage of Carbon Dioxide*, **233** S. J. Baines and R. H. Worden (eds.), p181- 192. Geological Society, Special Publications.
- Arts R., Eiken O., Chadwick A., Zweigel P., van der Meer L., and Zinszner B. (2004b) Monitoring of CO₂ injected at Sleipner using time-lapse seismic data. *Energy* **29** (9-10), 1383-1392.
- Arts R. and Winthaege P. (2005) Monitoring Options for CO₂ Storage. In *Carbon Dioxide Capture for Storage in Deep Geologic Formations*, 1001-1013. Elsevier Science.
- Arts R., Chadwick, A. , Eiken, O. , Thibeau, S., and Nooner, S.L. (2008) Ten Years' Experience of Monitoring CO₂ Injection in the Utsira Sand at Sleipner, Offshore Norway. *First Break* **26**.
- Baars D. L. and Stevenson G. M. (1981) Tectonic evolution of the Paradox Basin, Utah and Colorado. In *Geology of the Paradox Basin*. Field Conference - Rocky Mountain Association of Geologists. D. L. Wiegand (ed.), 23-31.
- Bachu S. (2008) CO₂ storage in geological media: Role, means, status and barriers to development. *Progress in Energy and Combustion Science* **34**, 254-273.
- Baer J. L., and Rigby, J.K. (1978) Geology of the Crystal Geysir and the environmental implications of its effluent, Grand County, Utah. *Utah Geology* **5**, 125-130.
- Barbeau D. L. (2003) A flexural model for the Paradox Basin: implications for the tectonics of the Ancestral Rocky Mountains. *Basin Research* **15** (1), 97-115.
- Baines S. J. and Worden R. H. (2004) Geological storage of carbon dioxide. *Geological Society, London, Special Publications* **233** (1), 1-6.
- Bard E., Fairbanks R. G., Hamelin B., Zindler A., and Chi Track H. (1991) Uranium-234 anomalies in corals older than 150,000 years. *Geochimica et Cosmochimica Acta* **55** (8), 2385-2390.
- Barnes J. W., Lang, E. J., and Potratz, H. A. (1956) Ratio of ionium to uranium in coral limestone. *Science* **124**, 175-176.
- Bartlein P. J., Anderson K. H., Anderson P. M., Edwards M. E., Mock C. J., Thompson R. S., Webb R. S., Webb T., and Whitlock C. (1998) Paleoclimate simulations for North America over the past 21,000 years: features of the simulated climate and comparisons with paleoenvironmental data. *Quaternary Science Reviews* **17** (6-7), 549-585.
- Becker J. A., Bickle, M.J., Galy, A., Holland, T.J.B. (2008) Himalayan metamorphic CO₂ fluxes: Quantitative constraints from hydrothermal springs. *Earth and Planetary Science Letters* **265**, 616-629.
- Becker J. S. (2003) Mass spectrometry of long-lived radionuclides. *Spectrochimica Acta Part B: Atomic Spectroscopy* **58** (10), 1757-1784.
- Beitler B., Chan M. A., and Parry W. T. (2003) Bleaching of Jurassic Navajo Sandstone on Colorado Plateau Laramide highs: Evidence of exhumed hydrocarbon supergiants? *Geology* **31** (12), 1041-1044.
- Benson S. M. and Hepple R. (2005) Prospects for Early Detection and Options for Remediation of Leakage from CO₂ Sequestration Projects. In *Carbon Dioxide Capture for Storage in Deep Geologic Formations- Results from the CO₂ Capture Project, Vol. 2: Geologic Storage of Carbon Dioxide with Monitoring and Verification* S. M. Benson (eds.), 1189-1203. Elsevier.
- Bentley M. (2008) Modelling flow along fault damage zones in a sandstone Reservoir; an unconventional modelling technique using conventional modelling tools in the Douglas Field, Irish Sea, UK. *Society of Petroleum Engineers, SPE* 113958-PP.
- Berg R. R., Habeck, M. H. (1982) Abnormal pressures in the lower Vicksburg, McAllen Ranch field, south Texas. *Gulf Coast Association of Geological Societies Transactions* **32**, 247- 253.
- Berryhill H. J. (1986) Late Quaternary facies and structure, northern Gulf of Mexico: Interpretations from seismic data. *AAPG studies in geology* **23**, 289p.
- Billi A., Salvini, F., Storti, F. (2003) The damage zone-fault core transition in carbonate rocks: implications for fault growth, structure and permeability. *Journal of Structural Geology* **25**, 1779-1794.

- Bischoff J. L., and Fyfe, W.S. (1968) Catalysis, inhibition, and the calcite-aragonite problem, 1: The aragonite-calcite transformation, *American Journal of Science* **266**, 65-79.
- Bischoff J. L. and Fitzpatrick J. A. (1991) U-series dating of impure carbonates: An isochron technique using total-sample dissolution. *Geochimica et Cosmochimica Acta* **55** (2), 543-554.
- Bodner D. P., Sharp Jr, J. M. (1988) Thermal variations in the South Texas subsurface. *AAPG Bulletin* **72** (1), 21-32.
- Bonilla M. G. (1988) Minimum Earthquake Magnitude Associated with Coseismic Surface Faulting. *Bulletin of the Association of Engineering Geologists* **XXV** (1), 17-29.
- Bourdon B., Turner S., Henderson G. M., and Lundstrom C. C. (2003) Introduction to U-series Geochemistry. *Reviews in Mineralogy and Geochemistry* **52** (1), 1-21.
- Boutareaud S., Wibberley, C.A.J, Fabbri, O., and Shinamoto, T. (2008) Permeability structure and co-seismic thermal pressurization on fault branches: insights from the Usukidani fault, Japan. In *The Internal Structure of Fault Zones.*, **299** C. A. J. Wibberley, W. Kurz, J. Imber, R.E. Holdsworth and C. Collettini (eds.), 341- 361. Geological Society, Special Publications.
- Braun J., Munroe, S. M., Cox, S. F. (2003) Transient fluid flow in and around a fault. *Geofluids* **3**, 81-87.
- Broecker W. S. (2008) CO₂ capture and storage: Possibilities and perspectives. *Elements* **4** (5), 295-296.
- Brodsky E. E. (2006) Long-range triggered earthquakes that continue after the wave train passes. *Geophys. Res. Lett.* **33**.
- Brodsky E. E., Roeloffs E., Woodcock D., Gall I., and Manga M. (2003) A mechanism for sustained groundwater pressure changes induced by distant earthquakes. *J. Geophys. Res.* **108**.
- Brogi A. (2007) Fault zone architecture and permeability features in siliceous sedimentary rocks: Insights from the Rapolano geothermal area (Northern Apennines, Italy). *Journal of Structural Geology* **30**, 237-256.
- Brosch F.-J., and Kurz, W. (2008) Fault damage zones dominated by high-angle fractures within layer-parallel brittle shear zones: examples from the eastern Alps. In *The Internal Structure of Fault Zones.*, **299** C. A. J. Wibberley, W. Kurz, J. Imber, R.E. Holdsworth and C. Collettini (ed. Geological Society, Special Publications.
- Bruhn R. L. (1993) Crack 2D: An unpublished Matlab computer program for deriving permeability tensors in two dimensions using the methods of Oda, 1986 and Oda et al., 1987: University of Utah, Department of Geology and Geophysics, structural geology lab.
- Bruhn R. L., Parry, W. T., Yonkee, W. A., Thompson, T. (1994) Fracturing and hydrothermal alteration in normal fault zones. *PAGEOPH* **142**, 609- 644.
- Bryan W. B. and Stephens R. S. (1993) Coastal bench formation at Hanauma Bay, Oahu, Hawaii. *Geological Society of America Bulletin* **105** (3), 377-386.
- Buranek A. M. (1942) The occurrence of vanadium-uranium ores in Utah and Colorado. The State of Utah Raw Minerals Division.
- Caine J. S., Coates, D. R., Timoffeef, N. P., Davis, W. D. (1991) Hydrogeology of the Northern Shawangunk Mountains. *New York State Geological Survey*.
- Caine J. S., Evans, J.P., Forster, C.B (1996) Fault zone architecture and permeability structure. *Geology* **24** (11), 1025-1028.
- Cantucci B., Montegrossi G., Vaselli O., Tassi F., Quattrocchi F., and Perkins E. H. (2009) Geochemical modelling of CO₂ storage in deep reservoirs: The Weyburn Project (Canada) case study. *Chemical Geology* **265** (1-2), 181-197.
- Cappa J. A. and Rice D.D., (1995) Carbon dioxide in Mississippian rocks of the Paradox Basin and adjacent areas, Colorado, Utah, New Mexico and Arizona. *U.S. Geological Survey Bulletin* **2000-H**, 21pp.
- Caputo R. (2007) Sea-level curves: Perplexities of an end-user in morphotectonic applications. *Global and Planetary Change* **57** (3-4), 417-423.
- Carbon Monitoring for Action. (2008) CARMA CO₂ emission database, accessed March 3, 2010 from <http://carma.org/>.

- Cartwright J., Huuse, M., Aplin, A. (2007) Seal bypass systems. *AAPG Bulletin* **91** (8), 1141-1166.
- Cater F. W. (1970) Geology of the salt anticline region in south-western Colorado. *U.S. Geological Survey Professional Paper* **637**.
- Chabaux F., Riotte J., and Dequincey O. (2003) U-Th-Ra Fractionation During Weathering and River Transport. *Reviews in Mineralogy and Geochemistry* **52** (1), 533-576.
- Chadwick R. A., Holloway S., Brook M. S., and Kirby G. A. (2004) The case for underground CO₂ sequestration in northern Europe. *Geological Society, London, Special Publications* **233** (1), 17-28.
- Chadwick A., Arts, R., Bernstone, C., May, F., Thibeau, S., and Zweigel, P. (2007) *Best Practice for the Storage of CO₂ in Saline Aquifers-Observations and Guidelines from the SACS and CO2STORE Projects*. British Geological Survey.
- Chadwick R. A., Noy D., Arts R., and Eiken O. (2009) Latest time-lapse seismic data from Sleipner yield new insights into CO₂ plume development. *Energy Procedia* **1** (1), 2103-2110.
- Chafetz H. S. and Folk R. L. (1984) Travertines; depositional morphology and the bacterially constructed constituents. *Journal of Sedimentary Research* **54** (1), 289-316.
- Chafetz H. S. and Guidry S. A. (1999) Bacterial shrubs, crystal shrubs, and ray-crystal shrubs: bacterial vs. abiotic precipitation. *Sedimentary Geology* **126** (1-4), 57-74.
- Chafetz H. S. and Guidry S. A. (2003) Deposition and diagenesis of Mammoth Hot Springs travertine, Yellowstone National Park, Wyoming, U.S.A. *Canadian Journal of Earth Sciences* **40**, 1515-1529.
- Chang W.-L. and Smith R. B. (2002) Integrated Seismic-Hazard Analysis of the Wasatch Front, Utah. *Bulletin of the Seismological Society of America* **92** (5), 1904-1922.
- Charlton R. (2008) *Fundamentals of fluvial geomorphology*. Routledge.
- Chen J. H., Edwards, R. L., and Wasserburg, G. J. (1992) Mass spectrometry and applications to uranium-series disequilibrium. In *Uranium-Series Disequilibrium: Applications to Earth, Marine, and Environmental Sciences, 2nd ed* M. Ivanovich and R. S. Harmon (eds.), 174-206. Clarendon.
- Chen J. H., Curran H. A., White B., and Wasserburg G. J. (1991) Precise chronology of the last interglacial period: ²³⁴U-²³⁰Th data from fossil coral reefs in the Bahamas. *Geological Society of America Bulletin* **103** (1), 82-97.
- Chen J. H., Edwards R.L., and Wasserburg G. J. (1986) ²³⁸U, ²³⁴U and ²³²Th in seawater. *Earth and Planetary Science Letters* **80** (3-4), 241-251.
- Chen L. and Talwani P. (2001) Renewed Seismicity near Monticello Reservoir, South Carolina, 1996-1999. *Bulletin of the Seismological Society of America* **91** (1), 94-101.
- Cheng H., Edwards R. L., Hoff J., Gallup C. D., Richards D. A., and Asmerom Y. (2000) The half-lives of uranium-234 and thorium-230. *Chemical Geology* **169** (1-2), 17-33.
- Cherdyntsev V. (1955) On isotopic composition of radio elements in natural objects, and problems of geochronology. In *Proc. 3rd Sess. Comiss. Determ. Absol. Age Geol. Form*, 175-233. Acad. Sci. U.S.S.R, Moscow.
- Chester F. M., Logan, J. M. (1986a) Composite planar fabric of gouge from the Punchbowl fault, California. *Journal of Structural Geology* **9**, 621-634.
- Chester F. M., Logan, J. M. (1986b) Implications for mechanical properties of brittle faults from observations of the Punchbowl fault zone, California. *Pure and Applied Geophysics* **124**, 79- 106.
- Chidsey T. C., and Morgan, C.D. (2005) Major oil plays in Utah and vicinity. In *Quarterly technical progress report*, pp. 22. Utah Geological Survey.
- Childs C., Watterson, J., and Walsh, J.J. (1997) Complexity in fault zone structure and implications for fault seal prediction. In *Hydrocarbon Seals: Importance for Exploration and Production* **7**, P. Moller-Pederson and A.G. Koestler, (eds.), 61- 72. Norwegian Petroleum Society (NPF) Special Publications.
- Claesson I., Skelton, A., Graham, C., Morth, C.-M. (2007) The timescale and mechanisms of fault sealing and water-rock interaction after an earthquake. *Geofluids* **7**, 427-440.
- Clark I., and Fritz, P. (1997) *Environmental Isotopes in Hydrogeology*. Lewis Publishers.

- Collettini C. (2002) Structural permeability control on the post-seismic fluid discharge and aftershocks triggering; hypothesis for the 1997 Colfiorito earthquakes. *Boll. Soc. Geol. It* **1**, 873-880.
- Collettini C., and Trippetta, F. (2007) A slip tendency analysis to test mechanical and structural control on aftershock rupture planes. *Earth and Planetary Science Letters* **255** (3-4), 402- 413.
- Collier R. E. L., Leeder M. R., Rowe P. J., and Atkinson T. C. (1992) Rates of tectonic uplift in the Corinth and Megara basins, central Greece. *Tectonics* **11** (6), 1159-1167.
- Condon S. M. (1997) Geology of the Pennsylvanian and Permian Cutler Group and Permian Kaibab Limestone in the Paradox Basin, south-eastern Utah and south-western Colorado. *U. S. Geological Survey Bulletin*, (2000-P).
- Cook P. J. (2009) Demonstration and Deployment of Carbon Dioxide Capture and Storage in Australia. *Energy Procedia* **1** (1), 3859-3866.
- Cooper F. J., Roberts G. P., and Underwood C. J. (2007) A comparison of 10^3 - 10^5 year uplift rates on the South Alkyonides Fault, central Greece: Holocene climate stability and the formation of coastal notches. *Geophys. Res. Lett.* **34**.
- Curewitz D., and Karson, J.A. (1997) Structural settings of hydrothermal outflow; fracture permeability maintained by fault propagation and interaction. *Journal of Volcanology and Geothermal Research* **79**, 149- 168.
- Daley T., Myer L., Peterson J., Majer E., and Hoversten G. (2008) Time-lapse crosswell seismic and VSP monitoring of injected CO₂ in a brine aquifer. *Environmental Geology* **54** (8), 1657-1665.
- Dalrymple G. B. (1991) *The Age of the Earth*. Stanford University Press.
- Davis G. H. (1978) Monocline fold pattern of the Colorado Plateau. In *Laramide folding associated with basement block faulting in the western United States*, **151** V. Matthews (ed.), 215-233. Memoir - Geological Society of America.
- De Meersman K., Kendall J.-M., and van der Baan M. (2007) Valhall microseismicity revisited: relocated sources, seismic multiplets and S-wave splitting. *proceedings of the 69th Mtg.: Eur. Assn. Geosci. Eng.*, A038.
- dePolo C. M. (1994) The maximum background earthquake for the Basin and Range province, western North America. *Bulletin of the Seismological Society of America* **84** (2), 466-472.
- Dethier D. P. (2001) Pleistocene incision rates in the western United States calibrated using Lava Creek B tephra. *Geology* **29** (9), 783-786.
- Detwiler R. L. (2008) Experimental observations of deformation caused by mineral dissolution in variable-aperture fractures. *Journal of Geophysical Research* **113**.
- Dia A. N., Cohen, A. S., O'Nions, R. K., and Shackleton, N. J. (1992) Seawater Sr- isotope variations over the last 300ka and global climate change. *Nature* **356**, 786-789.
- Dia A. N., Cohen A. S., O'Nions R. K., and Jackson J. A. (1997) Rates of uplift investigated through ²³⁰Th dating in the Gulf of Corinth (Greece). *Chemical Geology* **138**, 174-181.
- Dickerson P. W. (2003) Intraplate mountain building in response to continent-continent collision--the Ancestral Rocky Mountains (North America) and inferences drawn from the Tien Shan (Central Asia). *Tectonophysics* **365** (1-4), 129-142.
- Dickinson W. R. and Lawton T. F. (2003) Sequential intercontinental suturing as the ultimate control for Pennsylvanian Ancestral Rocky Mountains deformation. *Geology* **31** (7), 609-612.
- Dockrill B. (2006) *Understanding leakage from a fault-sealed CO₂ reservoir in east-central Utah: A natural analogue applicable to CO₂ storage*, University of Dublin, Trinity College.
- Dockrill B. and Shipton, Z.S. (2010) Structural controls on leakage from a natural CO₂ geologic storage site: central Utah, U.S.A. *Journal of Structural Geology* (in press doi:10.1016/j.jsg.2010.01.007).
- Dockrill B., Kirschner, D.L., and Shipton, Z.S. (in review) Internal structure and evolution of fault-related active and ancient travertine deposits in east-central Utah, U.S.A.
- Doelling H. H. (1967) Uranium deposits of Garfield County, Utah, pp. 113. Utah Geological and Mineralogical Survey, Special studies number 22.

- Doelling H. H. (1969) Mineral resources, San Juan County, Utah, and adjacent areas, Part II-Uranium and other metals in sedimentary host rocks, pp. 68. Utah Geological and Mineralogical Survey, Special studies number 24.
- Doelling H. H., Huntoon, P.W. and Oviatt, C.G. . (1988) Salt deformation in the Paradox region. *Utah Geological and Mineral Survey Bulletin* **122**.
- Doelling H. H. (1994) Tufa deposits in western Grand County. Survey Notes *Utah Geological Survey* **26**, 8- 10.
- Doelling H. H. (2001) Geologic map of the Moab and eastern part of the San Rafael Desert 30' x 60' quadrangles, Grand and Emery Counties, Utah, and Mesa County, Colorado. *Utah Geological Survey Map* **180**.
- Doelling H. H. (2002) Interim geological map of the San Rafael Desert 30'x60' quadrangle, Grand and Emery County, Utah. *Utah Geological Survey Map*, OFR-404.
- Dorn R. I. (1987) A rock varnish interpretation of alluvial-fan development in Death Valley, California *National Geographic Research* **4**, 56-73.
- Drewitt G. B., Black T. A., Nestic Z., Humphreys E. R., Jork E. M., Swanson R., Ethier G. J., Griffis T., and Morgenstern K. (2002) Measuring forest floor CO₂ fluxes in a Douglas-fir forest. *Agricultural and Forest Meteorology* **110** (4), 299-317.
- Dreybrodt W., Buhmann D., Michaelis J., and Usdowski E. (1992) Geochemically controlled calcite precipitation by CO₂ outgassing: Field measurements of precipitation rates in comparison to theoretical predictions. *Chemical Geology* **97** (3-4), 285-294.
- Dumas B., Hoang C. T., and Raffy J. (2006) Record of MIS 5 sea-level highstands based on U/Th dated coral terraces of Haiti. *Quaternary International* **145-146**, 106-118.
- Dyke A. S., Andrews J. T., Clark P. U., England J. H., Miller G. H., Shaw J., and Veillette J. J. (2002) The Laurentide and Innuitian ice sheets during the Last Glacial Maximum. *Quaternary Science Reviews* **21** (1-3), 9-31.
- Eberhart-Phillips D., Haeussler P. J., Freymueller J. T., Frankel A. D., Rubin C. M., Craw P., Ratchkovski N. A., Anderson G., Carver G. A., Crone A. J., Dawson T. E., Fletcher H., Hansen R., Harp E. L., Harris R. A., Hill D. P., Hreinsdottir S., Jibson R. W., Jones L. M., Kayen R., Keefer D. K., Larsen C. F., Moran S. C., Personius S. F., Plafker G., Sherrod B., Sieh K., Sitar N., and Wallace W. K. (2003) The 2002 Denali Fault Earthquake, Alaska: A Large Magnitude, Slip-Partitioned Event. *Science* **300** (5622), 1113-1118.
- Edwards R.L., Chen J. H., and Wasserburg G. J. (1987) ²³⁸U ²³⁴U ²³⁰Th ²³²Th systematics and the precise measurement of time over the past 500,000 years. *Earth and Planetary Science Letters* **81** (2-3), 175-192.
- Eichhubl P. and Boles J. R. (2000) Rates of fluid flow in fault systems; evidence for episodic rapid fluid flow in the Miocene Monterey Formation, coastal California. *Am J Sci* **300** (7), 571-600.
- Eichhubl P., Davatz N. C., and Becker S. P. (2009) Structural and diagenetic control of fluid migration and cementation along the Moab fault, Utah. *AAPG Bulletin* **93** (5), 653-681.
- El Moursi M., Hoang C. T., Fayoumy I. F. E., Hegab O., and Faure H. (1994) Pleistocene evolution of the Red Sea coastal plain, Egypt: Evidence from uranium-series dating of emerged reef terraces. *Quaternary Science Reviews* **13** (4), 345-359.
- Elkhoury J. E., Brodsky E. E., and Agnew D. C. (2006) Seismic waves increase permeability. *Nature* **441** (7097), 1135-1138.
- Elkhoury J. E., Niemeijer A., Brodsky E. E., and Marone C. (in press) Dynamic stress stimulates slow in fractures: Laboratory observations of permeability enhancement. Manuscript submitted to *Journal of Geophysical Research* 2009.
- Ellam R. M., and Keefe, K. (2006) MC-ICP-MS analysis of non-natural U isotope ratios using a ²²⁹Th/²³²Th external mass bias correction. *Journal of analytical atomic spectrometry* **22** (2), 147-152.
- Esposito E., Pece, R., Porfido, S., Tranfaglia, G. (2001) Hydrological anomalies connected to earthquakes in southern Apennines (Italy). *Natural Hazards and Earth System Sciences* (1), 137-144.
- Etiopie G. and Lombardi S. (1995) Evidence for radon transport by carrier gas through faulted clays in Italy. *Journal of Radioanalytical and Nuclear Chemistry* **193** (2), 291-300.

- Etiopio G. and Lombardi S. (1997) Levels of leakage in relation to geology. In *Plant responses to elevated CO₂* A. Raschi, F. Miglietta, R. Tognetti, and P. R. v. Gardingen (eds.), 21-33. Cambridge University Press.
- Etiopio G., Guerra M., and Raschi A. (2005) Carbon Dioxide and Radon Geohazards Over a Gas-bearing Fault in the Siena Graben (Central Italy). *Terrestrial, Atmospheric and Oceanic Sciences* **16** (4), 885-896.
- Evans J. P., Heath, J., Shipton, Z.K., Kolesar, P.T., Dockrill, B., Williams, A., Kirchner, D., Lachmar, T.E., Nelson, S.T. (2004) Natural leaking CO₂-charged systems as analogues for geologic sequestration sites. *Paper presented at 3rd annual conference on carbon capture and sequestration*.
- Faccenna C., Soligo M., Billi A., De Filippis L., Funiciello R., Rossetti C., and Tuccimei P. (2008) Late Pleistocene depositional cycles of the Lapis Tiburtinus travertine (Tivoli, Central Italy): Possible influence of climate and fault activity. *Global and Planetary Change* **63** (4), 299-308.
- Fairley J. P., Heffner, J., Hinds, J.J. . (2003) Geostatistical evaluation of permeability in an active fault zone. *Geophysical Research Letters* **30** (18).
- Fairley J. P. and Hinds, J.J. (2004a) Field observation of fluid circulation patterns in a normal fault system. *Geophysical Research Letters* **31**.
- Fairley J. P. and Hinds J. J. (2004b) Rapid transport pathways for geothermal fluids in an active Great Basin fault zone. *Geology* **32** (9), 825-828.
- Faulds J. E., Coolbaugh, M.F., Vice, G.S., and Edwards, M.L. (2006) Characterizing structural controls of geothermal fields in the north-western Great Basin: A progress report. *Geothermal Resources Council Transactions* **30**, 69-75.
- Faulkner D. R., Rutter, E.H. (2003) The effect of temperature, the nature of the pore fluid, and subyield differential stress on the permeability of phyllosilicate-rich fault gouge. *Journal of Geophysical Research* **108**, 2227.
- Felzer K. R. and Brodsky E. E. (2006) Decay of aftershock density with distance indicates triggering by dynamic stress. *Nature* **441** (7094), 735-738.
- Ferris F. G., Phoenix V., Fujita Y., and Smith R. W. (2004) Kinetics of calcite precipitation induced by ureolytic bacteria at 10 to 20°C in artificial groundwater. *Geochimica et Cosmochimica Acta* **68** (8), 1701-1710.
- Fetter C. W. (1993) *Containment hydrogeology 2nd Addition*. Prentice-Hall International (UK) Limited.
- Fetter C. W. (2001) *Applied Hydrogeology 4th Addition*. Prentice-Hall International (UK) Limited.
- Fisher D. M. and Brantley S. L. (1992) Models of quartz overgrowth and vein formation: deformation and episodic fluid flow in an ancient subduction zone. *J. Geophys. Res.* **97**.
- Fisher Q. J., Harris S. D., McAllister E., Knipe R. J., and Bolton A. J. (2001) Hydrocarbon flow across faults by capillary leakage revisited. *Marine and Petroleum Geology* **18**, 251-257.
- Flecker R., de Villiers S., and Ellam R. M. (2002) Modelling the effect of evaporation on the salinity-⁸⁷Sr/⁸⁶Sr relationship in modern and ancient marginal-marine systems: the Mediterranean Messinian Salinity Crisis. *Earth and Planetary Science Letters* **203** (1), 221-233.
- Flett M., Brantjes J., Gurton R., McKenna J., Tankersley T., and Trupp M. (2009) Subsurface development of CO₂ disposal for the Gorgon Project. *Energy Procedia* **1** (1), 3031-3038.
- Folk R. L., Chafetz H.S., and Tiezzi P. A. (1985) Bizarre forms of depositional and diagenetic calcite in hot-spring travertines, Central Italy. In *Carbonate Cements*, **36** N. Schneidermann and P. M. Harris (eds.), 349-369. The Society of Economic Paleontologists and Mineralogists Special Publications.
- Ford T. D., Pedley, H. M. (1996) A review of tufa and travertine deposits of the world. *Earth-Science Reviews* **41**, 117-175.
- Forster C. B. and Evans J. P. (1991) Hydrogeology of thrust faults and crystalline thrust sheets: Results of combined field and modelling studies. *Geophys. Res. Lett.* **18**, 979-982.
- Fossen H., Johansen T. E. S., Hesthammer J., and Rotevatn A. (2005) Fault interaction in porous sandstone and implications for reservoir management; examples from southern Utah. *AAPG Bulletin* **89** (12), 1593-1606.

- Fouke B. W., Farmer J. D., Des Marais D. J., Pratt L., Sturchio N. C., Burns P. C., and Discipulo M. K. (2000) Depositional Facies and Aqueous-Solid Geochemistry of Travertine-Depositing Hot Springs (Angel Terrace, Mammoth Hot Springs, Yellowstone National Park, U.S.A.). *Journal of Sedimentary Research* **70** (3), 565-585.
- Foxford K. A., Garden, I.R., Guscott, S.C., Burley, S.D., Lewis, J.L.L., Walsh, J.J., Watterson, J. (1996) The field geology of the Moab Fault. In *Geology and resources of the Paradox Basin*, **25** A. C. Huffman, Lund, W.R., and Godwin L.H. (eds.), 265-283. Utah Geological Association Guidebook.
- Frank A. B., Liebig M. A., and Hanson J. D. (2002) Soil carbon dioxide fluxes in northern semiarid grasslands. *Soil Biology and Biochemistry* **34** (9), 1235-1241.
- Fredrickson J. K., Zachara J. M., Kennedy D. W., Duff M. C., Gorby Y. A., Li S. W., and Krupka K. M. (2000) Reduction of U(VI) in goethite (α -FeOOH) suspensions by a dissimilatory metal-reducing bacterium. *Geochimica et Cosmochimica Acta* **64** (18), 3085-3098.
- Fridriksson T., Kristjánsson B. R., Ármannsson H., Margrétardóttir E., Ólafsdóttir S., and Chiodini G. (2006) CO₂ emissions and heat flow through soil, fumaroles, and steam heated mud pools at the Rekjanes geothermal area, SW Iceland. *Applied Geochemistry* **21** (9), 1551-1569.
- Frohlich K. (1990) On Dating of Old Groundwater. *Isotopenpraxis* **26** (12), 557-560.
- Gäbler H.-E. (2002) Applications of magnetic sector ICP-MS in geochemistry. *Journal of Geochemical Exploration* **75** (1-3), 1-15.
- Galloway W. E. (1982) Epigenic zonation and fluid flow history of uranium-bearing fluvial aquifer systems, South Texas uranium province. *The University of Texas at Austin, Bureau of Economic Geology, Report of Investigations* **119**, 31 pp.
- Garnett E. R., Gilmour M. A., Rowe P. J., Andrews J. E., and Preece R. C. (2004) ²³⁰Th/²³⁴U dating of Holocene tufas: possibilities and problems. *Quaternary Science Reviews* **23** (7-8), 947-958.
- Gartrell A., Zhang, Y., Lisk, M., Dewhurst, D. (2003) Enhanced hydrocarbon leakage at fault intersections: an example from the Timor Sea, Northwest Shelf, Australia. *Journal of Geochemical Exploration* **78-79**, 361- 365.
- Gartrell A., Zhang, Y., Lisk, M., Dewhurst, D. (2004) Fault intersections as critical hydrocarbon leakage zones: integrated field study and numerical modelling of an example from the Timor Sea, Australia. *Marine Petroleum Geology* **21**, 1165- 1179.
- Garvin, C.D., Hanks T.C., Finkel, R.C., Heimsath, A.M. (2005) Episodic incision of the Colorado River in Glen Canyon, Utah. *Earth Surface Processes and Landforms* **30**(8): 973–984.
- Gascoyne M., and Schwarcz, H.P. (1982) Carbonate and sulphate precipitates. In *Uranium-Series Disequilibrium. Applications to Environmental Problems* M. Ivanovich and R. S. Harmon (eds.), 268-301. Oxford University Press.
- Gascoyne M. (1982) Geochemistry of the actinides and their daughters. In *Uranium-Series Disequilibrium. Applications to Environmental Problems* M. Ivanovich and R. S. Harmon (eds.), 33-55. Oxford University Press.
- Gasse F. and Fontes J.-C. (1989) Palaeoenvironments and palaeohydrology of a tropical closed lake (Lake Asal, Djibouti) since 10,000 yr B.P. *Palaeogeography, Palaeoclimatology, Palaeoecology* **69**, 67-102.
- Geyh M. A. (2008) Selection of suitable data sets improves ²³⁰Th/U dates of dirty material. *Geochronometria* **30**, 69-77.
- Gilfillan S. M. V., Ballentine C. J., Holland G., Blagburn D., Lollar B. S., Stevens S., Schoell M., and Cassidy M. (2008) The noble gas geochemistry of natural CO₂ gas reservoirs from the Colorado Plateau and Rocky Mountain provinces, USA. *Geochimica et Cosmochimica Acta* **72** (4), 1174-1198.
- Gomberg J., Bodin P., Larson K., and Dragert H. (2004) Earthquake nucleation by transient deformations caused by the M = 7.9 Denali, Alaska, earthquake. *Nature* **427** (6975), 621-624.
- Gouveia F. J., Johnson M. R., Leif R. N., and Friedmann S. J. (2005) Aerometric measurement and modeling of the mass of CO₂ emissions from Crystal Geyser, Utah. *Lawrence Livermore National Laboratory, Livermore, CA, UCRL-TR-211870*.
- Griffiths C., Bertram, G.T., Richards, M., Milton, N., Sturrock, S., Reynolds, T. (1996) *Sequence Stratigraphy*. Wiley-Blackwell

- Grissino-Mayer H., Swetnam T. W., and Adams R. K. (1997) The rare, old-aged conifers of El Malpais: Their role in understanding climatic change in the American Southwest. In *Natural history of El Malpais National Monument. Bulletin 156*. K. Mabery (ed.), 155-161. New Mexico Bureau of Mines and Mineral Resources
- Gudmundsson A. (2001) Fluid overpressure and flow in fault zones: field measurements and models. *Tectonophysics* **336**, 183-197.
- Guo L. and Riding R. (1994) Origin and diagenesis of Quaternary travertine shrub fabrics, Rapolano Terme, central Italy. *Sedimentology* **41** (3), 499-520.
- Gupta H. K., Rastogi B. K., Chadha R. K., Mandal P., and Sarma C. S. P. (1997) Enhanced reservoir-induced earthquakes in Koyna region, India, during 1993-95. *Journal of Seismology* **1**, 47-53.
- Gutjahr A., Dabringhaus H., and Lacmann R. (1996) Studies of the growth and dissolution kinetics of the CaCO₃ polymorphs calcite and aragonite II. The influence of divalent cation additives on the growth and dissolution rates. *Journal of Crystal Growth* **158** (3), 310-315.
- Gvirtzman G., Friedman G. M., and Miller D. S. (1973) Control and distribution of uranium in coral reefs during diagenesis. *Journal of Sedimentary Research* **43** (4), 985-997.
- Halliday A. N., Lee D.-C., Christensen J. N., Rehkämper M., Yi W., Luo X., Hall C. M., Ballentine C. J., Pettke T., and Stirling C. (1998) Applications of Multiple Collector-ICPMS to Cosmochemistry, Geochemistry, and Paleoceanography. *Geochimica et Cosmochimica Acta* **62** (6), 919-940.
- Haluk Selim H. and Yanik G. (2009) Development of the Cambazlı (Turgutlu/MANISA) fissure-ridge-type travertine and relationship with active tectonics, Gediz Graben, Turkey. *Quaternary International* **199** (1-2), 157-163.
- Hamelin B., Bard E., Zindler A., and Fairbanks R. G. (1991) ²³⁴U/²³⁸U mass spectrometry of corals: How accurate is the U-Th age of the last interglacial period? *Earth and Planetary Science Letters* **106** (1-4), 169-180.
- Hammer Ø., Jamtveit B., Benning L. G., and Dysthe D. K. (2005) Evolution of fluid chemistry during travertine formation in the Troll thermal springs, Svalbard, Norway. *Geofluids* **5** (2), 140-150.
- Hancock P. L., Chalmers, R.M.L., Altunel, E., Cakir, Z. (1999) Travertines: using travertine in active fault studies. *Journal of Structural Geology* **21**, 903-916.
- Hancock P. L. and Altunel E. (1997) Faulted archaeological relics at Hierapolis (Pamukkale), Turkey. *Journal of Geodynamics* **24** (1-4), 21-36.
- Haney M., Snieder, R., Sheiman, J. and Losh, S. (2005) A moving fluid pulse in a fault zone. *Nature* **437**, 46.
- Harden J. W. (1982) A quantitative index of soil development from field descriptions: Examples from a chronosequence in central California. *Geoderma* **28** (1), 1-28.
- Harmon R. S., and Rosholt, J.N. (1982) Igneous rocks. In *Uranium-Series Disequilibrium. Applications to Environmental Problems* M. Ivanovich and R. S. Harmon (eds.), 145-166. Oxford University Press.
- Harris D., Yielding G., Levine P., Maxwell G., Rose P. T., and Nell P. (2002) Using Shale Gouge Ratio (SGR) to model faults as transmissibility barriers in reservoirs: an example from the Strathspey Field, North Sea. *Petroleum Geoscience* **8** (2), 167-176.
- Harry D. L. and Mickus K. L. (1998) Gravity constraints on lithospheric flexure and the structure of the late Paleozoic Ouachita orogen in Arkansas and Oklahoma, south-central North America. *Tectonics* **17** (2), 187-202.
- Hauksson E., Jones L. M., Hutton K., and Eberhart-Phillips D. (1993) The 1992 Landers Earthquake Sequence: Seismological Observations. *J. Geophys. Res.* **98**.
- Heath J. E., Lachmar, T.E., Shipton, Z.K., Nelson, S., and Evans, J.P. (2002) Hydrogeochemical analysis of leaking CO₂-charged fault zones: the Little Grand Wash and Salt Wash fault zones, Emery and Grand counties, Utah. *Geological Society of America Abstracts with Programs*, p392.
- Heath J. E. (2004) *Hydrogeochemical characterization of leaking carbon dioxide charged fault zones in east-central Utah*, Utah State University.
- Heath J. E., Lachmar, T.E., Evans J.P., Kolesar, P.T., Williams, A.P. (2009) Hydrogeochemical Characterization of Leaking, Carbon Dioxide-Charged Fault Zones in East-Central Utah, With

- Implications for Geological Carbon Storage. In *Carbon Sequestration and Its Role in the Global Carbon Cycle*, **183** B. J. McPherson and E. T. Sundquist (eds.), 147-158. Geophysical Monograph Series.
- Hecker S. (1993) Quaternary tectonics of Utah with emphasis on earthquake-hazard characterization. *Utah Geological Survey Bulletin* **127**, p. 157.
- Hedenquist J. W., Henley, R. (1985) Hydrothermal eruptions in the Waitopu geothermal system, New Zealand. *Economic Geology* **80**, 1640- 1668.
- Heffner J., Fairley, J.P. (2006) Using surface characteristics to infer the permeability structure of an active fault zone. *Journal of Sedimentary Geology* **184**, 255-265.
- Heggland R. (1997) Detection of gas migration from a deep source by the use of exploration 3D seismic data. *Marine Geology* **137** (1-2), 41-47.
- Heidbach O., Tingay, M., Barth, A., Reinecker, J., Kurfeß, D., and Müller, B. (2008) The World Stress Map database release 2008. doi:10.1594/GFZ.WSM.Rel2008.
- Henderson G. M. (2002) Seawater ($^{234}\text{U}/^{238}\text{U}$) during the last 800 thousand years. *Earth and Planetary Science Letters* **199** (1-2), 97-110.
- Henderson G. M., Cohen A. S., and O'Nions R. K. (1993) $^{234}\text{U}/^{238}\text{U}$ ratios and ^{230}Th ages for Hateruma Atoll corals: implications for coral diagenesis and seawater $^{234}\text{U}/^{238}\text{U}$ ratios. *Earth and Planetary Science Letters* **115** (1-4), 65-73.
- Herman J. S. and Lorah M. M. (1987) CO_2 outgassing and calcite precipitation in Falling Spring Creek, Virginia, U.S.A. *Chemical Geology* **62** (3-4), 251-262.
- Hermanrud C., Andresen T., Eiken O., Hansen H., Janbu A., Lippard J., Bolås H. N., Simmenes T. H., Teige G. M. G., and Østmo S. (2009) Storage of CO_2 in saline aquifers-Lessons learned from 10 years of injection into the Utsira Formation in the Sleipner area. *Energy Procedia* **1** (1), 1997-2004.
- Hesthammer J., and Fossen, H. (2000) Uncertainties associated with fault sealing analysis. *Petroleum Geoscience* **6**, 37- 45.
- Heyman O. G., Huntoon, P. W. and White-Heyman, M. A. (1986) Laramide deformation of the Uncompahgre Plateau; geometry and mechanisms. In *New interpretations of Northwest Colorado geology* D. S. Stone and K. S. Johnson (eds.), 65-76. Rocky Mountain Association of Geologists.
- Hill D. P., Reasenber P. A., Michael A., Arabaz W. J., Beroza G., Brumbaugh D., Brune J. N., Castro R., Davis S., dePolo D., Ellsworth W. L., Gomberg J., Harmsen S., House L., Jackson S. M., Johnston M. J. S., Jones L., Keller R., Malone S., Munguia L., Nava S., Pechmann J. C., Sanford A., Simpson R. W., Smith R. B., Stark M., Stickney M., Vidal A., Walter S., Wong V., and Zollweg J. (1993) Seismicity Remotely Triggered by the Magnitude 7.3 Landers, California, Earthquake. *Science* **260** (5114), 1617-1623.
- Hintz N. H., Faulds, J.E, Oppliger, G.L. (2008) Structural Controls of Lee Hot Springs, Southern Churchill County, Western Nevada: A Small Pull-Apart in the Dextral Shear Zone of the Walker Lane. *Geothermal Resources Council Transactions* **32**, 285-289.
- Hintze L. F. (1993) Geologic history of Utah. *Brigham Young University Geology Studies Special Publication* **7**, 202.
- Holloway S., Pearce J. M., Hards V. L., Ohsumi T., and Gale J. (2007) Natural emissions of CO_2 from the geosphere and their bearing on the geological storage of carbon dioxide. *Energy* **32** (7), 1194-1201.
- Hood J. W., and Patterson, D. J. (1984) Bedrock aquifers in the northern San Rafael Swell area, Utah, with special emphasis on the Navajo Sandstone. *Utah Department of Natural Resources, Technical Publication* **78**.
- Hood J. W. and Danielson T. W. (1981) Bedrock aquifers in the lower Dirt Devil Basin, Utah, with special emphasis on the Navajo sandstone. In *Utah Dept. Nat. Res. Tech. Pub.* **78**
- Hooper E. C. D. (1990) The movement of fluids through growth faults in compacting sedimentary basins, pp. 243. The University of Queensland, Australia.
- Hooper E. C. D. (1991) Fluid migration along growth faults in compacting sediments. *Journal of Petroleum Geology* **41** (s1), 161-180.

- Houghton S. L., Roberts G. P., Papanikolaou I. D., McArthur J. M., and Gilmour M. A. (2003) New ^{234}U - ^{230}Th coral dates from the western Gulf of Corinth: Implications for extensional tectonics. *Geophys. Res. Lett.* **30**.
- Hulme M. and Jenkins G. J. (1998) Climate change scenarios for the UK; Scientific Report. UKCIP. In *Technical Report No. 1*, pp. 80. Climatic Research Unit.
- Husen S., Taylor R., Smith R. B., and Healsler H. (2004) Changes in geyser eruption behaviour and remotely triggered seismicity in Yellowstone National Park produced by the 2002 M 7.9 Denali fault earthquake, Alaska. *Geology* **32** (6), 537-540.
- Imai T., and Sakanoue, M. (1973) Content of plutonium, thorium and protactinium in sea water and recent coral in the North Pacific. *Journal of the Oceanographical Society of Japan* **29** (76-82).
- Imbrie J., D. Hays, D. G. Martinson, A. McIntyre, A. C. Mix, J. J. Morley, N. G. Pisias, W. L. Prell, and Shackleton N. J. (1984) The orbital theory of Pleistocene climate: Support from a revised chronology of the marine record. In *Milankovitch and Climate, Part 1* A. L. Berger (ed.), 269-305. Norwell.
- Ingebritsen S. E. and Rojstaczer S. A. (1993) Controls on Geyser Periodicity. *Science* **262** (5135), 889-892.
- Ingebritsen S. E. and Rojstaczer S. A. (1996) Geyser periodicity and response of geysers to deformation. *Journal of Geophysical Research* **101**, 21,891- 21,905.
- Ivanovich M. (1982a) The phenomenon of radioactivity. In *Uranium-Series Disequilibrium. Applications to Environmental Problems* M. Ivanovich and R. S. Harmon (eds.), 1-32. Oxford University Press.
- Ivanovich M. (1982b) Uranium series disequilibria applications in geochronology. In *Uranium-Series Disequilibrium. Applications to Environmental Problems* M. Ivanovich and R. S. Harmon (eds.), 56-78. Oxford University Press.
- Jackson S. T., Betancourt J. L., Lyford M. E., Gray S. T., and Rylander K. A. (2005) A 40,000-year woodrat-midden record of vegetational and biogeographical dynamics in north-eastern Utah, USA. *Journal of Biogeography* **32**, 1085-1106.
- Jaffey A. H., Flynn K. F., Glendenin L. E., Bentley W. C., and Essling A. M. (1971) Precision Measurement of Half-Lives and Specific Activities of ^{235}U and ^{238}U . *Physical Review C* **4** (5), 1889.
- Jamtveit B., Hammer, Ø., Anderson, C., Dysthe, D.K., Heldmann, J., Vogel, M. (2006) Travertines from the Troll thermal springs, Svalbard. *Norwegian Journal of Geology* **86**, 387-395.
- Janssen A., Swennen R., Podoor N., and Keppens E. (1999) Biological and diagenetic influence in Recent and fossil tufa deposits from Belgium. *Sedimentary Geology* **126** (1-4), 75-95.
- Janssens I. A., Kowalski A. S., and Ceulemans R. (2001) Forest floor CO₂ fluxes estimated by eddy covariance and chamber-based model. *Agricultural and Forest Meteorology* **106** (1), 61-69.
- Jensen G. K. S., Nickel E. H., Whittaker S., and Rostron B. J. (2009) Geological model and hydrogeological framework of an active CO₂ sequestration project in the Weyburn-Midale area, Saskatchewan: Leading to a further understanding of possible CO₂ migration. *Energy Procedia* **1** (1), 2983-2989.
- Jin Z.-H., Johnson, S.E. (2008) Primary oil migration through buoyancy-driven multiple fracture propagation: Oil velocity and flux. *Geophysical Research Letters* **35**.
- Johansen T. E. S., Fossen H., and Kluge R. (2005) The impact of syn-faulting porosity reduction on damage zone architecture in porous sandstone: an outcrop example from the Moab Fault, Utah. *Journal of Structural Geology* **27**, 1469- 1485.
- Johnson R. C. (2003) Depositional Framework of the Upper Cretaceous Mancos Shale and the Lower Part of the Upper Cretaceous Mesaverde Group, Western Colorado and Eastern Utah. In *Petroleum Systems and Geologic Assessment of Oil and Gas in the Uinta-Piceance Province, Utah and Colorado*, Chapter 10. USGS Uinta-Piceance Assessment Team (eds.), U.S. Geological Survey Digital Data Series DDS-69-B.
- Johnson J. W., J.J. Nitao, and K.G. Knuass. (2004) Reactive transport modelling of CO₂ storage in saline aquifers to elucidate fundamental processes, trapping mechanisms and sequestration partitioning. In *Geological Storage of Carbon Dioxide.*, **233** S. J. Baines, and R. H. Worden (eds.), 107- 128. Geological Society, Special Publications.

- Johnston M. J. S., Hill D. P., Linde A. T., Langbein J., and Bilham R. (1995) Transient deformation during triggered seismicity from the 28 June 1992 Mw = 7.3 Landers earthquake at Long Valley volcanic caldera, California. *Bulletin of the Seismological Society of America* **85** (3), 787-795.
- Jourde H., Flodin E. A., Aydin A., Durlafsky L. J., and Wen X.-H. (2002) Computing Permeability of Fault Zones in Eolian Sandstone from Outcrop Measurements. *AAPG Bulletin* **86** (7), 1187-1200.
- Juhlin C., Giese R., Zinck-Jorgensen K., Cosma C., Kazemeini H., Juhonjuntti N., Luth S., Norden B., and Forster A. (2007) 3D baseline seismics at Ketzin, Germany: The CO₂ SINK project. *Geophysics* **72** (5), B121-B132.
- Kampman N., Bickle M., Becker J., Assayag N., and Chapman H. (2009) Feldspar dissolution kinetics and Gibbs free energy dependence in a CO₂-enriched groundwater system, Green River, Utah. *Earth and Planetary Science Letters* **284** (3-4), 473-488.
- Kaufman A. (1993) An evaluation of several methods for determining ages in impure carbonates. *Geochimica et Cosmochimica Acta* **57** (10), 2303-2317.
- Kaufman A., Wasserburg G. J., Porcelli D., Bar-Matthews M., Ayalon A., and Halicz L. (1998) U-Th isotope systematics from the Soreq cave, Israel and climatic correlations. *Earth and Planetary Science Letters* **156** (3-4), 141-155.
- Keller G. R. and Baldrige W. S. (1999) The Rio Grande rift: A geological and geophysical overview. *Rocky Mountain Geology* **34** (1), 121-130.
- Kench P. S., Smithers S. G., McLean R. F., and Nichol S. L. (2009) Holocene reef growth in the Maldives: Evidence of a mid-Holocene sea-level highstand in the central Indian Ocean. *Geology* **37** (5), 455-458.
- Khan D. K. and Rostron, B.J. . (2004) Regional hydrogeological investigation around the IEA Weyburn CO₂ monitoring and storage project site. In *Proceedings of the 7th International Conference on Greenhouse Gas Control Technologies (GHGT-7), Sept. 5-9, 2004, Volume 1* :Peer-Reviewed Papers and Plenary Sessions E. S. Rubin, D. W. Keith, and C. F. Gilboy (eds.), 741- 750. Elsevier, UK
- King C. Y., Basler D., Presser T. S., Evans W. C., White L. D., and Minissale A. (1994) In search of earthquake-related hydrologic and chemical changes along Hayward Fault. *Applied Geochemistry* **9** (1), 83-91.
- King C.-Y., Azuma S., Igarashi G., Ohno M., Saito H., and Wakita H. (1999) Earthquake-related water-level changes at 16 closely clustered wells in Tono, central Japan. *Journal of Geophysical Research* **104**, 13,073-13,082.
- Kitagawa Y., Fujimori K., and Koizumi N. (2007) Temporal change in permeability of the Nojima fault zone by repeated water injection experiments. *Tectonophysics* **443** (3-4), 183-192.
- Kitano Y. (1963) Geochemistry of calcareous deposits found in hot springs. *The Journal of earth sciences, Nagoya Univ* **11**, 68-100.
- Kluth C. F. (1986) Plate tectonics of the Ancestral Rocky Mountains. In *Paleotectonics and sedimentation in the Rocky Mountain region, United States*, **41** J. A. Peterson (ed.), 353-369. American Association of Petroleum Geologists Memoir.
- Kluth C. F. and Coney P. J. (1981) Plate tectonics of the Ancestral Rocky Mountains. *Geology* **9**, 10-15.
- Knight G. B. and Macklin R. L. (1948) Half-Life of (UX1) (Th234). *Physical Review* **74** (10), 1540.
- Knipe R. J. (1997) Juxtaposition and Seal Diagrams to Help Analyze Fault Seals in Hydrocarbon Reservoirs. *AAPG Bulletin* **81**, 187-195.
- Knipe R. J., Jones, G., Fisher, Q.J. (1998) Faulting, fault sealing and fluid flow in hydrocarbon reservoirs: an introduction. In *Faulting, Fault Sealing and Fluid Flow in Hydrocarbon Reservoirs*, **147** G. Jones, Fisher, Q.J., Knipe, R.J. (eds.), vii-xxi. Geological Society of London.
- Koledoye B. A., Aydin, A., May, E. (2003) A new process based methodology for the analysis of shale smear along normal faults in the Niger Delta. *AAPG Bulletin* **87** (3), 445- 463.
- Ku T. L., Knauss K. G., and Mathieu G. G. (1977) Uranium in open ocean: concentration and isotopic composition. *Deep Sea Research* **24** (11), 1005-1017.
- Ku T. L. (1965) An evaluation of the U234/U238 method as a tool for dating pelagic sediments. *Journal of Geophysical Research* **70**, 3457-74.

- Kuecher G. J., Roberts H. H., Thompson M. D., and Matthews I. (2001) Evidence for Active Growth Faulting in the Terrebonne Delta Plain, South Louisiana: Implications for Wetland Loss and the Vertical Migration of Petroleum. *Environmental Geosciences* **8** (2), 77-94.
- Kumar M. B. (1977) Geothermal and geopressure of Bayou Carlin- Lake Sand area, south Louisiana. *AAPG Bulletin* **61**, 65- 78.
- Kutzbach J. E., P. J. Guetter, P. J. Behling & R. Selin. (1993) Simulated climatic changes: results of the COHMAP climate-model experiments. In *Global climates since the Last Glacial Maximum* H. E. J. Wright, J. E. Kutzbach, T. Webb III, W. F. Ruddiman, F. A. Street-Perrott, and P. J. Bartlein (eds.), 24–93. University of Minnesota Press.
- Lafortune S., Moreira M., Agrinier P., Bonneville A., Schneider H., and Catalette H. (2009) Noble gases as tools for subsurface monitoring of CO₂ leakage. *Energy Procedia* **1** (1), 2185-2192.
- Lally A. E. (1982) Chemical procedures. In *Uranium-Series Disequilibrium. Applications to Environmental Problems* M. Ivanovich and R. S. Harmon (eds.), 79-106. Oxford University Press.
- Langmuir D. (1978) Uranium solution-mineral equilibria at low temperatures with applications to sedimentary ore deposits. *Geochimica et Cosmochimica Acta* **42** (6, Part 1), 547-569.
- Lee D. K., Doolittle J. J., and Owens V. N. (2006) Soil carbon dioxide fluxes in established switchgrass land managed for biomass production. *Soil Biology and Biochemistry* **39** (1), 178-186.
- Lee Y.-J., Morse J. W., and Wiltschko D. V. (1996) An experimentally verified model for calcite precipitation in veins. *Chemical Geology* **130** (3-4), 203-215.
- Lee Y.-J. and Morse J. W. (1999) Calcite precipitation in synthetic veins: implications for the time and fluid volume necessary for vein filling. *Chemical Geology* **156** (1-4), 151-170.
- Leeder M. R., McNeill L. C., Li Collier R. E., Portman C., Rowe P. J., Andrews J. E., and Gawthorpe R. L. (2003) Corinth rift margin uplift: New evidence from Late Quaternary marine shorelines. *Geophys. Res. Lett.* **30**.
- Leeder M. R., Portman C., Andrews J. E., Collier R. E. L., Finch E., Gawthorpe R. L., McNeill L. C., Perez-Arlucea M., and Rowe P. (2005) Normal faulting and crustal deformation, Alkyonides Gulf and Perachora peninsula, eastern Gulf of Corinth rift, Greece. *Journal of the Geological Society* **162** (3), 549-561.
- Levinson A. A. (1980) *Introduction to exploration geochemistry*. Applied Publishing Ltd.
- Li G. and Riding, R. (1999) Rapid facies changes in Holocene fissure ridge hot spring travertines, Rapolano Terme, Italy. *Sedimentology* **46** (6), 1145-1158.
- Ligtenberg J. H. (2005) Detection of fluid migration pathways in seismic data: implications for fault seal analysis. *Basin Research* **17** (1), 141-153.
- Lin G., Nunn, J. A. (1997) Evidence for recent migration of geopressured fluids along faults in Eugene Island, Block 330, offshore Louisiana, from estimates of pore water salinity. *Gulf Coast Association of Geological Societies Transactions* **47**, 419- 424.
- Lisiecki L. and Raymo M. (2005) A Pliocene-Pleistocene stack of 57 globally distributed benthic $\delta^{18}\text{O}$ records. *Paleoceanography* **20**, PA1003.
- Liu W., and Manga, M. (2009) Changes in permeability caused by dynamic stresses in fractured sandstone. *Geophys. Res. Lett.* **36**.
- Livnat A. and Kronfeld J. (1985) Paleoclimatic implications of U-series dates for lake sediments and travertines in the Arava Rift Valley, Israel. *Quaternary Research* **24** (2), 164-172.
- Long A., Warneke L. A., Betancourt J. L., and Thompson R. S. (1990) Deuterium variations in plant cellulose from fossil packrat middens. In *Packrat Middens: The Last 10,000 Years of Biotic Change* J. L. Betancourt, T. R. Van Devender, and P. S. Martin (eds.), 380-396. University of Arizona press.
- Lopez D. L. and Smith L. (1995) Fluid flow in fault zones: Analysis of the interplay of connective circulation and topography driven groundwater flow *Water resources research* **31** (6), 1489-1503.
- Lopez D. L. and Smith L. (1996) Fluid flow in fault zones: Influence of hydraulic anisotropy and heterogeneity on the fluid flow transfer regime. *Water resources research* **32** (10), 3227-3235.
- Lorius C., Jouzel J., Ritz C., Merlivat L., Barkov N. I., Korotkevich Y. S., and Kotlyakov V. M. (1985) A 150,000-year climatic record from Antarctic ice. *Nature* **316** (6029), 591-596.

- Løseth H., Gading M., and Wensaas L. (2009) Hydrocarbon leakage interpreted on seismic data. *Marine and Petroleum Geology* **26** (7), 1304-1319.
- Losh S., Eglinton, L., Schoell, M., Wood, J. (1999) Vertical and lateral fluid flow related to a large growth fault, South Eugene Island Block 330 field, offshore Louisiana. *AAPG Bulletin* **83** (2), 244-276.
- Losh S., Haney, M. (2006) Episodic fluid flow in an aseismic overpressured growth fault, Northern Gulf of Mexico. In *Earthquakes: Radiated energy and the physics of faulting* R. Abercrombie, A. McGarr, G. D. Toro, and H. Kanamori (eds.), 199- 205. American Geophysical Union.
- Lowell R. P., Van Cappellen P., and Germanovich L. N. (1993) Silica Precipitation in Fractures and the Evolution of Permeability in Hydrothermal Upflow Zones. *Science* **260** (5105), 192-194.
- Ludwig K. R. (2001) Isoplot/Ex version 2.49. *Berkeley Geochronology Center Special Publication No. 1^a*, 55pp.
- Lund W. R., Taylor W. J., Pearthree P. A., Stenner H., Amoroso L., and Hurlow H. (2002) Structural development and paleoseismicity of the Hurricane fault, south-western Utah and north-western Arizona. *2002 Rocky Mountain Section Annual Meeting*.
- Lund W. R., Hozik M. J., and Hatfield S. C. (2007) Paleoseismic investigation and long-term slip history of the Hurricane fault in south-western Utah. *Paleoseismology of Utah* **14** (Special study 119).
- Lunn R. J., Shipton, Z. K. and Bright, A. M. (2008) How can we improve estimates of bulk fault zone hydraulic properties? . In *The Internal Structure of Fault Zones: Implications for Mechanical and Fluid-Flow Properties*, **299** C. A. J. Wibberley, W. Kurz, J. Imber, R.E. Holdsworth and C. Collettini (eds.), Geological Society, Special Publication.
- Luo X., Rehkämper M., Lee D.-C., and Halliday A. N. (1997) High precision ²³⁰Th/²³²Th and ²³⁴U/²³⁸U measurements using energy filtered ICP magnetic sector multiple collector mass spectrometry. *International Journal of Mass Spectrometry and Ion Processes* **171** (1-3), 105-117.
- Machette M. N. (1986) History of quaternary offset and paleoseismicity along the La Jencia fault, central Rio Grande rift, New Mexico. *Bulletin of the Seismological Society of America* **76** (1), 259-272.
- Machette M. N., Personius S. F., Kelson K. I., Haller K. M., and Dart R. L. (1998) Map and data for Quaternary faults in New Mexico. In *U.S. Geol. Surv. Open-File Rept.*, pp. 98-521, 443 pp.
- Malkovsky V. I., Pek, A.A. (2004) Timescales for reaching steady-state fluid flow in systems perturbed by formation of highly permeable faults. *Geofluids* **4**, 253-258.
- Mallick R. and Frank N. (2002) A new technique for precise uranium-series dating of travertine micro-samples. *Geochimica et Cosmochimica Acta* **66** (24), 4261-4272.
- Manga M., and Wang, C.-Y. . (2007) Earthquake hydrology. In *Treatise on Geophysics*, **4** G. Schubert (ed.), 293-320.
- Manga M., and Rowland, J.C. (2009) Response of Alum Rock springs to the October 30, 2007 earthquake and implications for the origin of increased discharge after earthquakes. *Geofluids* **9**, 237-250.
- Manzocchi T., Walsh, J.J., Nell, P., Yielding, G. (1999) Fault transmissibility multipliers for flow simulation models. *Petroleum Geoscience* **5**, 53-63.
- Manzocchi T., Heath, A.E., Walsh, J.J., Childs, C. (2002) The representation of two phase fault-rock properties in flow simulation models. *Petroleum Geoscience* **8**, 119-132.
- Manzocchi T., Heath, A.E., Palanathakumar, B., Childs, C., Walsh, J.J. (2008) Faults in conventional flow simulation models: a consideration of representational assumptions and geological uncertainties. *Petroleum Geoscience* **14**, 91-100.
- Marchetti D. W., Dohrenwend J. C., and Cerling T. E. (2005) Geomorphology and rates of landscape change in the Fremont River drainage, north-western Colorado Plateau. *Field Guides* **6**, 79-100.
- Marks J. C., Parnell R., Carter C., Dinger E. C., and Haden G. A. (2006) Interactions between geomorphology and ecosystem processes in travertine streams: Implications for decommissioning a dam on Fossil Creek, Arizona. *Geomorphology* **77** (3-4), 299-307.

- Martel S. J. and Boger W. A. (1998) Geometry and mechanics of secondary fracturing around small three-dimensional faults in granitic rock. *J. Geophys. Res.* **103**, 21299-21314.
- Martinson D. G., Pisias N. G., Hays J. D., Imbrie J., Moore T. C., and Shackleton N. J. (1987) Age dating and the orbital theory of the ice ages: Development of a high-resolution 0 to 300,000-year chronostratigraphy. *Quaternary Research* **27** (1), 1-29.
- Mathieson A., Wright I., Roberts D., and Ringrose P. (2009) Satellite imaging to monitor CO₂ movement at Krechba, Algeria. *Energy Procedia* **1** (1), 2201-2209.
- McCalpin J. P. (1996) *Paleoseismology*. Academic Press.
- McCalpin J. P. (2000) Paleoseismicity of Quaternary faults near Albuquerque, New Mexico. In *Annual project summary*. GEO-HAZ Consulting, Inc.
- McCalpin J. P. (2005) Late Quaternary activity of the Pajarito fault, Rio Grande rift of northern New Mexico, USA. *Tectonophysics* **408** (1-4), 213-236.
- McCalpin J. P. and Nishenko S. P. (1996) Holocene paleoseismicity, temporal clustering, and probabilities of future large ($M > 7$) earthquakes on the Wasatch fault zone, Utah. *J. Geophys. Res.* **101**.
- McCalpin J. P. and Nelson C. V. (2001) Paleoearthquake chronology of the SLC segment of the Wasatch fault since 15 ka, and probability of the "big one" in the next 100 years. *Program with Abstracts: Geological Hazards in Utah: Practical Information for Geologists and Engineers*, ASCE, 17-18.
- McKnight E. T. (1940) Geology of the area between Green and Colorado rivers, Grand and San Juan counties, Utah. *U. S. Geological Survey Bulletin*, **908**.
- McNeill L. C. and Collier R. E. L. (2004) Uplift and slip rates of the eastern Eliko fault segment, Gulf of Corinth, Greece, inferred from Holocene and Pleistocene terraces. *Journal of the Geological Society* **161** (1), 81-92.
- Meinzer O. E. (1923) The occurrence of groundwater in the United States, with a discussion of principles. *U. S. Geological Survey Water-Supply* **489**.
- Merz-Preiß M. and Riding R. (1999) Cyanobacterial tufa calcification in two freshwater streams: ambient environment, chemical thresholds and biological processes. *Sedimentary Geology* **126** (1-4), 103-124.
- Meyer H. J. (1984) The influence of impurities on the growth rate of calcite. *Journal of Crystal Growth* **66** (3), 639-646.
- Michael K., Golab A., Shulakova V., Ennis-King J., Allinson G., Sharma S., and Aiken T. Geological storage of CO₂ in saline aquifers-A review of the experience from existing storage operations. *International Journal of Greenhouse Gas Control*, In Press, Corrected Proof (due for publication March 2010).
- Micklethwaite S. and Cox S. F. (2004) Fault-segment rupture, aftershock-zone fluid flow, and mineralization. *Geology* **32** (9), 813-816.
- Micklethwaite S. and Cox S. F. (2006) Progressive fault triggering and fluid flow in aftershock domains: Examples from mineralized Archaean fault systems. *Earth and Planetary Science Letters* **250** (1-2), 318-330.
- Miller S. A., Colletini C., Chiaraluce L., Cocco M., Barchi M., and Kaus B. J. P. (2004) Aftershocks driven by a high-pressure CO₂ source at depth. *Nature* **427** (6976), 724-727.
- Minissale A., Kerrick D. M., Magro G., Murrell M. T., Paladini M., Rihs S., Sturchio N. C., Tassi F., and Vaselli O. (2002) Geochemistry of Quaternary travertines in the region north of Rome (Italy): structural, hydrologic and paleoclimatic implications. *Earth and Planetary Science Letters* **203** (2), 709-728.
- Mohammed H. (1986) Geology of active uranium mines during 1982 in parts of the Paradox Basin, south-eastern Utah: A preliminary report, pp. 49. Utah Geological and Mineral Survey Open-file report 89.
- Montagna P., McCulloch M., Mazzoli C., Silenzi S., and Odorico R. (2007) The non-tropical coral *Cladocora caespitosa* as the new climate archive for the Mediterranean: high-resolution (~weekly) trace element systematics. *Quaternary Science Reviews* **26** (3-4), 441-462.

- Moore J., M. Adams, R. Allis, S. Lutz, and S. Rauzi. (2005) Mineralogical and geochemical consequences of the long-term presence of CO₂ in natural reservoirs: An example from the Springerville–St. Johns Field, Arizona, and New Mexico, U.S.A. *Chemical Geology* **217**, 365- 385.
- Moran S. B., Shen C. C., Edmonds H. N., Weinstein S. E., Smith J. N., and Edwards R. L. (2002) Dissolved and particulate ²³¹Pa and ²³⁰Th in the Atlantic Ocean: constraints on intermediate/deep water age, boundary scavenging, and ²³¹Pa/²³⁰Th fractionation. *Earth and Planetary Science Letters* **203** (3-4), 999-1014.
- Morewood N. C. and Roberts G. P. (1999) Lateral propagation of the surface trace of the South Alkyonides normal fault segment, central Greece: its impact on models of fault growth and displacement-length relationships. *Journal of Structural Geology* **21** (6), 635-652.
- Morgan C. D., McClure, K, Chidsey, T.C., Eby, D.E. (2007) The Mississippian Leadville Limestone exploration play, Utah and Colorado- exploration techniques and studies for independents. In *Deliverable 1-4 field maps and cross sections: Lisbon Field, San Juan County, Utah*, pp. 13. Utah Geological Survey.
- Mörner N.-A. and Etiope G. (2002) Carbon degassing from the lithosphere. *Global and Planetary Change* **33** (1-2), 185-203.
- Morrison S. J. and Parry W. T. (1988) Age and formation conditions of alteration associated with a collapse structure, Temple Mountain uranium district, Utah. *Geological Society of America Bulletin* **100** (7), 1069-1077.
- Morse J. W. and Mackenzie F. T. (1993) Geochemical constraints on CaCO₃ transport in subsurface sedimentary environments. *Chemical Geology* **105** (1-3), 181-196.
- Morton R. A., Land, L. S. (1987) Regional variations in formation water chemistry, Frio formation (Oligocene), Texas Gulf Coast. *AAPG Bulletin* **71** (2), 191- 206.
- Moucha R., Forte A. M., Rowley D. B., Mitrovica J. X., Simmons N. A., and Grand S. P. (2009) Deep mantle forces and the uplift of the Colorado Plateau. *Geophys. Res. Lett.* **36**, L19310, 6pp.
- Mualem Y. (1976) A new model for predicting the hydraulic conductivity of unsaturated porous media. *Water Resources Research* **12** (3), 513-522.
- Muir Wood R. and King G. C. P. (1993) Hydrological signatures of earthquake strain. *Journal of Geophysical Research* **98**, 22035-22068.
- Muir Wood R. (1994) Earthquakes, strain-cycling and the mobilization of fluids. *Geological Society, London, Special Publications* **78** (1), 85-98.
- Muir Wood R. K., and Geoffrey C. P. (1993) Hydrological signatures of earthquake strain. *Journal of Geophysical Research* **98**, 22035-22068.
- Müller N., Ramakrishnan T. S., Boyd A., and Sakruai S. (2007) Time-lapse carbon dioxide monitoring with pulsed neutron logging. *International Journal of Greenhouse Gas Control* **1** (4), 456-472.
- Naftz D. L., Peterman Z. E., and Spangler L. E. (1997) Using $\delta^{87}\text{Sr}$ values to identify sources of salinity to a freshwater aquifer, Greater Aneth Oil Field, Utah, USA. *Chemical Geology* **141** (3-4), 195-209.
- Nascimento A. F. D., Lunn R.J. and Cowie, P. (2005a) 3D numerical modelling of reservoir-induced seismicity: the impact of fault heterogeneity. *Journal of Geophysical Research* **110**.
- Nascimento A. F. D., Lunn R.J. and Cowie, P. (2005b) Numerical modelling of pore-pressure diffusion in a reservoir-induced seismicity site in NE Brazil. *Geophysical Journal International* **160**, 249- 262.
- Nihous G. C., Masutani S. M., Vega L. A., and Kinoshita C. M. (1994) Projected impact of deep ocean carbon dioxide discharge on atmospheric CO₂ concentrations. *Climatic Change* **27** (2), 225-244.
- Nuccio V. F., and Condon, S. M. (1996) Burial and Thermal History of the Paradox Basin, Utah and Colorado, and Petroleum Potential of the Middle Pennsylvanian Paradox Formation. *Evolution of Sedimentary Basins-Paradox Basin: U.S. Geological Survey Bulletin* **2000-O**, pp19.
- Nur A., and Walder, J. (1992) Hydraulic pulses in the Earth's crust. In *Fault Mechanics and Transport Properties of Rocks* B. Evans and T. F. Wong (eds.), pp 461-473. Academic Press Ltd.

- O'Brien G. R., Kaufman D. S., Sharp W. D., Atudorei V., Parnell R. A., and Crossey L. J. (2006) Oxygen isotope composition of annually banded modern and mid-Holocene travertine and evidence of paleomonsoon floods, Grand Canyon, Arizona, USA. *Quaternary Research* **65** (3), 366-379.
- Oda M., Hatsuyama, Y., Ohnishi, Y. (1987) Numerical experiments on permeability tensor and its application to jointed granite at Stripa mine, Sweden. *Journal of Geophysical Research* **92**, 8037-8048.
- Okada Y. (1992) Internal deformation due to shear and tensile faults in a half-space. *Bulletin of the Seismological Society of America* **82** (2), 1018-1040.
- Omura A., Maeda Y., Kawana T., Siringan F. P., and Berdin R. D. (2004) U-series dates of Pleistocene corals and their implications to the paleo-sea levels and the vertical displacement in the Central Philippines. *Quaternary International* **115-116**, 3-13.
- Onuma T. and Ohkawa S. (2009) Detection of surface deformation related with CO₂ injection by DInSAR at In Salah, Algeria. *Energy Procedia* **1** (1), 2177-2184.
- Osmond J. K. and Cowart J. B. (1982) Ground water. In *Uranium-Series Disequilibrium. Applications to Environmental Problems* Ivanovich, M. and Harmon, R.S. (eds.), 202-245. Oxford University Press.
- Pawar R. J., Warpinski N. R., Lorenz J. C., Benson R. D., Grigg R. B., Stubbs B. A., Stauffer P. H., Krumhansl J. L., Cooper S. P., and Svec R. K. (2006) Overview of a CO₂ sequestration field test in the West Pearl Queen reservoir, New Mexico. *Environmental Geosciences* **13** (3), 163-180.
- Pearce J. M., Nador A., and Toth E. (2002) Living with CO₂: Experiences from Hungary. *Greenhouse Issues* **58**.
- Pederson, J. L., Mackley, R. D. & Eddleman, J. L. (2002) Colorado Plateau uplift and erosion evaluated using GIS. *GSA Today* **12**, 4-10.
- Peirano A., Morri C., Bianchi C. N., Aguirre J., Antonioli F., Calzetta G., Carobene L., Mastronuzzi G., and Orrù P. (2004) The Mediterranean coral *Cladocora caespitosa*: a proxy for past climate fluctuations? *Global and Planetary Change* **40** (1-2), 195-200.
- Pentecost A. (1995a) The quaternary travertine deposits of Europe and Asia Minor. *Quaternary Science Reviews* **14** (10), 1005-1028.
- Pentecost A. (1995b) Geochemistry of carbon dioxide in six travertine-depositing waters of Italy. *Journal of Hydrology* **167** (1-4), 263-278.
- Pentecost A., Jones, B., Renaut, R. W. (2003) What is a hot spring? *Canadian Journal of Earth Sciences* **40** (11), 1443-1446.
- Pentecost A. (2005a) Hot springs, thermal springs and warm springs. What's the difference? *Geology Today* **21** (6), 222-224.
- Pentecost A. (2005b) *Travertine*. Springer-Verlag, Berlin Heidelberg.
- Personius S. F. and Mahan S. A. (2003) Paleoearthquakes and Eolian-Dominated Fault Sedimentation along the Hubbell Spring Fault Zone near Albuquerque, New Mexico. *Bulletin of the Seismological Society of America* **93** (3), 1355-1369.
- Peterson P. R. (1973) Salt Wash field. *Utah Geological Survey oil and gas field studies* **4** (3).
- Petit J.-P., Wibberley C. A. J., and Ruiz G. (1999) 'Crack-seal', slip: a new fault valve mechanism? *Journal of Structural Geology* **21** (8-9), 1199-1207.
- Petit J. R., Jouzel J., Raynaud D., Barkov N. I., Barnola J. M., Basile I., Bender M., Chappellaz J., Davis M., Delaygue G., Delmotte M., Kotlyakov V. M., Legrand M., Lipenkov V. Y., Lorius C., Pepin L., Ritz C., Saltzman E., and Stievenard M. (1999) Climate and atmospheric history of the past 420,000 years from the Vostok ice core, Antarctica. *Nature* **399** (6735), 429-436.
- Pingitore Jr N. E., Iglesias A., Lytle F., and Wellington G. M. (2002) X-Ray absorption spectroscopy of uranium at low ppm levels in coral skeletal aragonite. *Microchemical Journal* **71** (2-3), 261-266.
- Piper J. D. A., Mesci L. B., Gürsoy H., Tatar O., and Davies C. J. (2007) Palaeomagnetic and rock magnetic properties of travertine: Its potential as a recorder of geomagnetic palaeosecular variation, environmental change and earthquake activity in the Sıcak Çermik geothermal field, Turkey. *Physics of The Earth and Planetary Interiors* **161** (1-2), 50-73.

- Placzek C., Patchett P. J., Quade J., and Wagner J. D. M. (2006) Strategies for successful U-Th dating of paleolake carbonates: An example from the Bolivian Altiplano. *Geochem. Geophys. Geosyst.* **7**.
- Placzek C., Quade J., and Patchett P. J. (2006) Geochronology and stratigraphy of late Pleistocene lake cycles on the southern Bolivian Altiplano: Implications for causes of tropical climate change. *Geological Society of America Bulletin* **118** (5-6), 515-532.
- Polyak V. J., and Asmerom, Y. (2001) Late Holocene climate and cultural changes in the Southwestern United States. *Science* **294**, 148-151.
- Pope D., and Brough, C. . (1996) *Utah's Weather and Climate*. Publishers Press.
- Potter E.-K., Stirling C. H., Andersen M. B., and Halliday A. N. (2005) High precision Faraday collector MC-ICP-MS thorium isotope ratio determination. *International Journal of Mass Spectrometry* **247** (1-3), 10-17.
- Powell J. W. (1895) The Canyons of the Colorado. (now published as *The exploration of the Colorado River and its canyons*. Penguin Books 1997. 416 pages).
- Pratsch J.-C. (1991) Vertical hydrocarbon migration: A major exploration parameter. *Journal of Petroleum Geology* **14** (4), 429-444.
- Preston C., Monea M., Jazrawi W., Brown K., Whittaker S., White D., Law D., Chalaturnyk R., and Rostron B. (2005) IEA GHG Weyburn CO₂ monitoring and storage project. *Fuel Processing Technology* **86** (14-15), 1547-1568.
- Prevedel B., Wohlgemuth L., Legarth B., Henninges J., Schütt H., Schmidt-Hattenberger C., Norden B., Förster A., and Hurter S. (2009) The CO₂SINK boreholes for geological CO₂ -storage testing. *Energy Procedia* **1** (1), 2087-2094.
- Price N. J., Cosgrove, J. W. (1990) Analysis of geological structures, pp. 502pp. Cambridge University Press, Cambridge.
- Pruess K., and Garcia, J. (2002) Multiphase flow dynamics during CO₂ disposal into saline aquifers. *Environmental Geology* **42**, 282- 295.
- Pruess K. (2003) Numerical simulation of leakage from a geologic disposal reservoir for CO₂, with transitions between super- and sub-critical conditions. *Lawrence Berkeley National Laboratory. Paper*, LBNL-53016.
- Pruess K. (2004) The TOUGH Codes - A family of simulation tools for multiphase flow and transport processes in permeable media. *Vadose Zone Journal* **3**, 738- 746.
- Pruess K. (2005) Numerical studies of fluid leakage from a geologic disposal reservoir for CO₂ show self-limiting feedback between fluid flow and heat transfer. *Geophys. Res. Lett.* **32**.
- Przybyłowicz W., Schwarcz, H.P., and Latham, A.G. (1991) Dirty Calcites II: Uranium series dating of artificial detritus-calcite mixtures. *Chemical Geology (Isotope Geoscience)* **86**, 161-178.
- Rahmstorf S. (2003) Timing of abrupt climate change: A precise clock. *Geophys. Res. Lett.* **30** (10), 1510.
- Rawling G. C., Goodwin L. B., and Wilson J. L. (2001) Internal architecture, permeability structure, and hydrologic significance of contrasting fault zone types. *Geology* **29** (1), 43-46.
- Reading H. G. (1978) *Sedimentary Environments: Processes, Facies and Stratigraphy*. Blackwell Science Ltd.
- Reidy R. (2008) FEED finalised for Gorgon Project. *Pump Industry Analyst* **2008** (9), 4.
- Reiter M., J. Mansure A., and Shearer C. (1979) Geothermal characteristics of the colorado plateau. *Tectonophysics* **61** (1-3), 183-195.
- Renard F., Gratier J.-P., and Jamtveit B. (2000) Kinetics of crack-sealing, intergranular pressure solution, and compaction around active faults. *Journal of Structural Geology* **22** (10), 1395-1407.
- Richter F. M. and Turekian K. K. (1993) Simple models for the geochemical response of the ocean to climatic and tectonic forcing. *Earth and Planetary Science Letters* **119** (1-2), 121-131.
- Rice J. R., and Coco, M. (2007) Seismic fault rheology and earthquake dynamics. In *The dynamics of fault zones* Handy M. R., Hirth, G. and Hovious, N. (eds.), 99- 137. MIT Press.
- Riddiford F., Wright I., Bishop C., Espie T., Tourqui A., Rubin E. S., Keith D. W., Gilboy C. F., Wilson M., Morris T., Gale J., and Thambimuthu K. (2005) Monitoring geological storage the In

- Salah Gas CO₂ storage project. In *Greenhouse Gas Control Technologies 7*, 1353-1359. Elsevier Science Ltd.
- Ringrose P. S., Skjetne, E., Effenbein, C. (2003) Permeability estimation functions based on forward modelling of sedimentary heterogeneity. *SPE paper 84275*.
- Roberts G. P., Houghton S. L., Underwood C., Papanikolaou I., Cowie P. A., van Calsteren P., Wigley T., Cooper F. J., and McArthur J. M. (2009) Localization of Quaternary slip rates in an active rift in 105 years: An example from central Greece constrained by ²³⁴U-²³⁰Th coral dates from uplifted paleoshorelines. *J. Geophys. Res.* **114**.
- Roberts H. H., Sassen, R., Milkov, A. (2000) Seafloor expression of fluid and gas expulsion from deep petroleum systems, deepwater Gulf of Mexico. *SEPM 21st Annual Research Conference*, 401- 422.
- Roberts S. J., Nunn, J. A., Cathles, L. M., Cipriani, F. D. (1996) Expulsion of abnormally pressured fluids along faults. *Journal of Geophysical Research* **101**, 28,231- 28,252.
- Robinson L. F., Adkins J. F., Fernandez D. P., Burnett D. S., Wang S. L., Gagnon A. C., and Krakauer N. (2006) Primary U distribution in scleractinian corals and its implications for U series dating. *Geochem. Geophys. Geosyst.* **7** (5), 19pp.
- Rodolfo-Metalpa R., Peirano A., Houlbrèque F., Abbate M., and Ferrier-Pagès C. (2008) Effects of temperature, light and heterotrophy on the growth rate and budding of the temperate coral *Cladocora caespitosa*. *Coral Reefs* **27** (1), 17-25.
- Rojstaczer S., Galloway D. L., Ingebritsen S. E., and Rubin D. M. (2003) Variability in geyser eruptive timing and its causes: Yellowstone National Park. *Geophys. Res. Lett.* **30**.
- Rosholt J. N. (1982) Mobilization and weathering. In *Uranium-Series Disequilibrium. Applications to Environmental Problems* M. Ivanovich and R. S. Harmon (eds.), 167-180. Oxford University Press.
- Rowland J. C., Manga, M., Rose, T. P. (2008) The influence of poorly interconnected fault zone flow paths on spring geochemistry. *Geofluids* **8** (2), 93-101.
- Rubinstein J. L., Gomberg J., Vidale J. E., Wech A. G., Kao H., Creager K. C., and Rogers G. (2009) Seismic wave triggering of non-volcanic tremor, episodic tremor and slip, and earthquakes on Vancouver Island. *J. Geophys. Res.* **114**.
- Saller A. H. and Moore Jr C. H. (1989) Meteoric diagenesis, marine diagenesis, and microporosity in Pleistocene and Oligocene limestones, Enewetak Atoll, Marshall Islands. *Sedimentary Geology* **63** (3-4), 253-272.
- Scholtz C. H. and Krantz R. (1974) Notes on dilatation recovery. *Journal of Geophysical Research* **79**, 2132- 2135.
- Scholz C. H., and Anders, M.H. (1994) The permeability of faults. *The mechanical involvement of fluids in faulting: U.S Geological Survey Open-file report 94- 228*, 247- 253.
- Scholz C. H. (2002) *The Mechanics of Earthquakes and Faulting*. Cambridge University Press.
- Schroeder J. H., Miller D. S., and Friedman G. M. (1970) Uranium distributions in Recent skeletal carbonates. *Journal of Sedimentary Research* **40** (2), 672-681.
- Schulz S. E., and Evans, J.P. (1998) Spatial variability in microscopic deformation and composition of the Punchbowl fault, southern California: implications for mechanisms, fluid-rock interaction, and fault morphology. *Tectonophysics* **295**, 223-244.
- Schwarcz H. P. and Latham A. G. (1989) Dirty Calcites I: Uranium series dating of contaminated calcite using leachates alone. *Chemical Geology (Isotope Geoscience)* **80**, 35-43.
- Shen C.-C., Lawrence Edwards R., Cheng H., Dorale J. A., Thomas R. B., Bradley Moran S., Weinstein S. E., and Edmonds H. N. (2002) Uranium and thorium isotopic and concentration measurements by magnetic sector inductively coupled plasma mass spectrometry. *Chemical Geology* **185** (3-4), 165-178.
- Shen G. T. and Dunbar R. B. (1995) Environmental controls on uranium in reef corals. *Geochimica et Cosmochimica Acta* **59** (10), 2009-2024.
- Shipton Z. K., Evans J. P., Robeson K., Forster C. B. and Snelgrove S. (2002) Structural heterogeneity and permeability in faulted aeolian sandstone: implications for subsurface modelling of faults. *American Association of Petroleum Geologists Bulletin* **86** (863- 883).

- Shipton Z. K., Evans, J.P., Kirschner, D., Kolesar, P.T., Williams, A.P., and Heath, J. (2004) Analysis of CO₂ leakage through "low-permeability" faults from natural reservoirs in the Colorado Plateau, east-Central Utah. In *Geological Storage of Carbon Dioxide.*, Special Publications **233** S. J. Baines and R. H. Worden (eds.), 43-59. Geological Society.
- Shipton Z. K., Evans, J.P., Dockrill, B., Heath, J., Williams, A.P., Kirschner, D. and, Kolesar, P.T. (2005) Natural leaking CO₂-charged systems as analogues for failed geologic storage reservoirs. In *Carbon dioxide capture for storage in deep geological formations results from the CO₂ capture project, Volume Two: Geological storage of carbon dioxide with monitoring and verification* S. M. Benson, C. Oldenburg, M. Hoversten, and S. Imbus (eds.), 699-712. CO₂ Capture Project, Elsevier.
- Shipton Z. K., Evans, J. P. and Thompson L.B. (2006) The geometry and thickness of deformation band fault core, and its influence on sealing characteristics of deformation band fault zones. In *Faults, fluid flow and petroleum traps.*, **85** R. Sorkhabi, Tusuji, Y. (eds.), 181- 195. American Association of Petroleum Geologists Memoir
- Shipton Z. K. and Cowie P. A. (2001) Damage zone and slip-surface evolution over μm to km scales in high-porosity Navajo sandstone, Utah. *Journal of Structural Geology* **23** (12), 1825-1844.
- Shitashima K. (2008) Development of monitoring strategy for the assessment of Carbon Dioxide Capture and Storage (CCS). *AGU Fall Meeting Abstracts*.
- Shuman B., Bartlein P., Logar N., Newby P., and Webb T. (2002) Parallel climate and vegetation responses to the early Holocene collapse of the Laurentide Ice Sheet. *Quaternary Science Reviews* **21** (16-17), 1793-1805.
- Sibson R. H., McMoore, J., Rankin, A. H. (1975) Seismic pumping- a hydrothermal fluid transport mechanism. *Journal of the Geological Society of London* **131** (653- 659).
- Sibson R. H. (1977) Fault rocks and fault mechanisms. *Geological Society of London* **133**, 191-231.
- Sibson R. H. (1983) Continental fault structure and the shallow earthquake source. *Journal of the Geological Society* **140** (5), 741-767.
- Sibson R. H. (1985) A short note on fault reactivation. *Journal of Structural Geology* **7** (6), 751-754.
- Sibson R. H. (1987) Earthquake rupturing as a mineralizing agent in hydrothermal systems. *Geology* **15** (8), 701-704.
- Sibson R. H. (1990) Rupture nucleation of unfavourably orientated faults. *Bulletin of the Seismological Society of America* **80** (6), 1580-1604.
- Sibson R. H. (1992) Implications of fault-valve behaviour for rupture nucleation and recurrence. *Tectonophysics* **211** (1-4), 283-293.
- Sibson R. H. (1995) Selective fault reactivation during basin inversion: potential for fluid redistribution through fault-valve action. *Geological Society, London, Special Publications* **88** (1), 3-19.
- Siddall M., Rohling E. J., Almogi-Labin A., Hemleben C., Meischner D., Schmelzer I., and Smeed D. A. (2003) Sea-level fluctuations during the last glacial cycle. *Nature* **423** (6942), 853-858.
- Sieh K., Jones L., Hauksson E., Hudnut K., Eberhart-Phillips D., Heaton T., Hough S., Hutton K., Kanamori H., Lilje A., Lindvall S., McGill S. F., Mori J., Rubin C., Spotila J. A., Stock J., Thio H. K., Treiman J., Wernicke B., and Zachariasen J. (1993) Near-Field Investigations of the Landers Earthquake Sequence, April to July 1992. *Science* **260** (5105), 171-176.
- Silenzi S., Bard E., Montagna P., and Antonioli F. (2005) Isotopic and elemental records in a non-tropical coral (*Cladocora caespitosa*): Discovery of a new high-resolution climate archive for the Mediterranean Sea. *Global and Planetary Change* **49** (1-2), 94-120.
- Silliman S. E. and Wright A. L. (1988) Stochastic Analysis of Paths of High Hydraulic Conductivity in Porous Media. *Water Resour. Res.* **24** (11), 1901-1910.
- Simpson D. W., Leith W. S., and Scholz C. H. (1988) Two types of reservoir-induced seismicity. *Bulletin of the Seismological Society of America* **78** (6), 2025-2040.
- Smith L., Forster, C.B., Evans, J.P. (1990) Interaction of fault zones, fluid flow, and heat transfer at the basin scale. *Hydrogeology of permeability environments: International Association of Hydrogeologists* **2**, 41- 67.

- Smith R. B. and Sbar M. L. (1974) Contemporary Tectonics and Seismicity of the Western United States with Emphasis on the Intermountain Seismic Belt. *Geological Society of America Bulletin* **85** (8), 1205-1218.
- Smith D. H. (2004) MM&V Studies at West Pearl Queen Carbon Sequestration Pilot Site. *American Geophysical Union, Fall Meeting 2004*, GC54A-03.
- Smouse D. (1993) Salt Wash. In *Oil and gas fields of Utah*, **22** B. G. Hill and Bereskin, S.R. (eds). Utah Geological Association Publication.
- Spear J. R., Figueroa L. A., and Honeyman B. D. (1999) Modeling the removal of uranium U(VI) from aqueous solutions in the presence of sulfate reducing bacteria. *Environmental Science & Technology* **33** (15), 2667-2675.
- Sperner B., Muller B., Heidback O., Delvaux D., Reinecker J., and Fuchs K. (2003) Tectonic stress in the Earth's Crust: advances in the World Stress Map Project. In *New Insights in Structural Interpretation and Modelling, Geological Society Special Publication*, **212** D. Nieuwland (ed.), 101-116.
- Srivastava R. K., Huang, S.S., Dong M. . (2000) Laboratory investigation of Weyburn CO₂ miscible flooding. *Journal of Canadian Petroleum Technology* **39** (2), 41-51.
- Stalker L., Boreham C., Underschultz J., Freifeld B., Perkins E., Schacht U., and Sharma S. (2009) Geochemical monitoring at the CO₂CRC Otway Project: Tracer injection and reservoir fluid acquisition. *Energy Procedia* **1** (1), 2119-2125.
- Stark M. A. and Davis S. D. (1996) Remotely Triggered Microearthquakes at the Geysers Geothermal Field, California. *Geophys. Res. Lett.* **23**.
- Stein M., Wasserburg G. J., Lajoie K. R., and Chen J. H. (1991) U-series ages of solitary corals from the California coast by mass spectrometry. *Geochimica et Cosmochimica Acta* **55** (12), 3709-3722.
- Stein M., Wasserburg G. J., Aharon P., Chen J. H., Zhu Z. R., Bloom A., and Chappell J. (1993) TIMS U-series dating and stable isotopes of the last interglacial event in Papua New Guinea. *Geochimica et Cosmochimica Acta* **57** (11), 2541-2554.
- Stein S., and Wysession, M. (2003) *An Introduction to Seismology, Earthquakes and Earth Structure* Blackwell publishing.
- Streit J. E. and Hillis R. R. (2003) Building Geomechanical Models for the Safe Underground Storage of Carbon Dioxide in Porous Rock. In *Greenhouse Gas Control Technologies - 6th International Conference* J. Gale and Y. Kaya (eds.), 495-500. Pergamon.
- Streit J. E. and Watson M. N. (2004) Estimating Rates of Potential CO₂ Loss from Geological Storage Sites for Risk and Uncertainty Analysis (paper 152). *7th International Conference on Greenhouse Gas Control Technologies*.
- Streit J., Siggins A., and Evans B. (2005) Predicting and monitoring geomechanical effects of CO₂ injection, Carbon Dioxide Capture for Storage in Deep Geologic Formations. In *Results from the CO₂ Capture Project, v.2: Geologic Storage of Carbon Dioxide with Monitoring and Verification* S. M. Benson (ed.), 751-766. Elsevier Science.
- Stevenson G. M. and Baars D. L. (1986) The Paradox; a pull-apart basin of Pennsylvanian age. In *Paleotectonics and sedimentation in the Rocky Mountain region, United States*, **41** J. A. Peterson (ed.), 513-539. American Association of Petroleum Geologists Memoir.
- Stirling C. H. and Andersen M. B. (2009) Uranium-series dating of fossil coral reefs: Extending the sea-level record beyond the last glacial cycle. *Earth and Planetary Science Letters* **284** (3-4), 269-283.
- Stirling C. H., Esat T. M., Lambeck K., McCulloch M. T., Blake S. G., Lee D. C., and Halliday A. N. (2001) Orbital Forcing of the Marine Isotope Stage 9 Interglacial. *Science* **291** (5502), 290-293.
- Stirling C. H., Esat T. M., McCulloch M. T., and Lambeck K. (1995) High-precision U-series dating of corals from Western Australia and implications for the timing and duration of the Last Interglacial. *Earth and Planetary Science Letters* **135** (1-4), 115-130.
- Stone H. L. (1970) Probability model for estimating three-phase relative permeability. *Journal of Petroleum Technology* **22**, 212-215.
- Stone H. L. (1973) Estimation of three-phase relative permeability and residual oil data. *Journal of Canadian Petroleum Technology* **12**, 53-61.

- Sun H. and Liu Z. (2010) Wet-dry seasonal and spatial variations in the $\delta^{13}\text{C}$ and $\delta^{18}\text{O}$ values of the modern endogenic travertine at Baishuitai, Yunnan, SW China and their paleoclimatic and paleoenvironmental implications. *Geochimica et Cosmochimica Acta* **74** (3), 1016-1029.
- Suzuki Y. and Banfield J. F. (1999) Geomicrobiology of uranium. *Reviews in Mineralogy and Geochemistry* **38** (1), 393-432.
- Swart P. K. and Hubbard J. A. E. B. (1982) Uranium in scleractinian coral skeletons. *Coral Reefs* **1** (1), 13-19.
- Szabo B. J. (1990) Ages of travertine deposits in eastern Grand Canyon National Park, Arizona. *Quaternary Research* **34** (1), 24-32.
- Szabo B. J., Carr W. J., and Gottschall W. C. (1981a) Uranium-thorium dating of quaternary carbonate accumulations in the Nevada Test Site region, southern Nevada. In *U.S. Geological Survey Open-File Report 81-119*, 35pp.
- Szabo B. J., Miller G. H., Andrews J. T., and Stuiver M. (1981b) Comparison of uranium-series, radiocarbon, and amino acid data from marine molluscs, Baffin Island, Arctic Canada. *Geology* **9** (10), 451-457.
- Szabo B.J. and Rosholt J. N. (1982) Surficial continental sediments. In *Uranium Series Disequilibrium: Application to Environmental Problems* M. I. a. R. S. Harmon (ed.), 246-262. Oxford Univ. Press.
- Szabo B. J., Bush C. A., and Benson L. V. (1996) Uranium-series dating of carbonate (tufa) deposit associated with Quaternary fluctuations of Pyramid Lake, Nevada. *Quaternary Research* **45** (3), 271-281.
- Talwani P. (2000) Seismogenic properties of the crust inferred from recent studies of reservoir-induced seismicity - Application to Koyna. *Current Science* **79**, 1327-1333.
- Teanby N., Kendall, J.-M., Jones, R. H., Barkved, O. (2004) Stress-induced temporal variations in seismic anisotropy observed in microseismic data. *Geophysical Journal International* **156**, 459-466.
- Thompson R. S. (1990) Late Quaternary vegetation and climate in the Great Basin. In *Packrat Middens: The Last 10,000 Years of Biotic Change* J. L. Betancourt, T. R. Van Devender, and P. S. Martin (eds.), 200-239. University of Arizona press.
- Thompson R. S., Whitlock C., Bartlein P. J., Harrison S. P., and Spaulding W. G. (1993) Chapter 18: Climatic changes in the western United States since 18,000 yr B.P. In *Global Climates since the last glacial maximum* H. E. Wright, J. E. Kutzbach, T. Webb, W. F. Ruddiman, F. A. Street-Perrott, and P. J. Bartlien (eds.), 468-513. University of Minnesota Press.
- Thompson W. G. (2010) Strategies for the treatment of coral age data in the reconstruction of sea-level change. *Geochimica et Cosmochimica Acta* **74** (11), 1044.
- Thurber D. L. (1962) Anomalous U234/U238 in Nature. *J. Geophys. Res.* **67** (11), 4518-4520.
- Trimble L. M., and Doelling, H.H. (1978) Geology and uranium-vanadium deposits of the San Rafael River mining area. *Utah Geological and Mineral Survey Bulletin* **113**.
- U.S. Geological Survey and Utah Geological Survey (2007) Quaternary fault and fold database for the United States, accessed June 9, 2007, from USGS web site: <http://earthquake.usgs.gov/regional/qfaults/>.
- Underschultz J. (2007) Hydrodynamics and membrane seal capacity. *Geofluids* **7** (2), 148-158.
- University Of Utah. (2004, June 1st) Quake in Alaska changed Yellowstone geysers. *Science Daily* Retrieved February 26, 2009, from <http://www.sciencedaily.com/releases/2004/05/040527235046.htm>.
- Uysal I. T., Feng Y., Zhao J.-x., Altunel E., Weatherley D., Karabacak V., Cengiz O., Golding S. D., Lawrence M. G., and Collerson K. D. (2007) U-series dating and geochemical tracing of late Quaternary travertine in co-seismic fissures. *Earth and Planetary Science Letters* **257** (3-4), 450-462.
- Uysal I. T., Feng Y.-x., Zhao J.-x., Isik V., Nuriel P., and Golding S. D. (2009) Hydrothermal CO₂ degassing in seismically active zones during the late Quaternary. *Chemical Geology* **265** (3-4), 442-454.

- van Calsteren P. and Thomas L. (2006) Uranium-series dating applications in natural environmental science. *Earth-Science Reviews* **75** (1-4), 155-175.
- van der Zee W. (2002) Dynamics of fault gouge development in layered sand clay sequences, pp. 155pp. RWTH Aachen University, Shaker Verlag GmbH, Aachen.
- Van Noorden R. (2010) Buried trouble. *Nature* **463** (7283), 871-873.
- Van Rensbergen P., Rabaute A., Colpaert A., Ghislain T., Mathijs M., and Bruggeman A. (2007) Fluid migration and fluid seepage in the Connemara Field, Porcupine Basin interpreted from industrial 3D seismic and well data combined with high-resolution site survey data. *International Journal of Earth Sciences* **96** (1), 185-197.
- Vargaftik N. B. (1975) *Tables on the Thermophysical Properties of Liquids and Gases, 2nd Ed.* John Wiley & Sons.
- Veeh H. H., and Burnett, W.C. (1982) Carbonate and phosphate sediments. In *Uranium-Series Disequilibrium. Applications to Environmental Problems* M. Ivanovich and R. S. Harmon (eds.), 459-480. Oxford University Press.
- Viles H. A. and Goudie A. S. (1990) Tufas, travertines and allied carbonate deposits. *Progress in Physical Geography* **14** (1), 19-41.
- Vodnik D., Videmsek U., Pintar M., Macek I., and Pfanz H. (2009) The characteristics of soil CO₂ fluxes at a site with natural CO₂ enrichment. *Geoderma* **150** (1-2), 32-37.
- Vrolijk P., Myers R., Sweet M. L., Shipton Z. K., Dockrill B., Evans J. P., Heath J., and Williams A. P. (2005) Anatomy of reservoir-scale normal faults in central Utah: Stratigraphic controls and implications for fault zone evolution and fluid flow. *Field Guides* **6**, 261-282.
- Waelbroeck C., Labeyrie L., Michel E., Duplessy J. C., McManus J. F., Lambeck K., Balbon E., and Labracherie M. (2002) Sea-level and deep water temperature changes derived from benthic foraminifera isotopic records. *Quaternary Science Reviews* **21** (1-3), 295-305.
- Warren L. A., Maurice P. A., Parmar N., and Ferris F. G. (2001) Microbially Mediated Calcium Carbonate Precipitation: Implications for Interpreting Calcite Precipitation and for Solid-Phase Capture of Inorganic Contaminants. *Geomicrobiology Journal* **18** (1), 93-115.
- Watts N. L. (1987) Theoretical aspects of cap-rock and fault seals for single- and two-phase hydrocarbon columns. *Marine and Petroleum Geology* **4** (4), 274-307.
- Weber K., Mandl G., Pilaar, W., Lehner, F., Precious, R. (1978) The role of faults in hydrocarbon migration and trapping in Nigerian growth fault structures. *Tenth Annual Offshore Technology Conference Proceedings*, 2643- 2653.
- Wehmiller J. F., Simmons K. R., Cheng H., Lawrence Edwards R., Martin-McNaughton J., York L. L., Krantz D. E. D. E., and Shen C.-C. (2004) Uranium-series coral ages from the US Atlantic Coastal Plain-the "80 ka problem" revisited. *Quaternary International* **120** (1), 3-14.
- Wibberley C. A. J., Yielding G., and Di Toro G. (2008) Recent advances in the understanding of fault zone internal structure: a review. *Geological Society, London, Special Publications* **299** (1), 5-33.
- Wilkinson M., Gilfillan, S.M., Haszeldine, S.R., Ballentine, C.J. (2008) Plumbing the depths: Testing natural tracers of subsurface CO₂ origin and migration, Utah, USA. In *Carbon dioxide sequestration in geological media* **59** J. C. M. Grobe, Pashin, and R. L., Dodge (eds.). AAPG Studies.
- Williams P. L. (1964) Geology, structure, and uranium deposits of the Moab Quadrangle, Colorado and Utah. *U. S. Geological Survey Map*, I- 360.
- Williams P. L. and Hackman R. J. (1971) Geology, structure, and uranium deposits of the Salina Quadrangle, Utah. *U. S. Geological Survey Map*, I-591.
- Winograd I. J., Coplen T. B., Landwehr J. M., Riggs A. C., Ludwig K. R., Szabo B. J., Kolesar P. T., and Revesz K. M. (1992) Continuous 500,000-Year Climate Record from Vein Calcite in Devils Hole, Nevada. *Science* **258** (5080), 255-260.
- Wiprut D., Zoback, M. D. (2000) Fault reactivation and fluid flow along a previously dormant normal fault in the northern North Sea. *Geology* **28** (7), 595- 598.
- Wong I. G., and Humphrey, J.R. (1989) Contemporary seismicity, faulting and the state of stress in the Colorado Plateau. *GSA Bulletin* **101**, 1127- 1146.

- Wurster C. M., Patterson W. P., McFarlane D. A., Wassenaar L. I., Hobson K. A., Athfield N. B., and Bird M. I. (2008) Stable carbon and hydrogen isotopes from bat guano in the Grand Canyon, USA, reveal Younger Dryas and 8.2 ka events. *Geology* **36** (9), 683-686.
- Wycherley H., Fleet A., and Shaw H. (1999) Some observations on the origins of large volumes of carbon dioxide accumulations in sedimentary basins. *Marine and Petroleum Geology* **16** (6), 489-494.
- Xu T., Sonnenthal E., and Bodvarsson G. (2003) A reaction-transport model for calcite precipitation and evaluation of infiltration fluxes in unsaturated fractured rock. *Journal of Contaminant Hydrology* **64** (1-2), 113-127.
- Yielding G., Freeman, B., Needham, D. T. (1997) Quantitative fault seal prediction. *AAPG Bulletin* **81** (6), 897-917.
- Yielding G. (2002) Shale Gouge Ratio- calibration by geohistory. In *Hydrocarbon Seal Quantification*, **11** A. G. Koestler and Hunsdale, R. (eds.), 1-15. Elsevier.
- Yokoyama T., Makishima A., and Nakamura E. (1999) Separation of Thorium and Uranium from Silicate Rock Samples Using Two Commercial Extraction Chromatographic Resins. *Analytical Chemistry* **71** (1), 135-141.
- Zaihua L., Svensson U., Dreybrodt W., Daoxian Y., and Buhmann D. (1995) Hydrodynamic control of inorganic calcite precipitation in Huanglong Ravine, China: Field measurements and theoretical prediction of deposition rates. *Geochimica et Cosmochimica Acta* **59** (15), 3087-3097.
- Zentmyer R., Myrow P. M., and Newell D. L. (2008) Travertine deposits from along the South Tibetan Fault System near Nyalam, Tibet. *Geological Magazine* **145** (6), 753-765.
- Zhang D. D., Zhang Y., Zhu A., and Cheng X. (2001) Physical Mechanisms of River Waterfall Tufa (Travertine) Formation. *Journal of Sedimentary Research* **71** (1), 205-216.
- Zhao J.-x., Yu K.-f., and Feng Y.-x. (2009) High-precision ^{238}U - ^{234}U - ^{230}Th disequilibrium dating of the recent past: a review. *Quaternary Geochronology* **4** (5), 423-433.
- Zhu C., Waddell R. K., Jr., Star I., and Ostrander M. (1998) Responses of ground water in the Black Mesa basin, north-eastern Arizona, to paleoclimatic changes during the late Pleistocene and Holocene. *Geology* **26** (2), 127-130.
- Zoback M. L. and Zoback M. D. (1989) Tectonic stress field of the continental U.S. In *Geophysical Framework of the Continental United States*, GSA Memoir. **172** L. Pakiser and W. Mooney (eds.), 523-539.
- Zoback M. D. and Zoback M. L. (1991) Tectonic stress field of North America and relative plate motions. In *The Geology of North America, Decade Map, Neotectonics of North America* **1** B. Slemmons (ed.), 339-366.
- Zweigel P., Arts R., Lothe A. E., and Lindeberg E. B. G. (2004) Reservoir geology of the Utsira Formation at the first industrial-scale underground CO₂ storage site (Sleipner area, North Sea). *Geological Society, London, Special Publications* **233** (1), 165-180.